Simplified Numerical Modelling Strategies to Assess Tunnelling-Induced Damage to Masonry Buildings



Derya Burcu GÜLEN

University of Oxford

Department of Engineering Science

Christ Church

A thesis submitted for the degree of

Doctor of Philosophy

Trinity 2023

Simplified Numerical Modelling Strategies to Assess Tunnelling-Induced Damage to Masonry Buildings

Derya Burcu Gülen
Christ Church, University of Oxford

A thesis submitted for the degree of Doctor of Philosophy
Trinity Term 2023

Abstract

The tunnelling industry is growing rapidly and requires significant excavation work under congested cities to supply the increasing demands of urban populations. Thus, the effects of tunnelling-induced ground movements on nearby structures need to be assessed efficiently. Although detailed three-dimensional (3D) finite element (FE) models allow engineers to investigate the tunnel-soil-structure interaction at high fidelity, they require significant computational and material characterisation effort to perform the analyses. Due to the time and cost-related restrictions in industrial projects, these complex 3D FE models are generally applied only in special cases (e.g. historical structures). Otherwise, the buildings exposed to tunnelling-induced ground movements are typically assessed using a simple elastic Timoshenko beam approach, which completely neglects critical features of building and soil-structure interaction behaviour. An alternative numerical modelling approach is needed, which provides more detail on the building response compared to the simple elastic beam model in a computationally efficient manner. Thus, an equivalent frame modelling approach with deformable connectors ('EQFdc model') is developed in this thesis. The EQFdc model represents the masonry building geometry in terms of deformable spandrels, piers and connector elements, in which the building idealisation method significantly decreases the

number of elements required to model the masonry building compared to the FE continuum models in a computationally efficient way. The EQFdc modelling approach also incorporates the critical aspects of the tunnel-soil-building interaction problem by considering the effects of façade openings, soil-structure interaction and floor structures on the building responses.

This thesis explores a single orthogonal tunnel scenario constructed under a two-storey masonry façade with a strip footing founded on a typical London soil profile. The tunnel-soil-building interaction problem is examined for three different cases: the first one refers to linear elastic façade and linear elastic soil models, the second case adopts a nonlinear soil model combined with the elastic façade model and the final case is composed of nonlinear façade and nonlinear soil models. The tunnelling scenario adopted in each case study is investigated for varying tunnel eccentricities. To evaluate the EQFdc model, its analysis results are compared with reference FE continuum models. The comparisons demonstrate that EQFdc model presents excellent agreement with the reference 2D FE model for linear elastic behaviour. This indicates that the linear elastic EQFdc model can be an additional tool after conducting the simple elastic beam model used in the damage assessment procedures. In the case of nonlinear analyses, the EQFdc model successfully captures the overall building responses in terms of the displacements, major principal tensile strain distributions and plastic failure locations. As a result, the nonlinear EQFdc model can be considered a computationally efficient, intermediate complexity level tunnelling-induced damage assessment method that can be used as an additional assessment tool before adopting advanced 3D FE models.

In addition to the numerical case study comparisons, the building responses measured from settlement tests on half-scale buildings as part of a collaborative project are simulated with the EQFdc model. The EQFdc model responses are compared with the experimental results for the building specimens with varying self-weights, façade openings and floor structures. The displacements and damage distributions are shown to be captured by the EQFdc model.

Acknowledgements

A DPhil constitutes a challenging journey and I am thankful for the people who supported and encouraged me during my time at Oxford.

First, I would like to express my deepest gratitude to my supervisors, Prof. Sinan Acikgoz and Prof. Harvey Burd, for their invaluable supervision, insightful feedback and enormous support during my DPhil study. I would like to thank Sinan for consistently providing great support, offering thought-provoking solutions and for allowing me to gain hands-on experience in structural monitoring systems through a large-scale experimental project in addition to my numerical research. I am very grateful to Harvey for his thoughtful critiques, constructive suggestions and patience in teaching. I have gathered a wealth of knowledge from their expertise during our research discussions. This extends not only to my specific research area but also to cultivating a critical approach to efficiently solving complex engineering problems and effectively communicating these solutions in an accessible manner. I am also deeply grateful to my examiners, Prof. Giulia Viggiani and Prof. Barbara Rossi, for reviewing my thesis, facilitating an intellectually stimulating viva examination and providing constructive feedback.

Second, I would like to thank Dr. Marialuigia Sangirardi for all her valuable contributions to my work, especially for providing PLAXIS analysis results for the numerical validation of my model. It was always a pleasure to work with her in this collaborative work. I also want to thank my colleague, Asst. Prof. Deniz Dalgic, from the Izmir Institute of Technology in Turkey, for his supervision and great effort in our collaboration for the Turkey settlement tests project. Also, I thank my colleague, Yiyan Liu, especially for our collaborative effort in the preparation period before the fieldwork in Turkey and for his contribution to data validation and curation for the DIC measurements after the experiments.

I would also like to thank my professors from Istanbul Technical University, Prof. Recep İyisan, Assoc. Prof. Ece Bayat and Assoc. Prof. İsmail Hakkı Aksoy, for all their support and encouragement during my DPhil application process.

Third, my research was funded by the Department of Engineering Science, EPSRC and my college, Christ Church. I am grateful for their financial support.

I am very thankful for the amazing people I met in Oxford and all the wonderful moments and inspiring discussions we shared. I want to thank my dear college friends. Especially to Mark IJspeert, who shared this journey with me since our fresher's week on all good and difficult days. I deeply appreciate all his support, patience and kindness during the most stressful times, particularly during my thesis submission and viva exam days. Also, Georgios Vacalis, with whom we discussed topics ranging from the DPhil life to the common aspects of our cuisines and cultures. I am very grateful for all his encouragement and friendship. I would also like to thank my dear friends Zeynep Kaya, Ceren Yalaz and Noura Regli, who were always there during the most fun and tough times. I am sincerely thankful for all their kindness and support. Especially for Noura, who shared the stress of the final year with me and kept me motivated in all difficult days. I always felt the privilege of meeting people from diverse cultural and intellectual backgrounds through my college, department and various social events.

Finally, I am deeply thankful to my family in Istanbul, my parents and my brother. I am grateful for all their endless support during these years. This achievement would not have been possible without their care, love and encouragement.

This DPhil thesis is dedicated

to my dear family in Istanbul,

with enormous gratitude for all their support during this journey…

and

to the people who lost their lives in the earthquakes on 6th February 2023 in Turkey.

Their loss deeply saddened my heart while I was writing this thesis…

With sincere respect to their beloved memories and

with the hope to learn from the mistakes of the past to build a better future

under the guidance of science and engineering…

Oxford 2023

Contents

Abstract ..... **i**
Acknowledgements ..... **iii**
1 Introduction **1**
1.1 Background 1
1.2 Research Objectives 5
1.3 Research Scope 6
2 Literature Review **8**
2.1 Tunnelling-Induced Damage Assessment Procedures 8
2.1.1 Stage 1 assessment 10
2.1.2 Stage 2 assessment 10
2.1.3 Stage 3 assessment 13
2.2 Modelling Strategies Overview 13
2.3 Modelling Tunnelling-Induced Ground Movements 16
2.3.1 Empirical equations 18
2.3.2 Finite element models for ground movements 20
2.4 Modelling Masonry Building 21
2.4.1 Modelling complete building 21
2.4.1.1 Finite element continuum models 21
2.4.1.2 Macro-element models 24
2.4.1.3 Equivalent frame models 25
2.4.1.4 Equivalent solid models 29
2.4.1.5 Equivalent beam models 30
2.4.2 Modelling masonry material: model scale 31

2.4.2.1 Micro-scale 31
2.4.2.2 Meso-scale 32
2.4.2.3 Macro-scale 33
2.4.3 Modelling masonry material: constitutive models 34
2.4.3.1 Linear elastic models 34
2.4.3.2 Nonlinear models 35
2.5 Modelling Soil-Structure Interaction 37
2.5.1 Finite element soil-foundation models 38
2.5.2 Winkler soil-foundation models 40
2.5.2.1 S2M soil-foundation interaction model 41
2.6 Outcomes of Literature Review 45
3 Formulation of Equivalent Frame Model with Deformable Connectors 49
3.1 Introduction 49
3.2 Preliminary Work 50
3.2.1 Equivalent frame model with rigid connectors 50
3.2.2 Macro-element model 51
3.3 EQFdc Model Overview 53
3.4 Formulation of Flexibility-Based Elements 55
3.4.1 Global and reduced degrees of freedom 55
3.4.2 Virtual work for a single-beam element 59
3.4.3 Flexibility and stiffness matrices 60
3.4.4 Internal stress and strain resultants 62
3.4.5 Application of self-weight loads 63
3.5 Formulation of Stiffness-Based Elements 65
3.5.1 Quad Elements 65
3.5.1.1 Kinematics 66
3.5.1.2 Internal forces and stiffness matrix 69

3.5.1.3 External forces....69
3.5.2 Footing Elements....70
3.5.2.1 Kinematics....70
3.5.2.2 Internal forces and stiffness matrix....71
3.5.2.3 External forces....71
3.5.3 Structural Interface Elements....71
3.5.3.1 Kinematics....71
3.5.3.2 Internal forces and stiffness matrix....77
3.6 Determination of Strain Distributions....80
3.6.1 Macro-elements....80
3.6.2 Beam elements....82
3.7 Conclusion....83
4 EQFdc Analysis: Solution Procedure....84
4.1 Introduction....84
4.2 Global Level Iteration....84
4.3 Element Level Iteration....87
4.4 Gauss Point Level Iteration....89
4.5 Conclusion....93
5 EQFdc Model: Linear Elastic....94
5.1 Introduction....94
5.2 Flexibility-Based Elements: Linear Elastic Model....94
5.2.1 Fibre beam model....94
5.2.2 Beam shear model....95
5.3 Elastic Beam Element Numerical Validations....95
5.3.1 Test problem – 1: simply supported beam....97
5.3.2 Test problem – 2: fixed-end supported beam....102
5.4 Stiffness-Based Elements: Linear Elastic Model....106
5.4.1 Quad elements....106

5.4.2 Structural interface elements 106
5.5 Conclusion 107
6 EQFdc Model: Nonlinear 108
6.1 Introduction 108
6.2 Flexibility-Based Elements: Nonlinear Model 108
6.2.1 Fibre beam model 109
6.2.1.1 Fibre beam model: modelling procedure 109
6.2.1.2 Fibre beam model: tensile strength 111
6.2.2 Beam shear model 112
6.2.2.1 Beam shear model: modelling procedure 112
6.2.2.2 Beam shear model: shear force 115
6.3 Stiffness-Based Elements: Nonlinear Model 116
6.3.1 Quad shear model 116
6.3.1.1 Quad shear model: modelling procedure 116
6.3.1.2 Quad shear model: shear strength 117
6.3.2 Structural interface tension model 118
6.3.2.1 Structural interface tension model: modelling procedure 118
6.3.2.2 Structural interface tension model: tensile strength 119
6.4 Conclusion 120
7 Assessment of EQFdc Model: Linear Analysis 121
7.1 Introduction 121
7.2 Problem Definition 122
7.2.1 Building and tunnel configuration 122
7.2.2 Loading scenario 122
7.2.3 Masonry material properties 124
7.2.4 Soil and foundation properties 124
7.3 DIANA Model Implementation 125
7.3.1 Building model 125

7.3.2 Soil-foundation interaction model 126
7.3.3 Analysis procedure 126
7.4 EQFdc Model Implementation 127
7.4.1 Building model 127
7.4.2 Soil-foundation interaction model 127
7.4.3 Analysis procedure 127
7.5 Results Data Processing 128
7.5.1 DIANA model 129
7.5.2 EQFdc model 132
7.6 Results and Comparisons 133
7.6.1 Displacement responses 133
7.6.1.1 Building response to self-weight loading 133
7.6.1.2 Building response to greenfield displacements 135
7.6.2 Soil traction responses 136
7.6.2.1 Soil traction response to self-weight loading 136
7.6.2.2 Soil traction response to total loading 137
7.6.3 Major principal tensile strain responses 138
7.6.4 Variation of maximum tensile strain with tunnel eccentricity 140
7.7 Conclusion 141
8 Assessment of EQFdc Model: Nonlinear Analysis 142
8.1 Introduction 142
8.2 Problem Definition 143
8.2.1 Building and tunnel configuration 145
8.2.2 Loading scenario 145
8.2.3 Masonry material properties: EL façade 145
8.2.4 Masonry material properties: NL façade 145
8.2.5 Soil and foundation properties 146

8.3 PLAXIS Model Implementation 147
8.3.1 Building model 147
8.3.1.1 Building model: EL façade 147
8.3.1.2 Building model: NL façade 147
8.3.2 Soil-foundation interface model 148
8.3.3 Analysis procedure 148
8.4 S2M Model Implementation 149
8.4.1 Building model 149
8.4.2 S2M soil-foundation interaction model 149
8.4.3 Calibration analyses for the S2M soil-foundation interaction model 149
8.4.4 Analysis procedure 150
8.5 EQFdc Model Implementation 151
8.5.1 Building model 151
8.5.1.1 Building model: EL façade 151
8.5.1.2 Building model: NL façade 151
8.5.2 S2M soil-foundation interaction model 152
8.5.3 Analysis procedure 153
8.6 Results Data Processing 153
8.6.1 PLAXIS model 153
8.6.2 S2M model 154
8.6.3 EQFdc model 155
8.7 Results and Comparisons: EL façade 155
8.7.1 Displacement responses 155
8.7.2 Major principal tensile strain responses 160
8.7.3 Variation of maximum tensile strain with tunnel eccentricity 166
8.8 Results and Comparisons: NL façade 167
8.8.1 Displacement responses 167

8.8.2 Major principal tensile strain responses 170
8.8.3 Plastic failure responses 173
8.9 Conclusion 175
9 Comparison of EQFdc Model with Settlement Tests 178
9.1 Introduction 178
9.2 Experimental Setup 179
9.2.1 Tunnelling scenario and settlement application 179
9.2.2 Building classifications 181
9.2.3 Building material properties and scaling 185
9.3 Monitoring Measurement Techniques 185
9.3.1 FBG sensor strain measurements 185
9.3.2 DIC displacement measurements 188
9.4 Instrumentation Designs 189
9.4.1 FBG sensor laboratory calibration tests 189
9.4.1.1 FBG mechanical strain calibrations 189
9.4.1.2 Temperature compensation FBG sensors 191
9.4.2 FBG sensor and DIC monitoring setup 193
9.5 EQFdc Model Implementation 196
9.5.1 EQFdc model idealisations 196
9.5.2 Loading scenario 198
9.5.3 Steel-building interface model 199
9.5.4 Masonry constitutive model 200
9.6 Interpretation of DIC and FBG Measurements 201
9.7 Results and Comparisons 202
9.7.1 3O-RF-W1 test and analysis results 202
9.7.2 3O-RF-W3 test and analysis results 205
9.7.3 5O-RF-W1 test and analysis results 209

9.7.4 3O-JF-W1 test and analysis results 211
9.8 Conclusion 215
10 Conclusion 217
10.1 Research Contributions 217
10.1.1 Development of EQFdc modelling approach 217
10.1.2 Development of soil-structure interaction modelling approach 219
10.1.3 Practical representation of nonlinear masonry behaviour 221
10.1.4 Settlement tests on half-scale buildings 221
10.2 Validation of Numerical Model and Key Results 222
10.2.1 Linear elastic analysis comparisons 223
10.2.2 Nonlinear analysis comparisons: elastic façade 223
10.2.3 Nonlinear analysis comparisons: nonlinear façade 224
10.2.4 Nonlinear analysis comparisons: experimental results 225
10.3 Recommendations for Future Work 225
10.3.1 Improvements in nonlinear masonry models 225
10.3.2 Exploring building geometries with irregular openings 226
10.3.3 Modelling complete building with the EQFdc model 226
10.3.4 Investigating the effects of skew tunnelling and tunnel progression 227
10.3.5 Potential improvements to S2M soil-foundation interaction model 227
10.4 Final Research Outcomes 228
References 229

Chapter 1

Introduction

1.1 Background

According to a Tunnel Market Survey by the International Tunnelling and Underground Space Association (2019), the tunnelling industry is growing around 9% annually globally. Specifically, over 240 transportation projects have been planned in the UK for the next decade (Analysis of the National Infrastructure and Construction Pipeline, 2017). The High Speed 2 project (estimated cost in 2023 is more than £50bn according to the Department for Transport's Report) and the Bakerloo Extension upgrade project (estimated cost in 2017 prices was between £4.7bn to £7.9bn according to Bakerloo Line Extension Background to Consultation Summary Report, 2019) are two examples of major transportation projects involving underground construction.

Tunnelling allows the urban environment to be used effectively to provide solutions to transportation, pipeline, sewer and energy systems. However, the effect of tunnelling-induced ground movements on nearby structures needs to be assessed adequately. The ground displacements caused by tunnels, shafts or deep excavations can lead to the formation of cracks, particularly in masonry buildings, which offer limited resistance in tension. The crack widths can vary from fine cracks (e.g. < 1 mm) that can be repaired by normal decoration to large

splitting cracks (e.g. > 25 mm) that can threaten structural serviceability and require major repair or reconstruction (Burland & Wroth, 1974; Boscardin & Cording, 1989). The damage classes in masonry buildings are classified from 'very slight' to 'very severe' according to the standard building damage classification system presented in Table 1.1 (Burland & Wroth, 1974; Boscardin & Cording, 1989).

The existing tunnelling-induced damage risk assessment procedures mainly focus on masonry structures. According to the English Housing Survey (2008), approximately 90% of the English housing stock comprises load-bearing masonry buildings built on mostly shallow foundations. In addition, major civil and religious buildings, are typically constructed of masonry. For example, Macchiarulo et al. (2019) evaluated the buildings affected by the Crossrail tunnelling project in an area of 25 km^2 between Paddington to Farringdon stations in London; the authors stated that 68% of 1036 buildings are composed of load-bearing masonry structures, 93% of which have shallow foundation systems.

Table 1.1: Standard building damage classification system (Burland & Wroth, 1974; Boscardin & Cording, 1989).

Category of damage	Damage class	Ease of repair of visible damage	Approximate crack width (mm)	Limiting tensile strain levels (ε_{lim}) (με)
0	Negligible	No need	< 0.1	0 − 500
1	Very slight	Normal decoration	0.1 − 1	500 − 750
2	Slight	Probable redecoration and repainting	1 − 5	750 − 1500
3	Moderate	Small replacement	5 − 15	1500 − 3000
4	Severe	Extensive replacement	15 − 25	> 3000
5	Very severe	Major repair or rebuilding	> 25	> 3000

In current engineering practice, damage due to tunnelling-induced ground movements is assessed in three stages. Stage 1 provides a preliminary assessment to identify buildings potentially affected by ground surface settlements (Rankin, 1988). In Stage 2, an intermediate-level assessment is performed by determining the tensile strains expected in the building using

simple elastic beam models for the building and without considering soil-structure interaction (Burland et al., 1977; Boscardin & Cording, 1989). If a building's damage class is assessed as more than 'slight' (at least a small replacement is required to repair the damage as shown in Table 1.1), then detailed assessments, which are generally based on using 3D finite element (FE) models need to be performed in Stage 3 (Mair et al., 1996). For example, for the Crossrail project (Torp-Petersen & Black, 2001):

- More than 1200 buildings required an intermediate-level assessment at the end of Stage 1 assessment.
- As a result of the Stage 2 assessment, 220 buildings were classified in the 'moderate' or 'severe' to 'very severe' damage classes and required detailed assessments based on FE analysis. Another 208 buildings were also examined in Stage 3 assessments due to their historical significance.
- After the Stage 3 assessment, it was concluded that 68 buildings would potentially be subjected to either 'severe' or 'very severe' damage. These buildings required further investigation for damage mitigation.

The existing building damage assessment procedures have significant drawbacks. The simple elastic beam models used for Stage 2 assessments only require simple hand calculations. However, they neglect the critical influence of the effect of façade openings and the soil-structure interaction on the severity and location of potential damage. Due to these reasons, simple elastic beam models are not necessarily conservative. Detailed two or three-dimensional (2D or 3D) FE models are typically used in Stage 3 assessments. In contrast to the simple elastic beam models used in Stage 2 assessments, these models can consider key aspects of the tunnel-soil-building interaction problem but are computationally expensive. The computational time (in addition to effort required for the system and material identifications) required to carry out a single soil-structure interaction analysis may vary from several hours to days, depending

on the complexity of the modelling detail adopted for the assessment.

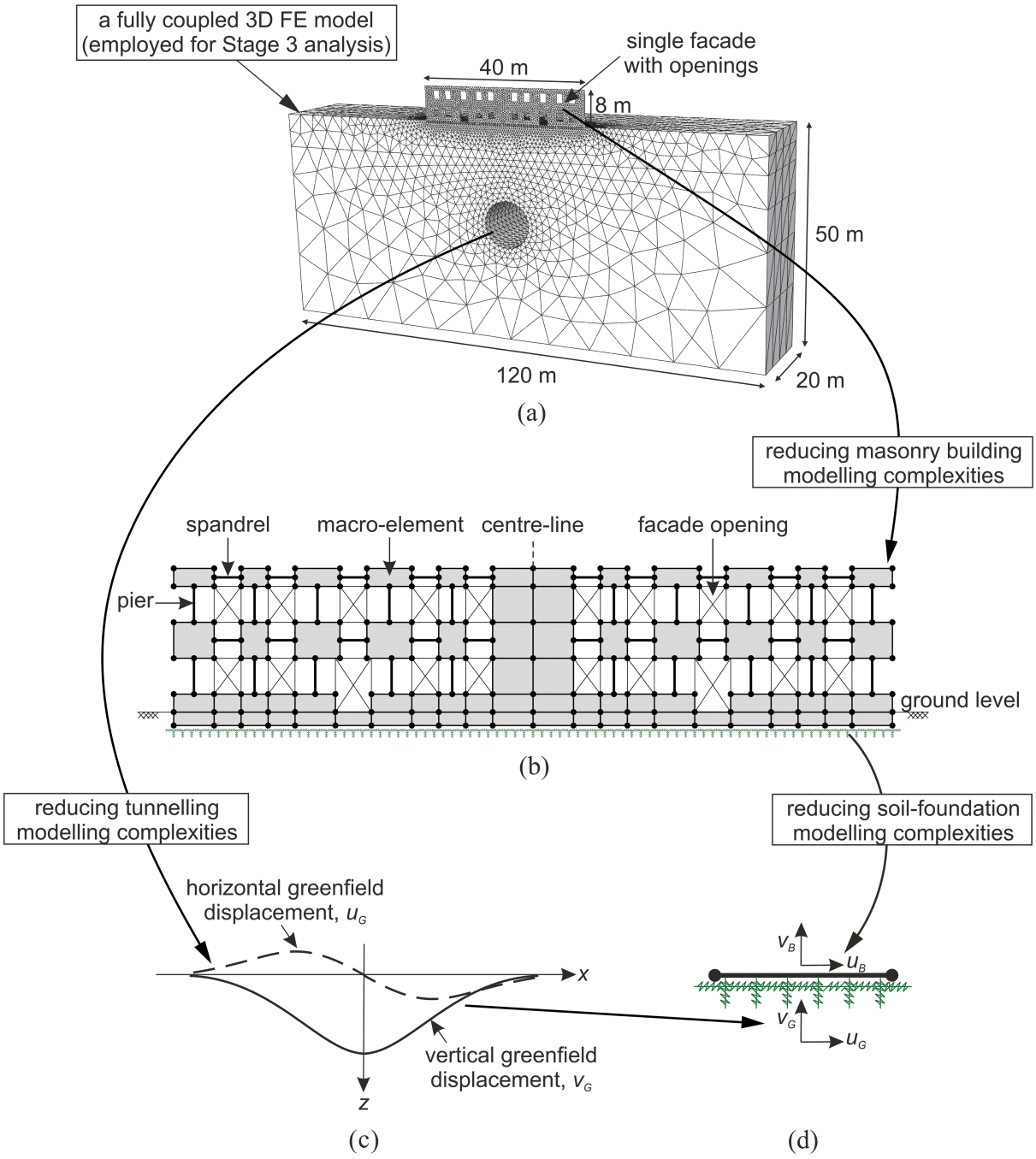


Figure 1.1: Proposed modelling approach: (a) a fully coupled 3D FE model featuring tunnel-soil-building modelling details (employed for Stage 3 analysis) (Yiu et al., 2017a), (b) EQFdc model idealisation of the façade, (c) prescribed tunnelling-induced ground displacements used as input data, (d) representation of the soil-foundation interaction.

It is important that assessment models are computationally efficient so that the large number of buildings affected by a major project can be assessed. Developing, running and evaluating

detailed 3D FE models in Stage 3 often require significant resources (in terms of time and cost). Due to this reason, practising engineers prefer to perform building damage assessments using simple elastic beam models whenever possible, despite their well-known limitations (e.g. disregarding the effects of soil-structure interaction and façade openings). There is a need to develop modelling tools that can represent building response more realistically than the simple elastic beam model while requiring computationally less effort than advanced 3D FE models.

1.2 Research Objectives

The research in this thesis aims to develop an intermediate-level damage assessment approach (Figure 1.1) that provides more detail on the building and soil behaviour than the simple elastic beam models used in Stage 2 while requiring less computational effort than the detailed complex FE models used in Stage 3. This research particularly addresses masonry buildings built on strip foundations in the UK. The research objectives considering the key aspects of the tunnel-soil-building interaction problem are:

1) To represent masonry building geometry with an intermediate complexity model as a combination of beams and 2D macro-elements by considering the layout of façade openings.
2) To simulate soil-structure interaction by using a 1D FE nonlinear Winkler soil-foundation interaction model.
3) To incorporate the tunnelling-induced ground displacements (determined from either using empirical models/ detailed 3D FE model/ field measurements) practically into the soil-foundation interaction model as prescribed input deformations.
4) To implement practical constitutive models to capture nonlinear masonry behaviour.
5) To validate the developed numerical models in comparison with advanced FE models and experimental results.

6) To provide visual tools to be used in the damage assessments by presenting the analysis results in terms of building displacements, soil-foundation tractions, major principal tensile strain distributions and plastic failure point locations.
7) To reduce the computational and system identification effort compared to the FE modelling techniques used in the Stage 3 assessments.

1.3 Research Scope

The thesis continues with a literature review in Chapter 2, presenting the existing tunnelling-induced damage assessment procedures and modelling methods to represent tunnelling-induced ground movements, masonry buildings and soil-foundation interactions. The formulations of the EQFdc modelling approach are explained in detail in Chapter 3. The analysis procedure employed for both linear and nonlinear models are presented in Chapter 4. The linear elastic and the nonlinear constitutive models implemented into the EQFdc model are described in Chapters 5 and 6, respectively. The subsequent chapters are organised according to the prioritised stages of damage assessment procedures, which start with linear elastic analyses and progress into nonlinear analyses. Accordingly, Chapter 7 describes the linear elastic analysis and results of the EQFdc model (elastic façade and soil model) and Chapter 8 presents two nonlinear models, where firstly, the façade is kept as elastic and the soil behaviour is modelled as nonlinear and secondly, the façade is also modelled using nonlinear constitutive relationships for masonry. The settlement experiments conducted as part of a separate collaborative project are described in Chapter 9, including comparisons between the experimental results and the EQFdc model analysis. Finally, the key research results with limitations and suggestions for future work are presented in Chapter 10.

All the numerical models developed in this research, including the building and soil-foundation interaction models, were coded as bespoke software in MATLAB R2017b. The linear elastic

model validations were performed in DIANA v10.3 finite element analyses (FEA) software (Chapter 7). The nonlinear analyses for the advanced 3D FE model were conducted in PLAXIS FEA software by Sangirardi (2023) and the results presented for 'Simplified 2D assessment Model' (S2M) were provided by Burd (2023) for this research (Chapter 8). Additionally, the settlement tests on half-scale buildings presented in Chapter 9 is a collaborative effort of Dalgic et al. (2023). Specific contributions of this DPhil research to the Turkey settlement tests project are presented in Chapter 9 in addition to the comparisons between the experimental and the numerical model results.

Chapter 2

Literature Review

The literature review is organised into six main sections. Firstly, the tunnelling-induced damage assessment procedures are explained. Secondly, an overview of the current modelling strategies used to represent the tunnel-soil-building interaction is briefly introduced. Later, the strategies employed for modelling tunnelling-induced ground movements, masonry buildings and soil-structure interactions are presented separately in three sections. The outcomes of the literature review are summarised in the final section.

2.1 Tunnelling-Induced Damage Assessment Procedures

In the current engineering practice, the risk of tunnelling-induced damage to buildings is investigated in three main phases termed Stage 1 preliminary assessment, Stage 2 simple elastic beam assessment and Stage 3 detailed evaluation (Mair et al., 1996; Burland, 2001; Harris & Franzius, 2006) as summarised in Figure 2.1. Table 1.1 presents the standard building damage classification system based on ease of repair and the relationship between the damage class and the limiting tensile strain. Firstly, Burland and Wroth (1974) proposed an empirical damage classification method to determine the serviceability and damage level of the structure due to differential settlements. The classification of visible damage was mainly based on the approximate crack widths and ease of repair of plaster, brickwork and masonry.

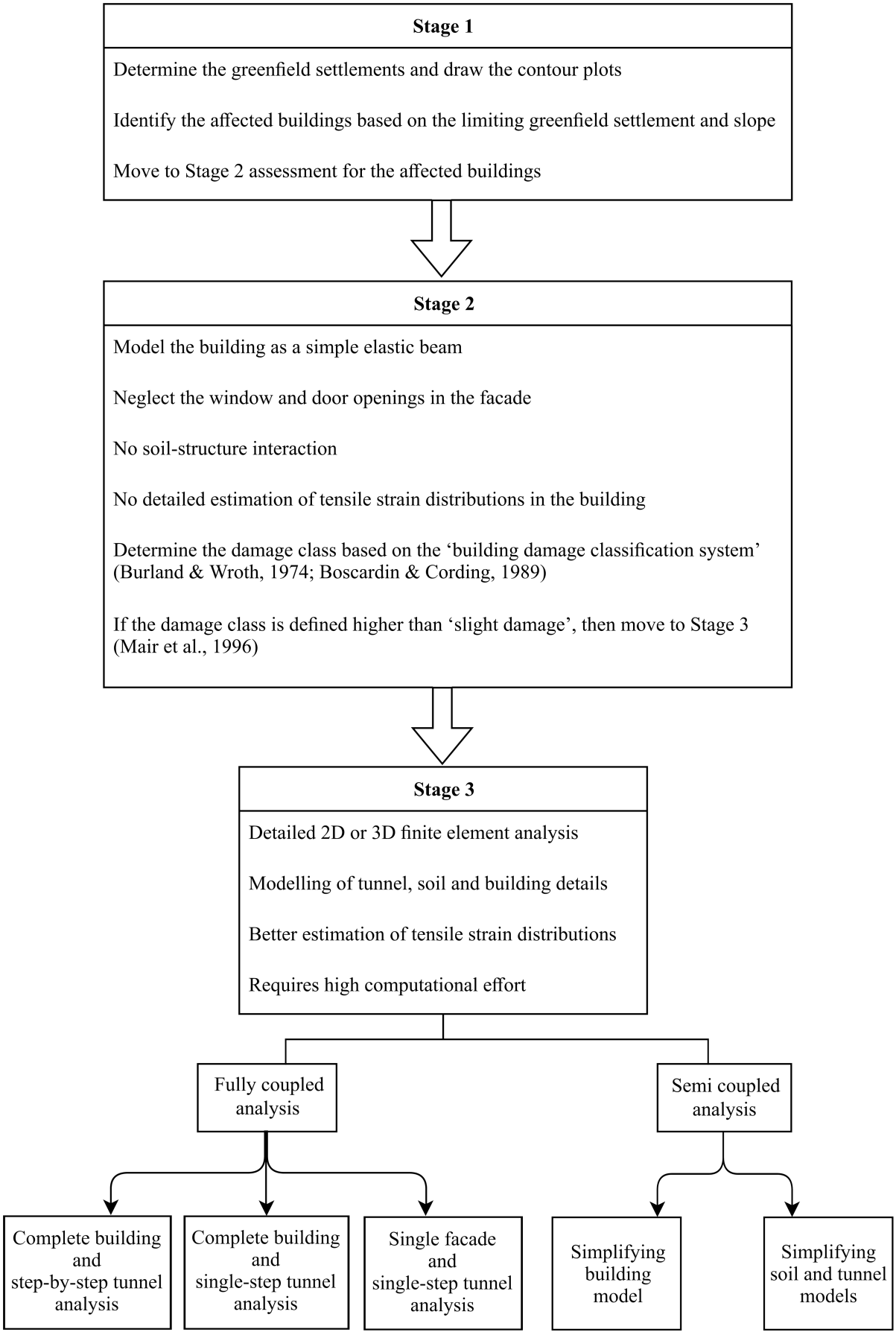


Figure 2.1: Tunnelling-induced damage assessment stages in current engineering practice.

2.1.1 Stage 1 assessment

Stage 1 involves a preliminary assessment, during which contour plots of ground surface settlements are drawn along the route of tunnel progression and buildings within a suitably defined influence zone are identified. Buildings likely to experience settlement of less than 10 mm and a maximum slope of less than 1/500 are considered to be at negligible risk of damage (Rankin, 1988). These settlement and maximum slope limits were utilized for the preliminary damage assessment of the Jubilee Line Extension in London (Burland et al., 2001). However, depending on the importance of the buildings exposed to tunnel excavations, the limits set for settlement and maximum slope can be adjusted. For instance, a maximum settlement of 5 mm was considered for the new Line C of the Rome Underground (Rampello et al., 2012). Buildings that exceed the maximum settlement and slope limits typically require further assessment in Stage 2.

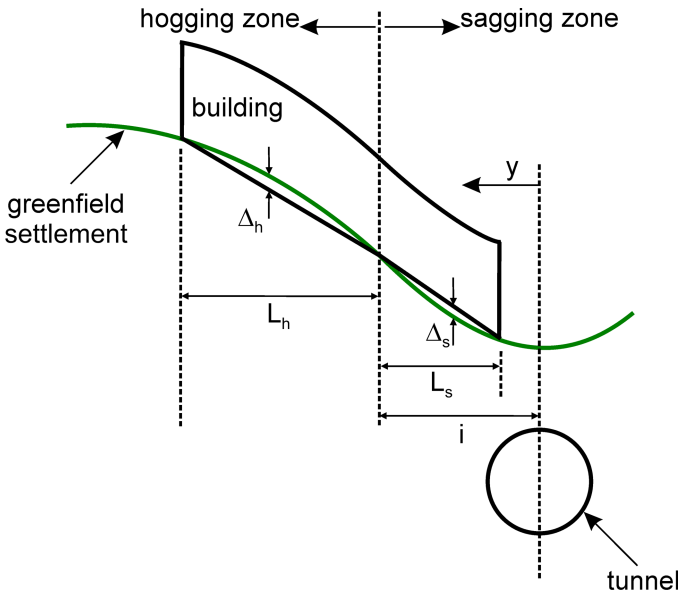


Figure 2.2: Schematic representation of the simple elastic beam model used in Stage 2 (modified from Mair et al., 1996).

2.1.2 Stage 2 assessment

In the Stage 2 assessment procedure, the masonry building is modelled as a simple elastic

Timoshenko beam without considering the effects of building stiffness, weight and soil-structure interaction (Figure 2.2). Details relating to the façade openings and foundation geometry are also neglected. The greenfield settlements and horizontal displacements at the foundation depth are imposed on the simple elastic beam model and the maximum tensile strain in the model is calculated. Burland and Wroth (1974) idealised the actual building as a rectangular Timoshenko beam with the corresponding building dimensions (i.e. length of L and height of H). For the Stage 2 assessment, the aim is to calculate the tensile strains for the deflected shape of the building foundations and to determine the deflection ratio, Δ/L, in sagging or hogging depending on the type of cracking behaviour (Burland & Wroth, 1974). To determine the limiting mode of deformation, two extreme deformation modes based on bending only about a neutral axis and shear only need to be calculated. Considering the calculation of the total mid-span deflection of a centrally loaded Timonshenko beam (Timoshenko, 1957) with unit thickness deforming in both bending and shear, Burland and Wroth (1974) demonsrated that the building is more prone to damage for the case of hogging with the neutral axis at the bottom edge of the beam than the sagging case with the neutral axis in the middle of the beam. The relationships between the deflection ratio, the maximum bending strain, $\varepsilon_{b(max)}$ and the maximum diagonal strain, $\varepsilon_{d(max)}$ are expressed as follows (Burland & Wroth, 1974; Burland et al., 1977):

$$\frac{\Delta}{L} = \left(\frac{L}{12t} + \frac{3I}{2tLH}\frac{E}{G}\right)\varepsilon_{b(max)} \tag{2.1}$$

$$\frac{\Delta}{L} = \left(1 + \frac{HL^2}{18I}\frac{G}{E}\right)\varepsilon_{d(max)} \tag{2.2}$$

where E is the Young's modulus, G is the shear modulus, I is the second moment of area of the equivalent beam (i.e. $H^3/12$ in the sagging zone and $H^3/3$ in the hogging zone) and t is the distance of the neutral axis from the edge of the beam in tension (i.e. $H/2$ in the sagging

zone and H in the hogging zone).

For a given value of limiting tensile strain, ε_{lim}, the limiting value of Δ/L (i.e. the minimum value) is determined from Equations (2.1) and (2.2) for $\varepsilon_{max} = \varepsilon_{lim}$. Burland and Wroth (1974) presented the relationship between the limiting deflection ratio normalised by ε_{lim}, $(\Delta/L)/\varepsilon_{lim}$ and the building dimension ratio, L/H for the rectangular isotropic beams (E/G = 2.6 for the Poisson's ratio, ν = 0.3) with the neutral axis at the bottom edge as follows: while the diagonal strains (Equation 2.2) govern the building damage behaviour for the case of $L/H < 1.5$, the bending strains (Equation 2.1) are dominant for the values of $L/H > 1.5$.

In addition to the calculation of tensile strains induced by the ground settlements, Boscardin and Cording (1989) expressed the resultant extreme fibre strain, ε_{br} and the resultant diagonal tensile strain, ε_{dr} terms with the addition of horizontal tensile strain, ε_h induced by the horizontal ground displacements occurred at the foundation level as follows:

$$\varepsilon_{br} = \varepsilon_{b(max)} + \varepsilon_h \tag{2.3}$$

$$\varepsilon_{dr} = \varepsilon_h \left(\frac{1-\nu}{2}\right) + \sqrt{{\varepsilon_h}^2 \left(\frac{1+\nu}{2}\right)^2 + {\varepsilon_{d(max)}}^2} \tag{2.4}$$

where ν is the Poisson's ratio. Using Equations (2.3) and (2.4), the maximum tensile strain is determined as the maximum value of ε_{br} and ε_{dr}.

According to the standard building damage classification system presented in Table 1.1 (Burland & Wroth, 1974; Boscardin & Cording, 1989; Burland, 2001), if the damage class is determined as equal to or below 'slight damage' considering the limiting tensile strain level of 1500 με, no further evaluation is required (Mair et al., 1996). However, buildings that are estimated to suffer more than 'slight damage' require a detailed assessment in Stage 3 by considering the effects of building-tunnel configuration, soil-structure interaction, geometry

and material properties of building and foundation.

2.1.3 Stage 3 assessment

Stage 3 assessments comprise advanced 2D or 3D FE models incorporating an analysis of tunnel-soil-building interaction effects. The computational effort required to generate the model and perform the analysis increases with modelling complexity. The modelling approaches used in Stage 3 can be considered in terms of fully coupled and semi-coupled models. While the fully coupled models explicitly incorporate the soil, tunnel excavation and building in a 3D FE environment, semi-coupled models aim to reduce the modelling complexities by either simplifying the building model (presented in Section 2.4) or the soil model (presented in Section 2.5) and the tunnel excavation to minimise the computational effort.

2.2 Modelling Strategies Overview

To develop a computationally efficient modelling strategy for the assessment of the tunnel-soil-building interaction, the existing modelling strategies are reviewed first. Although the fully coupled models used in Stage 3 are able to capture the tunnel-soil-building interaction in detail, researchers have explored ways to reduce the required computational resource to enable practical use of these models. For instance, the modelling complexity required to compute the tunnelling-induced ground movements can be decreased from the step-by-step tunnel excavation analysis (simulating the progressive tunnel construction) (Amorosi & Sangirardi, 2021) (Figure 2.3a) to the single-step tunnel excavation analysis (modelling only the final stage of the tunnel construction) (Yiu et al., 2017a; Amorosi & Sangirardi, 2021) (Figure 2.3b). Similarly, the computational effort to model the buildings can be reduced by modelling only the single façade (‘isolated façade approach’ proposed by Yiu et al., 2017a) (Figure 2.3c) instead of the complete building.

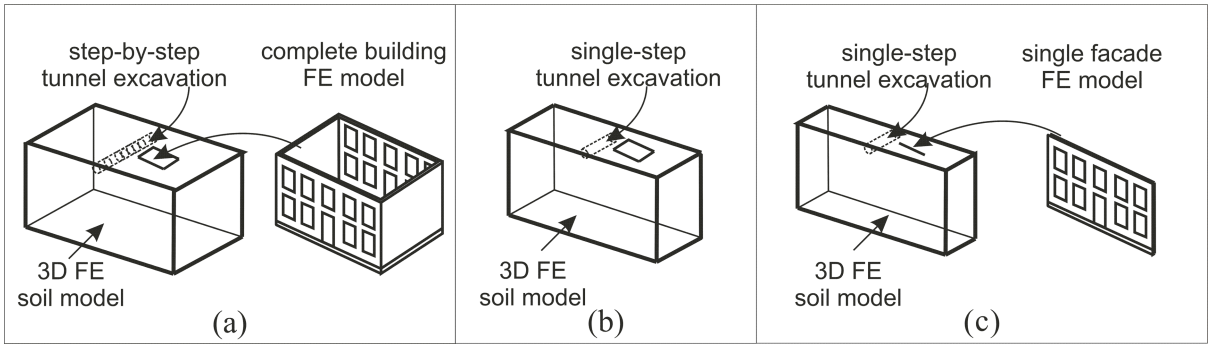
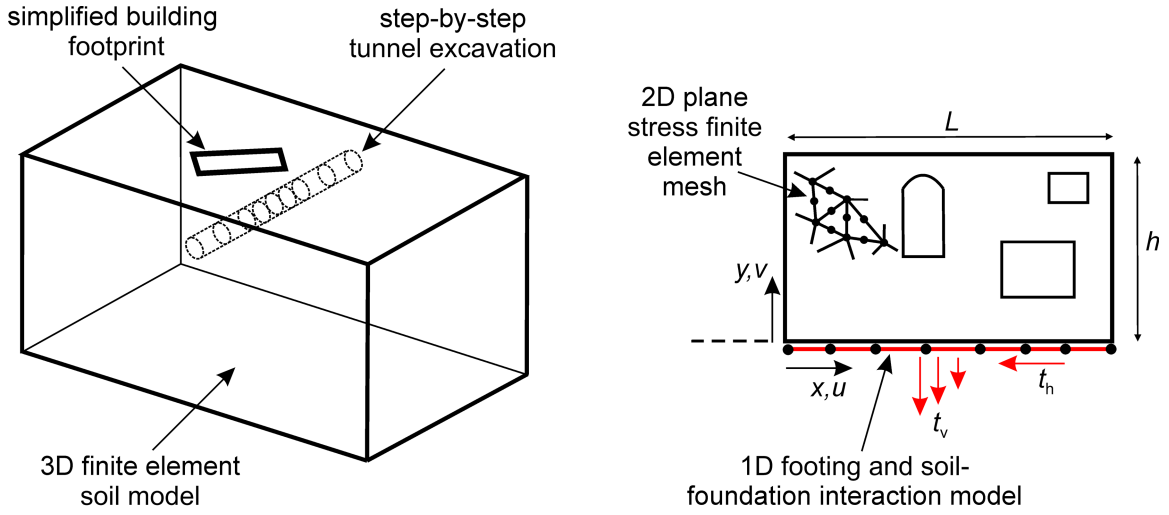


Figure 2.3: 3D FE fully coupled tunnel-soil-building interaction modelling approaches: (a) complete building and step-by-step tunnelling, (b) complete building and single step tunnelling, (c) single façade and single step tunnelling.

Amorosi and Sangirardi (2021) investigated the necessity of using fully coupled models with the complete building and step-by-step tunnel excavation instead of an isolated façade with single-step tunnel analysis. For the orthogonal tunnel scenarios (central and eccentric), Amorosi and Sangirardi (2021) stated that the single-step tunnel excavation analysis results were similar to the step-by-step tunnel analysis. Additionally, the footing displacements and damage distributions determined from the single façade analysis were similar to the complete building analysis. These results suggest that modeling the isolated façade with single-step tunnel excavation is generally sufficient to determine the tunnel-soil-building interaction behavior efficiently for the orthogonal tunnel cases. However, Amorosi and Sangirardi (2021) noted that the loading and unloading stages during progressive tunnel excavation significantly affect the damage class and damage distribution on buildings for the skew tunnel cases with angles of 45° and 60° (where the skew angle is defined on the building plan view as the angle with the horizontal axis when the building rotates clockwise). Therefore, conducting step-by-step tunnel excavation analysis was essential to determine the transient effects of progressive tunnel excavation on building damage response. However, in this thesis, only the orthogonal tunnel excavation scenario (including central and eccentric cases) is considered. Thus, representing the building as an isolated façade and considering the ground movements induced by the single-step tunnel excavation is chosen as the modelling strategy to model an orthogonal

tunnel excavation scenario under a masonry building (Chapters 3, 7 and 8). Additionally, the PLAXIS model based on the isolated façade with single-step tunnel excavation analysis (Amorosi & Sangirardi, 2021; Sangirardi, 2023) is chosen as the reference model to compare with the nonlinear analysis results determined from the numerical model developed in this thesis (Chapter 8).

As an alternative method to reduce the computational effort required for the fully coupled models, semi-coupled modelling techniques have been developed (Pickhaver et al., 2010; Giardina et al., 2013; Losacco et al., 2014; Dalgic et al., 2018; Burd et al., 2022; Pascariello et al., 2023). The semi-coupled models propose simplifying the building (e.g. Figure 2.4a) or the soil model (e.g. Figure 2.4b), in which the methods are reviewed in following Sections 2.4 and 2.5. In the developed numerical modelling approach, both the building and the soil models are simplified (Chapter 3).



(a) (b)

Figure 2.4: Semi-coupled tunnel-soil-building interaction modelling approaches: (a) simplifying the building model, (b) simplifying the soil model (modified from Pickhaver et al., 2010 and Burd et al., 2022 respectively).

Modelling strategies employed for tunnel-soil-building interaction are discussed below in separate sections in terms of modelling tunnelling-induced ground movements, masonry

buildings and soil-foundation interaction. As an overview, recent studies in the literature with the employed tunnel-soil-building modelling strategies are presented in Table 2.1.

2.3 Modelling Tunnelling-Induced Ground Movements

The construction of shallow tunnels causes vertical and horizontal ground movements in the surrounding soil (Figure 2.5). Tunnelling-induced ground movements determined immediately after the tunnel excavation are referred as short-term displacements (Rankin, 1988). Determining the short-term effects of tunnelling-induced ground displacements is important to investigate the immediate damage that might occur in the buildings during or after the tunnel excavation. The tunnelling-induced ground displacements determined on the ground surface or at the depth of foundation in the absence of a building are referred as greenfield displacements. The short-term greenfield displacements can be estimated using empirical equations or modelling the tunnel excavation using 2D or 3D FE analysis.

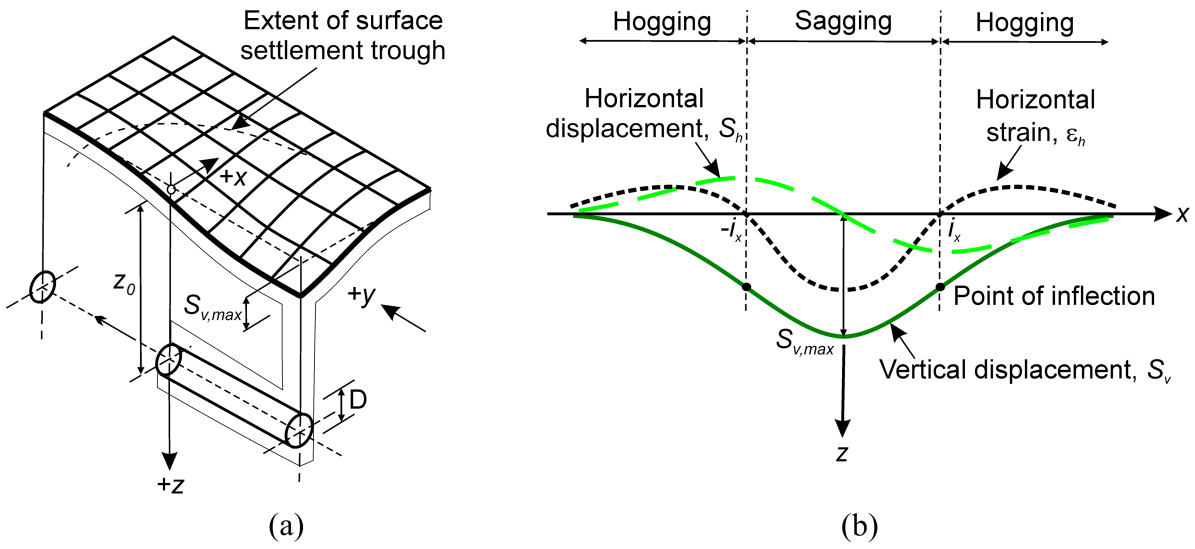


Figure 2.5: Tunnelling-induced ground movements: (a) greenfield settlements above the tunnel excavation progress (reproduced from Attewell et al., 1986), (b) greenfield displacements and strains shortly after tunnelling (reproduced from O'Reilly & New, 1982).

Table 2.1 Recent studies with the adopted modelling strategies for tunnel-soil-building interactions.

Reference	**Modelling tunnelling-induced ground movements**	**Modelling masonry building**		**Modelling soil-structure interaction**	
		Complete building model	**Constitutive model**	**Soil-foundation model**	**Constitutive model**
Sangirardi et al. (2023)	3D FE model: single-step	3D solid elements	Isotropic linear elastic	FE interface	No-tension and frictional interface
Pascariello et al. (2023)	3D FE model: step-by-step	Equivalent solid	Orthotropic linear elastic	No interface	-
Burd et al. (2022)	Prescribed deformations	2D plane stress	Isotropic linear elastic	1D FE Winkler	Nonlinear in normal and shear directions
Amorosi and Sangirardi (2021)	3D FE model: step-by-step	3D solid elements	Jointed masonry	FE interface	No-tension and frictional interface
Dalgic et al. (2021)	Prescribed deformations	2D shell elements	Total strain rotating crack	FE interface	No-tension and frictional interface
Dalgic et al. (2018)	Prescribed deformations	3D solid elements	Linear elastic	FE interface	Linear elastic
Yiu et al. (2017a)	3D FE model: single-step	2D shell elements	Concrete damage plasticity	FE interface	No tension and frictional interface
Losacco et al. (2014)	3D FE model: step-by-step	Equivalent solid	Anisotropic linearly elastic	No interface	-
Giardina et al. (2013)	Prescribed deformations	2D plane stress elements	Total strain rotating crack	FE interface	No-tension nonlinear in the normal direction
Deck and Singh (2012)	Empirical equations	Simple beam	Linear elastic	Winkler	Linear elastic
Pickhaver et al. (2010)	3D FE model: step-by-step	Equivalent beam	Linear elastic	No foundation	-
Viggiani and Soccodato (2004)	3D FE model: step-by-step	3D finite difference	Elastic perfectly plastic, Mohr Coulomb model with tension cut off	3D finite difference	Elastic perfectly plastic with Mohr Coulomb yielding

2.3.1 Empirical equations

The Gaussian distribution model is commonly used to estimate greenfield displacements since it presents a practical approach and a good agreement with field measurements (e.g., Withers, 2001; Wan et al., 2017). The short-term settlements induced by a single tunnel in greenfield conditions (i.e. where no buildings are present) can be represented by the Gaussian distribution (Peck, 1969; Rankin, 1988; Mair & Taylor, 1997) in the form:

$$S_v = S_{v,max} e^{-\frac{x^2}{2i^2}} \tag{2.5}$$

where $S_{v,max}$ is the maximum settlement on the ground surface above the tunnel central line, x is the horizontal distance from the tunnel centre, i is the transverse distance from the tunnel centre line to the inflection point of the settlement trough curve. Figure 2.6 demonstrates the greenfield settlement trough as a Gaussian distribution curve in the transverse direction of the tunnel.

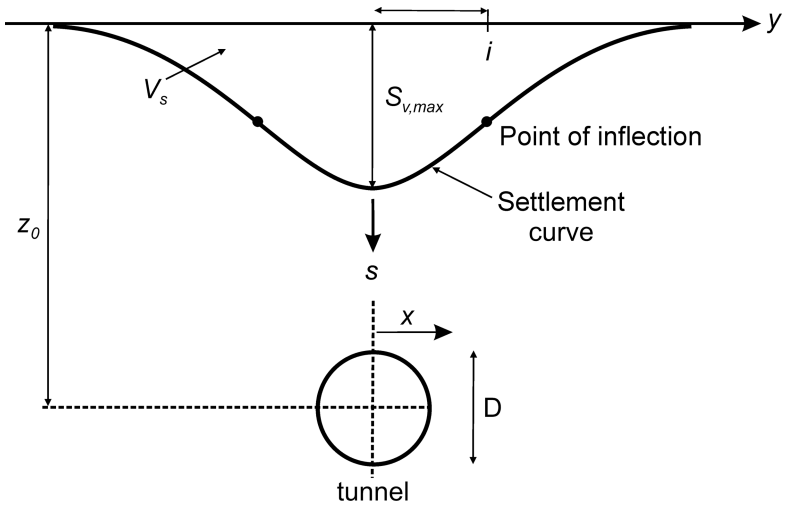


Figure 2.6: Transverse settlement trough: Gaussian curve (modified from Mair, 2013).

O'Reilly and New (1982) suggested that the horizontal displacement, S_h can be determined on the assumption that ground movements occur towards the tunnel axis. This gives,

$$S_h = \frac{S_v x}{z_0} \tag{2.6}$$

where z_0 is the depth from the ground surface to the tunnel axis. The assumption is based on considering vertical and horizontal strains as equal and opposite, under undrained conditions for the short-term deformations of fine-grained soils. Wan et al. (2017) demonstrated the consistency of this assumption with field measurements. O'Reilly and New (1982) proposed that i is linearly dependent on the tunnel depth, z_0, with a trough width parameter, K. The trough width parameter varies depending on the soil type and groundwater table level. For example, the trough width parameter changes from 0.4 to 0.7 for stiff to soft clay and from 0.2 to 0.3 for granular soils.

$$i = K z_0 \tag{2.7}$$

In tunnel construction, generally, a decrease is observed in the final tunnel volume compared to the initial volume of soil excavated for tunnelling. The soil movements towards the tunnel face and circumference cause this decrement in the final volume. This contraction is defined as tunnel volume loss; it is assumed to be equal to the settlement-induced volume loss under undrained conditions. The volume of the settlement trough, V_s, is calculated by integration of Gaussian distribution as follows:

$$V_s = \int_{-\infty}^{\infty} S_{v,max} e^{-\frac{x^2}{2i^2}} dx = \sqrt{2\pi} i S_{v,max} \tag{2.8}$$

For incompressible soil behaviour, the volume of the settlement trough is defined as settlement volume loss, V_L:

$$V_L = \frac{V_s}{\pi \frac{D^2}{4}} \tag{2.9}$$

where D is the diameter of the tunnel.

Despite the simplicity of the empirical models, they can still simulate the tunnelling-induced ground movements with high accuracy in comparison with the advanced 3D FE models, especially for the orthogonal tunnel scenarios (Yiu et al., 2017a; Amorosi & Sangirardi, 2021). In this thesis, the developed numerical model allows computing the greenfield displacements by the empirical models (Gulen et al., 2021; Gulen et al., 2022). However, the greenfield displacements determined from the reference models (i.e. advanced 3D FE models described in Chapters 7 and 8) are imposed into the developed numerical model for the direct comparison purpose for the damage assessments.

2.3.2 Finite element models for ground movements

Finite element models to compute the ground movements are employed, especially for the detailed damage assessment procedures adopted in Stage 3, where the tunnel excavation and the soil are modelled in 3D or 2D. As mentioned earlier, depending on the choice of the modelling strategy, the tunnel excavation can be simulated step-by-step or in a single-step analysis. By conducting the step-by-step analysis, the transient effect induced by the progressive tunnel excavation (Pickhaver et al., 2010; Losacco et al., 2014; Bilotta et al., 2017; Amorosi & Sangirardi, 2021) can be determined.

The main methods used to model the tunnel in the transverse plane are ‘load reduction’, ‘stiffness reduction’, ‘displacement field’ and ‘lining shrinkage’ methods. In the load reduction method, the tunnel excavation is modelled by removing the soil elements inside the excavated volume, applying an equivalent soil pressure to the tunnel periphery and gradually reducing the applied pressure (Brown & Booker, 1985). The method is defined as nodal force reduction in case of implemeting nodal forces instead of pressure to represent the effects of removed soil elements (Rowe et al., 1983). However, in the stiffness reduction method, the tunnel excavation

is reproduced by decreasing the soil stiffness (Potts & Zdravković, 2001). Alternatively, the displacement field method involves the application of defined displacements to the nodes of the soil elements at the tunnel periphery (Amorosi et al., 2014). Another technique in 2D tunnel modelling is the 'lining shrinkage' method. In this case, tunnel volume loss is simulated by applying the nodal forces (or temperature reduction) in the tunnel lining. Augarde and Burd (2001) stated that the additional stresses caused by the nodal forces do not influence the tunnel lining when modelled as an elastic material.

As the complexity of the 3D FE models in the calculation of the tunnelling-induced ground movements increases, the applicability of the models in the large number of cases decreases. Thus, practical approaches comprising empirical equations are preferred to determine the tunnelling-induced ground movements for the rapid assessments.

2.4 Modelling Masonry Building

2.4.1 Modelling complete building

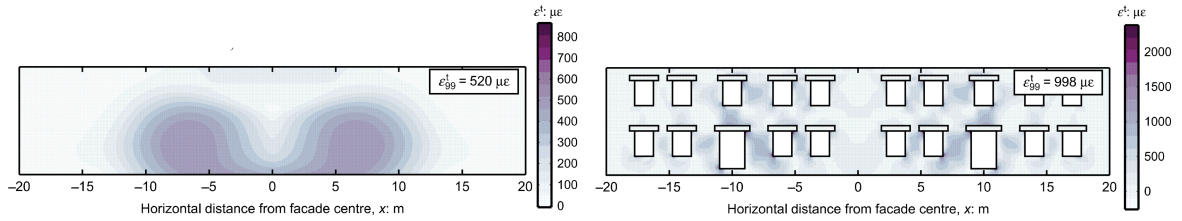
The overall geometry of the masonry buildings has been reviewed below, ranging from the advanced level of FE models to the simplified beam model.

2.4.1.1 Finite element continuum models

Finite element continuum models are used mainly when the tunnel-soil-building interaction needs to be assessed in detail. Depending on the level of complexity needs to be examined, either fully coupled 3D FE (e.g. Burd et al., 2000; Yiu et al., 2017a; Amorosi & Sangirardi, 2021) or semi-coupled (with the simplification of soil and tunnel models) 3D (e.g. Dalgic et al., 2018) or 2D FE (e.g. Giardina et al., 2013; Burd et al., 2022) analyses are conducted.

As one of the early examples of 3D FE tunnel-soil-building interaction analysis, Burd et al. (2000) modelled a masonry building consisting of two different façades (excluding the internal

walls, roof and floor) with window and door openings. The façades were modelled with 6-noded 2D plane stress triangular finite elements and each façade was connected by tie elements (Houlsby et al., 2000). The façade openings were modelled as empty spaces and the formation of the tensile failure due to local sagging effects was prevented by implementing elastic lintels over the openings.



(a) (b)

Figure 2.7: Major principal tensile strain distributions from the isolated façade analyses for a single tunnel orthogonal to the façade and passing under the façade centre: (a) plane façade, (b) façade with openings (Yiu et al. 2017a).

Yiu et al. (2017a) also conducted a fully coupled 3D FE tunnel-soil-building interaction analysis to simulate a single-step tunnel excavation under a two-storey masonry building. The building geometry was modelled in two different ways, in terms of a complete building and a single façade (i.e. isolated façade). In both cases, 6-noded shell elements were used to form the building geometry. For the complete building model, front and rear façades were connected with internal and end walls. However, floors and roof were not included in the model. For the isolated façade model, only the façade of interest was considered, where only the front façade of the building was modelled in this example. As a result of the building model comparisons, Yiu et al. (2017a) stated that the isolated façade analysis demonstrated similar results to the complete building analysis for the orthogonal single tunnel scenario. However, Prosperi et al. (2024) noted that the effect of transverse walls needs to be considered in the modelling geometry for the short buildings (e.g, a typical Dutch building), where the 2D FE isolated façade model (i.e. without transverse walls) demonstrates less damage and deformations

compared to the results determined from a 3D FE model.

The isolated façade analyses are also conducted for a plane façade and a façade with openings examples, where Yiu et al. (2017a) demonstrated that the façade with openings experienced higher damage level than the plain façade example and the high magnitude tensile strains are localised around the corners of openings (Figure 2.7). These findings highlight the effect of façade openings on the damage intensity and the distribution of tensile strains. Thus, the EQFdc model (Chapter 3) is developed in a way to consider the layout of façade openings while forming the building geometry.

Here, it is important to note that the maximum major principal tensile strain, ε_1 is a critical parameter to determine the tunnelling-induced damage in masonry buildings according to the building classification system (Burland & Wroth, 1974; Boscardin & Cording, 1989), which is still used in current engineering practice. However, the maximum ε_1 strains in the FE continuum models tend to be localised in the sharp corners of the model (Hills & Dini, 2011). Thus, as different than the reality, the corners in the FE continuum models create sudden and localised increments in the strain magnitudes at the integration points (where the mesh size is smaller than the rest of the façade) compared to the values at the nearby integration points as shown in Figure 2.7. To eliminate the strain localisations around the corners, a characteristic tensile strain ε_{99}^{t} method was used by Yiu et al. (2017a), which suggests eliminating the strains that are higher than the ones occurred in 99% of the façade area. However, the characteristic strain method might result in removing the higher strains that also exist outside of the corners, which can lead to an underestimation of the maximum ε_1 strain in the façade. Thus, a new method (Section 7.5.1), which only focuses on the extreme strains around the corners of the openings needs to be developed to estimate the damage determined from the FE continuum models.

Amorosi and Sangirardi (2021) also adopted the same tunnel-soil-building configuration scenario used by Yiu et al. (2017a) and modelled the masonry building with 3D FE solid elements (10-node tetrahedral). For the isolated façade with single-step tunnel excavation analysis, the 3D masonry façade demonstrated similar damage patterns with the façade modelled with 2D FE shell elements (Yiu et al., 2017a).

2.4.1.2 Macro-element models

Macro-elements are used to capture the response of masonry buildings exposed to earthquakes in a computationally efficient manner (D'Asdia & Viskovic, 1995; Caliò et al., 2012; Minga, 2017). For the modelling of masonry buildings with 2D macro-elements, Caliò et al. (2012) used quad elements with four rigid edges and two internal diagonal shear springs surrounded by deformable zero-thickness spring elements (Figure 2.8). The axial and flexural deformations of the macro-element occur at the surrounding spring elements, while its shear behaviour is determined by the internal springs placed diagonally across the quad. The appropriate selection of the mechanical parameters for the spring stiffness plays an important role in modelling the nonlinear behaviour of a masonry façade.

Caliò et al. (2012) stated that using a relatively coarse mesh (Figure 2.8c) in the façade discretisation process is sufficient to produce accurate results but increasing the mesh resolution (Figure 2.8d) can simulate the nonlinear behaviour of the masonry panel more precisely. Caliò et al. (2012) also defined the difference between the macro-element model and the equivalent frame modelling approaches (discussed in the next section) as the macro-element model does not require defining the pier and spandrel structural elements based on questionable crack inclination criteria (see Figure 2.10). This presents an important advantage when modelling buildings with irregularly distributed openings.

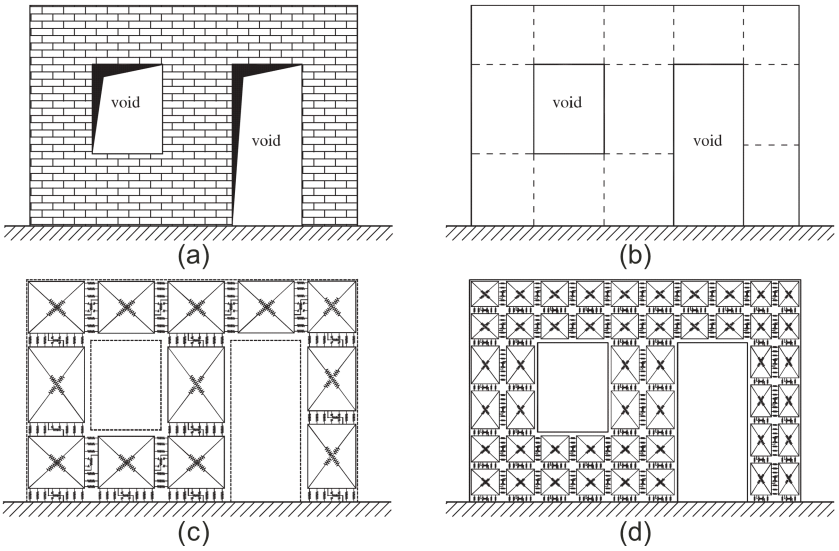


Figure 2.8: Macro-element modelling approach: (a) masonry wall, (b) determining macro-element boundaries, (c) macro-element model with coarse mesh, (d) macro-element model with fine mesh (Caliò et al., 2012).

Using macro-element models within the context of tunnelling-induced damage assessments presents specific challenges. Existing model formulations (Caliò et al., 2012) do not consider the soil-structure interaction and do not provide strain interpretations within the macro-elements, which are required to estimate the tunnelling-induced damage. To address these issues, a novel FE formulation-based macro-element model, which can estimate strains due to building movements and represent the soil-structure interaction, is developed in this thesis (Chapter 3).

2.4.1.3 Equivalent frame models

In structural earthquake engineering practice, equivalent frame (EQF) models are used to investigate the seismic response of masonry buildings (Magenes & Della Fontana, 1998; Roca et al., 2005; Belmouden & Lestuzzi, 2009; Lagomarsino et al., 2013; Bracchi et al., 2015; Quagliarini et al., 2017; Siano et al., 2018). The EQF model is typically based on the idealisation of the structures in terms of deformable structural elements (spandrels and piers) and rigid connections (Figure 2.9).

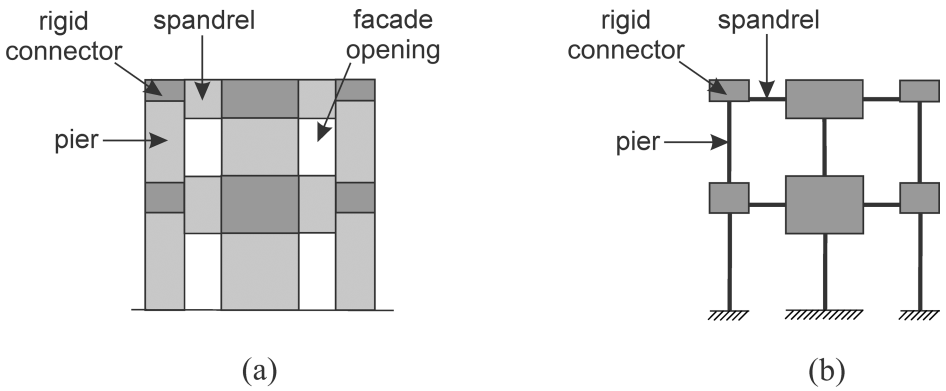


Figure 2.9: Equivalent frame idealisation of a façade with regularly distributed openings: (a) identification of spandrels, piers and rigid connectors, (b) equivalent frame model representation of the façade (reproduced from Lagomarsino et al., 2013).

To determine the element boundaries for the EQF model idealisation of a masonry façade, several methods are applied to identify the pier length as shown in Figure 2.10. In contrast, the spandrel length is determined according to the layout of façade openings. Since the EQF modelling approach is initially developed for the structural earthquake engineering practice, the idealisation of the pier length mainly depends on the crack inclination criteria (shown by black dashed lines in Figure 2.10) under seismic loading and the layout of the façade openings. However, it is convenient to adopt these methods to form the EQF model within the context of tunnelling-induced damage assessments (Section 3.2.1). In the EQF model idealization, the layout of façade openings plays an important role. For example, Augenti (2006) and Bracchi et al. (2015) proposed façade idealization methods, in which the dimensions of adjacent façade openings are used to determine the geometric boundaries of piers and spandrels defined between the openings (see Figures 2.10a-c). Additionally, Dolce (1991) and Lagomarsino et al. (2013) suggested façade idealization methods based on the propagation of cracks under earthquake loads. In these methods, crack development is assumed to start from the corners of façade openings and propagate towards the adjacent corners at varying inclination angles, which are suggested based on experimental results (see Figures 2.10d-f).

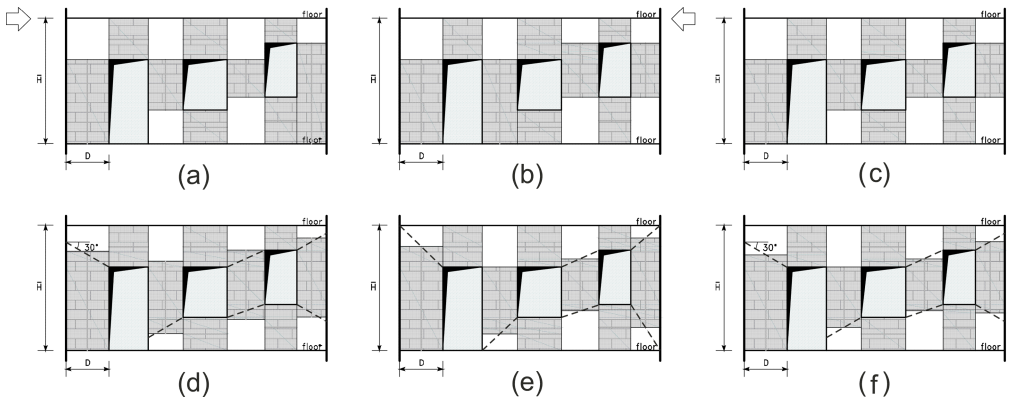


Figure 2.10: Comparisons of the methods for the determination of pier element length for the EQF model idealisation (adapted from Quagliarini et al., 2017) (grey area: deformable spandrel and pier elements, white area: rigid elements): (a) and (b) Augenti (2006) approach, (c) full rigid offsets (minimum clear height) approach (Bracchi et al., 2015), (d) Dolce (1991) approach based on crack inclination angle of 30º, (e) TREMURI approach based on the steepest inclination angle (Lagomarsino et al., 2013), (f) TREMURI with cone diffusion's limitation.

The commonly used EQF model idealisation criteria (referred to as the TREMURI approach) developed by Lagomarsino et al. (2013) assumes that in the case of earthquake loading, the propagation of cracks starts from the corner of the openings and continues with the steepest inclination angle up to the corner of the external walls, façade openings, floors or footing (Figure 2.10e). However, Bracchi et al. (2015) stated that the TREMURI approach and the other crack inclination-based criteria employed for identifying the geometry of the pier elements contain various uncertainties. Because the propagation of cracks can change according to the direction of shaking, this presents challenges, particularly for the façades with irregularly distributed openings, where the crack inclination method is harder to apply compared to the façades with regular openings. Thus, Bracchi et al. (2015) developed the full rigid offsets approach, which is only based on the layout of façade openings without considering the crack inclination criteria (Figure 2.10c). Here, it should be noted that the area defined as the rigid connectors in the full rigid offsets method (Figure 2.10c) is larger than the TREMURI approach with the steepest inclination angle (Figure 2.10e). The increased rigid area can lead to an increased building stiffness.

In conclusion, the deformable spandrel and pier elements employed for the EQF models are useful to represent the frame-like response of the masonry buildings. Their widespread adoption in the field of earthquake engineering indicates potential for industrial applications. Thus, the developed numerical model in this thesis adopts mainly the concept of idealising the masonry building according to the EQF modelling approach (Chapter 3). However, alternative solutions need to be developed in place of the rigid connectors, which can significantly affect the computation of building stiffness (Section 3.2.1). The uncertainties in the idealisation of pier elements must be addressed in the developed numerical model (Section 3.3).

Modelling beam elements: stiffness-based formulations

Conventional stiffness-based formulations are widely used to model the deformable beam elements according to either Euler-Bernoulli or Timoshenko beam theories, for example, in the studies presented for the EQF modelling approaches by Lagomarsino et al. (2013) and Bracchi et al. (2015). The interpolation functions are derived in the element displacement fields in the stiffness-based formulations. However, this can create difficulties in achieving force equilibrium, particularly for nonlinear models. Thus, alternative methods are sought to formulate the beam elements in this research.

Modelling beam elements: flexibility-based formulations

The alternative method to model the beam elements is based on flexibility formulations. In the literature (e.g. Taucer et al., 1991; Spacone et al., 1996; Marini & Spacone, 2006), the flexibility-based formulations are mostly used for the reinforced concrete structures to model the nonlinearity in the beam elements. The interpolation functions derived for the flexibility formulations depend on the internal force equilibrium in the element cross-section; no assumptions are made regarding element displacements. This facilitates the integration of nonlinear stress-strain constitutive models by simply considering the force equilibrium.

Another advantage of using flexibility-based formulations is that they can be implemented directly into a model formulated with conventional stiffness-based functions from the global structural stiffness level.

Spacone et al. (1996) used flexibility-based formulations to model the nonlinear beam elements according to the Euler-Bernoulli beam theory in 3D. Also, they presented a fibre beam approach to compute the section forces in each fibre in the element cross-section. Later, Martino et al. (2000) and Marini and Spacone (2006) modified the flexibility formulations presented by Spacone et al. (1996) to adjust them to the Timoshenko beam theory by including the shear behaviour (Section 3.4).

Different from the conventional stiffness-based formulations, the flexibility-based formulation analysis requires an iteration procedure to determine the element displacements by updating the internal stress and strain resultants. This iteration procedure is named 'element state determination' (Spacone et al., 1996; Neuenhofer & Filippou, 1997) (Section 4.4). Another difference is that the self-weight of the beam element is imposed into the model as internal loads (Taucer et al., 1991; Neuenhofer & Filippou, 1997) instead of applying it through the external force vector as used in the stiffness-based formulations (Section 3.4.5).

Considering their advantage in modelling nonlinear beam behaviour, flexibility-based formulations are employed for the beam elements (e.g. spandrels and piers) in this thesis. The formulations are presented in Section 3.4 and the iteration procedures used in the flexibility analysis are explained in Sections 4.3 and 4.4 in detail. Thus, the relevant formulations are not repeated here.

2.4.1.4 Equivalent solid models

Considering the semi-coupled models developed by simplifying the masonry buildings, Maleki et al. (2011) modelled the building as an equivalent plate with the corresponding building

dimensions in length and width on the ground surface, in which the soil and the tunnel excavation were modelled in 3D FE. The bending and axial stiffnesses of the equivalent plate were defined to represent the overall stiffness of the building.

Losacco et al. (2014) presented an equivalent solid model (Figure 2.11a), in which the masonry building was represented as the embedded portion of the façades (Losacco et al., 2014). Similarly, Bilotta et al. (2017) modelled the masonry building as a stiff plate (i.e. a continuous embedded foundation slab) loaded by a uniform surface load to examine the effects of tunnel excavation in a 3D FE analysis. Soil-structure interaction was allowed at the foundation base while still modelling the tunnel advancements in steps in a 3D FE environment. The stiffness of the equivalent solid was determined from calibrations performed on the complete building. Accordingly, the stiffness parameter that can reproduce the complete building response under the same boundary conditions is chosen as the equivalent solid's stiffness. The study showed the importance of considering the vertical and horizontal tunnelling-induced displacements in calibrating equivalent solid elements' stiffness to match vertical displacement and horizontal strain results determined from a reference 3D complete building model. In addition to the realistic representation of building stiffness and weight with the equivalent solid elements, Pascariello et al. (2023) demonstrated the critical contribution of including the effect of pre-existing damage in the building on the stiffness of embedded solid elements.

2.4.1.5 Equivalent beam models

In the case of simplifying the building model, Pickhaver et al. (2010) proposed the equivalent beam approach to model the masonry building. In this study, each masonry façade was represented by equivalent beam elements (Figure 2.11b) employing Timoshenko beam theory. The soil was modelled separately while still modelling the progressive tunnel excavation with the 3D FE. Although in this approach, the contribution of building stiffness in the soil-structure

interaction was incorporated, their approach was limited to masonry buildings with shallow foundations and the embedded portion of the façade was neglected.

Pickhaver et al. (2010) emphasised that the appropriate calibration of beam stiffness parameters becomes critical for comparisons with the 3D complete building analysis. For the calibration process of the model, the building was divided into horizontal and vertical strips according to the layout of the façade openings. Each strip's effective height and length corresponds to the dimensions of the equivalent beams. The effective height assumption was used to calibrate flexural and shear stiffnesses of each equivalent beam element. Accordingly, the masonry strips with openings were associated with a reduced effective height; in contrast, the actual height of the strip was considered for the solid masonry sections.

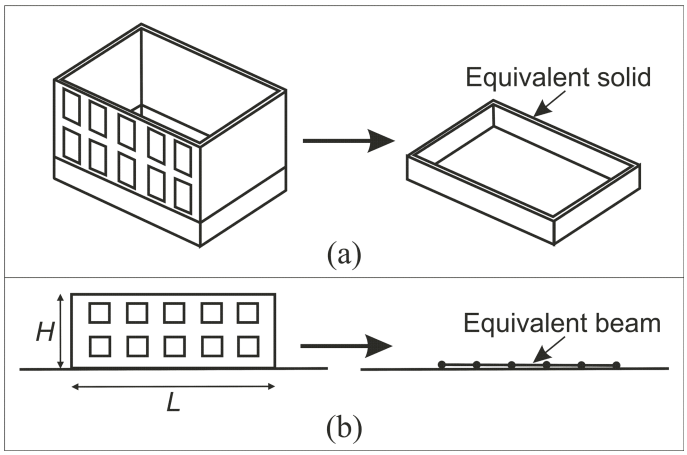


Figure 2.11: Equivalent beam and equivalent solid idealisations of the buildings: (a) equivalent solid representation of a complete building (modified from Losacco et al., 2014), (b) equivalent beam representation of a façade (reproduced from Pickhaver et al., 2010).

2.4.2 Modelling masonry material: model scale

The modelling complexity of the masonry material models decreases from the micro-scale to the macro-scale (Figure 2.12).

2.4.2.1 Micro-scale

Micro-scale models individually consider the masonry units and mortar joints with unit-mortar

interfaces (Figure 2.12b) by implementing different constitutive models for each components, which leads to an anisotropic masonry model (Giordano et al., 2002). The choice of constitutive models for the joints is especially important to capture the sliding behaviour in case of crack developments in these components. In this type of model, the material properties and geometries of all the masonry units and the joints are specified in detail, which increases the computational effort. Thus, the micro-modelling approach is generally preferred for small-scale masonry models (e.g. small scale experiments), for example, to investigate the masonry behaviour under different loadings and failure mechanisms. Furthermore, it is difficult to determine the in-situ material properties of the unit-mortar interface elements to enable the model to be calibrated (Giordano et al., 2002).

2.4.2.2 Meso-scale

The masonry can also be modelled in meso-scale (Figure 2.12c), which is a simplified version of the micro-scale approach. Meso-scale models idealise the mortar with a zero-thickness interface element and represent the units by conventional continuum elements using linear elastic or nonlinear constitutive models (Giordano et al., 2002). For example, for a meso-scale 3D FE model, the block units are represented as 3D FE solid elements and the 2D zero-thickness cohesive-frictional interface elements are used to model the mortar and block-mortar interfaces (Macorini & Izzuddin, 2011; Minga, 2017). In this modelling approach, the bricks are typically modelled as elastic and the nonlinear masonry behaviour is represented by the cohesive-frictional interface elements (Macorini & Izzuddin, 2011; Minga, 2017). Thus, the material constitutive relationships for the interface elements need to be defined carefully. Although using a meso-scale modelling approach decreases the computational effort compared to micro-scale models, it is still computationally demanding to model a complete masonry building. Thus, both micro and meso-scale models do not present practical solutions to conduct a rapid damage assessment for a tunnel-soil-building interaction problem.

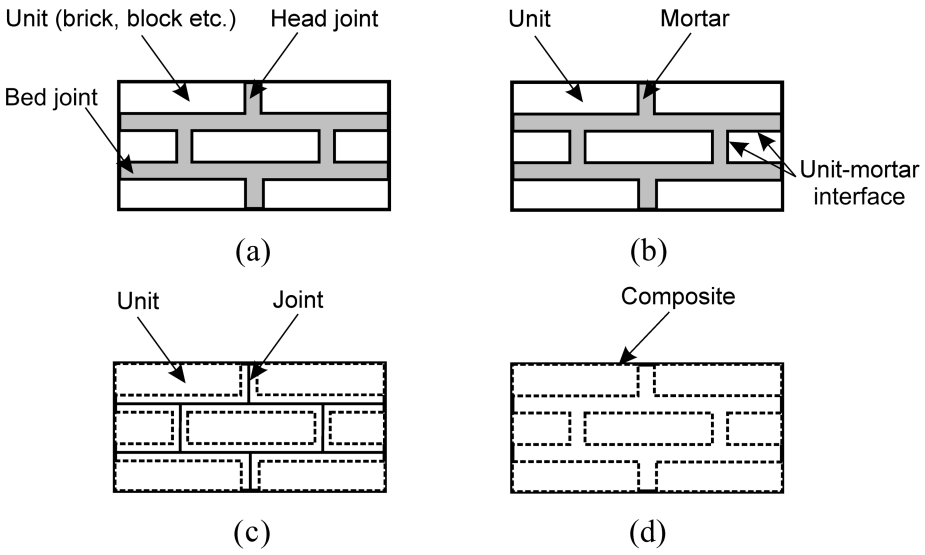


Figure 2.12: Modelling scales for masonry structures: (a) masonry sample, (b) micro-scale, (c) meso-scale and (d) macro-scale (reproduced from Lourenço, 1996).

2.4.2.3 Macro-scale

The macro-scale modelling considers the structure as a single continuum rather than modelling the mortar and unit/mortar interface in detail (Figure 2.12d). It presents a practical approach for estimating the general damage pattern when modelling large structures since it requires less computational time than micro and meso-scale models. For example, recent studies developed for assessing the tunnel-soil-building interaction (Table 2.1) modelled the masonry material on a macro-scale.

It is important to determine the macroscopic material properties in the macro-scale modelling procedure. Accordingly, Lourenço (1996) proposed the definition of a 'basic masonry cell' for a running bond masonry wall section, which aims to identify the repetitive arrangement of the block units with mortar joints (Figure 2.13). In this case, the properties of the basic masonry cell represent the whole masonry section. For this purpose, Lourenço (1996) developed the continuum FE modelling approach, which assumes the masonry as a homogenous material in terms of global structural geometry and adopts the constitutive law of the homogenised masonry block cell for the whole masonry structure. This homogenisation method significantly

reduces the computational effort compared to the micro and meso-scale models and can be easily applied to complex structural geometries. Particularly, the masonry material properties employed for the FE continuum models presented in Section 2.4.1.1 and further chapters of this thesis are developed according to the homogenisation method.

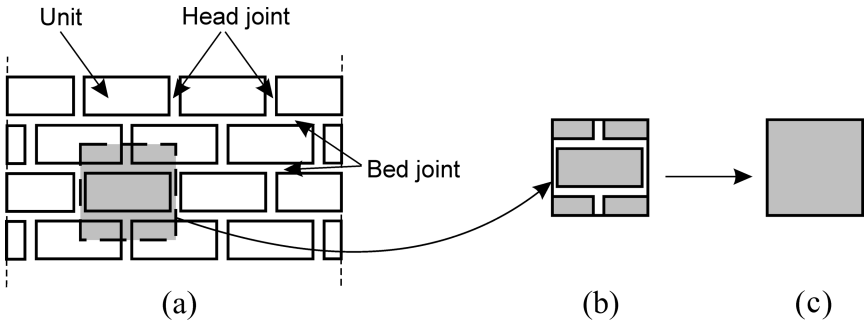


Figure 2.13: Basic masonry cell: (a) masonry sample with running bond, (b) basic cell and (c) homogenised cell (reproduced from Lourenço, 1996).

2.4.3 Modelling masonry material: constitutive models

The constitutive laws used to describe the masonry material behaviour are considered below in terms of linear elastic and advanced nonlinear models.

2.4.3.1 Linear elastic models

The linear elastic constitutive relationship is the preliminary step to assess the masonry building behaviour. In research, this approach is mainly adopted to demonstrate the performance of a newly developed tunnel-soil-building interaction modelling approach. For example, Pickhaver et al. (2010) and Losacco et al. (2014) used linear elastic masonry models to test the applicability of their newly formulated masonry modelling approaches based on equivalent beam and equivalent solid modelling approaches, respectively. Similarly, Burd et al. (2022) and Sangirardi et al. (2023) selected linear elastic masonry models to calibrate the soil-foundation interface models and perform a parametric study for the calibration analyses of a tunnel-soil-building interaction problem. Thus, the linear elastic masonry model is employed first for the numerical model described in Chapter 3 and the developed model is compared with

a linear elastic 2D FE continuum model for the validation purpose (Chapter 7).

2.4.3.2 Nonlinear models

Masonry material has low tensile strength and behaves in a brittle manner under tensile loading. To capture this behaviour, selecting a suitable nonlinear constitutive model for the masonry building has an important effect on stress distribution and the building response. In recent studies, various constitutive models have been used to describe the nonlinear masonry behaviour. However, this field is still open to improvements and choosing a nonlinear model depends on its practicability and the complexity level that needs to be captured in the masonry behaviour.

For example, Burd et al. (2000) used an elastic no-tension material model for the masonry façades. In contrast, Giardina et al. (2013) and Dalgic et al. (2021) adopted a continuum cracking model for the masonry façade, which behaves as linear elastic before the cracking and then demonstrates a nonlinear orthotropic behaviour. Alternatively, Yiu et al. (2017a) modelled the masonry using the concrete-damaged plasticity model. Separately, Amorosi and Sangirardi (2021) used the jointed masonry model (JMM) that considers linear elastic-perfect plasticity (developed by Lasciarrea et al., 2019) as a modified version of the jointed rock model available as a built-in PLAXIS 3D (Brinkgreve et al., 2022). In the JMM, failure mechanisms in the head and bed joints of the masonry section are defined based on the Mohr-Coulomb yield criterion with tension cut-off.

In this thesis, the nonlinear masonry models are formulated to mimic the JMM (Chapter 6). The JMM is chosen since it is a practical model that can capture the critical nonlinear behaviour of the masonry representing the low tensile strength of the masonry medium and the frictional shear along the joints and it can be practically represented by the EQFdc model formulations, which comprise 1D stress-strain constitutive relationships. The nonlinear model

implementations for the EQFdc model are assessed and compared with the results determined from the PLAXIS 3D FE continuum model (Amorosi & Sangirardi, 2021; Sangirardi, 2023), which employs the JMM for the masonry façade. The nonlinear constitutive relationships adopted in the JMM are described below.

Jointed masonry model (JMM)

The JMM (Lasciarrea et al., 2019) assumes isotropic elastic behaviour and predefined failure planes for the masonry. Amorosi and Sangirardi (2021) used two failure planes corresponding to head and bed joints (Figure 2.14), where the failure mechanism is governed by the Mohr-Coulomb yield criterion with tension cut-off.

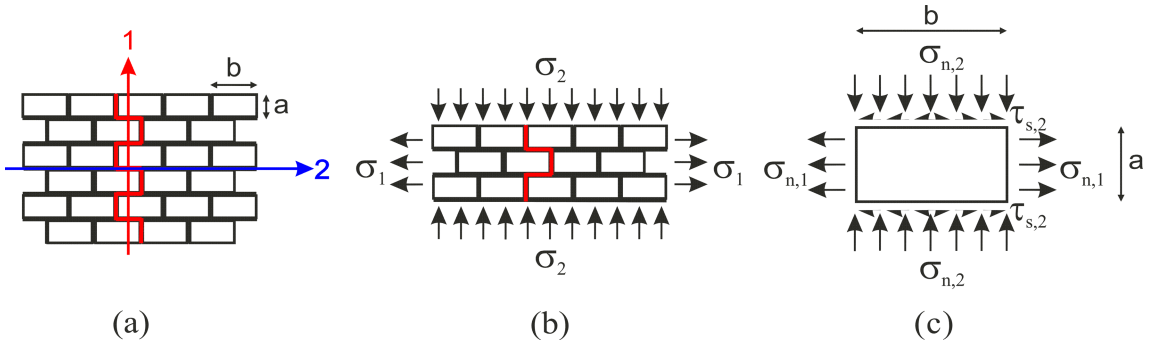


Figure 2.14: JMM: (a) demonstration of plane 1 and plane 2, (b) stress states on a masonry block and (c) stress states on a single brick (reproduced from Lasciarrea et al., 2019).

The strength parameters of the JMM are defined according to the repeating cell in a running brick bond (Lasciarrea et al., 2019). By considering the interlocking effect of brick joints, the tensile strength on the head joints (plane 1) of the masonry medium, $\sigma_{t,1}$ is expressed by Lasciarrea et al. (2019) as:

$$\sigma_{t,1} = \sigma_{t0,1} + \frac{b}{2a} c_{0,2} - \frac{b}{2a} \sigma_{n,2} tan\varphi_2 \tag{2.10}$$

where $\sigma_{t0,1}$ refers to the contribution of tensile strength on the brick head joints while the second term stands for the effect of cohesion on the bed joints, $c_{0,2}$ with the block aspect ratio

of b/a (b is the block width and a is the block height), the final term corresponds to the frictional effect along the bed joints ($tan\varphi_2$) induced by the vertical stress acting on the brick block, $\sigma_{n,2}$. Since the tensile and shear behaviour is assumed to be coupled in the JMM, the increment defined for the tensile strength of the head joints induced due to the interlocking effect also causes an increment in the cohesion on the head joints as:

$$c_1 = c_{0,1} - \left(\frac{b}{2a}\sigma_{n,2}tan\varphi_2 - \frac{b}{2a}c_{0,2}\right)tan\varphi_1 \tag{2.11}$$

where c_1 is the cohesion on the head joints (plane 1) of the masonry medium considering the interlocking of brick joints, $c_{0,1}$ is the cohesion on the head joints and $tan\varphi_1$ is the frictional contribution on the head joints.

As no interlocking is acting on the bed joints, the tensile strength on the plane 2, $\sigma_{t,2}$ is induced simply due to the tensile strength on the bed joints, $\sigma_{t0,2}$, which is based on isotropic elasticity ($\sigma_{t0,2} = \sigma_{t0,1}$) thus, $\sigma_{t,2} = \sigma_{t0,2}$. Similarly, the cohesion on the plane 2 (without considering the interlocking effect) is defined as $c_2 = c_{0,2}$ (due to isotropic elasticity $c_{0,1} = c_{0,2}$).

In the JMM, Mohr-Coulomb theory is adopted to represent the shear failure mechanism of the masonry. Accordingly, the shear failure criterion is defined as:

$$|\tau_i| = c_i - \sigma_{n,i}tan\varphi_i \tag{2.12}$$

where τ_i and $\sigma_{n,i}$ are the shear and normal stresses along each plane orientation, i. Additionally, c_i and φ_i are the cohesion and friction angle on the joints, respectively.

2.5 Modelling Soil-Structure Interaction

Modelling soil-structure interaction is an important feature that affects the building response to tunnelling. For example, Farrell et al. (2014) performed centrifuge tests and investigated the

effect of building weight and stiffness in the building response on the tunnelling-induced ground displacements. They observed that the building weight and stiffness under the settlements affect the development of a gap between the structure and the soil.

Giardina et al. (2012) performed laboratory settlement experiments on a 1/10-scale masonry façade (with openings). This experiment had no foundation system but a rubber layer between the façade and the I-shape beam was used to transmit the greenfield settlements to the structure. The results show that the soil-structure interaction causes a significant reduction in the vertical displacements experienced by the façade, in which the stress and damage distributions in the façade are dependent on the relative stiffness between the façade and the rubber layer.

Ritter (2018) conducted centrifuge experiments on 1/75-scale 2-storey building specimens to investigate the effect of tunnelling-induced ground displacements on building responses at 75g. Regarding the horizontal building responses, the test results show that the horizontal displacements determined at the foundation level are smaller than the tunnelling-induced horizontal ground displacements due to the effect of soil-structure interaction.

These findings highlight the importance of a realistic representation of the soil-structure interaction, which should be addressed in the damage assessment procedures. In current Stage 2 assessment procedure, the greenfield displacements at the foundation depth are applied directly to the simple elastic beam model by neglecting the soil-structure interaction. A key aspect in modelling soil-structure interaction is to select a suitable constitutive model to represent the stiffness and nonlinear behaviour of the soil. The soil-structure interaction is commonly represented by the soil-foundation models based on the finite element and Winkler modelling approaches, as reviewed below.

2.5.1 Finite element soil-foundation models

The finite elements are widely used in fully and semi-coupled FE models to model the soil and

the soil-foundation interaction (with interface elements). Applications of this sort are reviewed below.

As an example of semi-coupled FE models, Giardina et al. (2013) modelled the masonry building with 2D FE and simulated the soil-structure interaction with nonlinear interface elements. The interface elements were governed by the normal stiffness and had a no-tension capacity while defining the shear stiffness as almost zero. The choice of normal stiffness of the interface elements played a crucial role in reproducing the damage behaviour of the masonry building consistent with the settlement experiments performed on a 1/10 scale masonry façade (Giardina et al., 2012).

As an example of fully coupled FE models, Yiu et al. (2017a) used 10-noded tetrahedral finite elements to model the soil and the foundation. For the choice of soil constitutive models, Yiu et al. (2017a) adopted the extended Mohr–Coulomb model (Doherty & Muir Wood, 2013) to represent the Terrace gravel soil behaviour, whereas the multiple yield surface kinematic hardening model (Houlsby, 1999; Burd et al., 2000) was employed for the London Clay. For the same soil profiles that presented by Yiu et al. (2017a), Amorosi and Sangirardi (2021) used Hardening Soil Model with Small Strain (HSsmall) (Schanz et al., 1999; Benz et al., 2009). These advanced nonlinear soil models can capture the nonlinear small-strain stiffness behaviour of the soil, which affects the estimation of the greenfield settlements (e.g. Addenbrooke et al., 1997). Yiu et al. (2017a) also represented the soil-foundation interaction with nonlinear interface elements by providing a frictional surface at the shear direction and defining no tensile strength in the normal direction to provide gapping between the ground and the footing surface. The frictional shear and no-tension models are also employed for the numerical models that are used to simulate these settlement field experiments, as explained in Chapter 9.

Another important modelling detail is related to the effect of footing depth on the building displacements and damage response. Accordingly, Sangirardi et al. (2023) and Yiu et al. (2017b) demonstrated that for the case of elastic façade with openings, the increase in the footing depth (i.e. the embedded façade portion under the ground increases) increases the displacements and the major principal tensile strains experienced by the building. Thus, the numerical model explained in Chapter 3 also considers the geometry of the embedded façade portion.

Additionally, the effect of frictional interface contact between the soil and the embedded façade portion was investigated by Sangirardi et al. (2023). The results showed that the horizontal displacements at the footing base are slightly higher than the values obtained from the case, where the frictional surface is only defined at the footing base. It is also concluded that the difference between the horizontal displacements is likely to increase with increasing footing depth (the embedded portion of the façade). Modelling the frictional interface between the soil and the embedded façade portion is also considered in the soil-foundation interaction model (as a modified version of the model explained in Section 2.5.2.1) used in this thesis.

2.5.2 Winkler soil-foundation models

As an alternative to detailed soil models, soil-structure interaction can be captured using simplified approaches such as Winkler soil-foundation models based on elastic or elastoplastic behaviour.

For example, Deck and Singh (2012) modelled the soil based on the Winkler model and the building according to beam theory to capture the soil-structure interaction caused by tunnelling-induced ground movements. The building self-weight and the greenfield ground displacements were included in the model. The soil was modelled with elastic springs in which the vertical pressure was considered as linearly dependent on the soil spring stiffness, vertical

displacement and width of the foundation. The contribution of shear stiffness was neglected in the soil model.

For the preliminary assessment of the developed numerical model within the scope of tunnelling-induced ground movements, the soil-structure interaction is represented by the Winkler soil-foundation model as elastic in both normal and shear directions (Section 3.2 and Chapter 7). The greenfield displacements are imposed as prescribed deformations to the soil-foundation interface elements and the building displacements are computed at the footing elements as a result of the soil-structure interaction.

2.5.2.1 S2M soil-foundation interaction model

As an example of the semi-coupled models formed by simplifying the soil and tunnelling details, Burd et al. (2022) developed the 'simplified 2D assessment model' (S2M), which incorporates a 2D FE (6-noded plane stress isoparametric triangular elements) masonry model with 1D FE (3-noded Lagrangian elements) 'S2M soil-foundation interaction model' to compute the relationship between the greenfield displacements and the footing displacements (Figure 2.15). The S2M soil-foundation interaction model is formulated according to a nonlinear Winkler soil-foundation modelling approach and provides nonlinearity in both normal and shear directions of the soil. The S2M soil-foundation interaction model also considers the contribution of the embedded façade portion in the calculations.

The S2M soil-foundation interaction model formulations are derived based on the virtual work concept (Burd et al., 2022). Accordingly, the internal virtual work of the soil-foundation interaction model, $\delta W_{int,soil-foundation}$ is given by,

$$\delta W_{int,soil-foundation} = \int_0^L (\delta u_f t_h + \delta v_f t_v) dx \tag{2.13}$$

where δu_f and δv_f are the virtual displacements in horizontal and vertical directions of the footing, t_h and t_v are the net horizontal and vertical tractions (positive direction as shown in Figure 2.15a) applied by the soil elements to the footing and L is the footing length.

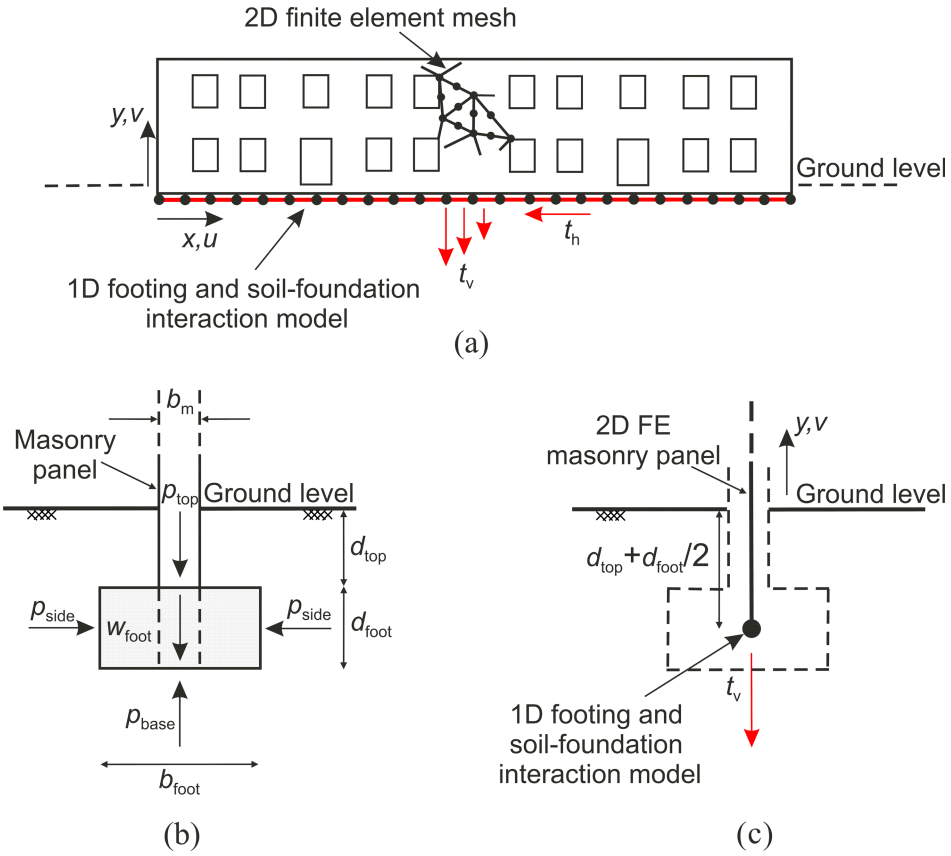


Figure 2.15: S2M modelling approach: (a) a 2D FE masonry mesh is integrated with the S2M soil-foundation interaction model, (b) strip footing cross-section demonstrating the normal tractions acting on top, base and sides of the footing, (c) cross-section detail of the 2D masonry panel with the 1D soil-foundation model (reproduced from Burd et al., 2022).

Burd et al. (2022) formulated the constitutive relationships for the S2M soil-foundation interaction model to capture the gapping and frictional sliding behaviour beneath a shallow foundation under the application of self-weight and greenfield displacements. Firstly, the initial geostatic stress analysis is considered in the absence of the façade but with the embedment of the strip footing, which has the same unit weight as the surrounding soil layer. Then, the soil tractions which are in equilibrium in the initial geostatic stress conditions around the strip footing (at the top, base and side are defined as p_{top}, p_{base} and p_{side} as shown in Figure 2.15b)

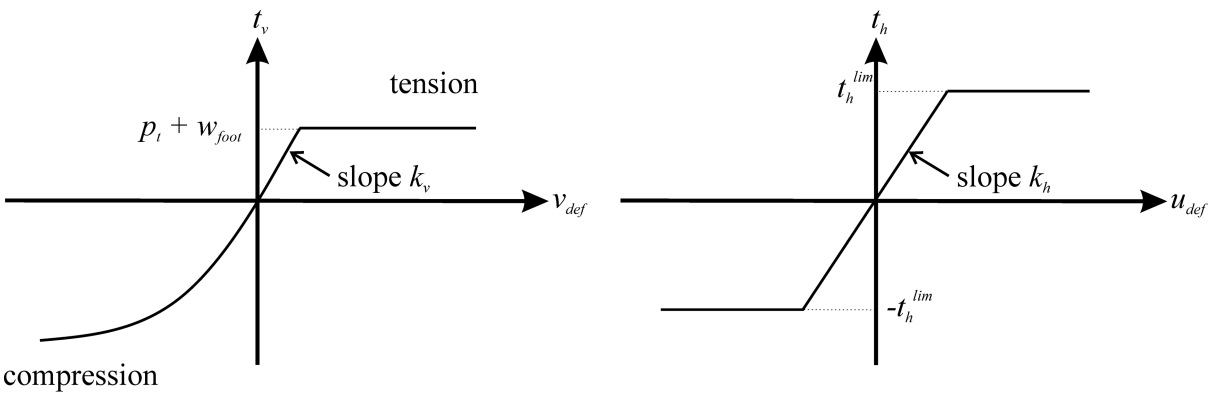
are determined as:

$$p_{top} = \gamma_s(d_{top}\, b_{foot}) \tag{2.14}$$

$$p_{base} = \gamma_s(d_{top} + d_{foot})b_{foot} \tag{2.15}$$

$$p_{side} = K_0\gamma_s(d_{top} + d_{foot}/2)d_{foot} \tag{2.16}$$

where γ_s is the unit weight of the soil, d_{top} is the thickness of the embedded façade above the footing, d_{foot} is the thickness of the footing, b_{foot} is the width of the footing and K_0 is the lateral earth pressure coefficient.



(a) (b)

Figure 2.16: Soil-foundation constitutive model: (a) net vertical traction vs. vertical traction-induced displacement, (b) horizontal traction vs. horizontal traction-induced displacement (adapted from Burd et al., 2022).

The nonlinear constitutive relationships used for the net vertical traction, t_v vs. vertical traction induced displacements, v_{def} and the horizontal traction, t_h vs. horizontal traction induced displacements, u_{def} are shown in Figure 2.16. Burd et al. (2022) defined the nonlinear compression behaviour in the vertical direction as follows:

$$t_v = \frac{k_v v_{def}}{1 + a_v|v_{def}|} \tag{2.17}$$

where k_v is the small displacement vertical soil stiffness and a_v is the nonlinearity parameter. Additionally, the vertical and horizontal traction-induced displacements are computed as follows:

$$v_{def} = v_f - v_g \qquad u_{def} = u_f - u_g \tag{2.18}$$

where the vertical and horizontal displacements determined at the footing elements of the building are represented as v_f and u_f and the corresponding greenfield displacements are defined as v_g and u_g, respectively. In Figure 2.16(a), the linear elastic behaviour is defined in tension direction up to the limiting uplift condition, which refers to the summation of uplifting pressure, p_t and the footing weight, w_{foot}. When the gap is formed at the footing base, the normal traction at the footing base vanishes, $p_{base} = 0$. The limiting uplifting pressure, p_t, is calculated according to the vertical pull-out resistance defined for a strip anchor in sandy soil by Murray and Geddes (1987):

$$p_t = \gamma_s(b_{foot}d_{top})\left[1 + \frac{d_{top}}{b_{foot}}tan\varphi'\right] \tag{2.19}$$

where φ' is the friction angle of the soil layer. Elastic perfectly plastic frictional constitutive relationship (considering μ is the friction coefficient of the soil-foundation interface, where $\mu = tan\varphi'$ for all soil types) is defined for the shear behaviour of the soil (Figure 2.16b). Accordingly, the shear behaviour in the elastic region is defined as:

$$t_h = k_h u_{def} \tag{2.20}$$

where k_h is the shear stiffness of the soil. In case of exceeding the limiting shear traction value, $\pm t_h^{lim}$, the sliding occurs and the horizontal traction is set as the limiting value, $t_h = \pm t_h^{lim}$. Burd et al. (2022) considered the frictional sliding for all surfaces around the footing. Thus, the limiting horizontal traction is computed by using the current values of the normal traction as:

$$t_h^{lim} = \mu\left(p_{top} + 2p_{side} + p_{base}\right) \tag{2.21}$$

The soil stiffness parameters and the nonlinearity coefficient required to calculate the net vertical traction in compression direction are determined through 3D FE calibration analyses (Burd et al., 2022). According to the results, the vertical displacement comparisons between the S2M model and the 3D FE model presented a good agreement.

This finding indicate that the S2M soil-foundation interaction model can be used as a practical approach to compute the building responses with the soil-structure analysis. Thus, the S2M soil-foundation interaction model is implemented into the developed numerical model to represent the nonlinear soil-structure interaction (Chapter 8). The modified version of the S2M soil-foundation interaction model (Burd, 2023) employed in this thesis also considers the frictional effect on the side walls of the embedded façade as:

$$p_{side,wall} = K_0\gamma_s\left(d_{top}/2\right)d_{top}(tan\varphi_{wall})/\mu \tag{2.22}$$

where $p_{side,wall}$ is the soil traction acting in normal direction to the side of the embedded façade and φ_{wall} is the fictional interface angle in the embedded façade (considering that $tan\varphi_{wall}$ can be different than the friction coefficient of the soil-foundation interface, $\mu = tan\varphi'$). Accordingly, p_{side} given in Equation (2.16) is updated as:

$$p_{side} = K_0\gamma_s\left(d_{top} + d_{foot}/2\right)d_{foot} + p_{side,wall} \tag{2.23}$$

In the modified version of the S2M soil-foundation interaction model (Burd, 2023), the rest of the formulations are same as presented above.

2.6 Outcomes of Literature Review

As an outcome of the literature review, a gap was identified between Stage 2 and Stage 3 of the tunnelling-induced damage assessment procedures. Considering that the modelling

strategies range from simplifying the building as a simple elastic beam (without considering the effects of openings and soil-structure interaction) to detailed advanced 3D FE models used to represent the tunnel-soil-building interactions, this thesis aims to fill this gap by developing alternative practical modelling strategies. A summary of the modelling strategies developed in this thesis to represent tunnel-soil-building interactions is presented in Table 2.2.

Firstly, the modelling strategies are chosen to reduce the complexities of all soil, tunnel and masonry building models. Thus, all the models developed from preliminary to the most recent work can be defined as simplified approaches. Additionally, the modelling scale for the masonry material is chosen as a macro-scale. The most recent work, where the model is named 'EQFdc model', combines the equivalent frame modelling approach with the macro-elements (Chapter 3). In this approach, the rigid connectors used in the existing EQF models are replaced by the deformable macro-elements (Section 3.5.1). This new modelling strategy retains the advantages of both modelling approaches; the spandrels and piers in the EQF model idealise the frame-like response of the masonry buildings while the macro-elements replace rigid connectors to accurately capture the building's stiffness and damage behaviour. This treatment allows a simple definition of piers in buildings where openings are regularly or irregularly distributed.

Considering their advantages in the application of nonlinear material models, the beam elements in the EQFdc model are formulated by flexibility-based formulations. While the initial damage assessment is conducted with the linear elastic models, the nonlinearity for the masonry material is defined with plasticity-based constitutive models, which aim to mimic the JMM. More advanced constitutive models which capture softening behaviour of masonry exist and can be implemented in further studies. The implementation of a model mimicking JMM (which is implemented in PLAXIS software typically used for Stage 3 tunnelling-induced damage assessments) is considered sufficient in this study.

Table 2.2 The modelling strategies developed in this thesis to represent tunnel-soil-building interactions.

Model		**Modelling tunnelling-induced ground movements**	**Modelling masonry building**			**Modelling soil-structure interaction**	
			Complete building model	**Beam elements**	**Material model**	**Soil-foundation model**	**Material model**
Preliminary work	EQF model (Gulen et al., 2021)	Empirical equations	Equivalent frame with rigid connectors	Stiffness-based, Euler-Bernoulli beam	Linear elastic	1D FE Winkler	Linear elastic
	Macro-element model (Gulen et al., 2022)	Empirical equations	Macro-element	–	Linear elastic	1D FE Winkler	Linear elastic
The most recent work	EQFdc model	Prescribed deformations	Equivalent frame with deformable connectors (macro-elements)	Flexibility-based, Timoshenko beam	Linear elastic	1D FE Winkler	Linear elastic
	EQFdc model	Prescribed deformations	Equivalent frame with deformable connectors (macro-elements)	Flexibility-based, Timoshenko beam	Plasticity based nonlinear models that mimic JMM	S2M soil-foundation interaction model (Burd et al., 2022; Burd, 2023)	Nonlinear model (based on Burd et al., 2022)

Regarding the modelling of the soil-structure interaction, the S2M soil-foundation interaction model (Burd et al., 2022; Burd, 2023) is implemented into the EQFdc model and the nonlinearity in the soil-foundation interface is defined according to the constitutive models described in Section 2.5.2.1. Burd et al. (2022) demonstrated that the S2M soil-foundation interaction model captures the key aspects of soil-structure interaction in comparison with the vertical displacements at the foundation base determined from a 3D FE model. The tunneling-

induced ground movements determined from the 3D FE models are imposed into the soil-foundation interaction model as prescribed deformations. The building displacements at the footing elements are computed as a result of the soil-structure interaction.

Chapter 3

Formulation of Equivalent Frame Model with Deformable Connectors

3.1 Introduction

This chapter introduces the formulation of a new computationally efficient modelling approach named ‘equivalent frame model with deformable connectors’ (shortened as ‘EQFdc model’) to be used in tunnelling-induced damage assessment of masonry buildings. This approach idealises the building as an equivalent frame by using beam elements to model piers and spandrels, similar to the concept used in the earthquake engineering field. However, instead of defining the connections between the piers and spandrels as rigid, deformable connectors are used, which are modelled with 2D macro-elements. Macro-elements are intended to eliminate the overestimation of building stiffness caused by the rigid sections defined in the original equivalent frame modelling approach (Section 2.4.1.3). Although macro-elements alone are sufficient to determine the overall building response in tunnel-soil-structure interaction problems, beam elements have some advantages in capturing strain distributions and accounting for material nonlinearity. Consequently, they are utilised alongside macro-elements.

3.2 Preliminary Work

Preliminary work conducted on the development of the equivalent frame model with rigid connectors (EQF model) and the macro-element model is briefly presented in this section. The EQF and macro-element modelling approaches are mostly employed for the seismic assessment of masonry buildings in the literature but they were used to address tunnelling-induced damage assessment of masonry buildings for the first time in this research. The EQF and 2D macro-element models are assessed with linear elastic analysis, considering it as an initial step of the damage assessment procedure. The soil-structure interactions in the EQF and the 2D macro-element models are provided by a 1D FE Winkler soil-foundation model, where the greenfield displacements are computed by the empirical equations. Building responses determined from the EQF and the macro-element models are compared with the results obtained from a 2D FE continuum model. The outcomes of the preliminary work provide a basis for the development of the EQFdc modelling approach, which is explained in the following sections in detail.

3.2.1 Equivalent frame model with rigid connectors

To idealise the masonry façade according to the EQF model, the TREMURI approach (Figures 2.9 and 2.10e) was adopted from Lagomarsino et al. (2013), considering the layout of the façade openings. Figure 3.1 shows the EQF model idealisation of a two-storey masonry building in terms of spandrels, piers and rigid connectors and its interaction with the soil elements through the 1D FE Winkler soil-foundation model. The FE formulations employed for the EQF model are presented in detail by Gulen et al. (2021). Soil-structure interaction analyses were carried out using the EQF model. The EQF model demonsrated stiffer response than the 2D FE continuum model due to the presence of the rigid connector elements (Gulen et al., 2021).

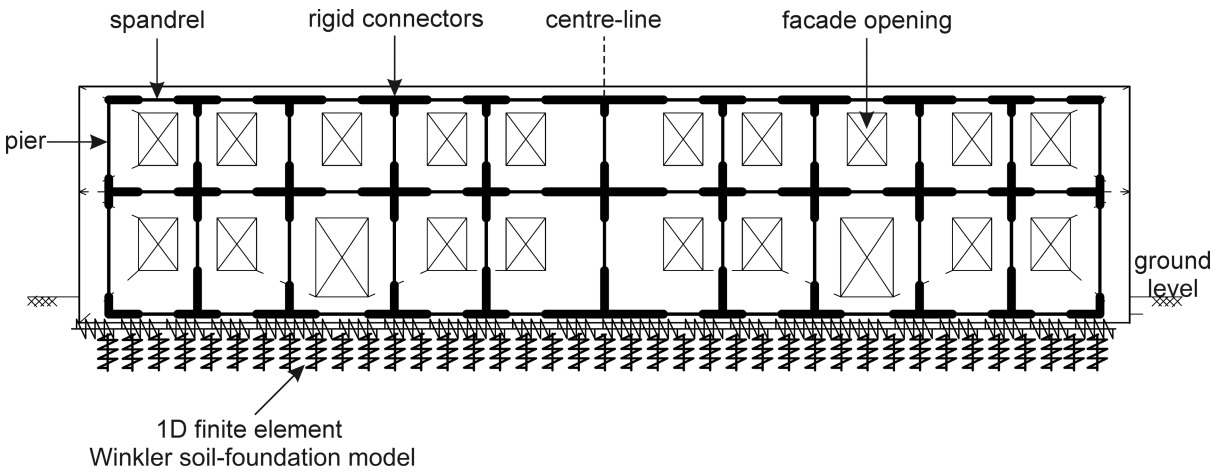


Figure 3.1: Equivalent frame model with rigid connectors (Gulen et al., 2021).

3.2.2 Macro-element model

After encountering a stiffer response (compared to the 2D FE continuum model) in the EQF model due to the rigid connectors, a macro-element model is developed in 2D. A macro-element comprises a 4-noded quadrilateral (referred to as 'quad') element with surrounding interfaces. The macro-element modelling approach idealises the masonry building in terms of macro-elements based on the layout of the façade openings without requiring the identification of beam elements and rigid connections. Masonry sections between the façade openings are modelled by the macro-elements (Caliò et al., 2012). Figure 3.2 shows the macro-element idealisation of a masonry building (same in Figure 3.1) with coarse (Figure 3.2a) and fine (Figure 3.2b) mesh discretisation options.

The formulations developed for the macro-element model in this research are different from those developed by Caliò et al. (2012). Caliò et al. (2012) used discrete element-based formulations, whereas finite element formulations are developed in this study. Additionally, the choice of degrees of freedom (DOF) formulated in this macro-element model is completely different from the ones used by Caliò et al. (2012). The formulations used in the macro-element model are presented by Gulen et al. (2022) in detail.

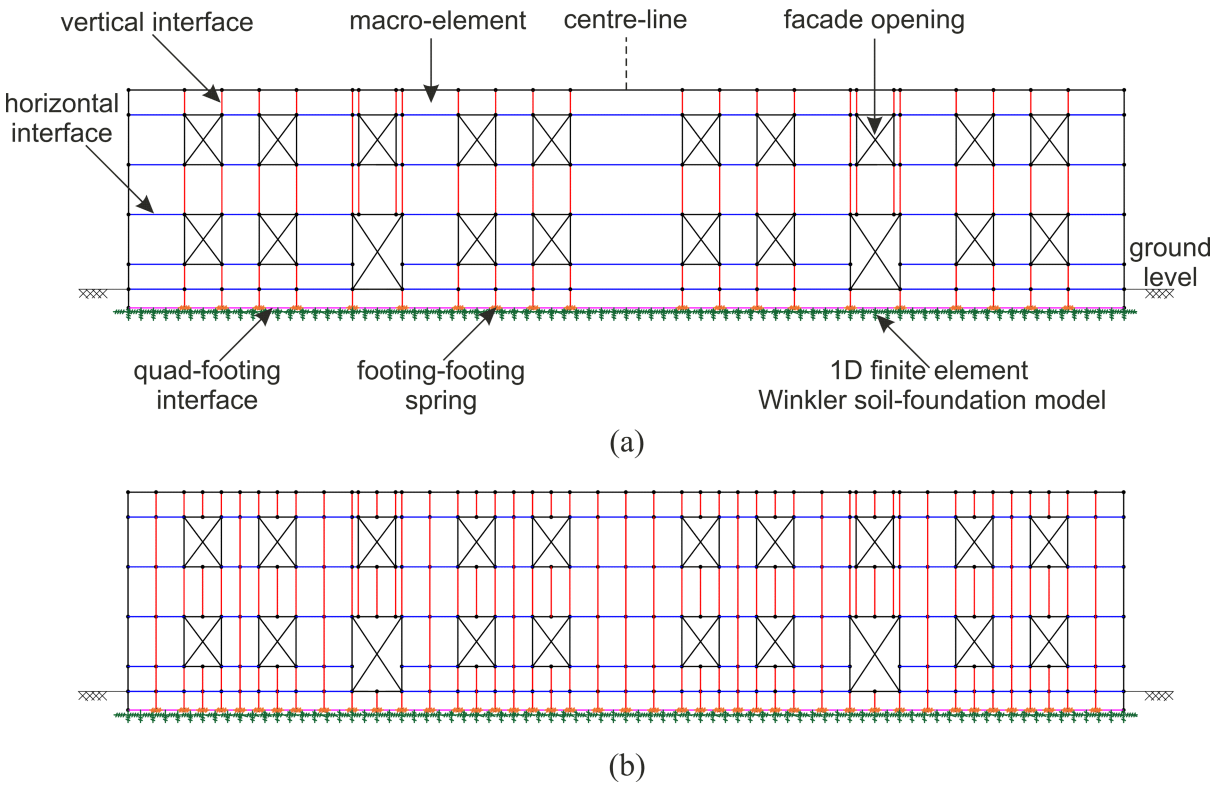


Figure 3.2: The 2D macro-element model idealisation of a masonry façade: (a) coarse mesh, (b) fine mesh (Gulen et al., 2022).

In this macro-element model, a novel approach is presented to model the interaction between the building and the foundation (Figure 3.16), which is neglected in the existing macro-element models available in the literature. Another advantage of the developed macro-element model is that it enables the calculation of strains inside the macro-element (Section 3.6.1) for tunnelling-induced damage assessment purposes.

According to linear elastic analysis comparisons, the building displacements determined from the macro-element models presented good agreements with the 2D FE continuum model, even for the coarse mesh model. For the comparison of the major principal tensile strain distributions, using a finer mesh (Figure 3.2b) of macro-elements captures the strain distributions in the building slightly better than the coarse mesh model (Figure 3.2a) compared to the 2D FE continuum model. However, to capture the bending and shear stress distributions in the element axis and cross-sections accurately, it is concluded that implementing the beam

behaviour directly to the building model is more practical than using a fine mesh macro-element model.

3.3 EQFdc Model Overview

The EQFdc modelling approach aims to combine the advantageous features of both EQF and macro-element models in one model, which can formulate the beam behaviour directly as in the EQF model but eliminate the overestimation of façade stiffness induced by the rigid connectors by replacing them with deformable macro-elements as in the macro-element model.

The EQFdc modelling concept for a simple building example is shown in Figure 3.3. In the EQFdc model idealisation, the element geometries are determined according to the layout of adjacent façade openings. The pier and spandrel elements of the building are defined using the full rigid offset method (Figure 2.10c) proposed by Bracchi et al. (2015). Flexibility-based Timoshenko beam element formulations are used to model the spandrels and piers. These formulations are different from the ones developed for spandrel and pier elements in the EQF model (i.e. with rigid connectors), which are based on conventional stiffness-based FE formulations. Using flexibility-based FE formulations provides advantages for the nonlinear constitutive model implementations. The nonlinear constitutive models used for the structural elements in this thesis are formulated from 1D stress-strain relationships (Iwan, 1967). Since the flexibility-based FE formulations are based on force-equilibrium equations instead of displacement-based equations (i.e. used for the conventional stiffness-based FE formulations), the 1D stress-strain based constitutive models can be practically implemented into the EQFdc model from the element and Gauss point level iterations (explained in Chapters 4 and 6).

The masonry sections, where spandrels are connected to piers (Figure 3.3), are modelled with deformable macro-elements (referred to as ‘deformable connectors’). Each macro-element interacts with adjacent quad, beam or footing elements via zero-thickness structural interface

elements (Figures 3.3b and 3.3c). The formulation of the macro-elements is based on the preliminary work (Gulen et al., 2022).

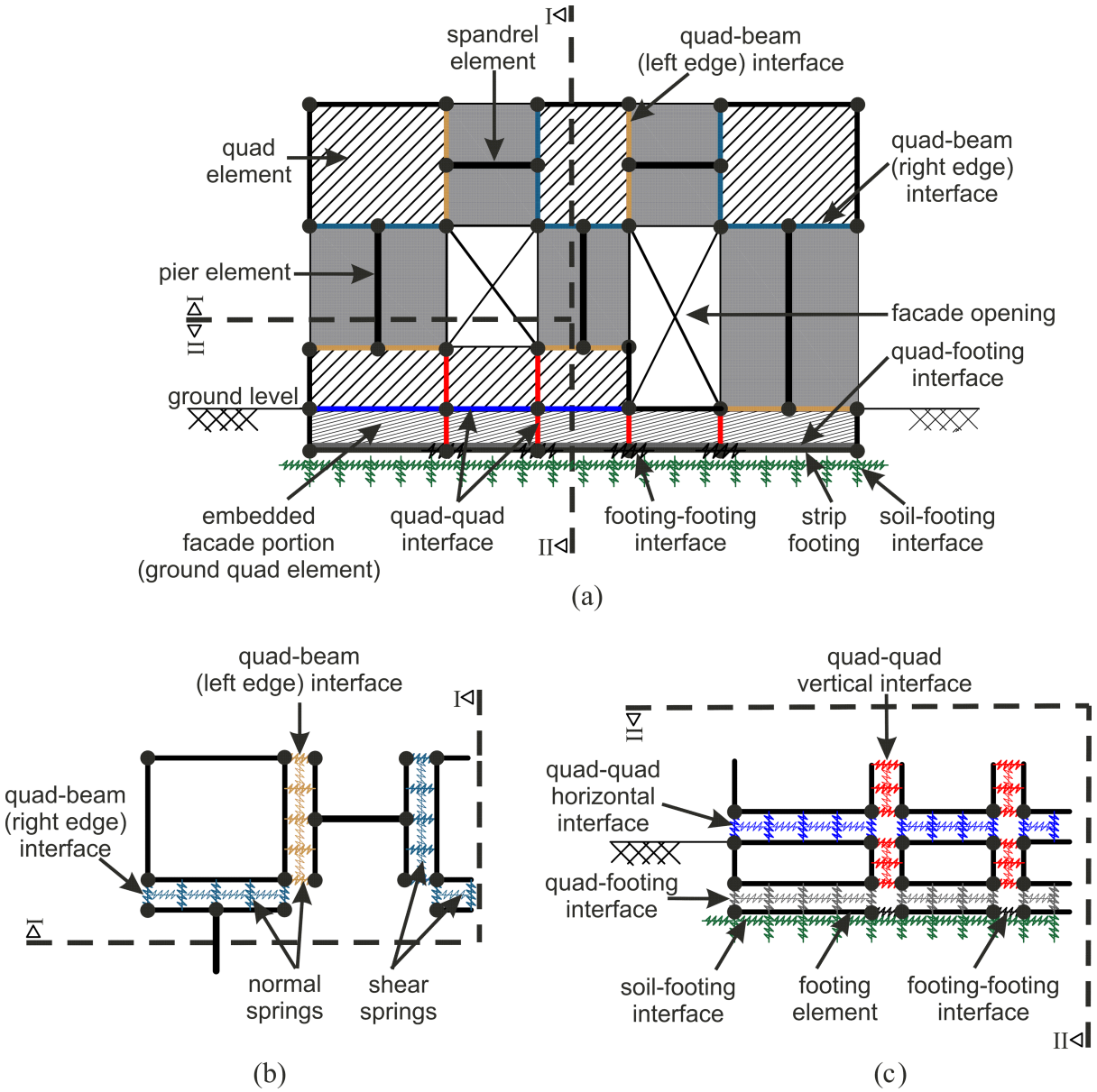


Figure 3.3: EQFdc modelling approach: (a) EQFdc discretisation of a simple building, (b) quad-beam interface representation, (c) quad-quad, quad-footing and soil-footing interface representations.

The masonry portions interacting with the footing elements below the ground level are also modelled with macro-elements (Figure 3.3c). The soil-structure interaction is modelled using the S2M soil-foundation interaction model (Section 2.5.2.1). Rigid footing elements are modelled between the soil-foundation interaction model and the macro-elements. These

footing elements ensure displacement compatibility between soil-footing interface and macro-elements through rigid bar elements but incorporate the axial deformability of foundations by placing axial springs between the rigid bar elements (Figure 3.3c). The axial stiffness of the footings is lumped in axial springs (footing-footing interface in Figure 3.3c).

Tunnelling-induced greenfield displacements are applied to the EQFdc model from the soil-footing interface elements (Figure 3.3c) as prescribed deformations.

The finite element formulations developed in this chapter are based on the virtual work form of the governing equations. Small deformations are assumed and infinitesimal strains are considered. Vectors and matrices are written in bold type. Formulations presented in this chapter form a basis for the further implementations of the EQFdc model into linear and nonlinear models, explained in the following chapters.

3.4 Formulation of Flexibility-Based Elements

2D flexibility-based formulations are employed to model beam elements in the EQFdc model. The flexibility-based formulations presented in this chapter comprising axial and bending behaviour of the beam elements are based on those developed for the Euler-Bernoulli beam element by Spacone et al. (1996). However, the formulations are modified to include the shear terms. The contribution of shear is included in the flexibility formulations with additional terms placed into the force interpolation functions, the section forces and the section flexibility matrix (Martino et al., 2000; Marini & Spacone, 2006).

3.4.1 Global and reduced degrees of freedom

The beam element formulations are derived according to Timoshenko beam theory with constant shear strain. In Timoshenko beam theory, the cross-section of the beam remains plane. However, the beam experiences a constant shear strain, γ_0, in addition to the rotation of the

neutral axis of the beam, $\frac{dv}{dx}$ (where v is the vertical displacement) and the rotation of the beam cross-section, θ.

$$u = u_c - y\theta \tag{3.1}$$

where u is the horizontal displacement in the beam element, u_c is the axial displacement at the element centroid and y is the distance from the element centroid along the beam cross-section. Accordingly, the shear strain and the relationship with the cross-section rotation are:

$$\gamma_0 = \frac{du}{dy} + \frac{dv}{dx} \qquad\qquad \theta = \frac{dv}{dx} - \gamma_0 \tag{3.2}$$

The single beam element defined in the local member coordinate system is shown in Figure 3.4, where the nodal degrees of freedom vector, $\mathbf{U}^*_{\text{beam}}$ and the corresponding element nodal forces, $\mathbf{P}^*_{\text{beam}}$, are represented as:

$$\mathbf{U}^*_{\text{beam}} = [\mathrm{U}^*_1 \quad \mathrm{V}^*_1 \quad \theta^*_1 \quad \mathrm{U}^*_2 \quad \mathrm{V}^*_2 \quad \theta^*_2]^{\mathrm{T}} \tag{3.3}$$

$$\mathbf{P}^*_{\text{beam}} = [\mathrm{F}^*_{\mathrm{x1}} \quad \mathrm{F}^*_{\mathrm{y1}} \quad \mathrm{M}^*_1 \quad \mathrm{F}^*_{\mathrm{x2}} \quad \mathrm{F}^*_{\mathrm{y2}} \quad \mathrm{M}^*_2]^{\mathrm{T}} \tag{3.4}$$

Accordingly, the nodal degrees of freedom vector, $\mathbf{U}_{\text{beam}}$ and corresponding element nodal forces, $\mathbf{P}_{\text{beam}}$, in the global coordinate system are defined as:

$$\mathbf{U}_{\text{beam}} = [\mathrm{U}_1 \quad \mathrm{V}_1 \quad \theta_1 \quad \mathrm{U}_2 \quad \mathrm{V}_2 \quad \theta_2]^{\mathrm{T}} \tag{3.5}$$

$$\mathbf{P}_{\text{beam}} = [\mathrm{F}_{\mathrm{x1}} \quad \mathrm{F}_{\mathrm{y1}} \quad \mathrm{M}_1 \quad \mathrm{F}_{\mathrm{x2}} \quad \mathrm{F}_{\mathrm{y2}} \quad \mathrm{M}_2]^{\mathrm{T}} \tag{3.6}$$

The nodal degrees of freedom and forces in the global coordinates system are transformed to the vectors in the local coordinates by the rotation matrix, $\mathbf{R}$:

$$\mathbf{U}^*_{\text{beam}} = \mathbf{R}\,\mathbf{U}_{\text{beam}} \qquad\qquad \mathbf{P}^*_{\text{beam}} = \mathbf{R}\,\mathbf{P}_{\text{beam}} \tag{3.7}$$

$$\mathbf{R} = \begin{bmatrix} c & s & 0 & 0 & 0 & 0 \\ -s & c & 0 & 0 & 0 & 0 \\ 0 & 0 & 1 & 0 & 0 & 0 \\ 0 & 0 & 0 & c & s & 0 \\ 0 & 0 & 0 & -s & c & 0 \\ 0 & 0 & 0 & 0 & 0 & 1 \end{bmatrix} \tag{3.8}$$

where $c = cos\emptyset$ and $s = sin\emptyset$ and $\emptyset$ is the (anti-clockwise) angle of rotation from the global coordinates to member coordinates (Figure 3.5).

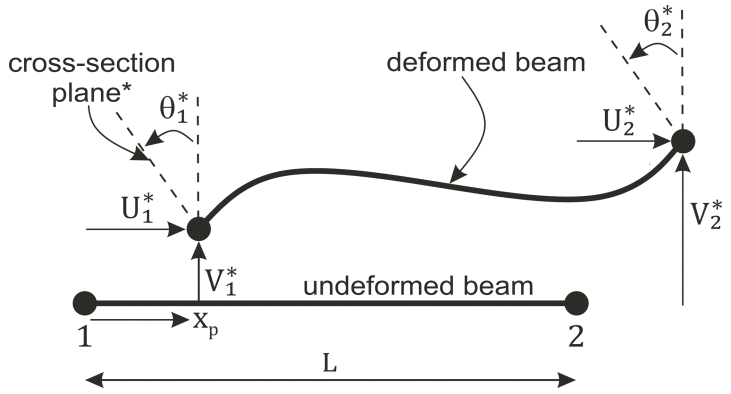


Figure 3.4: A finite beam element showing the degrees of freedom in member coordinates.

The global degrees of freedom vector includes three rigid body modes. To formulate the flexibility formulations, the reduced degrees of freedom need to be used (Spacone et al., 1996; Neuenhofer & Filippou, 1997). The displacement and force vectors generated by removing the rigid body modes are defined as reduced sets of displacements, $\mathbf{U_r}$, and forces, $\mathbf{P_r}$ (Figure 3.6). The reduced set of displacements comprises the relative axial displacement, U_r, the rotation of node-1 relative to node-2, θ_{1r} and the rotation of node-2 relative to node-1, θ_{2r}.

$$\mathbf{U_r} = [U_r \quad \theta_{1r} \quad \theta_{2r}]^T \tag{3.9}$$

$$U_r = U_2^* - U_1^* \qquad \theta_{1r} = \theta_1^* - \left(\frac{V_2^* - V_1^*}{L}\right) \qquad \theta_{2r} = \theta_2^* - \left(\frac{V_2^* - V_1^*}{L}\right) \tag{3.10}$$

The reduced set of displacements vector is related to the degrees of freedom vector in the local coordinates by a reduced transformation matrix, $\mathbf{T_r}$.

$$\mathbf{U_r} = \mathbf{T_r}\,\mathbf{U}^*_{\text{beam}} \tag{3.11}$$

where $\mathbf{T_r}$ is,

$$\mathbf{T_r} = \begin{bmatrix} -1 & 0 & 0 & 1 & 0 & 0 \\ 0 & 1/L & 1 & 0 & -1/L & 0 \\ 0 & 1/L & 0 & 0 & -1/L & 1 \end{bmatrix} \tag{3.12}$$

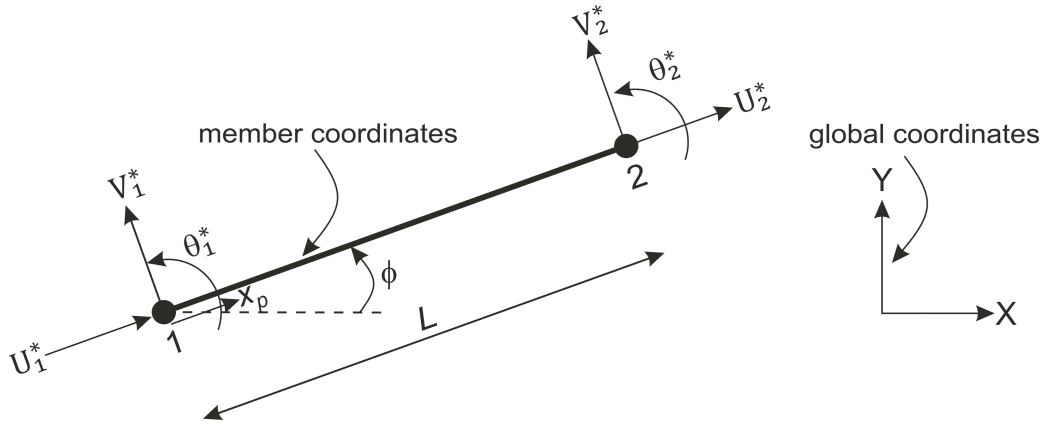


Figure 3.5: A finite beam element showing member and global coordinates.

The nodal forces satisfy three independent equilibrium equations based on horizontal force and moment equilibrium for a reduced, simply supported beam element. It is convenient to derive the reduced set of forces, $\mathbf{P_r}$, in terms of axial force (N) and bending moments (M_1 and M_2) at the element nodes.

$$\mathbf{P_r} = [\mathrm{N} \quad M_1 \quad M_2]^{\mathrm{T}} \tag{3.13}$$

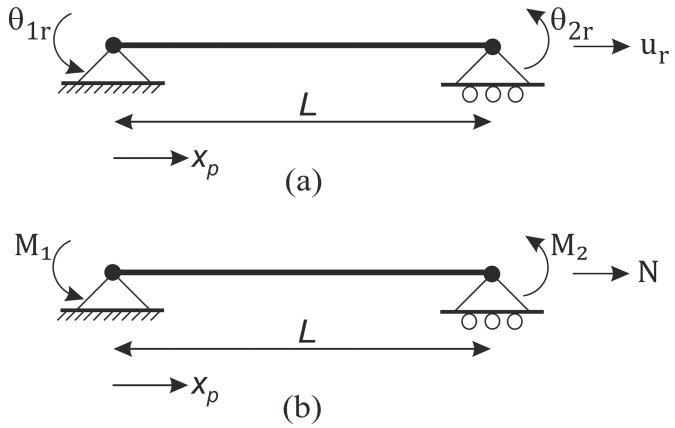


Figure 3.6: Beam element without rigid body modes showing a reduced set of: (a) displacements, $\mathbf{U_r}$ and (b) forces, $\mathbf{P_r}$ (modified from Marini & Spacone, 2006).

3.4.2 Virtual work for a single-beam element

The flexibility-based virtual work equations are derived for a single beam element with a length of L, based on Timoshenko beam theory with six degrees of freedom (Marini & Spacone, 2006). The internal and external virtual work equilibrium is written for a set of virtual forces, $\delta\mathbf{P}_{\text{beam}}$ applied to the beam element as:

$$(\delta\mathbf{P}_{\text{beam}})^{\mathbf{T}}\mathbf{U}_{\text{beam}} = (\delta\mathbf{P}_{\mathbf{r}})^{\mathbf{T}}\mathbf{U}_{\mathbf{r}} = \int_0^L \int_0^{Area}(\delta\sigma\ \varepsilon\ dA)\ dx + \int_0^{\text{L}} \delta V\ \gamma\ dx \tag{3.14}$$

where $\delta\sigma$ is the virtual axial stress and ε is the axial strain in the infinitesimal cross-section area, dA. The axial strain, ε is defined in terms of the axial strain in the centroid of the beam cross-section, ε_c and the curvature, κ at distance, y, from the centroid as $\varepsilon = (\varepsilon_c + \kappa\ y)$.

The second term of internal virtual work represents the shear behaviour, where V and γ are the shear force and shear strain in the beam cross-section. The internal virtual work expression can be written in the open form of the section forces and deformations as follows:

$$\int_0^L \int_0^{Area}(\delta\sigma\ \varepsilon_c + \delta\sigma\ \kappa\ y)\ dA\ dx + \int_0^L \delta V\ \gamma\ dx = \int_0^L(\delta N\ \varepsilon_c + \delta M\ \kappa + \delta V\ \gamma)dx \tag{3.15}$$

The relationship between the section forces and the deformations can be summarised in a compact form of a set of internal stress resultants, $\mathbf{p}$ and strain resultants, $\boldsymbol{\varepsilon}$ vectors as (Figure 3.7):

$$\int_0^L(\delta N\ \varepsilon_c + \delta M\ \kappa + \delta V\ \gamma)dx = \int_0^L \delta\mathbf{p}^{\mathbf{T}}\boldsymbol{\varepsilon}\ dx \tag{3.16}$$

$$\mathbf{p} = [N \quad M \quad V]^{\text{T}} \qquad\qquad \boldsymbol{\varepsilon} = [\varepsilon_c \quad \kappa \quad \gamma]^{\text{T}} \tag{3.17}$$

Here, it is convenient to determine the internal stress resultants vector from the reduced forces vector through the force interpolation functions, $\mathbf{b}$:

$$\mathbf{p} = \mathbf{b}\,\mathbf{P_r} \tag{3.18}$$

$$\mathbf{b} = \begin{bmatrix} 1 & 0 & 0 \\ 0 & \alpha - 1 & \alpha \\ 0 & -1/L & -1/L \end{bmatrix} \tag{3.19}$$

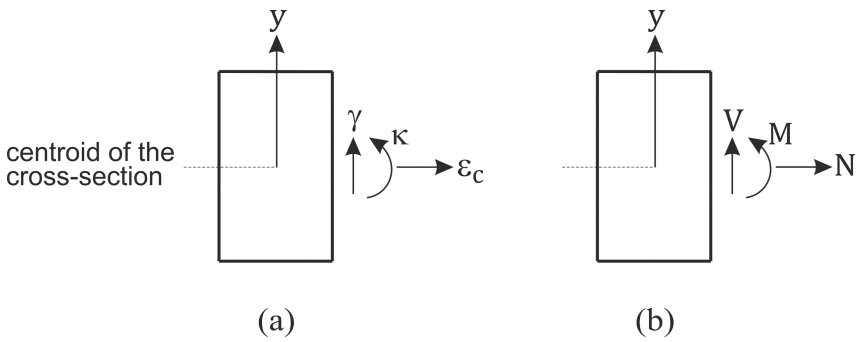


Figure 3.7: Beam cross-section level: (a) internal strain resultants, **ε** and (b) internal stress resultants, **p** (modified from Marini & Spacone, 2006).

where $\alpha = x_p/L$ for any position of the Gauss point. Accordingly, substituting Equation (3.18) into (3.16) and (3.14) gives the relationship between the reduced displacements and the section deformations as summarised:

$$(\delta\mathbf{P_r})^{\mathbf{T}}\mathbf{U_r} = \int_0^L (\delta\mathbf{P_r})^{\mathbf{T}}\mathbf{b}^{\mathbf{T}}\boldsymbol{\varepsilon}\, dx \tag{3.20}$$

Since $\delta\mathbf{P_r}$ is arbitrary, this gives,

$$\mathbf{U_r} = \int_0^L \mathbf{b}^{\mathbf{T}}\boldsymbol{\varepsilon}\, dx \tag{3.21}$$

The nodal forces in the global coordinates, $\mathbf{P}_{\text{beam}}$, can also be expressed in terms of a reduced set of forces, $\mathbf{P_r}$, as:

$$\mathbf{P_{beam}} = \mathbf{R}^{\mathbf{T}}\,\mathbf{T_r}^{\mathbf{T}}\,\mathbf{P_r} \tag{3.22}$$

3.4.3 Flexibility and stiffness matrices

The section deformations, **ε** are related to the section forces, **p** through the local flexibility matrix, **f** as:

$$\boldsymbol{\varepsilon} = \mathbf{f}\,\mathbf{p} \tag{3.23}$$

where the local flexibility matrix can be determined according to the material constitutive relationship as $\mathbf{f} = \left(\frac{\partial \boldsymbol{\varepsilon}}{\partial \mathbf{p}}\right)$. Substituting Equations (3.23) and (3.18) into (3.21) gives the relationship between the reduced displacements, $\mathbf{U_r}$ and the reduced forces, $\mathbf{P_r}$, as:

$$\mathbf{U_r} = \int_0^L \mathbf{b}^{\mathbf{T}} \left(\frac{\partial \boldsymbol{\varepsilon}}{\partial \mathbf{p}}\right) \mathbf{b}\,\mathbf{P_r}\,dx \tag{3.24}$$

The element flexibility matrix in the local coordinates, $\mathbf{F}$, is determined as:

$$\mathbf{F} = \int_0^L \mathbf{b}^{\mathbf{T}} \left(\frac{\partial \boldsymbol{\varepsilon}}{\partial \mathbf{p}}\right) \mathbf{b}\,dx \tag{3.25}$$

The relationship between the reduced displacements, $\mathbf{U_r}$ and the reduced forces, $\mathbf{P_r}$, can be expressed using the element flexibility matrix, $\mathbf{F}$, as:

$$\mathbf{U_r} = \mathbf{F}\,\mathbf{P_r} \qquad\qquad \mathbf{P_r} = \mathbf{F}^{-1}\mathbf{U_r} \tag{3.26}$$

Accordingly, substituting Equations (3.26), (3.11) and (3.7) into (3.22) gives the relationship between the nodal force, $\mathbf{P}_{\text{beam}}$ and the nodal displacement vectors, $\mathbf{U}_{\text{beam}}$, in the global coordinates as:

$$\mathbf{P}_{\text{beam}} = \mathbf{R}^{\mathbf{T}}\,\mathbf{T_r}^{\mathbf{T}}\mathbf{F}^{-1}\mathbf{T_r}\,\mathbf{R}\,\mathbf{U}_{\text{beam}} \tag{3.27}$$

The element stiffness matrix in the global coordinates, $\mathbf{K}_{\text{beam}}$, is determined as:

$$\mathbf{K}_{\text{beam}} = \mathbf{R}^{\mathbf{T}}\,\mathbf{T_r}^{\mathbf{T}}\mathbf{F}^{-1}\mathbf{T_r}\,\mathbf{R} \tag{3.28}$$

$\mathbf{K}_{\text{beam}}$ matrix can be directly assembled into the global stiffness matrix used in a stiffness-based finite element analysis.

3.4.4 Internal stress and strain resultants

Internal stress resultants are composed of axial force, bending moment and shear force at the beam cross-section level. The determination of shear force is decoupled from the axial force and bending moment responses at the section level (Marini & Spacone, 2006). While the fibre beam model calculates the axial force and bending moment as a summation of the axial stresses at each fibre area, the shear force is considered constant through the cross-section and computed at each Gauss point (Martino et al., 2000). The internal stress resultants, $\mathbf{p}$ and the section stiffness matrix, $\mathbf{k_{section}}$ (the local flexibility matrix, $\mathbf{f}$ is the inverse of $\mathbf{k_{section}}$ as $\mathbf{f} = \mathbf{k_{section}}^{-1}$) are determined by the fibre beam formulations with the addition of shear force (Martino et al., 2000; Marini & Spacone, 2006):

$$\mathbf{p} = \begin{bmatrix} N \\ M \\ V \end{bmatrix} = \begin{bmatrix} \sum_{i=1}^{nfibre} \sigma_{fibre} A_{fibre} \\ \sum_{i=1}^{nfibre} \sigma_{fibre} A_{fibre} y_{fibre} \\ V = V(\gamma) \end{bmatrix} \tag{3.29}$$

$$\mathbf{k_{section}} = \begin{bmatrix} \sum_{i=1}^{nfibre} \left(\frac{d\sigma}{d\varepsilon}\right)_{fibre} A_{fibre} & \sum_{i=1}^{nfibre} \left(\frac{d\sigma}{d\varepsilon}\right)_{fibre} A_{fibre} y_{fibre} & 0 \\ \sum_{i=1}^{nfibre} \left(\frac{d\sigma}{d\varepsilon}\right)_{fibre} A_{fibre} y_{fibre} & \sum_{i=1}^{nfibre} \left(\frac{d\sigma}{d\varepsilon}\right)_{fibre} A_{fibre} y_{fibre}^2 & 0 \\ 0 & 0 & \frac{dV}{d\gamma} \end{bmatrix} \tag{3.30}$$

where $nfibre$ is the number of fibre elements in the cross-section, σ_{fibre} is the axial stress in the fibre, A_{fibre} area of the fibre, y_{fibre} is the distance from the centroid of the cross-section to the centroid of the fibre (Figure 3.8), $\left(\frac{d\sigma}{d\varepsilon}\right)_{fibre}$ is the fibre tangent modulus and $dV/d\gamma$ is the shear tangent modulus. The section stiffness matrix can be represented as a partition of the tangent stiffness contributions of the fibre beam model, $\mathbf{k_{fibre}}_{(2\times2)}$ and the shear behaviour, $dV/d\gamma$ as:

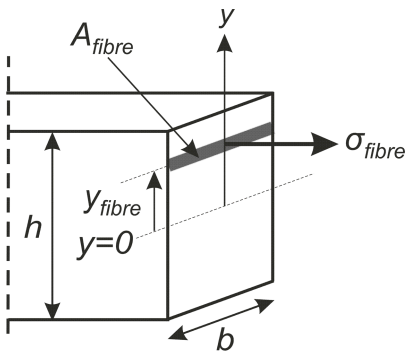


Figure 3.8: Demonstration of a single fibre element at the beam cross-section.

$$\mathbf{k_{section}} = \left(\frac{\partial \mathbf{p}}{\partial \boldsymbol{\varepsilon}}\right) = \begin{bmatrix} \mathbf{k_{fibre}}_{(2\times2)} & \mathbf{0}_{(2\times1)} \\ \mathbf{0}_{(1\times2)} & dV/d\gamma \end{bmatrix} \tag{3.31}$$

Similarly, the internal stress, $\mathbf{p}$ and strain, $\boldsymbol{\varepsilon}$ resultants can be expressed as a partition of the fibre beam and shear behaviour contributions as:

$$\mathbf{p} = \begin{bmatrix} N \\ M \\ V \end{bmatrix} = \begin{bmatrix} \mathbf{p_{fibre}}_{(2\times1)} \\ V \end{bmatrix} \qquad \boldsymbol{\varepsilon} = \begin{bmatrix} \varepsilon_c \\ \kappa \\ \gamma \end{bmatrix} = \begin{bmatrix} \boldsymbol{\varepsilon_{fibre}}_{(2\times1)} \\ \gamma \end{bmatrix} \tag{3.32}$$

where, $\mathbf{p_{fibre}}_{(2\times1)} = [N \quad M]^T$ and $\boldsymbol{\varepsilon_{fibre}}_{(2\times1)} = [\varepsilon_c \quad \kappa]^T$.

The axial stress in the fibre needs to be determined according to the material constitutive law for the relationship between the axial strain, ε_i and the axial stress, σ_i, where σ_i is the function of ε_i as $\sigma_i = f(\varepsilon_i)$.

3.4.5 Application of self-weight loads

The self-weight loads of the beam elements are implemented into the flexibility formulations as element loads, which affect the distribution of the internal stress resultants (Taucer et al., 1991; Neuenhofer & Filippou, 1997). The application of self-weight loading is associated with the element loads, $\mathbf{p_0}$ occurring under uniformly distributed loading applied to a simply supported beam element (Figure 3.9). The self-weight-induced element loads have similar components as the internal stress resultants vector (Equation 3.17):

$$\mathbf{p_0} = [N_0 \quad M_0 \quad V_0]^{\mathbf{T}} \tag{3.33}$$

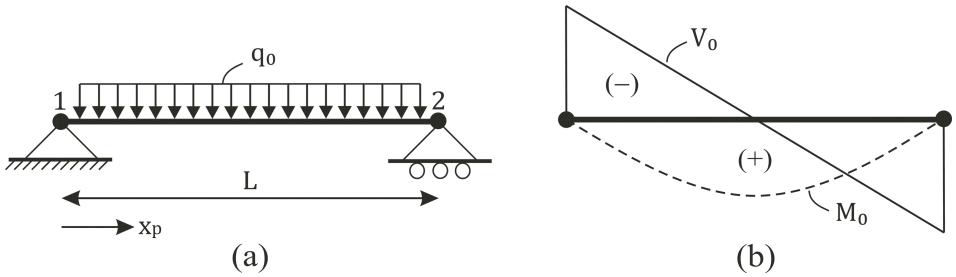


Figure 3.9: A simply supported beam element: (a) under uniformly distributed loading, (b) application of element loads without rigid body modes.

Firstly, the uniformly distributed load applied to the element, q_0, is calculated using the unit weight of the beam element, γ_m and the cross-sectional dimensions in terms of height, h and width, b of the element as $q_0 = \gamma_m\, h\, b$. Then, the element loads are computed for the spandrel $\mathbf{p_{0,spandrel}}$ and pier, $\mathbf{p_{0,pier}}$ element orientations as:

$$\mathbf{p_{0,spandrel}} = q_0 \begin{bmatrix} 0 \\ 1/2(L\, x_p - {x_p}^2) \\ (-L/2 + x_p) \end{bmatrix} \qquad \mathbf{p_{0,pier}} = q_0 \begin{bmatrix} (x_p - L) \\ 0 \\ 0 \end{bmatrix} \tag{3.34}$$

where x_p refers to the position of the Gauss point along the beam length, L, which is defined in the range of $[0, L]$.

The element loads are incorporated in the flexibility formulations at the beginning of the analysis, where only the self-weight loads are applied to the system. To achieve this, the internal stress resultants vector needs to be initialised with the application of element loads. The element loads are determined for the case of a simply supported beam in the absence of rigid body modes in the element level (Figure 3.9b). However, while transferring the internal beam forces to the global equilibrium level, the force reactions at each end of the spandrel/pier must be explicitly included in the global internal nodal force vector (Taucer et al., 1991). Thus, in addition to the nodal internal beam forces calculated in Equation (3.22), the vertical

equilibrium configuration forces (in $+Y$ direction) exerted on the beam element, $\mathbf{F_{eq}}$ is calculated as:

$$\mathbf{F_{eq,spandrel}} = \mathbf{R}^{-1}\,[0 \quad q_0\,L/2 \quad 0 \quad 0 \quad q_0\,L/2 \quad 0]^{\mathrm{T}} \tag{3.35}$$

$$\mathbf{F_{eq,pier}} = \mathbf{R}^{-1}\,[q_0\,L/2 \quad 0 \quad 0 \quad q_0\,L/2 \quad 0 \quad 0]^{\mathrm{T}} \tag{3.36}$$

where, $\mathbf{F_{eq,spandrel}}$ and $\mathbf{F_{eq,pier}}$ refer to the spandrel and pier orientations of the beam elements. The rotation matrix, $\mathbf{R}$, transforms the rigid body forces computed in the local member coordinates to the global coordinate system.

In the presence of the self-weight loads, in addition to the $\mathbf{P_{beam}}$ vector, the vertical equilibrium configuration forces, $\mathbf{F_{eq}}$ (Equations 3.35 and 3.36), also need to be added into the global internal nodal force vector of the beam elements, $\mathbf{F_{INT\ beams}}$. Only for the self-weight analysis $\mathbf{F_{INT\ beams}}$ is calculated as:

$$\mathbf{F_{INT,beams}} = \mathbb{A}[\mathbf{P_{beam}}] + \mathbb{A}\left[\mathbf{F_{eq}}\right] \tag{3.37}$$

where $\mathbb{A}$ is the assembly operator. In contrast to the stiffness-based finite element formulations, the calculation of external nodal forces is not needed for flexibility-based analysis. Application of self-weight loads to the system is implemented by initialising the internal stress resultants at the beginning of the analysis as element forces determined for simply supported beams.

3.5 Formulation of Stiffness-Based Elements

3.5.1 Quad Elements

Quad element is the key component of a macro-element, which comprises a 4-noded rectangular quad element and continuous interface elements surrounding the edges of the quad element. The quad geometry is determined according to the layout of the façade openings.

Depending on the full rigid offset method (Bracchi et al., 2015), the corners of openings are used to determine the element geometries. This element discretisation approach can be easily applied to the masonry buildings with both regular and irregular façade openings.

The quad element is formulated to translate and rotate as a rigid body while deforming only in shear (Figure 3.10). The interaction of a quad element with adjacent quads or rigid footing elements is governed by the 4-noded edge/line structural interface elements. These deformable interface elements have zero thickness and exert tractions in their normal and tangential directions depending on the relative displacements between two sides of the interface. The normal interface spring stiffness is defined to account for the axial compressibility of the masonry that is defined by the quad element (Caliò et al., 2012).

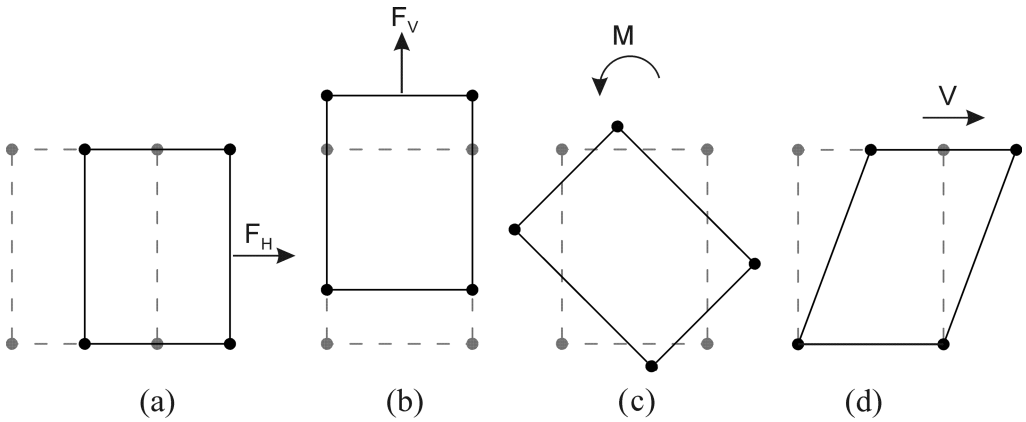


Figure 3.10: The rigid body movements and the deformation mode of a macro-element: (a) axial movement, (b) transverse movement, (c) rotation movement and (d) shear deformation.

3.5.1.1 Kinematics

A quad element (in dimensions of length, *L* and height, *H*) with its degrees of freedom (DOF) at the element centroid is demonstrated in Figure 3.11. The quad kinematics is characterised by 4-DOF including horizontal, u_0 and vertical, v_0 displacements, constant shear strain, γ_0 and constant rotation, θ_0. The quad kinematics presented in the EQFdc model is different than the DOF defined by Caliò et al. (2012).

The displacement vector of a quad element at the centroid, $\mathbf{U}_q$, is:

$$\mathbf{U}_q = [u_0, v_0, \gamma_0/2, \theta_0]^T \tag{3.38}$$

Consistent with Caliò et al.'s (2012) approach, the quad element does not deform in the axial and transverse directions; the horizontal and vertical strains ε_{xx}^{quad} and ε_{yy}^{quad} are therefore zero.

$$\varepsilon_{xx}^{quad} = \frac{\partial u}{\partial x} = 0; \;\; \varepsilon_{yy}^{quad} = \frac{\partial v}{\partial y} = 0 \tag{3.39}$$

where $\frac{\partial u}{\partial x}$ and $\frac{\partial v}{\partial y}$ refer to the partial derivatives of the axial, u and transverse, v displacements.

The quad's motion is characterised by constant shear strain and rotation as:

$$\gamma_0 = \frac{\partial u}{\partial y} + \frac{\partial v}{\partial x}; \;\; 2\theta_0 = \frac{\partial v}{\partial x} - \frac{\partial u}{\partial y} \tag{3.40}$$

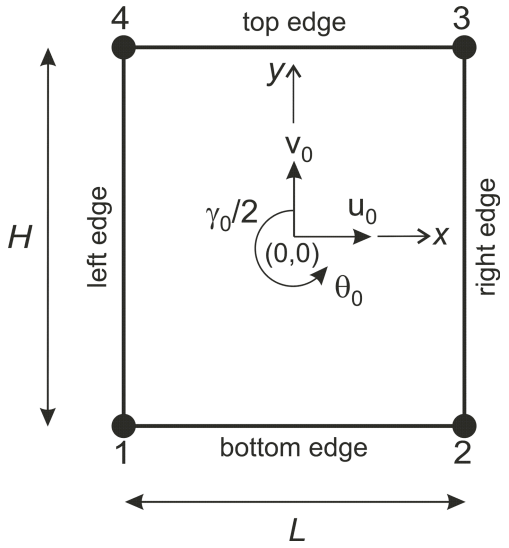


Figure 3.11: Quad element with 4-DOF at the element centroid.

The relationship between the constant shear strain and the 4-DOF of the quad element is:

$$\gamma_0 = \mathbf{B}_q \mathbf{U}_q = [0 \quad 0 \quad 2 \quad 0] \begin{bmatrix} u_0 \\ v_0 \\ \gamma_0/2 \\ \theta_0 \end{bmatrix} \tag{3.41}$$

where $\mathbf{B}_{\mathrm{q}}$ is referred to as the 'quad kinematic matrix'. The strain and rotation fields in Equation (3.40) define the displacement field of the element in terms of the DOF (Equation 3.42). The axial (u) and transverse (v) displacement fields, determined in the quad local coordinate system (shown by the coordinates x and y in Figure 3.11), are:

$$u = \mathrm{u}_0 + \frac{1}{2}(\gamma_0 - 2\theta_0)y; \quad v = \mathrm{v}_0 + \frac{1}{2}(\gamma_0 + 2\theta_0)x \tag{3.42}$$

Each quad element interacts with an adjacent quad through interface elements connected to the quads' edges. To describe relative displacements at the interface, the axial and transverse displacements at each edge of the quad need to be calculated in global coordinates. The displacement vectors at the four edges of the quad, $\mathbf{u} = [u \quad v]^{\mathrm{T}}$, are accordingly derived in the global coordinates, which have the same orientation as local quad coordinates x and y, as indicated in Figure 3.11. The relationship between the displacement vector at the base edge of the quad and the DOF vector is expressed as:

$$\mathbf{u}_{\mathrm{B}}^{\mathrm{e}} = \mathbf{B}_{\mathrm{B}}^{\mathrm{e}}\,\mathbf{U}_{\mathrm{q}} = \begin{bmatrix} 1 & 0 & -H/2 & H/2 \\ 0 & 1 & x & x \end{bmatrix} \begin{bmatrix} \mathrm{u}_0 \\ \mathrm{v}_0 \\ \gamma_0/2 \\ \theta_0 \end{bmatrix} \tag{3.43}$$

where $\mathbf{u}_{\mathrm{B}}^{\mathrm{e}}$ is the vector of displacements on the base edge and $\mathbf{B}_{\mathrm{B}}^{\mathrm{e}}$ is the base edge kinematic matrix. Similarly, the displacements on the right, top and left edges (denoted by $\mathbf{u}_{\mathrm{R}}^{\mathrm{e}}$, $\mathbf{u}_{\mathrm{T}}^{\mathrm{e}}$ and $\mathbf{u}_{\mathrm{L}}^{\mathrm{e}}$) of the quad are formulated by using the right, top and left edge kinematic matrices (expressed by $\mathbf{B}_{\mathrm{R}}^{\mathrm{e}}$, $\mathbf{B}_{\mathrm{T}}^{\mathrm{e}}$ and $\mathbf{B}_{\mathrm{L}}^{\mathrm{e}}$) as given in Equations (3.44) – (3.46).

$$\mathbf{u}_{\mathrm{R}}^{\mathrm{e}} = \mathbf{B}_{\mathrm{R}}^{\mathrm{e}}\,\mathbf{U}_{\mathrm{q}} = \begin{bmatrix} 1 & 0 & y & -y \\ 0 & 1 & L/2 & L/2 \end{bmatrix} \begin{bmatrix} \mathrm{u}_0 \\ \mathrm{v}_0 \\ \gamma_0/2 \\ \theta_0 \end{bmatrix} \tag{3.44}$$

$$\mathbf{u}_{\mathrm{T}}^{\mathrm{e}} = \mathbf{B}_{\mathrm{T}}^{\mathrm{e}}\,\mathbf{U}_{\mathrm{q}} = \begin{bmatrix} 1 & 0 & H/2 & -H/2 \\ 0 & 1 & x & x \end{bmatrix} \begin{bmatrix} \mathrm{u}_0 \\ \mathrm{v}_0 \\ \gamma_0/2 \\ \theta_0 \end{bmatrix} \tag{3.45}$$

$$\mathbf{u}_{\mathrm{L}}^{\mathrm{e}} = \mathbf{B}_{\mathrm{L}}^{\mathrm{e}}\,\mathbf{U}_{\mathrm{q}} = \begin{bmatrix} 1 & 0 & y & -y \\ 0 & 1 & -L/2 & -L/2 \end{bmatrix} \begin{bmatrix} \mathrm{u}_0 \\ \mathrm{v}_0 \\ \gamma_0/2 \\ \theta_0 \end{bmatrix} \tag{3.46}$$

3.5.1.2 Internal forces and stiffness matrix

The internal virtual work of a quad element, $\delta W_{int,quad}$ is formulated as:

$$\delta W_{int,quad} = \int_0^V (\delta\gamma_0)^{\mathrm{T}} \tau dV \tag{3.47}$$

where $\delta\gamma_0$ is the virtual shear strain, τ is the shear stress and V is the element volume. Determination of shear stress depends on the constitutive model used for the quad element (Sections 5.4.1 and 6.3.1). The internal force vector, $\mathbf{f}_{\mathrm{int,quad}}$ and the stiffness matrix, $\mathbf{K}_{\mathrm{quad}}$ of the quad element are derived in (4×1) and (4×4) forms, respectively as:

$$\mathbf{f}_{\mathrm{int,quad}} = \int_0^V \mathbf{B}_{\mathrm{q}}{}^{\mathrm{T}} \left(\frac{d\tau}{d\gamma_0}\right) \mathbf{B}_{\mathrm{q}}\,\mathbf{U}_{\mathrm{q}}\, dV \tag{3.48}$$

$$\mathbf{K}_{\mathrm{quad}} = \mathbf{B}_{\mathrm{q}}{}^{\mathrm{T}} \left(\frac{d\tau}{d\gamma_0}\right) \mathbf{B}_{\mathrm{q}}\, t_q\, L\, H \tag{3.49}$$

where $\left(\frac{d\tau}{d\gamma_0}\right)$ is the quad tangent modulus (depends on the constitutive model used for the quad), t_q is the quad thickness and dV is an infinitesimal volume element.

3.5.1.3 External forces

The external virtual work associated with a quad element, $\delta W_{ext,quad}$ is,

$$\delta W_{ext,quad} = -\int \delta v \, \gamma_q \, dV \tag{3.50}$$

where δv is the virtual vertical displacement, γ_q is the unit weight of the quad. The self-weight vector of a quad element, $\mathbf{f}_{\text{ext,quad}}$ can be calculated directly as:

$$\mathbf{f}_{\text{ext,quad}} = -[0 \quad H\,L\,t_q\,\gamma_q \quad 0 \quad 0]^{\text{T}} \tag{3.51}$$

3.5.2 Footing Elements

Footing elements (Figure 3.12) are modelled between the quad elements below the ground level and the soil-foundation interface elements (Figure 3.3c).

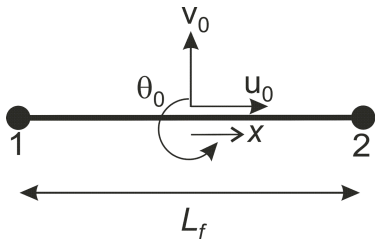


Figure 3.12: Footing element with 3-DOF at the element centroid.

3.5.2.1 Kinematics

The footing element is modelled as a rigid bar element composed of 3-DOF at the element centroid (Figure 3.12). The rigid footing element ensures that the displacement fields of the footing elements are consistent with the edge displacements of the quad elements just above. The footing element DOF vector, $\mathbf{U}_{\text{f}}$, is formulated in (3×1) form as:

$$\mathbf{U}_{\text{f}} = [\text{u}_0 \quad \text{v}_0 \quad \theta_0]^{\text{T}} \tag{3.52}$$

Thus, the local displacement vector along the footing x-axis, $\mathbf{u}_{\text{f}} = [u \quad v]^T$ is determined as:

$$\mathbf{u}_{\text{f}} = \mathbf{B}_{\text{f}}\,\mathbf{U}_{\text{f}} = \begin{bmatrix} 1 & 0 & 0 \\ 0 & 1 & x \end{bmatrix} \begin{bmatrix} \text{u}_0 \\ \text{v}_0 \\ \theta_0 \end{bmatrix} \tag{3.53}$$

where $\mathbf{B}_\mathrm{f}$ is the footing kinematic matrix, x is any point along x-axis ($x \in [-L_f/2,\ L_f/2]$) and L_f is the length of the footing element.

3.5.2.2 Internal forces and stiffness matrix

In the rigid footing (bar) elements, deformation is prevented. The internal virtual work of a rigid footing element is therefore zero.

3.5.2.3 External forces

The self-weight vector of the footing element, $\mathbf{f}_{\mathrm{ext,footing}}$ is given as:

$$\mathbf{f}_{\mathrm{ext,footing}} = -[0, \quad h_f\ L_f\ t_f\ \gamma_f, \quad 0]^T \tag{3.54}$$

where h_f, L_f, t_f and γ_f are the height, length, width and unit weight of the footing, respectively.

3.5.3 Structural Interface Elements

Structural interface elements are classified according to the type of elements they connect. They are referred to as quad-quad, quad-beam, quad-footing and footing-footing interface elements in the EQFdc model.

3.5.3.1 Kinematics

Quad-quad interface elements

The interface elements between the adjacent quad elements are formulated according to the orientation of the interface in the vertical or horizontal directions (Figures 3.13 and 3.14). The interface local coordinate system is indicated with relative displacements in shear, u_r and normal, v_r directions.

The relative displacements in the interface elements, $\mathbf{u}_\mathrm{r} = [u_r\ \ v_r]^T$ are determined using the edge kinematic matrices and the element displacement vectors of the adjacent quad elements

for vertical (Equation 3.55) and horizontal interface orientations (Equation 3.56).

$$\mathbf{u}_{\mathrm{r}} = \mathbf{T}\left[\mathbf{B}_{\mathrm{L}}^{\mathrm{right}} \quad -\mathbf{B}_{\mathrm{R}}^{\mathrm{left}}\right]\begin{bmatrix}\mathbf{U}^{\mathrm{right}} \\ \mathbf{U}^{\mathrm{left}}\end{bmatrix} \tag{3.55}$$

$$\mathbf{u}_{\mathrm{r}} = \mathbf{T}\left[\mathbf{B}_{\mathrm{B}}^{\mathrm{upper}} \quad -\mathbf{B}_{\mathrm{T}}^{\mathrm{lower}}\right]\begin{bmatrix}\mathbf{U}^{\mathrm{upper}} \\ \mathbf{U}^{\mathrm{lower}}\end{bmatrix} \tag{3.56}$$

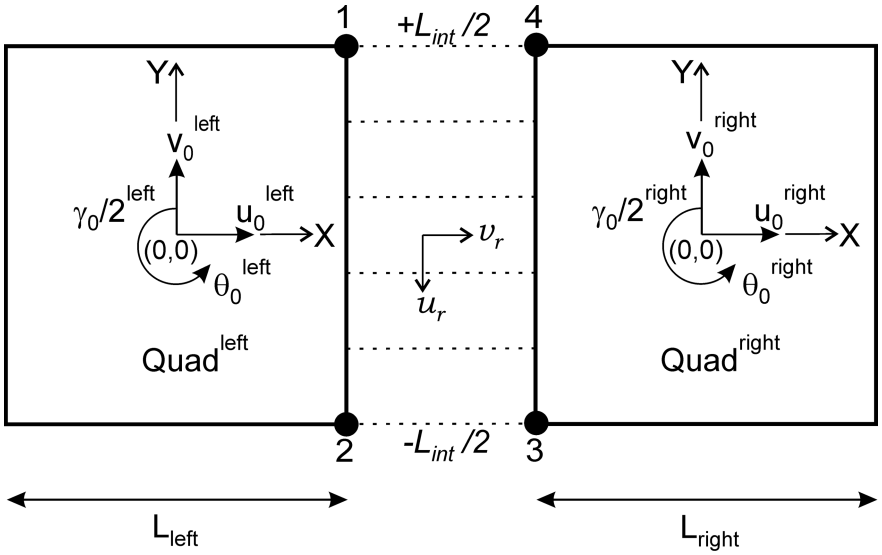


Figure 3.13: Quad-quad interface element in the vertical orientation.

where $\mathbf{B}_{\mathrm{L}}^{\mathrm{right}}$, $\mathbf{B}_{\mathrm{R}}^{\mathrm{left}}$, $\mathbf{B}_{\mathrm{B}}^{\mathrm{upper}}$ and $\mathbf{B}_{\mathrm{T}}^{\mathrm{lower}}$ are the edge kinematic matrices (i.e. the superscript and subscript refer to the quad element position and its corresponding edge, respectively) in (2×4) form defined in Equations (3.43) – (3.46). $\mathbf{U}^{\mathrm{right}}$ is the element displacement vector for the right quad element written in (4×1) form. Similarly, $\mathbf{U}^{\mathrm{left}}$, $\mathbf{U}^{\mathrm{upper}}$ and $\mathbf{U}^{\mathrm{lower}}$ are the element displacement vectors of the left, upper and lower quads, respectively. Additionally, $\mathbf{T}$ is a transformation matrix in (2×2) form used to transform the relative displacements calculated in the global coordinate system to the local coordinates of the interfaces. The relative displacement calculation can be written in a compact form by generalising the interface edge kinematic matrix as $\mathbf{B}_{\mathrm{int}}$ and the interface element displacement vector as $\mathbf{U}_{\mathrm{int}}$:

$$\mathbf{u}_r = \mathbf{T}\mathbf{B}_{\text{int}}\mathbf{U}_{\text{int}} \tag{3.57}$$

where $\mathbf{B}_{\text{int}}$ is in (2×8) and $\mathbf{U}_{\text{int}}$ is in (8×1) form for the quad-quad interface elements.

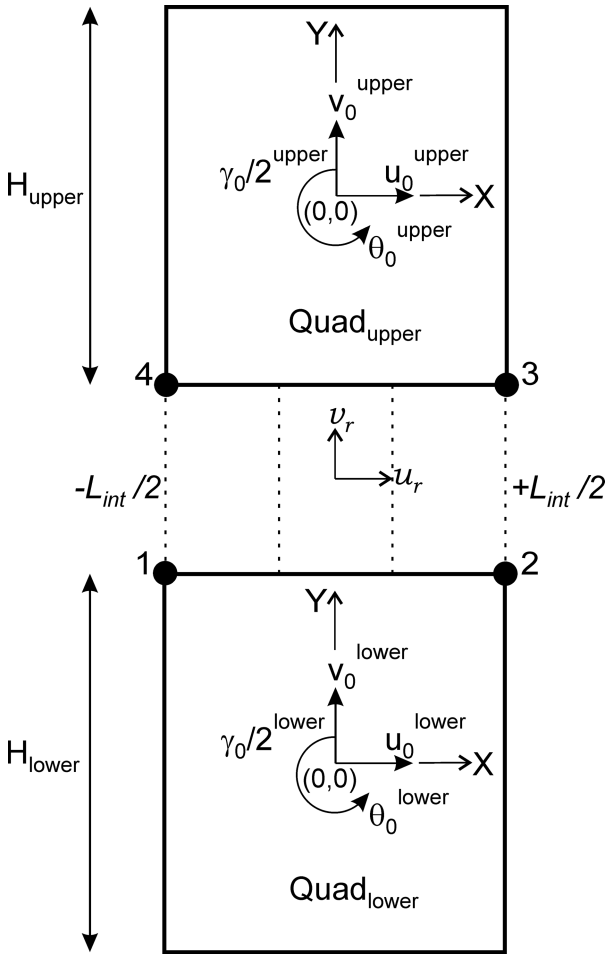


Figure 3.14: Quad-quad interface element in horizontal orientation.

Quad-beam interface elements

In the quad-beam interfaces, the beam edges are connected rigidly to the quad's edges (Figure 3.15). The kinematics of quad-beam interfaces are defined with 7-DOF, in which 4-DOF is from the quad element and 3-DOF is from the beam element. Notably, the normal stiffness of the quad-beam interface element only depends on the contribution of the quad element since the axial compliance of the beam is incorporated in the beam element formulation. The beam's start and end node displacements are expressed with the vectors $\mathbf{U}_{\text{beam,i}}$ and $\mathbf{U}_{\text{beam,i+1}}$ in

(3×1) forms separately. Accordingly, the global u_B and v_B displacements at any point along with the beam height, $-L_{int}/2 \leq h \leq L_{int}/2$, are calculated at $x = 0$ for the beam's left edge and at $x = L$ for the beam's right edge as given as follows:

$$\begin{bmatrix} u_B^{left} \\ v_B^{left} \end{bmatrix} = \mathbf{B}_h \mathbf{U}_{beam,i} = \mathbf{B}_h \begin{bmatrix} u_{B,i} \\ v_{B,i} \\ \theta_{B,i} \end{bmatrix} \tag{3.58}$$

$$\begin{bmatrix} u_B^{right} \\ v_B^{right} \end{bmatrix} = \mathbf{B}_h \mathbf{U}_{beam,i+1} = \mathbf{B}_h \begin{bmatrix} u_{B,i+1} \\ v_{B,i+1} \\ \theta_{B,i+1} \end{bmatrix} \tag{3.59}$$

where the edge kinematic matrix along the beam height, $\mathbf{B}_h$, is derived in the global coordinates of the spandrel (Equation 3.60) and pier (Equation 3.61) elements as:

$$\mathbf{B}_h = \begin{bmatrix} 1 & 0 & -h \\ 0 & 1 & 0 \end{bmatrix} \tag{3.60}$$

$$\mathbf{B}_h = \begin{bmatrix} 1 & 0 & 0 \\ 0 & 1 & -h \end{bmatrix} \tag{3.61}$$

The relative displacements at the beam left edge interface, $\mathbf{u}_r$, are computed as:

$$\mathbf{u}_r = \mathbf{T}\left(\mathbf{B}_{quad-beam}^{left}\, \mathbf{U}_{quad-beam}^{left}\right) = \mathbf{T}\left(\begin{bmatrix} \mathbf{B}_h & -\mathbf{B}_{quad,iR} \end{bmatrix} \begin{bmatrix} \mathbf{U}_{beam,i} \\ \mathbf{U}_{quad,i} \end{bmatrix}\right) \tag{3.62}$$

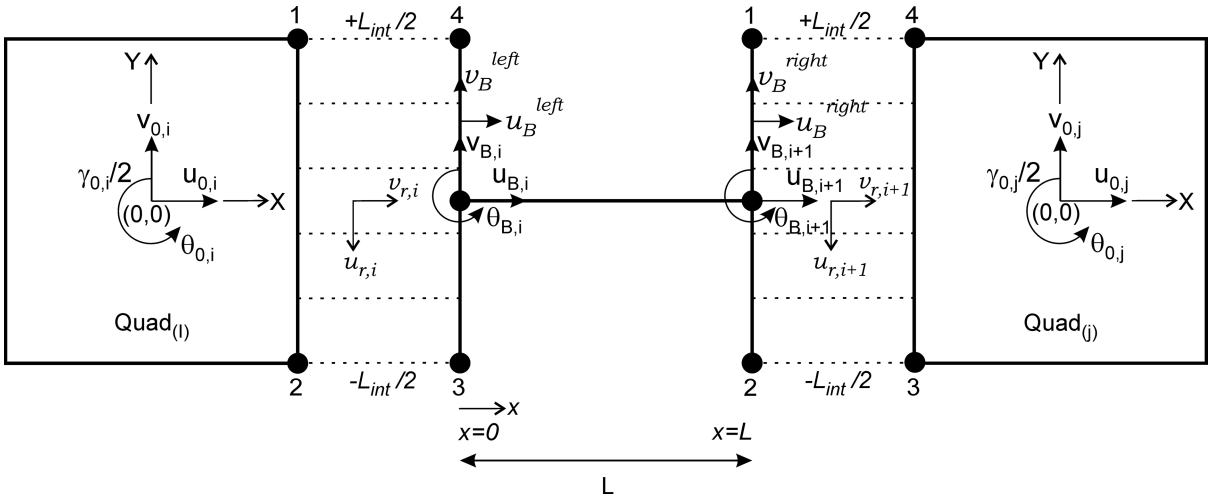


Figure 3.15: The quad-beam interface connection.

where $\mathbf{B}^{\text{left}}_{\text{quad}-\text{beam}}$ is the combined (2×7) form of edge kinematic matrices for the beam left edge interface. $\mathbf{B}^{\text{left}}_{\text{quad}-\text{beam}}$ comprises the edge kinematic matrix, $\mathbf{B}_{\text{h}}$, along the beam height and the right edge kinematic matrix of the quad element, $\mathbf{B}_{\text{quad,iR}}$, which is connected to the beam's left edge. The edge kinematic matrices of $\mathbf{B}_{\text{h}}$ and $-\mathbf{B}_{\text{quad,iR}}$ are the sub-matrices of $\mathbf{B}^{\text{left}}_{\text{quad}-\text{beam}}$ and they are formulated in (2×3) and (2×4) forms, respectively. Similarly, $\mathbf{U}^{\text{left}}_{\text{quad}-\text{beam}}$ is the combination of DOF vectors which is formulated in (7×1) form, including the DOF vector of the beam element at the start node, $\mathbf{U}_{\text{beam,i}}$ and the element displacement vector of the Quad$_{\text{i}}$, $\mathbf{U}_{\text{quad,i}}$. Additionally, $\mathbf{T}$ is a transformation matrix derived in (2×2) form. Since both quad and beam edge kinematic matrices are formulated in global coordinates, $\mathbf{T}$ matrix is needed to transform the relative displacements computed in the structure's global coordinates to the interface elements' local coordinates. Similarly, the relative displacements at the beam right edge interface are computed as:

$$\mathbf{u}_{\text{r}} = \mathbf{T}\left(\mathbf{B}^{\text{right}}_{\text{quad}-\text{beam}}\mathbf{U}^{\text{right}}_{\text{quad}-\text{beam}}\right) = \mathbf{T}\left(\begin{bmatrix}\mathbf{B}_{\text{quad,jL}} & -\mathbf{B}_{\text{h}}\end{bmatrix}\begin{bmatrix}\mathbf{U}_{\text{quad,j}} \\ \mathbf{U}_{\text{beam,i+1}}\end{bmatrix}\right) \tag{3.63}$$

In this case, $\mathbf{B}^{\text{right}}_{\text{quad}-\text{beam}}$ is the combined (2×7) form of the edge kinematic matrices derived at the left edge of the quad $(\mathbf{B}_{\text{quad,jL}})$ and at the right edge of the beam $(\mathbf{B}_{\text{h}})$. Similarly, $\mathbf{U}^{\text{right}}_{\text{quad}-\text{beam}}$ represents the compact (7×1) form of the DOF vectors belonging to the Quad$_{\text{j}}$, $\mathbf{U}_{\text{quad,j}}$ and the beam's end node, $\mathbf{U}_{\text{beam,i+1}}$.

Quad-footing interface elements

The quad-footing interface elements connect the base edge of the quads and the centroidal axis of the footing elements (Figure 3.16). In this approach, a quad is employed to represent the underground part of the masonry wall with a height of h_{wg} (Figure 3.16a). The height of the quad is determined as $h_{qg} = h_{wg} + h_f/2$, which extends up to the centroidal axis of the footing

element (Figure 3.16b). Here, h_f represents the height of the rectangular footing cross-section. Thus, the quad-footing interface connects the underground section of the masonry wall to the rigid footing element (which represents the wide strip with a width of t_f and length of L_f) interacting with the soil underneath. The relative displacements in the quad-footing interface are derived in Equation (3.64). In this case, $\mathbf{B}_{\mathrm{qf}}$ is the edge kinematic matrix and $\mathbf{U}_{\mathrm{qf}}$ is the element displacement vector of the quad-footing interface.

$$\mathbf{u}_{\mathrm{r}} = \mathbf{B}_{\mathrm{qf}}\,\mathbf{U}_{\mathrm{qf}} = \begin{bmatrix}\mathbf{B}_{\mathrm{B}}^{\mathrm{upper}} & -\mathbf{B}_{\mathrm{f}}\end{bmatrix}\begin{bmatrix}\mathbf{U}^{\mathrm{upper}} \\ \mathbf{U}_{\mathrm{f}}\end{bmatrix} \tag{3.64}$$

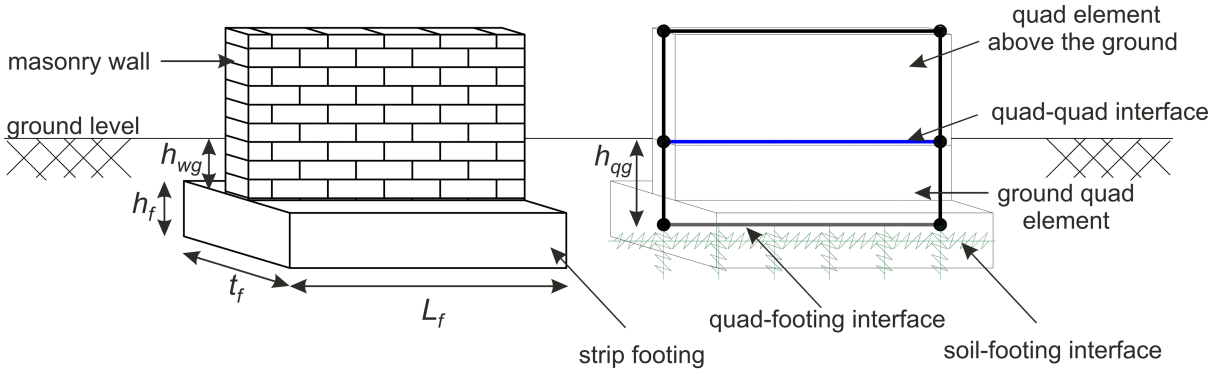


Figure 3.16: Modelling of the masonry section underground: (a) footing detail, (b) quad-footing interface detail.

Footing-footing interface elements

Between the nodes of the footing elements (e.g. node denoted as $i+1$ and $i+2$), 2-noded axial springs are used as compliant elements to allow the deformations between the adjacent rigid footing elements (Figure 3.17).

The relative displacements between footing elements are calculated using the kinematic matrix, $\mathbf{B}_{\mathrm{ff}}$ and the element displacement vector, $\mathbf{U}_{\mathrm{ff}}$ of the footing-footing interface elements, which are derived in (2×6) and (6×1) forms as:

$$\mathbf{u}_{\mathrm{r}} = \mathbf{B}_{\mathrm{ff}}\,\mathbf{U}_{\mathrm{ff}} = \begin{bmatrix} 1 & 0 & 0 & -1 & 0 & 0 \\ 0 & 0 & 0 & 0 & 0 & 0 \end{bmatrix} \begin{bmatrix} \mathbf{U}_{\mathrm{f}}^{\mathrm{right}} \\ \mathbf{U}_{\mathrm{f}}^{\mathrm{left}} \end{bmatrix} \tag{3.65}$$

where $\mathbf{U}_{\mathrm{f}}^{\mathrm{right}}$ and $\mathbf{U}_{\mathrm{f}}^{\mathrm{left}}$ refer to the element displacement vectors of the adjacent footings.

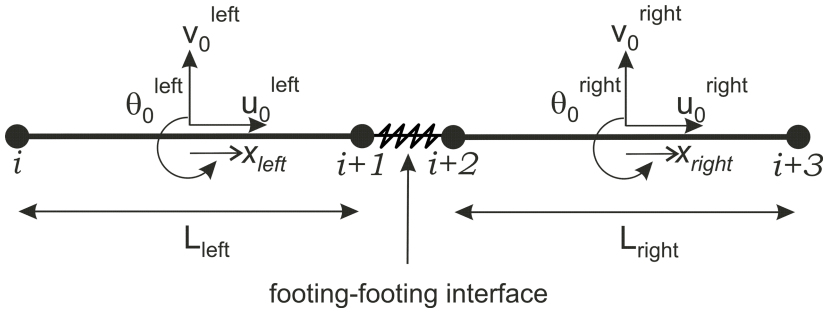


Figure 3.17: Footing-footing interface.

3.5.3.2 Internal forces and stiffness matrix

The normal stiffness of each interface element represents the elastic stiffness of the masonry portion corresponding to the influenced area of the quad element (Caliò et al., 2012; Minga, 2017). Figure 3.18 shows the definition of interface influence areas for the vertical (Figure 3.18a) and horizontal (Figure 3.18b) orientation of the quad-quad interfaces. The shear, $K_{s,i}$ and normal, $K_{n,i}$ stiffness contributions of a corresponding quad in an interface element are computed as:

$$K_{s,i} = 10^{\,6} K_{n,i} \qquad\qquad K_{n,i} = \frac{E_i}{L_i/2} \tag{3.66}$$

where the interface influence length that considers the half dimension of the corresponding quad element, such as $L_i/2$ and $H_i/2$, for the vertical and horizontal interface elements associated with $\mathrm{Quad_i}$. For the adjacent $\mathrm{Quad_i}$ and $\mathrm{Quad_j}$ elements (Young's modulus are E_i and E_j whereas the interface influence lengths are L_i and L_j respectively), the normal stiffness of the interface element, $K_{n,int}$ computed as:

$$K_{n,int} = \frac{K_{n,i}\, K_{n,j}}{K_{n,i} + K_{n,j}} = \frac{E_i\, E_j}{E_j L_i + E_i L_j} \tag{3.67}$$

where $K_{n,i}$ and $K_{n,j}$ refer to the normal stiffness contributions of Quad_i and Quad_j, respectively.

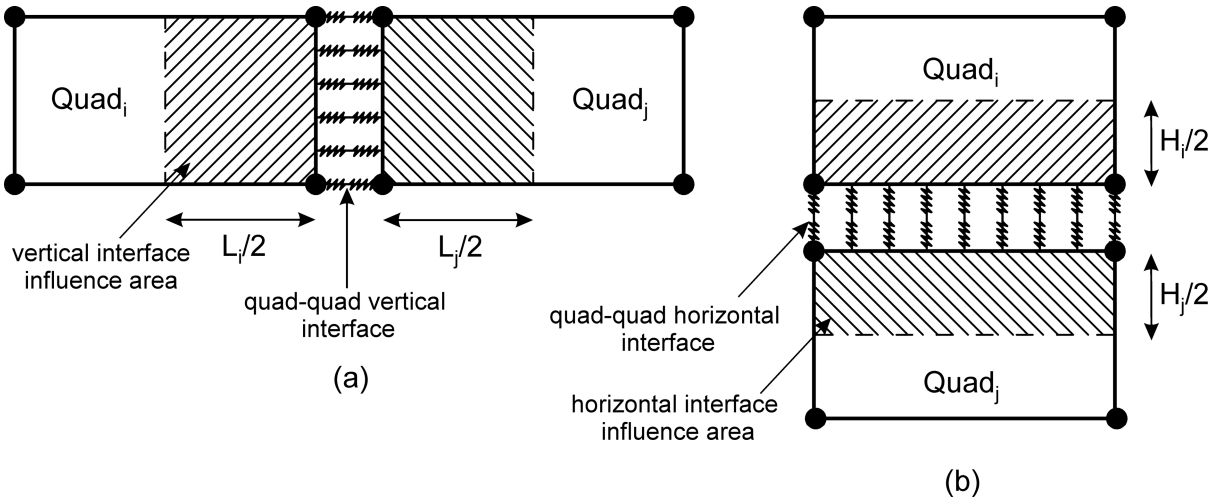


Figure 3.18: Quad-quad interface influence area: (a) vertical orientation, (b) horizontal orientation.

For the quad-footing interface elements (Figure 3.19), $K_{n,int}$ only depends on the ground quad element's stiffness contribution. For the footing-footing interface, the axial stiffness contributions of the footing elements at the right, K_r and the left, K_l sides of the nodes are employed to determine the constitutive matrix of the axial spring, $\mathbf{D}_{\text{spring}}$ as follows:

$$\mathbf{D}_{\text{spring}} = \begin{bmatrix} K_r\, K_l/(K_r + K_l) & 0 \\ 0 & 0 \end{bmatrix} \tag{3.68}$$

$$K_r = \frac{E_r A_f}{L_r/2} \qquad\qquad K_l = \frac{E_l A_f}{L_l/2} \tag{3.69}$$

where E_r and E_l are the Young's modulus, L_r and L_l are the length and A_f is the cross-sectional area of the footing elements at the right and left sides of the shared footing node.

The internal virtual work of an interface element is related to the relative displacements, $\mathbf{u}_\text{r}$ and the tractions, $\mathbf{p}$. The traction vector, $\mathbf{p} = [t \quad p]^T$ is composed of shear, t and normal p

tractions computed in the local coordinates of the interface element. The internal virtual work of any interface element, $\delta W_{int,interface}$ is determined by,

$$\delta W_{int,interface} = \int_{-L_{int}/2}^{L_{int}/2} (\delta \mathbf{u}_{\mathrm{r}})^{\mathrm{T}} \mathbf{p}\, t_{int}\, dX \tag{3.70}$$

where $\delta \mathbf{u}_{\mathrm{r}}$ is the virtual relative displacements, L_{int} is the interface length and t_{int} is the interface thickness. For the horizontal quad-quad interface, L_{int} is the quad length and the integration is performed over the global X axis. In contrast, for the vertical quad-quad interface, L_{int} is the quad height and the integration is performed over the global Y axis. The internal force vector, $\mathbf{f}_{\mathrm{int,interface}}$ and the element stiffness matrix, $\mathbf{K}_{\mathrm{int,interface}}$ of the interface elements are represented in terms of the interface tangent modulus, $\left(\frac{d\mathbf{p}}{d\mathbf{u}_{\mathrm{r}}}\right)$ (depends on the constitutive model used for the interface element) as follows:

$$\mathbf{f}_{\mathrm{int,interface}} = \int_{-L_{int}/2}^{L_{int}/2} (\mathbf{TB}_{\mathrm{int}})^{\mathrm{T}} \left(\frac{d\mathbf{p}}{d\mathbf{u}_{\mathrm{r}}}\right) (\mathbf{TB}_{\mathrm{int}}) \mathbf{U}_{\mathrm{int}} t_{int} dX \tag{3.71}$$

$$\mathbf{K}_{\mathrm{int,interface}} = \int_{-L_{int}/2}^{L_{int}/2} (\mathbf{TB}_{\mathrm{int}})^{\mathrm{T}} \left(\frac{d\mathbf{p}}{d\mathbf{u}_{\mathrm{r}}}\right) (\mathbf{TB}_{\mathrm{int}}) t_{int} dX \tag{3.72}$$

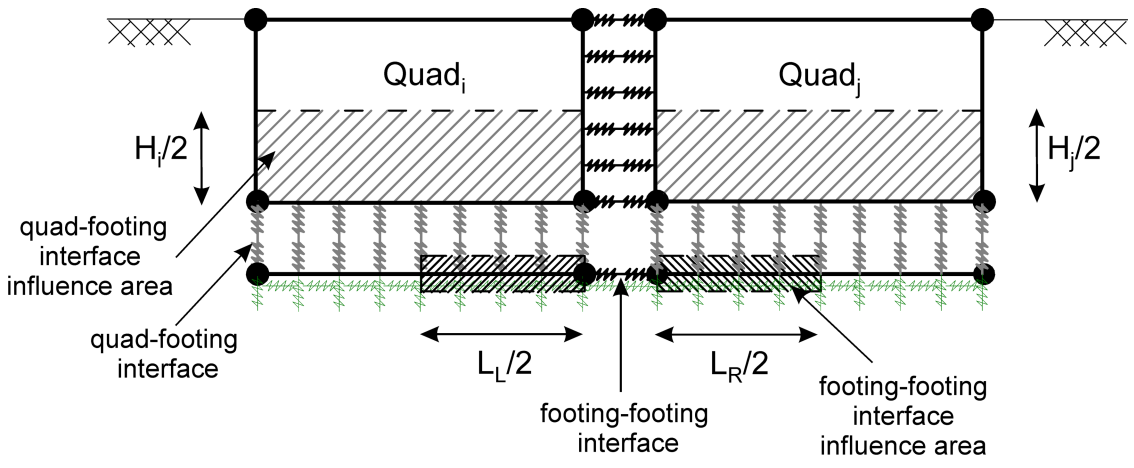


Figure 3.19: Quad-footing and footing-footing interface influence areas.

where t_{int} is the quad thickness (t_q) for the quad-quad and quad-beam interface elements and it represents the footing width (t_f) for the quad-footing interfaces. Note that when calculating footing-footing interfaces, the thickness parameter, t_{int}, needs to be removed from the internal force vector and the stiffness matrix equations.

Here, according to the type of interface elements, the specific edge kinematic matrices need to be used in place of $\mathbf{B}_{\text{int}}$ and the specific element displacement vectors in place of $\mathbf{U}_{\text{int}}$. Similarly, the element constitutive matrix, $\mathbf{D}_{\text{int}} = [K_{s,int} \quad 0\,;\, 0 \quad K_{n,int}]$ (i.e. $K_{s,int}$ is the shear stiffness and $K_{n,int}$ is the normal stiffness of the interface element) needs to be chosen according to the type of interface elements. The relative displacements calculated in the global coordinate system need to be transformed to the local coordinates of the interface element by using the transformation matrix, $\mathbf{T}$ in (2×2) form. When the quad-beam interface is orientated vertically, the integrations are performed over the global Y axis as dY. Likewise, dX is used for the global X axis for the horizontal interface orientation.

3.6 Determination of Strain Distributions

Calculation of major principal tensile strains is required to determine the damage class in a tunnel-soil-structure interaction problem.

3.6.1 Macro-elements

To find the strains experienced by the macro-element (i.e. combination of a quad and surrounding interfaces) and consequently, the masonry structure it represents, it is necessary to develop a procedure that accounts for the combination of shear strains inside the quad and the transverse deformations of the interface. The procedure involves setting up an internal grid in axial and transverse directions within the macro-element (Figure 3.20). The quad element experiences uniform shear strain (γ_0) and zero plane strains in axial and transverse directions.

The interfaces idealise the axial and transverse deformability of the masonry. Thus, the deformations that the interfaces experience can be attributed to the grids inside the macro-element (Figure 3.20). Since the relative shear displacements in the interface elements are expected to be negligible due to the high value of interface shear stiffness, only the relative normal displacements are considered.

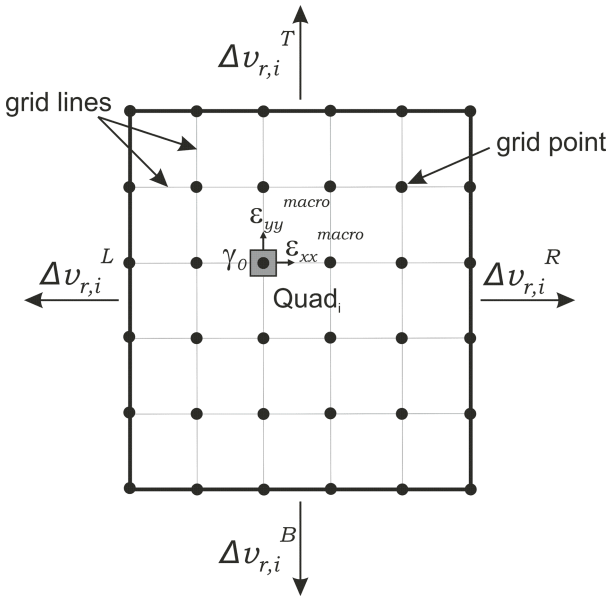


Figure 3.20: A macro-element showing the internal grids and the relative normal displacements induced by Quad$_i$ at the quad edges.

The total relative displacements at the interfaces arise due to the deformation of adjacent quads. To find the plane strains at the grid points of a macro-element in axial, ε_{xx}^{macro} and transverse, ε_{yy}^{macro} directions, it is necessary to partition off the total interface relative displacements into components that belong to each macro-element. This is achieved by noting that each interface spring is composed of two springs arranged in series. K_B, K_T, K_R and K_L are the total normal stiffness modulus at the bottom, top, right and left edge interfaces surrounding the quad, Quad$_i$. Accordingly, $K_{B,i}$, $K_{T,i}$, $K_{R,i}$ and $K_{L,i}$ are the normal stiffness modulus contributions of the quad, Quad$_i$ to the total normal stiffness modulus. The relative normal displacements induced by Quad$_i$ at the bottom, top, right and left ($\Delta v_{r,i}{}^{B}$, $\Delta v_{r,i}{}^{T}$, $\Delta v_{r,i}{}^{R}$ and $\Delta v_{r,i}{}^{L}$ respectively, where

superscript refers to the quad edge) interfaces are computed at each grid along the edges:

$$\Delta {v_{r,i}}^{B} = \frac{K_B}{K_{B,i}} {v_r}^{B}, \quad \Delta {v_{r,i}}^{T} = \frac{K_T}{K_{T,i}} {v_r}^{T}, \quad \Delta {v_{r,i}}^{R} = \frac{K_R}{K_{R,i}} {v_r}^{R}, \qquad \Delta {v_{r,i}}^{L} = \frac{K_L}{K_{L,i}} {v_r}^{L} \tag{3.73}$$

Then, ε_{xx}^{macro} and ε_{yy}^{macro} are computed at each grid point inside the macro-element:

$$\varepsilon_{xx}^{macro} = \frac{\Delta {\mathrm{v_{r,i}}}^{\mathrm{R}} + \Delta {\mathrm{v_{r,i}}}^{\mathrm{L}}}{\mathrm{L}} \qquad\qquad \varepsilon_{yy}^{macro} = \frac{\Delta {\mathrm{v_{r,i}}}^{\mathrm{T}} + \Delta {\mathrm{v_{r,i}}}^{\mathrm{B}}}{\mathrm{H}} \tag{3.74}$$

where L is the length and H is the height of the quad. Finally, the major principal tensile strain, ε_1 is computed at each grid point as:

$$\varepsilon_1 = \frac{\varepsilon_{xx}^{macro} + \varepsilon_{yy}^{macro}}{2} + \sqrt{\frac{(\varepsilon_{xx}^{macro} - \varepsilon_{yy}^{macro})^2 + {\gamma_0}^2}{4}} \tag{3.75}$$

3.6.2 Beam elements

In the flexibility-based beam element formulations, the axial strain is computed and stored in a database, $\boldsymbol{\varepsilon}_{\mathrm{fibre}}^{\mathrm{database}}$ for each corresponding beam (*ibeam*), Gauss point (*igauss*) and fibre element (*ifibre*). Thus, the axial strain in the x-axis of the cross-section, ε_{xx}, is extracted from the axial strain database as $\varepsilon_{xx} = \boldsymbol{\varepsilon}_{\mathrm{fibre}}^{\mathrm{database}}$(*ibeam, igauss, ifibre*). However, the transverse strain in y-axis is considered zero, $\varepsilon_{yy} = 0$. At the end of the flexibility analysis, the shear strains are extracted from the internal strain resultants vector as $\gamma = \boldsymbol{\varepsilon}(3)$. The shear strain is formulated as constant across the beam cross-section as mentioned in the flexibility formulations. However, while post processing the analysis results for the calculation of the major principal tensile strain, a parabolic distribution of the shear strain is assumed for a linear elastic beam model. In contrast, the constant shear strain approach is maintained for the nonlinear beam model. The distribution of major principal tensile strains in a beam element is computed at each fibre element across the cross-section and along each Gauss point.

3.7 Conclusion

In this chapter, the formulation of a novel EQFdc model is explained. The modelling approach combines the advantageous features of both EQF (i.e. with rigid connectors used widely in the earthquake engineering field) and macro-element models. This is achieved by representing the frame behaviour through spandrels and piers according to the EQF modelling approach but by replacing the rigid connectors with the deformable macro-elements to eliminate the overestimation of building stiffness. Using macro-elements in the EQFdc modelling approach also solves the uncertainties specified in the idealisations of element geometries in the original EQF models because the macro-element idealisation of the masonry buildings is quite straightforward and can be applied to both façades with regular and irregular openings easily. The EQFdc model also provides a practical method to represent the building and foundation interaction by modelling the embedded portion of the façade below the ground level with the quad elements and employing footing elements underneath to allow the connection with soil-foundation interface elements.

Flexibility-based beam element formulations are used to model the spandrels and the piers in the EQFdc model. Flexibility-based formulations are chosen since they can easily be incorporated with the 1D nonlinear constitutive material models (Chapter 6). The macro-elements are modelled with the stiffness-based formulations, but the kinematics formulation allows for practically representing the quad shear behaviour and translational deformations in the interface elements. Conveniently, these can also be represented with the same 1D nonlinear constitutive material models used for beams.

The EQFdc model enables the determination of major principal tensile strains to estimate the damage class of masonry buildings affected by tunnelling-induced displacements based on the standard building damage classification system that is widely used in the tunnelling industry.

Chapter 4

EQFdc Analysis: Solution Procedure

4.1 Introduction

A general solution procedure employed for both linear and nonlinear analyses in the EQFdc model is explained in this chapter. The EQFdc analysis comprises three main iteration procedures conducted at global, element and Gauss point levels for both linear and nonlinear analysis. The global level is defined for the whole structure, including the quad, the beam and the interface elements. However, the element and cross-section levels are only required for the beams, which are modelled according to the flexibility formulations.

4.2 Global Level Iteration

The general solution procedure used for the EQFdc analysis in the global equilibrium level comprising the whole elements is explained in this section. Figure 4.1 shows the summary of the EQFdc analysis solution procedure, which starts iterating to satisfy the equilibrium at the global level and then updates the global internal forces in each element. The global internal forces are computed based on the finite element formulations adopted for the specified element (i.e. either according to stiffness-based or flexibility-based formulations). The aim is to find an equilibrium between the external global forces applied to the system, $\mathbf{F_{EXT}}$ and the internal global forces $\mathbf{F_{INT}}$ computed for each element depending on the specified constitutive models.

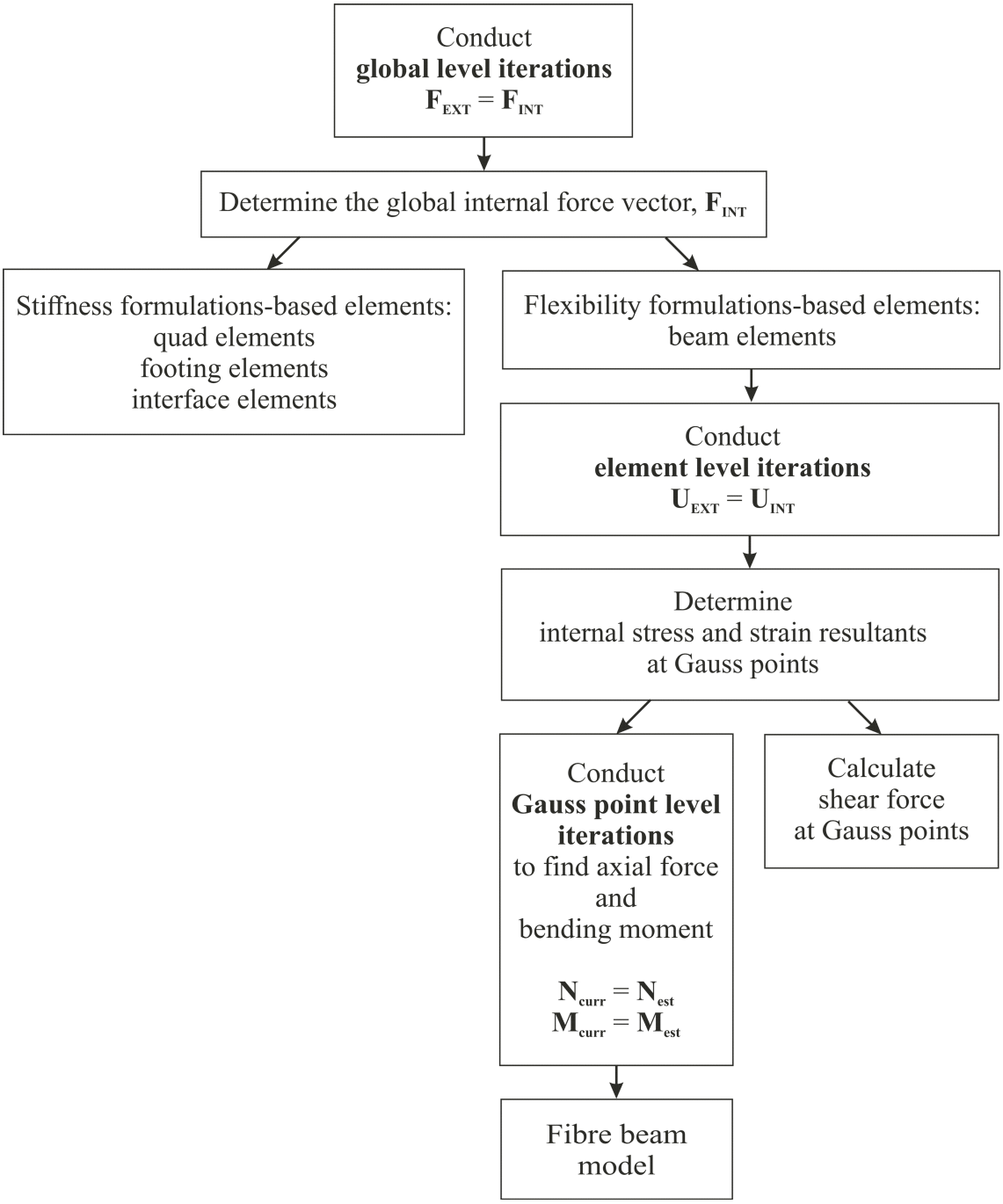


Figure 4.1: The general solution procedure for the EQFdc analysis.

External loads are applied to the model in steps. At each global iteration, the equilibrium between the external and internal global forces are checked to satisfy:

$$\mathbf{G}(\mathbf{U_{ite}}) = \mathbf{F_{EXT}} - \mathbf{F_{INT}}(\mathbf{U_{ite}}) \tag{4.1}$$

where $\mathbf{G}$ is the out-of-balance force vector at the global (whole structure) level and $\mathbf{U_{ite}}$ is the

global nodal displacement vector at the specified global iteration number ('ite'). The solution to the global force equilibrium is sought to find the corresponding $\mathbf{U_{ite}}$ that satisfies $\mathbf{G} = 0$. To solve Equation (4.1), $\mathbf{G(U)}$ is linearised at $\mathbf{U} = \mathbf{U_{ite}}$ as:

$$\mathbf{G(U)} \approx \mathbf{G(U_{ite})} + \frac{\partial \mathbf{G}}{\partial \mathbf{U}} \Delta \mathbf{U} \tag{4.2}$$

where $\Delta \mathbf{U} = \mathbf{U} - \mathbf{U_{ite}}$ is the incremental global nodal displacements and $\frac{\partial \mathbf{G}}{\partial \mathbf{U}}$ is the global tangent stiffness matrix.

The Modified Newton Raphson iteration scheme is used to solve Equation (4.2) for the specified global nodal displacements vector of $\mathbf{U_{ite}}$. First, the internal global force vector, $\mathbf{F_{INT}(U_{ite})}$, is calculated for all elements in the model and then the global force out-of-balance vector is determined for the specified global iteration as $\mathbf{G(U_{ite})}$. Here, it is important to note that the calculation of the internal global force vector for the beam elements require complex iterative procedures for the flexibility analysis that described in the next sections. If $\|\mathbf{G(U_{ite})}\| < tol$, where tol is the global tolerance value chosen as 10 N (or 10 Nm), then the result of the current iteration is selected as $\mathbf{U} = \mathbf{U_{ite}}$. Otherwise, the incremental global nodal displacements, $\Delta \mathbf{U}$, are computed by solving,

$$0 = \mathbf{G(U_{ite})} + \frac{\partial \mathbf{G}}{\partial \mathbf{U}} \Delta \mathbf{U} \tag{4.3}$$

The nodal displacement vector is then updated for the next iteration as follows:

$$\mathbf{U_{ite+1}} = \mathbf{U_{ite}} + \Delta \mathbf{U} \tag{4.4}$$

The process continues to iterate until $\|\mathbf{G(U_{ite+1})}\| < tol$.

The global level iterations are performed separately for the self-weight and the greenfield displacement loadings. For the EQFdc analysis conducted under the self-weight loading only,

the current internal stress resultants, $\mathbf{p_{curr}}$, need to be initialised once according to the presence of the self-weight loads of the beam elements as $\mathbf{p_{curr}} = \mathbf{p_0}$ (Equation 3.33) at the beginning of the global level iterations. Then, in the continuation of the EQFdc analysis for both self-weight and greenfield loading cases, the internal stress resultants need to be updated, $\mathbf{p_{up}}$ (Equation 4.14) at each Gauss point level iteration as presented later in the chapter.

4.3 Element Level Iteration

The element level iteration is required for the flexibility analysis in the beam elements. To explain the determination of the global nodal internal forces for the beam elements, the force equilibrium between the external and internal forces is expressed separately for the beam elements in Equation (4.5). However, Equation (4.5) does not present an additional iteration procedure; in contrast, it is only represented in this way to highlight the vectors that correspond to the beam elements in Equation (4.1) as follows:

$$\mathbf{G}\left(\mathbf{U_{ite,beams}}\right) = \mathbf{F_{EXT,beams}} - \mathbf{F_{INT,beams}}(\mathbf{U_{ite,beams}}) \tag{4.5}$$

where $\mathbf{F_{EXT,beams}}$ is global nodal external forces applied to the beams, $\mathbf{F_{INT,beams}}$ is the global nodal internal forces associated with the beam elements and $\mathbf{U_{ite,beams}}$ is the global nodal displacement vector of the whole beam elements at a particular iteration (abbreviation of 'ite' refers to the global level iterations). $\mathbf{U_{ite,beams}}$ is incorporated as the external displacements in the flexibility analysis. Firstly, the reduced set of external displacements, $\mathbf{U_{r,ext}}$ need to be determined according to Equation (3.11) for the specified beam element in the flexibility analysis. To satisfy the compatibility between the reduced set of external, $\mathbf{U_{r,ext}}$ and internal displacements, $\mathbf{U_{r,int}}$ for the specified beam element, at a particular element level iteration ('iteES'), the residual displacement vector is determined as $\mathbf{G}\left(\mathbf{P_r}^{iteES}\right)$ for an estimate of a reduced set of forces, $\mathbf{P_r}^{iteES}$:

$$\mathbf{G}\left(\mathbf{P_r}^{iteES}\right) = \mathbf{U_{r,int}}\left(\mathbf{P_r}^{iteES}\right) - \mathbf{U_{r,ext}} \tag{4.6}$$

To find the internal forces that satisfy the compatibility between $\mathbf{U_{r,int}}$ and $\mathbf{U_{r,ext}}$, the following updates are needed for: the internal stress resultants, $\mathbf{p}$, the internal strain resultants, $\boldsymbol{\varepsilon}$ and the reduced set of force vector, $\mathbf{P_r}$. The iteration procedure described in Section 4.4 is for the determination of internal stress and strain resultants at Gauss point level according to the element state determination (Spacone et al., 1996; Neuenhofer & Filippou, 1997). The element level updating procedure iterates until the compatibility between $\mathbf{U_{r,ext}}$ and $\mathbf{U_{r,int}}$ is reached (Equation 4.6). An iterative solution is required to find the suitable $\mathbf{P_r}$ value by updating the incremental reduced set of forces, $\Delta\mathbf{P_r}$, at each iteration. According to the Newton-Raphson approach, $\mathbf{G}(\mathbf{P_r})$ is linearised to get a better estimate of $\mathbf{P_r}^{iteES}$ to give $\mathbf{P_r} = \mathbf{P_r}^{iteES}$ as:

$$\mathbf{G}(\mathbf{P_r}) \approx \mathbf{G}\left(\mathbf{P_r}^{iteES}\right) + \frac{\partial \mathbf{G}}{\partial \mathbf{P_r}} \Delta \mathbf{P_r} \tag{4.7}$$

where $\frac{\partial \mathbf{G}}{\partial \mathbf{P_r}}$ is the tangent flexibility matrix (Equation 3.25) and depends on the relationship between the internal stress and strain resultants for the specified material constitutive law (Sections 5.2 and 6.2).

$$\frac{\partial \mathbf{G}}{\partial \mathbf{P_r}} = \int_0^L \mathbf{b^T} \left(\frac{\partial \boldsymbol{\varepsilon}}{\partial \mathbf{p}}\right) \mathbf{b}\, dx \tag{4.8}$$

By solving the following equation, incremental reduced set of forces, $\Delta\mathbf{P_r}$ is determined as:

$$\Delta \mathbf{P_r} = -\frac{\partial \mathbf{G}}{\partial \mathbf{P_r}} \mathbf{G}\left(\mathbf{P_r}^{iteES}\right) \tag{4.9}$$

Thus, the improved estimate of the reduced set of forces, $\mathbf{P_r}^{iteES+1}$, is computed as:

$$\mathbf{P_r}^{iteES+1} = \mathbf{P_r}^{iteES} + \Delta \mathbf{P_r} \tag{4.10}$$

The element state iterations continue until the residual displacements, $\mathbf{G}$ reach a value less than the desired tolerance value ($tol = 10^{-3}$) of the magnitude of initial residual displacements, $\|\mathbf{G}(\mathbf{P_r}^1)\|$.

$$\|\mathbf{G}(\mathbf{P_r}^{iteES})\| < tol \times \|\mathbf{G}(\mathbf{P_r}^1)\| \tag{4.11}$$

When the compatibility between the reduced set of external and internal displacements is achieved for the specified beam element, the internal nodal force vector, $\mathbf{P}_{\text{beam}}$, needs to be calculated by using the rotation and reduced transformation matrices for the updated value of $\mathbf{P_r}$ at the end of the element level iteration according to Equation (3.22). Then, the global internal nodal force vector of all beam elements, $\mathbf{F}_{\text{INT,beams}}$ is determined by assembling the $\mathbf{P}_{\text{beam}}$ vector of each beam element.

$$\mathbf{F}_{\text{INT,beams}} = \mathbb{A}[\mathbf{P}_{\text{beam}}] \tag{4.12}$$

where $\mathbb{A}$ is the assembly operator. If the EQFdc analysis is performed under the self-weight loading, then $\mathbf{F}_{\text{INT beams}}$ needs to be determined according to Equation (3.37). For the EQFdc analysis performed under the greenfield displacement loading, only Equation (4.12) needs to be considered to determine $\mathbf{F}_{\text{INT beams}}$. At the end of the element level iterations, the updated $\mathbf{F}_{\text{INT beams}}$ are combined with the global internal force vectors of the stiffness formulations-based elements in the EQFdc model to compute the updated value of $\mathbf{F_{INT}}(\mathbf{U_{ite}})$ for the specified global nodal displacements, $\mathbf{U_{ite}}$. The updated $\mathbf{F_{INT}}(\mathbf{U_{ite}})$ is sent back into the global force equilibrium iterations and the analysis iterates until the global force equilibrium (Equation 4.1) is reached.

4.4 Gauss Point Level Iteration

The Gauss point level iteration is only employed for the fibre beam model to determine the

corresponding internal stress, $\mathbf{p_{fibre}}$ and strain, $\boldsymbol{\varepsilon}_{\mathbf{fibre}}$ resultants of the fibre elements (Equation 3.32). The shear terms (V, γ) in Equation (3.32) are calculated without using an iterative solution. Firstly, the internal stress and strain resultants induced by $\Delta\mathbf{P_r}$ (determined from the element level iteration) need to be computed at each Gauss point along the beam length. The incremental internal stress resultants, $\Delta\mathbf{p}$, are computed as:

$$\Delta\mathbf{p} = \mathbf{b}\,\Delta\mathbf{P_r} \tag{4.13}$$

where $\mathbf{b}$ is the force interpolation matrix given in Equation (3.19). Then, the current internal stress resultants in the beam, $\mathbf{p_{curr}}$, need to be updated ($\mathbf{p_{up}}$) with $\Delta\mathbf{p}$ as:

$$\mathbf{p_{up}} = \mathbf{p_{curr}} + \Delta\mathbf{p} \tag{4.14}$$

The incremental stress resultants, $\Delta\mathbf{p}$ applied to the beam create incremental strain resultants, $\Delta\boldsymbol{\varepsilon}$ at each Gauss point. To determine $\Delta\boldsymbol{\varepsilon}$, first, the local flexibility matrix, $\mathbf{f}$, needs to be computed. At the beginning of the EQFdc analysis, the local flexibility matrix is determined based on the linear elastic constitutive law for the beam's flexural and shear behaviour (Section 5.2). Later, the local flexibility matrix, $\mathbf{f_{up}}$ is updated as $\mathbf{f_{up}} = \left(\frac{\partial\boldsymbol{\varepsilon}}{\partial\mathbf{p}}\right)$ at each Gauss level iteration according to the specified material constitutive laws (Section 6.2). Then, $\Delta\boldsymbol{\varepsilon}$ at each Gauss point is calculated and the current internal strain resultants, $\boldsymbol{\varepsilon}_{\mathbf{curr}}$, are updated as $\boldsymbol{\varepsilon}_{\mathbf{up}}$:

$$\Delta\boldsymbol{\varepsilon} = \mathbf{f_{up}}\,\Delta\mathbf{p} \tag{4.15}$$

$$\boldsymbol{\varepsilon}_{\mathbf{up}} = \boldsymbol{\varepsilon}_{\mathbf{curr}} + \Delta\boldsymbol{\varepsilon} \tag{4.16}$$

From this point, to determine the internal stress and strain resultants for the fibre beam model, the Gauss point level iteration procedure ('iteP' refers to the iteration number) is employed. The iterative solution based on the Newton-Raphson method is explained as follows:

1) Start the iteration process with the initial linear elastic estimate of the section stiffness of the fibre beam model, $\mathbf{k_{fibre}}$ (Equations 3.30 and 3.31). After the first iteration, $\mathbf{k_{fibre}}$ needs to be updated with the current values of $\left(\frac{d\sigma}{d\varepsilon}\right)_{fibre}$ determined from the fibre beam model based on the axial stress/strain constitutive relationship (Sections 5.2.1 and 6.2.1).
2) Estimate the incremental strain resultants for the fibre beam, $\Delta\boldsymbol{\varepsilon}_{\mathbf{fibre}}{}^{iteP}$ induced by the incremental stress resultants, $\Delta\mathbf{p}_{\mathbf{fibre}}{}^{iteP}$ as:

$$\Delta\boldsymbol{\varepsilon}_{\mathbf{fibre}}{}^{iteP} = \mathbf{k}_{\mathbf{fibre}}{}^{-1}\,\Delta\mathbf{p}_{\mathbf{fibre}}{}^{iteP} \tag{4.17}$$

At the first estimate of the Gauss point level iterations, $\Delta\mathbf{p}_{\mathbf{fibre}}{}^{1}$ is extracted as the fibre beam terms from Equation (4.13), where the first value of $\Delta\mathbf{P}_{\mathbf{r}}{}^{1}$ is determined according to Equation (4.9).

3) Update the current internal strain resultants of the fibre beam, $\boldsymbol{\varepsilon}_{\mathbf{fibre}}{}^{curr}$ with $\Delta\boldsymbol{\varepsilon}_{\mathbf{fibre}}{}^{iteP}$ at each iteration to find the best estimate of updated $\boldsymbol{\varepsilon}_{\mathbf{fibre}}{}^{up}$ as:

$$\boldsymbol{\varepsilon}_{\mathbf{fibre}}{}^{up} = \boldsymbol{\varepsilon}_{\mathbf{fibre}}{}^{curr} + \Delta\boldsymbol{\varepsilon}_{\mathbf{fibre}}{}^{iteP} \tag{4.18}$$

4) Calculate the incremental axial strain of each fibre element, $\Delta\varepsilon_{fibre}{}^{iteP}$ using the values estimated in $\Delta\boldsymbol{\varepsilon}_{\mathbf{fibre}}{}^{iteP}$. Accordingly, the incremental axial strain for a fibre element, $\Delta\varepsilon_{fibre}{}^{iteP}$ in the cross-sectional area is:

$$\Delta\varepsilon_{fibre}{}^{iteP} = \Delta\varepsilon_c + y_{fibre}\Delta\kappa \tag{4.19}$$

where $\Delta\varepsilon_c$ is the incremental axial strain at the centre of the cross-section, $\Delta\kappa$ is the incremental curvature and y_{fibre} is the distance from the centroid of the cross-section to the centre of the fibre element (Figure 3.8).

5) Determine the axial stress in each fibre, σ_{fibre}, using $\Delta\varepsilon_{fibre}{}^{iteP}$ according to the

material constitutive law defined for the fibre beam elements (Sections 5.2.1 and 6.2.1).

6) Calculate the estimated values of axial force, N_{est} and the bending moment, M_{est} as the components of $\mathbf{p_{fibre}}$.

7) Find the residual internal force value, $\mathbf{G}(\Delta\boldsymbol{\varepsilon}^{iteP})$ between the applied element loads and the estimated values of N_{est} and M_{est} as:

$$\mathbf{G}(\Delta\boldsymbol{\varepsilon}^{iteP}) = \mathbf{p_{applied}} - \mathbf{p_{fibre}}(\Delta\boldsymbol{\varepsilon}^{iteP}) \tag{4.20}$$

where $\mathbf{p_{applied}}$ only includes the axial force and bending moment terms of $\mathbf{p_{up}}$ in Equation (4.14) as $\mathbf{p_{applied}} = \mathbf{p_{up}}([1, 2])$. Accordingly, $\mathbf{p_{fibre}}(\Delta\boldsymbol{\varepsilon}^{iteP})$ is composed of the estimated values of the axial force and the bending moment as $\mathbf{p_{fibre}}(\Delta\boldsymbol{\varepsilon}^{iteP}) = [N_{est} \quad M_{est}]^T$.

8) Stop the Gauss point level iteration if:

$$\left\|\mathbf{G}(\Delta\boldsymbol{\varepsilon}^{iteP})\right\| < tol \tag{4.21}$$

where $\left\|\mathbf{G}(\Delta\boldsymbol{\varepsilon}^{iteP})\right\|$ is residual internal stress resultants and tol is the desired tolerance value (chosen as 10 N or 10 Nm). Otherwise, the incremental stress resultants vector for the fibre beam is updated as $\Delta\mathbf{p_{fibre}}^{iteP+1} = \mathbf{G}(\Delta\boldsymbol{\varepsilon}^{iteP})$ for the next cross-section level iteration and repeats the procedure from Step 2.

When the Gauss point level iteration is completed, the final value of $\boldsymbol{\varepsilon}_{\mathbf{fibre}} = \boldsymbol{\varepsilon}_{\mathbf{fibre}}{}^{up}$ is placed into Equation (3.32). After that, the shear strain, γ and the shear term of $\mathbf{k_{section}}$ matrix need to be calculated according to the material constitutive models defined for the beam shear behaviour (Sections 5.2.2 and 6.2.2).

When the internal strain resultants are determined at each Gauss point, it is convenient to calculate the reduced set of internal displacements, $\mathbf{U_{r,int}}$ as:

$$\mathbf{U_{r,int}} = \int_0^L \mathbf{b^T \varepsilon}\, dx = \int_0^L \mathbf{b^T} \begin{bmatrix} \boldsymbol{\varepsilon}_{\mathbf{fibre}} \\ \gamma \end{bmatrix} dx \tag{4.22}$$

The updated $\mathbf{U_{r,int}}$ returns to the element level iteration to be used in the compatibility check in Equation (4.6).

4.5 Conclusion

The general solution procedures employed for the EQFdc analysis comprise three main iterations in global, element and Gauss point levels. The global level iterations are performed for the whole structure. In addition to the global level iterations, the flexibility formulations-based beam elements also require element and Gauss point level iterations to conduct the flexibility analysis before they are incorporated with the whole structure. To solve the flexibility analysis, the Newton-Raphson method is chosen for the element and Gauss point level iterations. In contrast, the Modified Newton-Raphson method is considered for the stiffness formulation-based global level iteration.

Chapter 5

EQFdc Model: Linear Elastic

5.1 Introduction

The EQFdc model formulations presented in Chapter 3 are implemented into linear elastic constitutive models in this chapter. In addition to presenting the linear elastic formulations for the flexibility and stiffness-based elements, the numerical validations for the flexibility analysis are also provided with two test problems on the beam elements. To conduct the linear elastic EQFdc analysis, the solution procedures described in Chapter 4 are employed.

5.2 Flexibility-Based Elements: Linear Elastic Model

5.2.1 Fibre beam model

For a linear elastic constitutive model, the fibre tangent modulus, $\left(\frac{d\sigma}{d\varepsilon}\right)_{fibre}$ given in Equation (3.30) is represented by Young's modulus, E. Thus, the section stiffness matrix of the fibre beam elements, $\mathbf{k_{fibre}}$ is defined as:

$$\mathbf{k_{fibre}} = \begin{bmatrix} \sum_{i=1}^{nfibre} EA_{fibre} & \sum_{i=1}^{nfibre} EA_{fibre}y_{fibre} \\ \sum_{i=1}^{nfibre} EA_{fibre}y_{fibre} & \sum_{i=1}^{nfibre} EA_{fibre}y_{fibre}^2 \end{bmatrix} \tag{5.1}$$

To determine the internal stress and strain resultants in for the linear elastic model, $\mathbf{k_{fibre}}$ determined in Equation (5.1) is used in the Gauss point level iterations (Section 4.4).

5.2.2 Beam shear model

For a linear elastic shear model, the shear tangent modulus, $dV/d\gamma$ in Equation (3.30) is represented by G is shear modulus and A_s is the shear cross-section area. For a rectangular cross-section area $A_s = \kappa_s A$, where κ_s is a non-dimensional shear coefficient based on the geometry of the beam cross-section. The shear coefficient, κ_s of the rectangular cross-sections is computed as a function of the Poisson's ratio, ν (Timoshenko, 1957):

$$\kappa_s = 5(1+\nu)/(6+5\nu) \tag{5.2}$$

The section stiffness matrix, $\mathbf{k_{section}}$ at a Gauss point along the beam length is computed as:

$$\mathbf{k_{section}} = \begin{bmatrix} \sum_{i=1}^{nfibre} EA_{fibre} & \sum_{i=1}^{nfibre} EA_{fibre}y_{fibre} & 0 \\ \sum_{i=1}^{nfibre} EA_{fibre}y_{fibre} & \sum_{i=1}^{nfibre} EA_{fibre}y_{fibre}^2 & 0 \\ 0 & 0 & \kappa_s AG \end{bmatrix} \tag{5.3}$$

To determine the internal stress and strain results for the beam shear behaviour, the shear strain, γ can be calculated directly from the applied shear force in the section level, V_{up}, as:

$$V_{up} = \mathbf{p_{up}}(3) \qquad \gamma = V_{up}/(\kappa_s AG) \tag{5.4}$$

5.3 Elastic Beam Element Numerical Validations

The validations of flexibility-based formulations are performed for two elastic beam test problems: 1) a simply supported system composed of two beam elements, 2) a fixed-end supported system composed of two beam elements. Each beam element has a length of $L/2$, where L is the total length of the two beams. Elastic spring elements with high stiffness (k_x, k_y and k_θ given in Table 5.1) are used at the end nodes to represent the boundary conditions.

Uniformly distributed loads induced by the self-weights of the beams are applied to both test problems and the flexibility analyses are conducted for each problem. The material and geometrical properties of the beam and spring elements used in the test problems are given in Table 5.1.

Table 5.1: Material and geometrical properties of the beam and spring elements for the test problems given in Sections 5.3.1 and 5.3.2.

Beam elements	
Young's modulus, E (N/m^2)	3×10^9
Poisson's ratio, ν	0.2
Unit weight, γ (N/m^3)	12500
Beam length, L (m)	4.0
Beam height, h (m)	1.0
Beam width, b (m)	0.40
Uniformly distributed load, q_0 (N/m)	5000
Spring elements	
Horizontal, k_x and vertical, k_y spring stiffness modulus (N/m)	10^{15}
Rotational spring stiffness modulus, k_θ (Nm/rad)	10^{15}

The uniformly distributed loading is implemented into the system as element loads in terms of bending moment distribution, M_0 and shear force distribution, V_0, that are developed in each simply supported beam element (Figure 5.1b). The element loads are applied in a single loading step in the global level iterations (ite). Then, a flexibility analysis is performed.

The global nodal displacement vector, $\mathbf{U_{str}}$, determined at the end of the flexibility analysis is compared to the results calculated from the exact solutions used for a Timoshenko-type beam for the corresponding test problems. The flexibility analysis results showing the global nodal displacements are also compared for the various numbers of fibre elements ('nfibre') used in the model generation. The difference between the flexibility analysis results and the exact solution is expressed as error values in percentage.

5.3.1 Test problem – 1: simply supported beam

A simply supported system (with pinned and roller supports at the end nodes) composed of two beam elements connected with a shared node at the centre (node-2) is tested under a uniformly distributed load, q_0 (Figure 5.1).

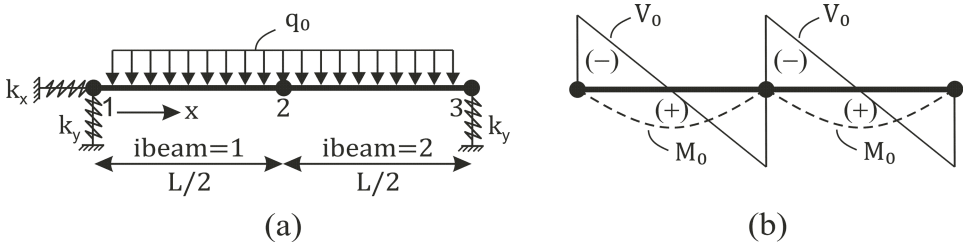


Figure 5.1: A simply supported system composed of two beam elements: (a) under uniformly distributed loads and (b) application of element loads.

The closed form formulation of the vertical displacement, v, for a Timoshenko-type beam element with pinned-pinned support condition, is adopted from Fogang (2021) as:

$$v = -\frac{q_0}{EI}\left(\frac{x^4}{24} - \frac{L\,x^3}{12} - \alpha_s\frac{L^2x^2}{2} + \left(\frac{1}{24} + \frac{\alpha_s}{2}\right)L^3x\right) \tag{5.5}$$

where α_s is the bending shear factor defined as $\alpha_s = \mathrm{EI}/(L^2\kappa_s\mathrm{AG})$. The cross-section rotations are calculated according to Equation (3.2), where $\frac{dv}{dx}$ is determined from Equation (5.5) and shear strain is defined as $\gamma_0 = (q_0x - q_0L/2)/(\kappa_s AG)$:

$$\theta = -\frac{q_0}{EI}\left(\frac{x^3}{6} - \frac{L\,x^2}{4} - \alpha_s L^2x + \left(\frac{1}{24} + \frac{\alpha_s}{2}\right)L^3\right) - \frac{(q_0x - q_0L/2)}{\kappa_s AG} \tag{5.6}$$

Using the exact solutions for the Timoshenko beam elements, the vertical displacement at $x =$ 2 m is calculated by Equation (5.5) as $v(2) = V_2 = -1.90 \times 10^{-4}$ m, where the material and geometrical properties are determined from Table 5.1 and κ_s is computed from Equation (5.2). The cross-section rotations at $x = 0$, $x = 2$ m and $x = 4$ m are calculated according to Equation (5.6) as $\theta(0) = \theta_1 = -1.33 \times 10^{-4}$ rad, $\theta(2) = \theta_2 = 0$ and $\theta(4) = \theta_3 = 1.33 \times 10^{-4}$ rad

(see Table 5.4). Additionally, using the results from the exact solutions, the reduced set of internal rotations (Equation 3.10) for ibeam = 1 are determined as $\theta_{1r} = -3.83 \times 10^{-5}$ rad and $\theta_{2r} = 9.50 \times 10^{-5}$ rad (see rows 11-12 for $\mathbf{U_{r,int}}$ in Table 5.2). The changes in the reduced set of internal displacements, $\mathbf{U_{r,int}}$ and in the incremental reduced set of forces, $\Delta\mathbf{P_r}$ are shown in each element level iteration (iteES) of the corresponding global level iteration (Table 5.2) of the specified beam element (i.e. 'ibeam' is the beam element number).

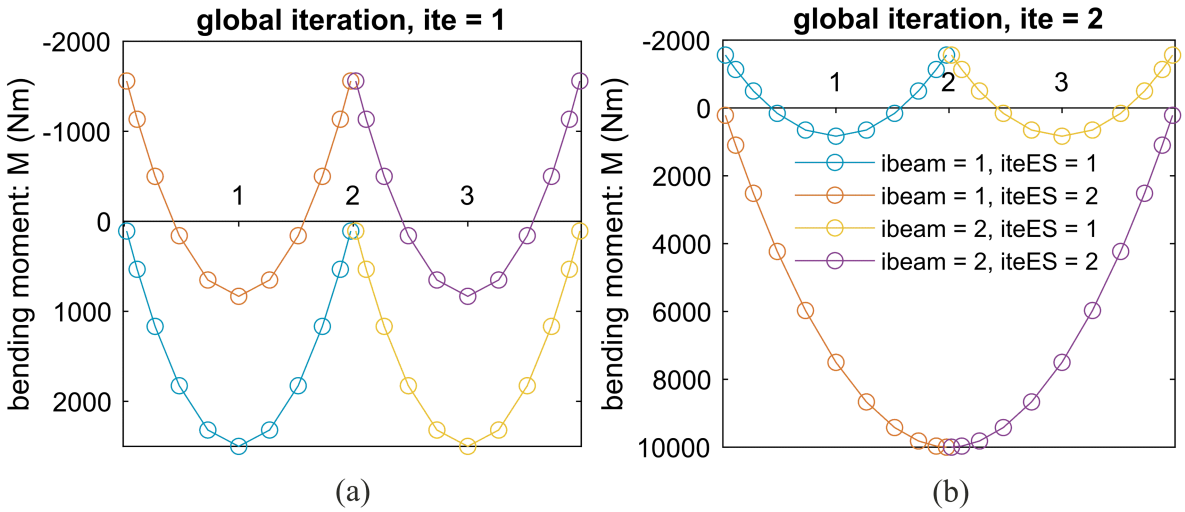


Figure 5.2: Bending moment diagrams for the test problem–1: (a) $ite = 1$, (b) $ite = 2$.

When the element loads are first introduced into the system, at the end of the first element state determination (iteES = 1), the applied bending moment distribution (Figure 5.2a) creates rotations as $\theta = \pm q_0(L/2)^3/(24EI) = \pm 1.67 \times 10^{-5}$ rad (see rows 2-3 in Table 5.2 for θ_{1r} and θ_{2r}) at each end node of the beam elements. Since the external reduced set of displacements, $\mathbf{U_{r,ext}}$ is zero at the beginning of the flexibility analysis (see rows 1-6 in Table 5.2), these rotations lead to an incompatibility in the element state determination and generate an incremental reduced set of forces, $\Delta\mathbf{P_r}$, which corresponds to fixed-end moments as $M = \pm q_0(L/2)^2/12 = \pm 1.67 \times 10^3$ Nm (see rows 5-6 in Table 5.2 for ΔM_1 and ΔM_2) in each beam element when ite = 1 and iteES = 2 (Figure 5.2a).

Table 5.2: Reduced set of forces and displacements for the test problem–1.

				$\boldsymbol{ite = 1}$				
Row no	*iteES=1*	$\mathbf{\Delta P_r}$		*iteES=1*	$\mathbf{U_{r,int}}$		$\mathbf{U_{r,ext}}$	
		ibeam=1	*ibeam=2*		*ibeam=1*	*ibeam=2*	*ibeam=1*	*ibeam=2*
1	ΔN	0.00	0.00	U_r	0.00	0.00	0.00	0.00
2	ΔM_1	0.00	0.00	θ_{1r}	-1.67E-05	-1.67E-05	0.00	0.00
3	ΔM_2	0.00	0.00	θ_{2r}	1.67E-05	1.67E-05	0.00	0.00
Row no	*iteES=2*	$\mathbf{\Delta P_r}$		*iteES=2*	$\mathbf{U_{r,int}}$		$\mathbf{U_{r,ext}}$	
		ibeam=1	*ibeam=2*		*ibeam=1*	*ibeam=2*	*ibeam=1*	*ibeam=2*
4	ΔN	0.00	0.00	U_r	0.00	0.00	0.00	0.00
5	ΔM_1	1.67E+03	1.67E+03	θ_{1r}	0.00	0.00	0.00	0.00
6	ΔM_2	-1.67E+03	-1.67E+03	θ_{2r}	0.00	0.00	0.00	0.00
				$\boldsymbol{ite = 2}$				
Row no	*iteES=1*	$\mathbf{\Delta P_r}$		*iteES=1*	$\mathbf{U_{r,int}}$		$\mathbf{U_{r,ext}}$	
		ibeam=1	*ibeam=2*		*ibeam=1*	*ibeam=2*	*ibeam=1*	*ibeam=2*
7	ΔN	0.00	0.00	U_r	0.00	0.00	0	0
8	ΔM_1	0.00	0.00	θ_{1r}	0.00	0.00	-3.83E-05	-9.50E-05
9	ΔM_2	0.00	0.00	θ_{2r}	0.00	0.00	9.50E-05	3.83E-05
Row no	*iteES=2*	$\mathbf{\Delta P_r}$		*iteES=2*	$\mathbf{U_{r,int}}$		$\mathbf{U_{r,ext}}$	
		ibeam=1	*ibeam=2*		*ibeam=1*	*ibeam=2*	*ibeam=1*	*ibeam=2*
10	ΔN	0.00	0.00	U_r	0.00	0.00	0	0
11	ΔM_1	-1.67E+03	-1.17E+04	θ_{1r}	-3.83E-05	-9.50E-05	-3.83E-05	-9.50E-05
12	ΔM_2	1.17E+04	1.67E+03	θ_{2r}	9.50E-05	3.83E-05	9.50E-05	3.83E-05

The element level iteration completes (ite = 1 and iteES = 2) when $\mathbf{U_{r,int}}$ becomes compatible with the zero external reduced set of displacements (see rows 4-6 in Table 5.2 for $\mathbf{U_{r,int}}$ and $\mathbf{U_{r,ext}}$). However, the fixed-end moment-like reduced set of forces (see rows 5-6 for $\mathbf{\Delta P_r}$ in Table 5.2) generates a global nodal force vector of $\mathbf{P_{beam}}$ (see rows 3, 6, 9 for $\mathbf{P_{beam}}^{ibeam=1}$ and $\mathbf{P_{beam}}^{ibeam=2}$ in Table 5.3). Besides, the vertical equilibrium configuration forces (contribution of the shear forces as stated by Taucer et al., 1991) occur in the system, $\mathbf{F_{eq}}$ (see rows 2, 5, 8 for $\mathbf{F_{eq}}^{ibeam=1}$ and $\mathbf{F_{eq}}^{ibeam=2}$ in Table 5.3). The assembly and summation of $\mathbf{P_{beam}}$ and $\mathbf{F_{eq}}$ according to Equation (5.7) resulted in the internal nodal force vector of the beams, $\mathbf{F_{beam}}$, which includes the fixed-end forces and moments (see rows 1-9 for $\mathbf{F_{beam}}$ in Table 5.3).

In the first global level iteration, no internal forces occur in the nodal springs, $\mathbf{F_{spring}}$ (see rows 1-9 for $\mathbf{F_{spring}}$ in Table 5.3) due to the lack of external global nodal displacements applied to

the system. Accordingly, the system's global internal nodal force vector, $\mathbf{F_{int}}$ is expressed as a summation of $\mathbf{F_{beam}}$ and $\mathbf{F_{spring}}$ (Equation 5.8). Because of the nonequilibrium between the external and internal global nodal forces as $\mathbf{F_{ext}} = 0$ (considering the absence of quad and footing elements in the test problem) and $\mathbf{F_{int}} \neq 0$ (see rows 1-9 for $\mathbf{F_{int}}$ in Table 5.3) at the end of the first global iteration, another global level iteration (ite = 2) is needed in the flexibility analysis.

$$\mathbf{F_{beam}} = \mathbb{A}[\mathbf{P}_{\text{beam}}] + \mathbb{A}\left[\mathbf{F}_{\text{eq}}\right] \tag{5.7}$$

$$\mathbf{F_{int}} = \mathbf{F_{beam}} + \mathbf{F_{spring}} \tag{5.8}$$

In the second global level iteration, the element level iteration starts from the existing condition of fixed-end moments-like behaviour in the beam elements (see Figure 5.2b, when iteES = 1). However, in this case, the $\mathbf{U_{r,ext}} \neq 0$ due to the out-of-balance global forces from the previous global iteration (see rows 7-9 for $\mathbf{U_{r,ext}}$ in Table 5.2). Thus, the element level iteration continues for the second time (iteES = 2) to reach compatibility with $\mathbf{U_{r,ext}}$.

At the end of the second element level and global level iterations (when ite = 2 and iteES = 2), the internal forces in the beam elements with additional vertical configuration forces and the internal forces of spring elements are demonstrated in Table 5.3. It is important to note that $\mathbf{F_{spring}} \neq 0$ (see rows 11 and 17 for $\mathbf{F_{spring}}$ in Table 5.3) is because of the system's nonzero external global nodal displacements (see rows 7-12 for $\mathbf{U_{r,ext}}$ in Table 5.2) in this global level iteration (ite = 2). However, with the summation of $\mathbf{F_{beam}}$ (see rows 11 and 17 for $\mathbf{F_{beam}}$ in Table 5.3) and $\mathbf{F_{spring}}$ (see rows 11 and 17 for $\mathbf{F_{spring}}$ in Table 5.3) the system's internal global nodal force vector, $\mathbf{F_{int}}$ becomes zero at the end of the second iteration of the element level iteration (see rows 10-18 for $\mathbf{F_{int}}$ in Table 5.3). This zero $\mathbf{F_{int}}$ vector satisfies the global force equilibrium at the end of the second global iteration since $\mathbf{F_{ext}} = 0$ in this problem. The final

situation of the bending moment distributions in the system is shown in Figure 5.2(b), which demonstrates a simply supported beam-like response (as a whole system) at the end of the global level iteration.

Table 5.3: Internal forces for the test problem–1.

$ite = 1, iteES = 2$								
Row no		$\mathbf{P_{beam}}^{ibeam=1}$	$\mathbf{P_{beam}}^{ibeam=2}$	$\mathbf{F_{eq}}^{ibeam=1}$	$\mathbf{F_{eq}}^{ibeam=2}$	$\mathbf{F_{beam}}$	$\mathbf{F_{spring}}$	$\mathbf{F_{int}}$
1	F_{x1}	0.00		0.00		0.00	0.00	0.00
2	F_{y1}	0.00		5.00E+03		5.00E+03	0.00	5.00E+03
3	M_1	1.67E+03		0.00		1.67E+03	0.00	1.67E+03
4	F_{x2}	0.00	0.00	0.00	0.00	0.00	0.00	0.00
5	F_{y2}	0.00	0.00	5.00E+03	5.00E+03	1.00E+04	0.00	1.00E+04
6	M_2	-1.67E+03	1.67E+03	0.00	0.00	0.00	0.00	0.00
7	F_{x3}		0.00		0.00	0.00	0.00	0.00
8	F_{y3}		0.00		5.00E+03	5.00E+03	0.00	5.00E+03
9	M_3		-1.67E+03		0.00	-1.67E+03	0.00	-1.67E+03
$ite = 2, iteES = 2$								
Row no		$\mathbf{P_{beam}}^{ibeam=1}$	$\mathbf{P_{beam}}^{ibeam=2}$	$\mathbf{F_{eq}}^{ibeam=1}$	$\mathbf{F_{eq}}^{ibeam=2}$	$\mathbf{F_{beam}}$	$\mathbf{F_{spring}}$	$\mathbf{F_{int}}$
10	F_{x1}	0.00		0.00		0.00	0.00	0.00
11	F_{y1}	5.00E+03		5.00E+03		1.00E+04	-1.00E+04	0.00
12	M_1	0.00		0.00		0.00	0.00	0.00
13	F_{x2}	0.00	0.00	0.00	0.00	0.00	0.00	0.00
14	F_{y2}	-5.00E+03	-5.00E+03	5.00E+03	5.00E+03	0.00	0.00	0.00
15	M_2	1.00E+04	-1.00E+04	0.00	0.00	0.00	0.00	0.00
16	F_{x3}		0.00		0.00	0.00	0.00	0.00
17	F_{y3}		5.00E+03		5.00E+03	1.00E+04	-1.00E+04	0.00
18	M_3		0.00		0.00	0.00	0.00	0.00

The global nodal displacements determined from both flexibility analysis and the exact solutions give a very close answer with a maximum error of less than 0.2%, depending on the number of fibres used in the model generation (Table 5.4). Here, it is important to note that the accuracy of the flexibility analysis increases with the increase in the number of fibre elements used to represent the axial and the bending behaviour of the beam elements. In this example, 100 fibres are used to capture a high accuracy in the flexibility analysis. The optimum number of fibres can be determined according to the complexity of the specified problem.

Table 5.4: Comparison of the global nodal displacements for the test problem–1.

	flexibility analysis result			exact solution	error (%)	error (%)	error (%)
	nfibre=25	*nfibre=50*	*nfibre=100*		*nfibre=25*	*nfibre=50*	*nfibre=100*
U_1	0.00	0.00	0.00	0.00			
V_1	0.00	0.00	0.00	0.00			
θ_1	-1.335E-04	-1.334E-04	-1.333E-04	-1.333E-04	0.160	0.040	0.010
U_2	0.00	0.00	0.00	0.00			
V_2	-1.903E-04	-1.901E-04	-1.900E-04	-1.900E-04	0.141	0.035	0.009
θ_2	0.00	0.00	0.00	0.00			
U_3	0.00	0.00	0.00	0.00			
V_3	0.00	0.00	0.00	0.00			
θ_3	1.335E-04	1.334E-04	1.333E-04	1.333E-04	0.160	0.040	0.010

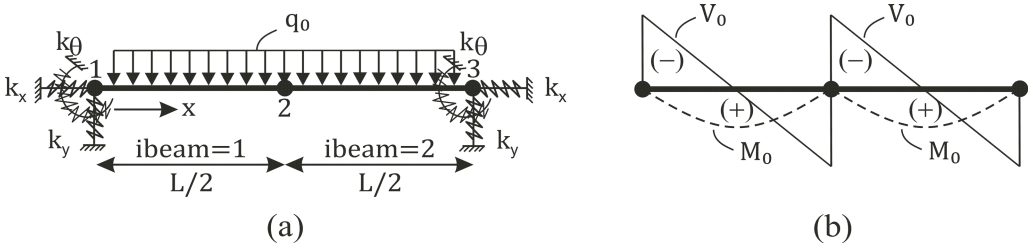


Figure 5.3: A fixed-end supported system composed of two beam elements: (a) under the uniformly distributed load and (b) application of element loads.

5.3.2 Test problem – 2: fixed-end supported beam

Another test problem conducted for the numerical validation of the flexibility analysis is based on a fixed-end supported system composed of two beam elements (Figure 5.3). The material and geometrical properties given in Table 5.1 are also used for this example. The uniformly distributed load is applied to the flexibility analysis as element loads occurred in a simply supported system (Figure 5.3b). The vertical displacement, v and the cross-section rotation, θ under the uniformly distributed load for a Timoshenko beam with fixed-fixed ends is given as (Fogang, 2021):

$$v = -\frac{q_0}{EI}\left(\frac{x^4}{24} - \frac{L\,x^3}{12} - \left(\alpha_s - \frac{1}{12}\right)\frac{L^2x^2}{2} + \alpha_s\frac{L^3x}{2}\right) \tag{5.9}$$

$$\theta = -\frac{q_0}{EI}\left(\frac{x^3}{6} - \frac{L\,x^2}{4} - \left(\alpha_s - \frac{1}{12}\right)L^2 x + \frac{\alpha_s L^3}{2}\right) - \frac{(q_0 x - q_0 L/2)}{\kappa_s AG} \tag{5.10}$$

By using Equation (5.9) given for the Timoshenko beam with fixed-fixed ends, the vertical displacement at $x = 0$ and $x = 2$ m are calculated as $v(0) = V_1 = 0$ and $v(2) = V_2 = -5.67 \times 10^{-5}$ m (see Table 5.7) by using the same material and geometrical properties given in Table 5.1. The cross-section rotations are determined as zero at the end nodes (at x = 0 and x = 4 m) of the fixed-end beam element as consistent with the flexibility analysis results determined for θ_1 and θ_3 (Table 5.7). Using the results (θ_1, V_1 and V_2) from the exact solutions, the reduced set of rotations for ibeam = 1 are calculated according to Equation (3.10) as $\theta_{1r} = \theta_{2r} = 2.83 \times 10^{-5}$ rad, which validate the flexibility analysis results (see rows 11-12 for $\mathbf{U_{r,int}}$ in Table 5.5).

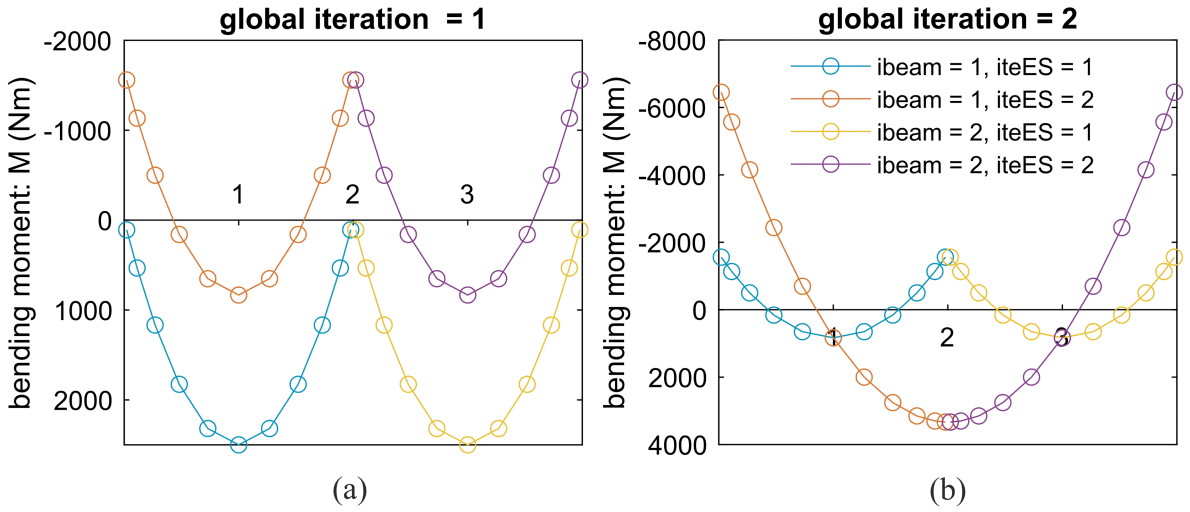


Figure 5.4: Bending moment diagrams for test problem–2: a) $ite = 1$, b) $ite = 2$.

The changes in $\mathbf{\Delta P_r}$ and $\mathbf{U_{r,int}}$ at each global and element level iteration are presented in Table 5.5. For ite = 1, the flexibility analysis shows the same bending moment distributions observed in test problem-1 (Figures 5.2a and 5.4a). Although the internal force vector determined at the end of the first global iteration (for ite = 1 and iteES = 2) for the fixed-end system (see rows 1-9 for $\mathbf{F_{beam}}$ in Table 5.6) is the same as the system with pinned support (see rows 1-9 for $\mathbf{F_{beam}}$

in Table 5.3), the reduced set of external displacements (see rows 7-9 for $\mathbf{U_{r,ext}}$ in Table 5.5) are computed as different than the ones in the test problem-1 (see rows 7-9 for $\mathbf{U_{r,ext}}$ in Table 5.2) due to the existence of rotational springs at the end nodes of the system, which make the structure stiffness matrix different.

Table 5.5: Reduced set of forces and displacements for the test problem–2.

$ite = 1$								
Row no	*iteES=1*	$\Delta\mathbf{P_r}$		*iteES=1*	$\mathbf{U_{r,int}}$		$\mathbf{U_{r,ext}}$	
		ibeam=1	*ibeam=2*		*ibeam=1*	*ibeam=2*	*ibeam=1*	*ibeam=2*
1	ΔN	0.00	0.00	U_r	0.00	0.00	0.00	0.00
2	ΔM_1	0.00	0.00	θ_{1r}	-1.67E-05	-1.67E-05	0.00	0.00
3	ΔM_2	0.00	0.00	θ_{2r}	1.67E-05	1.67E-05	0.00	0.00
Row no	*iteES=2*	$\Delta\mathbf{P_r}$		*iteES=2*	$\mathbf{U_{r,int}}$		$\mathbf{U_{r,ext}}$	
		ibeam=1	*ibeam=2*		*ibeam=1*	*ibeam=2*	*ibeam=1*	*ibeam=2*
4	ΔN	0.00	0.00	U_r	0.00	0.00	0.00	0.00
5	ΔM_1	1.67E+03	1.67E+03	θ_{1r}	0.00	0.00	0.00	0.00
6	ΔM_2	-1.67E+03	-1.67E+03	θ_{2r}	0.00	0.00	0.00	0.00
$ite = 2$								
Row no	*iteES=1*	$\Delta\mathbf{P_r}$		*iteES=1*	$\mathbf{U_{r,int}}$		$\mathbf{U_{r,ext}}$	
		ibeam=1	*ibeam=2*		*ibeam=1*	*ibeam=2*	*ibeam=1*	*ibeam=2*
7	ΔN	0.00	0.00	U_r	0.00	0.00	0	0
8	ΔM_1	0.00	0.00	θ_{1r}	0.00	0.00	2.83E-05	-2.83E-05
9	ΔM_2	0.00	0.00	θ_{2r}	0.00	0.00	2.83E-05	-2.83E-05
Row no	*iteES=2*	$\Delta\mathbf{P_r}$		*iteES=2*	$\mathbf{U_{r,int}}$		$\mathbf{U_{r,ext}}$	
		ibeam=1	*ibeam=2*		*ibeam=1*	*ibeam=2*	*ibeam=1*	*ibeam=2*
10	ΔN	0.00	0.00	U_r	0.00	0.00	0	0
11	ΔM_1	5.00E+03	-5.00E+03	θ_{1r}	2.83E-05	-2.83E-05	2.83E-05	-2.83E-05
12	ΔM_2	5.00E+03	-5.00E+03	θ_{2r}	2.83E-05	-2.83E-05	2.83E-05	-2.83E-05

The effect of rotational springs in the fixed-end beam system can be easily seen from the internal beam (see rows 10-18 for $\mathbf{F_{beam}}$ in Table 5.6) and spring (see rows 10-18 for $\mathbf{F_{spring}}$ in Table 5.6) forces computed at the end of the second global level iteration (ite = 2). At the end of the analysis (ite = 2 and iteES = 2), the bending moment diagram represents the fixed-end moment behaviour (Figure 5.4b).

The global nodal displacement vector, $\mathbf{U_{str}}$, determined at the end of the flexibility analysis (Table 5.7), is compared with the resulted calculated from the exact solutions used for a

Timoshenko-type beam element with fixed-fixed end supports (Equations 5.9 and 5.10).

Another numerical validation can also be confirmed through the fixed-end moments determined from the statics as $M = \pm q_0(L)^2/12 = \pm 6.67 \times 10^3$ Nm at the fixed-end supports, which are consistent with the nodal moments (M_1 and M_3) determined at the end of the flexibility analysis (see rows 12 and 18 for $\mathbf{F}_{\mathbf{beam}}$ in Table 5.6). Additionally, the vertical support reaction forces (F_{y1} and F_{y3}) achieved from the flexibility analysis (see rows 11 and 17 for $\mathbf{F}_{\mathbf{beam}}$ in Table 5.6) are identical with the results computed from the statics as $V = +q_0 L/2 = 10^4$ N. As observed from the previous test problem, using a higher number of fibres in the flexibility analysis gives a closer match with the results obtained from the exact solutions (Table 5.7).

Table 5.6: Internal forces for the test problem–2.

$\boldsymbol{ite = 1, iteES = 2}$								
Row no		$\mathbf{P}_{\mathbf{beam}}^{\text{ibeam=1}}$	$\mathbf{P}_{\mathbf{beam}}^{\text{ibeam=2}}$	$\mathbf{F}_{\mathbf{eq}}^{\text{ibeam=1}}$	$\mathbf{F}_{\mathbf{eq}}^{\text{ibeam=2}}$	$\mathbf{F}_{\mathbf{beam}}$	$\mathbf{F}_{\mathbf{spring}}$	$\mathbf{F}_{\mathbf{int}}$
1	F_{x1}	0.00		0.00		0.00	0.00	0.00
2	F_{y1}	0.00		5.00E+03		5.00E+03	0.00	5.00E+03
3	M_1	1.67E+03		0.00		1.67E+03	0.00	1.67E+03
4	F_{x2}	0.00	0.00	0.00	0.00	0.00	0.00	0.00
5	F_{y2}	0.00	0.00	5.00E+03	5.00E+03	1.00E+04	0.00	1.00E+04
6	M_2	-1.67E+03	1.67E+03	0.00	0.00	0.00	0.00	0.00
7	F_{x3}		0.00		0.00	0.00	0.00	0.00
8	F_{y3}		0.00		5.00E+03	5.00E+03	0.00	5.00E+03
9	M_3		-1.67E+03		0.00	-1.67E+03	0.00	-1.67E+03
$\boldsymbol{ite = 2, iteES = 2}$								
Row no		$\mathbf{P}_{\mathbf{beam}}^{\text{ibeam=1}}$	$\mathbf{P}_{\mathbf{beam}}^{\text{ibeam=2}}$	$\mathbf{F}_{\mathbf{eq}}^{\text{ibeam=1}}$	$\mathbf{F}_{\mathbf{eq}}^{\text{ibeam=2}}$	$\mathbf{F}_{\mathbf{beam}}$	$\mathbf{F}_{\mathbf{spring}}$	$\mathbf{F}_{\mathbf{int}}$
10	F_{x1}	0.00		0.00		0.00	0.00	0.00
11	F_{y1}	5.00E+03		5.00E+03		1.00E+04	-1.00E+04	0.00
12	M_1	6.67E+03		0.00		6.67E+03	-6.67E+03	0.00
13	F_{x2}	0.00	0.00	0.00	0.00	0.00	0.00	0.00
14	F_{y2}	-5.00E+03	-5.00E+03	5.00E+03	5.00E+03	0.00	0.00	0.00
15	M_2	3.33E+03	-3.33E+03	0.00	0.00	0.00	0.00	0.00
16	F_{x3}		0.00		0.00	0.00	0.00	0.00
17	F_{y3}		5.00E+03		5.00E+03	1.00E+04	-1.00E+04	0.00
18	M_3		-6.67E+03		0.00	-6.67E+03	6.67E+03	0.00

Table 5.7: Comparison of the global nodal displacements for the test problem – 2.

	flexibility analysis result			exact solution	error (%)	error (%)	error (%)
	nfibre=25	*nfibre=50*	*nfibre=100*		*nfibre=25*	*nfibre=50*	*nfibre=100*
U_1	0.00	0.00	0.00	0.00			
V_1	0.00	0.00	0.00	0.00			
θ_1	0.00	0.00	0.00	0.00			
U_2	0.00	0.00	0.00	0.00			
V_2	-5.672E-05	-5.668E-05	-5.667E-05	-5.667E-05	0.094	0.024	0.006
θ_2	0.00	0.00	0.00	0.00			
U_3	0.00	0.00	0.00	0.00			
V_3	0.00	0.00	0.00	0.00			
θ_3	0.00	0.00	0.00	0.00			

5.4 Stiffness-Based Elements: Linear Elastic Model

5.4.1 Quad elements

The deformation mode is only provided by the shear strain in the quad element. For elastic behaviour, constant shear stress, τ, in each quad element is related to shear strain by the shear modulus, G, where $\tau = G\gamma_0$. Thus, the quad tangent modulus, $\left(\frac{d\tau}{d\gamma_0}\right)$ used in the internal force vector, $\mathbf{f}_{\text{int,quad}}$ and the stiffness matrix, $\mathbf{K}_{\text{quad}}$ (Equations 3.48 and 3.49) are defined by G for the linear elastic quad model as:

$$\mathbf{f}_{\text{int,quad}} = \int \mathbf{B}_{\text{q}}{}^{\text{T}} G \mathbf{B}_{\text{q}} \mathbf{U}_{\text{q}} \, dV \tag{5.11}$$

$$\mathbf{K}_{\text{quad}} = \mathbf{B}_{\text{q}}{}^{\text{T}} G \mathbf{B}_{\text{q}} \, t_q \, L \, H \tag{5.12}$$

5.4.2 Structural interface elements

For elastic behaviour, the tractions are linearly dependent on the relative displacement $\mathbf{u}_{\text{r}}$, via the constitutive matrix of interface elements, $\mathbf{D}_{\text{int}}$ as:

$$\mathbf{p} = \mathbf{D}_{\text{int}} \mathbf{u}_{\text{r}} \tag{5.13}$$

where $\mathbf{D}_{\text{int}}$ is given by,

$$\mathbf{D}_{\text{int}} = \begin{bmatrix} K_{s,int} & 0 \\ 0 & K_{n,int} \end{bmatrix} \tag{5.14}$$

The shear traction component of the interface is considered to be very stiff (Equation 3.66). Due to this high stiffness, relative shear displacements at the interfaces, u_r are negligible. To compute the internal force vector, $\mathbf{f}_{\text{int,interface}}$ and the element stiffness matrix, $\mathbf{K}_{\text{int,interface}}$ of the interface elements for the linear constitutive relationship, the interface tangent modulus, $\left(\frac{d\mathbf{p}}{d\mathbf{u}_{\text{r}}}\right)$ (Equations 3.71 and 3.72) is represented by $\mathbf{D}_{\text{int}}$ as:

$$\mathbf{f}_{\text{int,interface}} = \int_{-L_{int}/2}^{L_{int}/2} (\mathbf{TB}_{\text{int}})^{\text{T}} \mathbf{D}_{\text{int}} (\mathbf{TB}_{\text{int}}) \mathbf{U}_{\text{int}} t dX \tag{5.15}$$

$$\mathbf{K}_{\text{int,interface}} = \int_{-L_{int}/2}^{L_{int}/2} (\mathbf{TB}_{\text{int}})^{\text{T}} \mathbf{D}_{\text{int}} (\mathbf{TB}_{\text{int}}) t dX \tag{5.16}$$

5.5 Conclusion

To provide a practical preliminary step for the building damage assessment, linear elastic constitutive models are incorporated into the EQFdc model formulations (presented in Chapter 3). The linear elastic analysis is conducted according to the iteration procedures explained in Chapter 4. The numerical validations are performed on the elastic beam elements to test the veracity of flexibility-based formulation implementations. As a result, the flexibility analysis results approach to the exact solutions by the increasing number of fibres. However, even for using 25 fibres, the maximum error between the results determined from the flexibility analysis and the exact solutions is less than 0.2%, which validates the accurate implementation of flexibility formulations and analysis procedures.

Chapter 6

EQFdc Model: Nonlinear

6.1 Introduction

This chapter presents the nonlinear constitutive models employed for the EQFdc model. The nonlinear constitutive relationships for the tensile and shear failure mechanisms are formulated to mimic the JMM (i.e. jointed masonry model) (Amorosi & Sangirardi, 2021). Iwan models (Iwan, 1967) are used to formulate the stress/strain relationships since they can be practically implemented into the EQFdc model formulations. Specifically, Iwan models define the constitutive relationships for tensile and shear behaviour in the beams, shear behaviour in the quads and tensile behaviour in the structural interface elements. First, to employ the material state determination algorithms for the Iwan models, the state variables, which are stored and updated at each Gauss point level iteration (Section 4.4), need to be identified before the analysis. The choice of state variables is free and the ones specified in this chapter are user-defined.

6.2 Flexibility-Based Elements: Nonlinear Model

The nonlinear constitutive models employed for the flexibility formulations-based beam elements are defined separately for tensile and shear mechanisms as outlined below.

6.2.1 Fibre beam model

6.2.1.1 Fibre beam model: modelling procedure

The fibre beam represents the axial and bending responses of the beam element at the fibre level. Both axial force and the bending moment are the functions of the axial stress in each fibre. Thus, it is important to describe the constitutive relationship between the axial stress, σ_{fibre} and strain in the fibre element, ε_{fibre}. The axial stress in a fibre element, σ_{fibre} is determined with the iterative estimate of $\Delta\varepsilon_{fibre}{}^{iteP}$ as mentioned in Section 4.4.

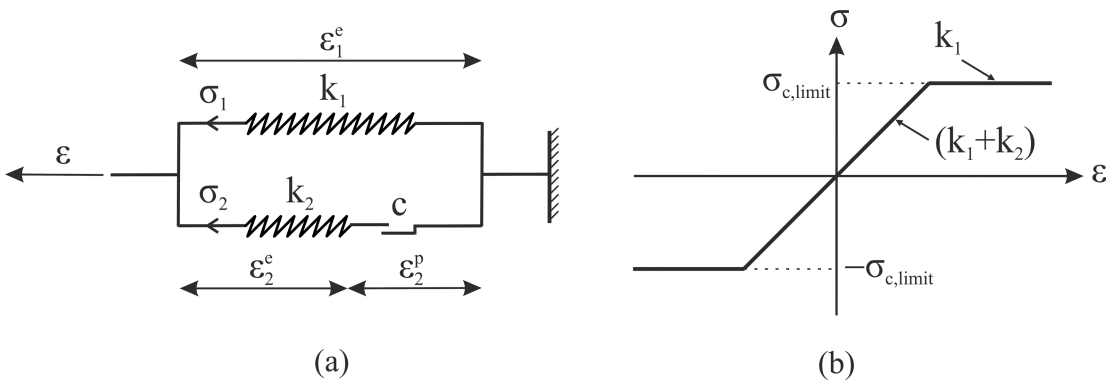


Figure 6.1: Parallel Iwan model: (a) schematic representation, (b) stress/strain constitutive relationship.

The fibre beam's axial stress/strain relationship is formulated by using a parallel Iwan model (Iwan, 1967) with the schematic representation in Figure 6.1(a). This modelling approach is suitable for cases, where strain is an input and the model delivers stress as an output. The axial stress/strain constitutive relationship is defined according to elastic-perfectly plastic behaviour (Figure 6.1b). In the parallel Iwan model, two parallel springs with stiffnesses of k_1 and k_2 are used to describe the elastic behaviour and a slider element, c, is placed in series mode to the second spring element. In Figure 6.1(a), σ_1 and σ_2 are the stresses and ε_1^e and ε_2^e are the elastic strains. Plastic strain in k_2 spring, ε_2^p occurs when σ_2 reaches the strength of the slider element, $\sigma_{c,limit}$ (Figure 6.1b). Plasticity is defined only in tension behaviour in the fibre beams. The axial stress/strain relationship in compression behaviour is considered linear elastic.

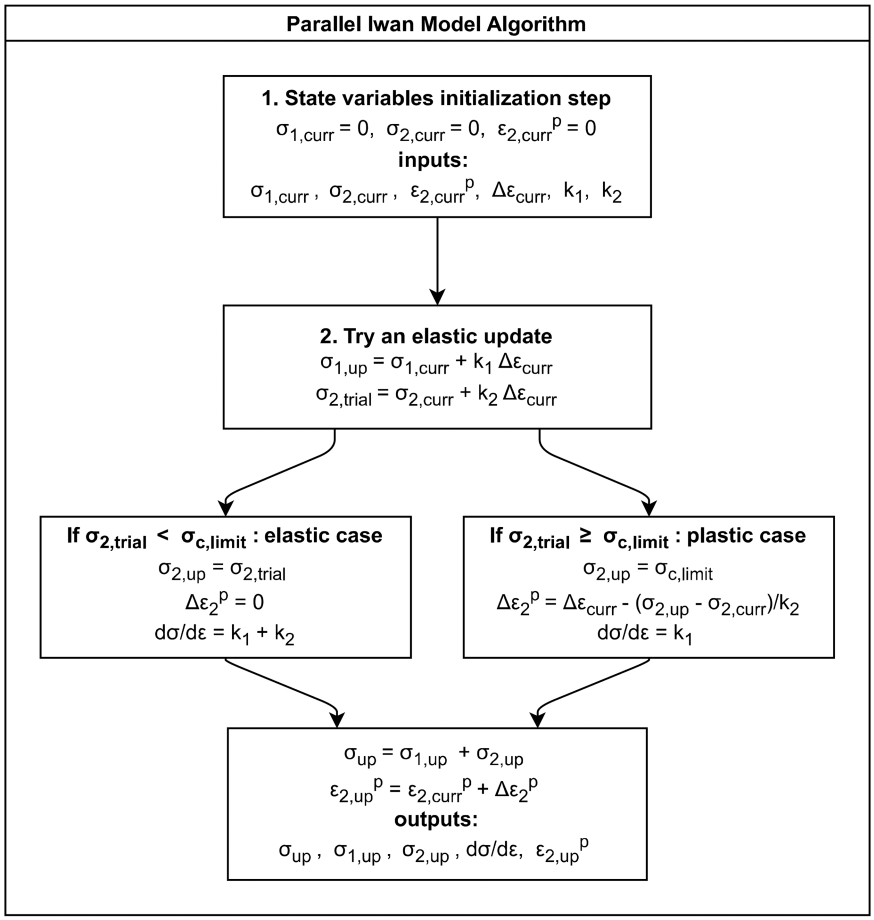


Figure 6.2: Material state determination algorithm for the parallel Iwan model.

The state variables are chosen as: σ_1 and σ_2 and ε_2^p. The input parameters are defined as the current values of the axial stresses $\sigma_{1,curr}$ and $\sigma_{2,curr}$, the plastic strain $\varepsilon_{2,curr}^p$ and the incremental axial strain, $\Delta\varepsilon_{curr}$. The output parameters are the updated values of total axial stress, σ_{up} ($\sigma_{up} = \sigma_{1,up} + \sigma_{2,up}$) and the total plastic strain, $\varepsilon_{2,up}^p$. The increment in plastic strain is expressed as, $\Delta\varepsilon_2^p$; it is computed when the algorithm enters the plastic region.

The material state determination algorithm formulated for the parallel Iwan model is summarised in Figure 6.2. The fibre beam model representation of the specific parameters used in the parallel Iwan model is presented in Table 6.1. The rest of the parameters employed for the fibre beam model are expressed identical to ones defined in the parallel Iwan model.

Table 6.1: Parameters defined in the parallel Iwan model and their correspondence in the fibre beam model.

	Parallel Iwan model		**Fibre beam model**	
Parameter status	**Definition**	**Parameter**	**Definition**	**Parameter**
Constant value	Slider strength Total elastic spring stiffness	$\sigma_{c,limit}$ $k_1 + k_2$	Fibre tensile strength Fibre Young's modulus	$\sigma_{T,fibre}$ E_{fibre}
Current value	Incremental axial strain	$\Delta\varepsilon_{curr}$	Incremental axial strain in the fibre*	$\Delta\varepsilon_{fibre}^{iteP}$
Updated value	Axial stress	σ_{up}	Axial stress in the fibre	σ_{fibre}
* $\Delta\varepsilon_{fibre}^{iteP}$ is computed at each Gauss point iteration (iteP)				

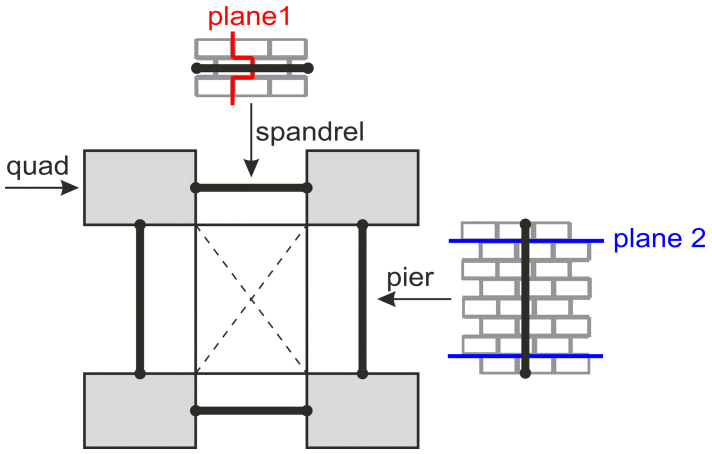


Figure 6.3: Critical planes for the spandrels and piers defined to mimic the JMM.

6.2.1.2 Fibre beam model: tensile strength

To mimic the material constitutive relationships defined in the JMM, the mechanisms that govern tensile strength capacities of spandrel and pier elements must be determined. Figure 6.3 shows simple spandrel and pier elements corresponding to homogenised masonry portions with the interlocking of brick blocks. The interlocking of the brick blocks on the head joints (plane 1 in Figure 6.3) affects the tensile strength of spandrels. The tensile strength of spandrels, $\sigma_{T,s}$, is calculated according to Equation (2.10) developed by Lasciarrea et al. (2019). However, the frictional contribution in the equation is neglected due to its low value resulting from low vertical stresses on the spandrel elements so that the equation is modified as:

$$\sigma_{T,s} = \sigma_{t0,1} + \frac{b}{2a} c_{0,2} \tag{6.1}$$

where $\sigma_{t0,1}$ is the contribution of tensile strength on the brick head joints, $c_{0,2}$ the cohesion on the bed joints, $c_{0,2}$ and b/a is the block aspect ratio (b is the block width and a is the block height). The orientation of piers corresponds to the failure mechanism along the bed joints (plane 2 in Figure 6.3). Therefore, the tensile strength of piers, $\sigma_{T,p}$ is equal to the tensile strength of the bed joints, $\sigma_{t0,2}$ which is expressed as $\sigma_{t0,2} = \sigma_{t0,1}$ due to isotropic elasticity adopted in the JMM. Thus, $\sigma_{T,p}$ is defined as $\sigma_{T,p} = \sigma_{t0,1}$ in the EQFdc model. As a result, the tensile strength of the fibre element is defined in terms of either $\sigma_{T,s}$ or $\sigma_{T,p}$ depending on the orientation of the beam element unless another value is assigned as input (e.g. lintels are represented as specific fibres in the spandrel elements, which are modelled with high stiffness and tensile strength).

6.2.2 Beam shear model

6.2.2.1 Beam shear model: modelling procedure

Shear behaviour in the beam elements is defined by using a series Iwan model (Iwan, 1967) with the schematic representation shown in Figure 6.4(a). This model is suitable for a case, where stress or force is used as an input and the model delivers strain as an output. In this case, the spring elements are placed in the series form to each other and a slider element is placed parallel to the second element (Figure 6.4a). The spring stiffnesses are defined as k_1 and k_2. The stress in the spring k_2 is represented by σ_s referring to the spring stress and the stress in the slider element is expressed by σ_c (where the current values of the spring and slider stresses are: $\sigma_{s,curr}$ and $\sigma_{c,curr}$ and the updated stresses for the corresponding elements are: $\sigma_{s,up}$ and $\sigma_{c,up}$). Additionally, the slider strength and the plastic strain are defined as $\sigma_{c,limit}$ and ε^p, respectively. In this model, the total stress, σ applied to the model produces elastic strain, ε^e.

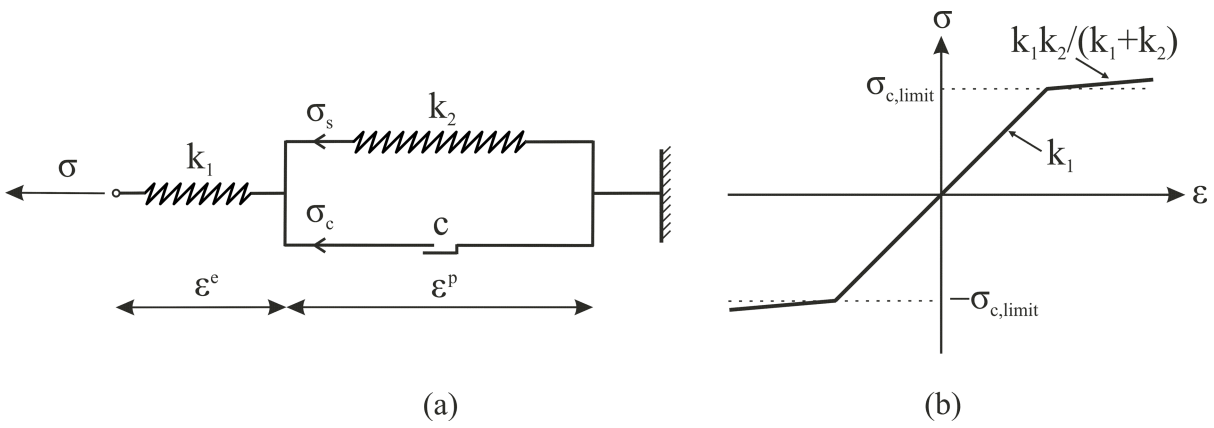


Figure 6.4: Series Iwan model: (a) schematic representation, (b) stress/strain constitutive relationship.

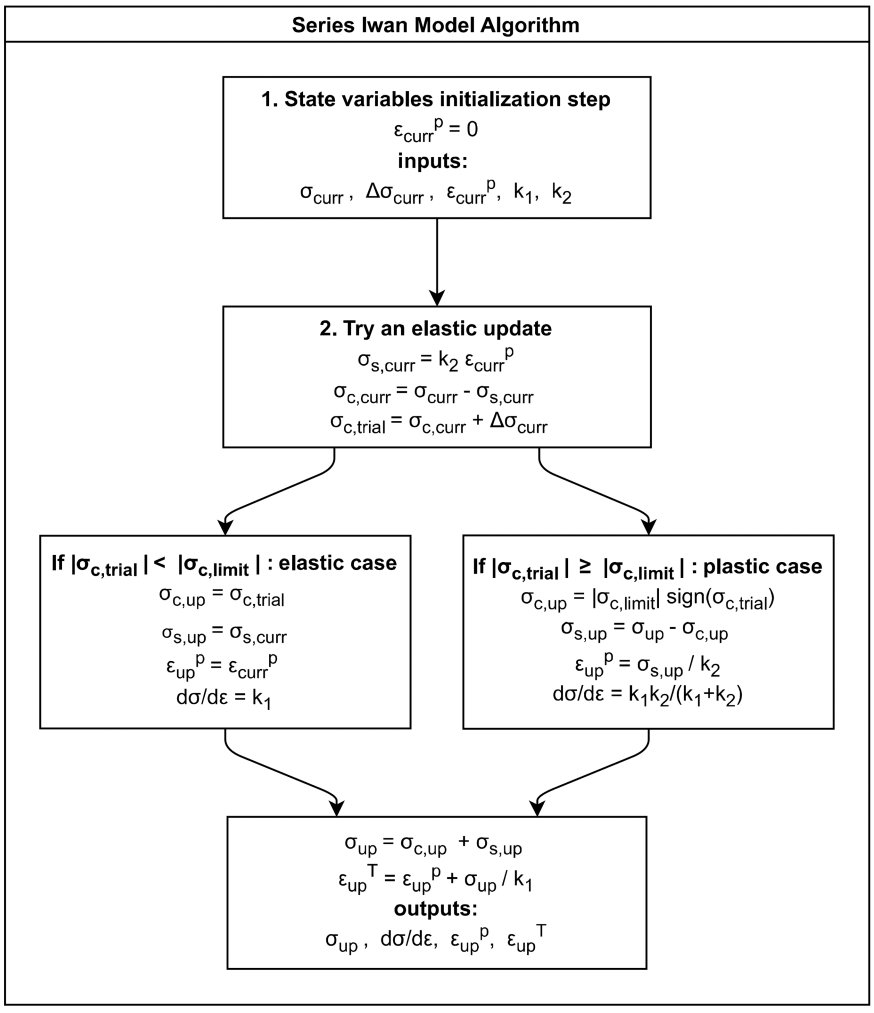


Figure 6.5: Material state determination algorithm for the series Iwan model.

The input parameters employed for the constitutive model calculation are the current values of plastic strain, ε_{curr}^{p} (which is chosen as the state variable), total stress, σ_{curr} and incremental

stress, $\Delta\sigma_{curr}$. The outputs are delivered as the updated values of plastic strain, ε_{up}^{p}, total strain, ε_{up}^{T}, and total stress, σ_{up}. The stress/strain constitutive relationship is presented in Figure 6.4(b). The material state determination algorithm for the series Iwan model is summarised in Figure 6.5. The parameters defined in the series Iwan model and their correspondence employed in the beam shear model to represent the shear force and shear strain relationship are presented in Table 6.2.

This procedure is repeated for each Gauss point along the beam length to determine the corresponding shear force and shear strain as a part of determining nonlinear internal stress and strain resultants. As a result, the outputs (V_{up} and γ_{up}^{T}) of the beam shear model are incorporated into the internal stress and strain resultants vectors as:

$$\mathbf{p} = \begin{bmatrix} N \\ M \\ V \end{bmatrix} = \begin{bmatrix} \mathbf{p}_{\mathbf{fibre}(2\times1)} \\ V_{up} \end{bmatrix} \qquad \boldsymbol{\varepsilon} = \begin{bmatrix} \varepsilon_c \\ \kappa \\ \gamma \end{bmatrix} = \begin{bmatrix} \boldsymbol{\varepsilon}_{\mathbf{fibre}(2\times1)} \\ \gamma_{up}^{T} \end{bmatrix} \tag{6.2}$$

Table 6.2: Parameters defined in the series Iwan model and their correspondence in the beam shear model.

	Series Iwan model		**Beam shear model**	
Parameter status	**Definition**	**Parameter**	**Definition**	**Parameter**
Constant value	Slider strength	$\sigma_{c,limit}$	Shear force limit*	V_{limit}
	Elastic spring stiffness	k_1	Shear tangent modulus	$\kappa_s AG$
Current value	Total axial stress	σ_{curr}	Total shear force	$V_{curr} = \mathbf{p_{curr}}(3)$
	Incremental axial stress	$\Delta\sigma_{curr}$	Incremental shear force	$\Delta V_{curr} = \Delta\mathbf{p}(3)$
	Plastic axial strain	ε_{curr}^{p}	Plastic shear strain	γ_{curr}^{p}
Updated value	Total axial stress	σ_{up}	Total shear force	V_{up}
	Plastic axial strain	ε_{up}^{p}	Plastic shear strain	γ_{up}^{p}
	Total axial strain	ε_{up}^{T}	Total shear strain	γ_{up}^{T}

G: shear modulus, $\kappa_s A$: shear cross-section area.
* shear force capacity of the beam element at the specified Gauss point

6.2.2.2 Beam shear model: shear force

To mimic the shear failure criterion employed in the JMM for the beam elements according to Equation (2.12), the plane 1 and the plane 2 are chosen for the shear failure mechanisms for the spandrels and the piers, respectively (Figure 6.3). The shear force limits for the spandrels, $\left(V_{limit,spandrel}\right)_{igauss}$ and the piers, $\left(V_{limit,pier}\right)_{igauss}$ at each Gauss point ('igauss') are calculated as:

$$\left(V_{limit,spandrel}\right)_{igauss} = c_{0,1}\kappa_s A \tag{6.3}$$

$$\left(V_{limit,pier}\right)_{igauss} = c_{0,2}\kappa_s A - (N)_{igauss}\, tan\varphi_2 \tag{6.4}$$

where $c_{0,1}$ and $c_{0,2}$ are the cohesions on the joints ($c_{0,1} = c_{0,2}$), $tan\varphi_2$ is the bed joint friction angle and $(N)_{igauss}$ is the axial force at each Gauss point acting in compression for the pier elements. For the spandrel elements, the contribution of the horizontal compressive stress (σ_{n1}) to its shear force limit is neglected compared to the expression given in Equation (2.12). However, the effect of vertical compressive stress (σ_{n2}) is included in the shear force limit calculations for the pier elements, as presented in Equation (6.4).

The shear force limits for the spandrels and piers are calculated after the application of self-weight loading with the assumption of using constant values for the rest of the EQFdc analysis (i.e. during the application of the greenfield displacements). Specifically, for a pier element, the axial force, $(N_0)_{igauss}$ determined (at each Gauss point) from the EQFdc analysis conducted under the self-weight loading is used in the calculation of $\left(V_{limit,pier}\right)_{igauss}$.

6.3 Stiffness-Based Elements: Nonlinear Model

6.3.1 Quad shear model

6.3.1.1 Quad shear model: modelling procedure

The shear behaviour in the quad elements is formulated by using the parallel Iwan model (Figure 6.1). For the quads, the parallel Iwan model is formulated in terms of shear stress, τ and shear strain, γ. The parameters defined in the parallel Iwan model and their correspondence in the quad shear model is given in Table 6.3.

Table 6.3: Parameters defined in the parallel Iwan model and their correspondence in the quad shear model.

	Parallel Iwan model		**Quad shear model**	
Parameter status	**Definition**	**Parameter**	**Definition**	**Parameter**
Constant value	Slider strength	$\sigma_{c,limit}$	Shear strength of the quad	τ_{limit}
	Total elastic spring stiffness	$k_1 + k_2$	Shear modulus of the quad	G
Current value	Axial stress in k_1 spring	$\sigma_{1,curr}$	Shear stress in k_1 spring	$\tau_{1,curr}$
	Axial stress in k_2 spring	$\sigma_{2,curr}$	Shear stress in k_2 spring	$\tau_{2,curr}$
	Plastic axial strain in k_2	$\varepsilon^p_{2,curr}$	Plastic shear strain in k_2	$\gamma^p_{2,curr}$
	Incremental axial strain	$\Delta\varepsilon_{curr}$	Incremental shear strain	$\Delta\gamma_{curr}$
Updated value	Total axial stress	σ_{up}	Total shear stress	τ_{quad}
	Axial stress in k_1 spring	$\sigma_{1,up}$	Shear stress in k_1 spring	$\tau_{1,up}$
	Axial stress in k_2 spring	$\sigma_{2,up}$	Shear stress in k_2 spring	$\tau_{2,up}$
	Plastic axial strain in k_2	$\varepsilon^p_{2,up}$	Plastic shear strain in k_2	$\gamma^p_{2,up}$

The shear failure criterion is defined in both positive and negative directions. Thus, the plasticity criterion needs to be checked by considering the absolute values of $|\sigma_{2,trial}|$ and the slider strength, $|\sigma_{c,limit}|$. If $|\sigma_{2,trial}|$ exceeds the strength of the slider ($|\sigma_{2,trial}| \geq |\sigma_{c,limit}|$), then the stress in spring k_2 is set to:

$$\sigma_{2,up} = |\sigma_{c,limit}| \times sign(\sigma_{2,trial}) \tag{6.5}$$

The rest of the calculations resemble the material state determination algorithm defined for the parallel Iwan model (Figure 6.2).

6.3.1.2 Quad shear model: shear strength

To define the shear strength of the quad elements according to the Mohr-Coulomb theory, the shear failure criterion, f is written as follows:

$$f = (\sigma_1 - \sigma_2) - (\sigma_1 + \sigma_2)sin\varphi_i - 2c_{0,i}cos\varphi_i = 0 \tag{6.6}$$

The major, σ_1 and minor, σ_2 principal stresses based on the vertical, σ_{vi} and horizontal compressive, σ_{hi} stresses can be defined in terms of radius, r, at the shear strength (τ_{limit}) by using the Mohr-Coulomb circle (Figure 6.6b). By substituting $\sigma_1 = ((\sigma_{vi} - \sigma_{hi})/2 + r)$ and $\sigma_2 = ((\sigma_{vi} - \sigma_{hi})/2 - r)$, (where $\sigma_{hi} = 0$ is assumed in this model) into Equation (6.6), the radius of the shear limit, r, is expressed as follows:

$$r = (\sigma_{vi}sin\varphi_i + 2c_{0,i}cos\varphi_i)/2 \tag{6.7}$$

Accordingly, the shear strength, τ_{limit}, is defined as:

$$\tau_{limit} = \sqrt{r^2 - (\sigma_{vi}/2)^2} \tag{6.8}$$

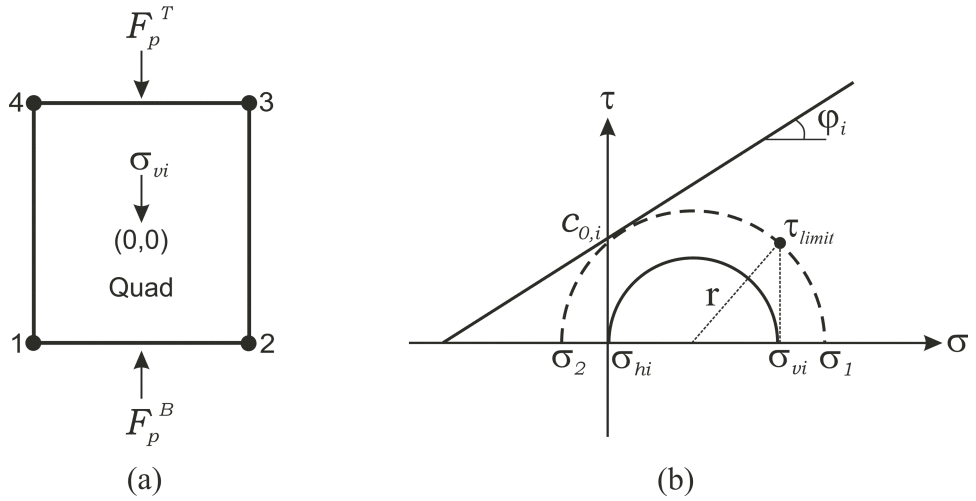


Figure 6.6: Determination of shear strength of a quad element: (a) vertical compressive stress at the quad centre, (b) Mohr-Coulomb circle shear behaviour.

After conducting the self-weight loading in the EQFdc analysis, the shear strength of the quad element, τ_{limit} needs to be determined. To compute τ_{limit}, the vertical compressive stress, σ_{vi} at the centre of the quad needs to be calculated in addition to the material properties required for the cohesion, $c_{0,i}$ and the friction angle, φ_i of the masonry joints. For the calculation of σ_{vi} at the quad centre, the vertical stresses acting to the centre of the top, ${\sigma_{vi}}^T$ and bottom, ${\sigma_{vi}}^B$ edge interfaces of the specified quad are determined. For this purpose, the normal forces acting to the centre of the top, ${F_p}^T$ and bottom, ${F_p}^B$ edge interfaces (Figure 6.6a) need to be computed. For example, the vertical stress acting to the centre of the top edge interface of a quad element, ${\sigma_{vi}}^T$, is calculated as:

$$ {\sigma_{vi}}^T = {F_p}^T/(t_q L_{int}) = \left(\int_{-L_{int}/2}^{L_{int}/2} \mathbf{p_i}\, t_q dX \right)/(t_q L_{int}) \tag{6.9} $$

where $\mathbf{p_i}$ is the normal tractions acting on the interface, t_q is the quad thickness and L_{int} is the interface length. Then the vertical compressive stress, σ_{vi} at the quad centre is computed as:

$$ \sigma_{vi} = \frac{{\sigma_{vi}}^T + {\sigma_{vi}}^B}{2} \tag{6.10} $$

where ${\sigma_{vi}}^B$ is the vertical stress at the centre of the bottom edge interface of a quad element, which can be determined according to Equation (6.9) as ${\sigma_{vi}}^B = {F_p}^B/t_q L_{int}$.

6.3.2 Structural interface tension model

6.3.2.1 Structural interface tension model: modelling procedure

The normal traction behaviour in the structural interface elements is modelled by using the parallel Iwan model (Figure 6.1). In this model, plasticity occurs only in tension; compressive behaviour is elastic. The constitutive relationship for the shear tractions is kept linear elastic. To represent the normal traction behaviour in the structural interface tension model, the parallel

Iwan model parameters need to be considered in terms of the normal traction, p and the relative vertical displacements (shorten as 'rel. vert. disp.'), v_r as presented in Table 6.4.

Table 6.4: Parameters defined in the parallel Iwan model and their correspondence in the structural interface tension model.

	Parallel Iwan model		**Structural interface tension model**	
Parameter status	**Definition**	**Parameter**	**Definition**	**Parameter**
Constant value	Slider strength	$\sigma_{c,limit}$	Interface tensile strength	$\sigma_{T,limit}$
	Total elastic spring stiffness	$k_1 + k_2$	Interface normal stiffness	$K_{n,int}$
Current value	Axial stress in k_1 spring	$\sigma_{1,curr}$	Normal traction in k_1	$p_{1,curr}$
	Axial stress in k_2 spring	$\sigma_{2,curr}$	Normal traction in k_2	$p_{2,curr}$
	Plastic axial strain in k_2	$\varepsilon^p_{2,curr}$	Plastic rel. vert. disp. in k_2	$v^p_{r2,curr}$
	Incremental axial strain	$\Delta\varepsilon_{curr}$	Incremental rel. vert. disp.	$\Delta v_{r,curr}$
Updated value	Total axial stress	σ_{up}	Total normal traction	p_{up}
	Axial stress in k_1 spring	$\sigma_{1,up}$	Normal traction in k_1	$p_{1,up}$
	Axial stress in k_2 spring	$\sigma_{2,up}$	Normal traction in k_2	$p_{2,up}$
	Plastic axial strain in k_2	$\varepsilon^p_{2,up}$	Plastic rel. vert. disp. in k_2	$v^p_{r2,up}$

Here, it is important to note that the spring stiffnesses in the structural interface model are in the dimensions of N/m^3. However, the spring stiffness dimensions are N/m^2 for the Iwan models. Considering the dimension of the relative vertical displacements (dimension is in m), the formulations regarding normal traction (dimension is in N/m^2) still satisfy the dimensional consistency in the equations.

6.3.2.2 Structural interface tension model: tensile strength

The tensile strength of the interface elements in the normal direction is defined based on the tensile strength of the beam elements. While the vertical interface elements have the same tensile strength as the spandrels, the tensile strength of the horizontal interface elements is associated with the value employed for the piers.

6.4 Conclusion

This chapter develops a practical approach to represent the nonlinear masonry behaviour for the EQFdc model. To achieve this, the constitutive models that mimic the nonlinear masonry behaviour described in the JMM are employed for the EQFdc model and the stress/strain constitutive relationships are formulated using the Iwan models (Iwan, 1967).

Chapter 7

Assessment of EQFdc Model: Linear Analysis

7.1 Introduction

This chapter comprises the assessment of the EQFdc model in the linear elastic domain for a tunnel-soil-building interaction problem adopted from the literature. To compare the results determined from the EQFdc model, an intermediate level 2D FE continuum model is generated in the DIANA finite element analysis (FEA) v10.3 software as a reference model (referred to as 'DIANA model' for the rest of the chapter). Linear elastic models are employed for the building and the soil in the EQFdc and the DIANA models.

The comparison between the EQFdc and the DIANA models are presented in terms of the number of elements, nodes and degrees of freedom in Table 7.1. A fine mesh size is chosen for the DIANA model to show the compatibility of the EQFdc model with even a fine mesh size continuum model. It is important to highlight that the EQFdc model comprises significantly fewer elements and degrees of freedom than the DIANA model.

Table 7.1: Comparisons between the EQFdc and the DIANA models in terms of the number of elements, nodes and degrees of freedom.

	Description	Number
EQFdc model	Quad elements	70
	Beam elements	40
	Footing elements	22
	Interface elements	172
	Elements in total	304
	Nodes in total	241
	Degrees of freedom in total	586
DIANA 2D FE continuum model	Façade mesh elements	10620
	Footing mesh elements	646
	Soil interface mesh elements	160
	Elements in total	11426
	Nodes in total	6263
	Degrees of freedom in total	12526

7.2 Problem Definition

A two-storey masonry building example with a strip footing (Yiu et al., 2017a; Burd et al., 2022) is chosen as a case study to examine the effects of the tunnel-soil-building interactions through linear elastic analysis (Figure 7.1). Only a single façade of the building with a regular opening layout and its foundation is considered in this problem, similar to the isolated façade approach of Yiu et al. (2017a).

7.2.1 Building and tunnel configuration

The problem comprises a single tunnel scenario passing under a two-storey masonry London-type building example with a strip footing system. The tunnel is excavated in London clay, which is deposited under 8 m Terrace gravel soil layer. The geometrical details of the façade, footing and single tunnel scenario adopted from Yiu et al. (2017a) are shown in Figure 7.1.

7.2.2 Loading scenario

The loading scenario of the case study is composed of two steps, first the application of

structural self-weight and then the tunnelling-induced greenfield displacements. Self-weight loading is applied to validate the accuracy of structural weight transfer to the soil-foundation interface elements in comparison with the DIANA model. Self-weight loads are calculated from the unit weights of the façade and footing.

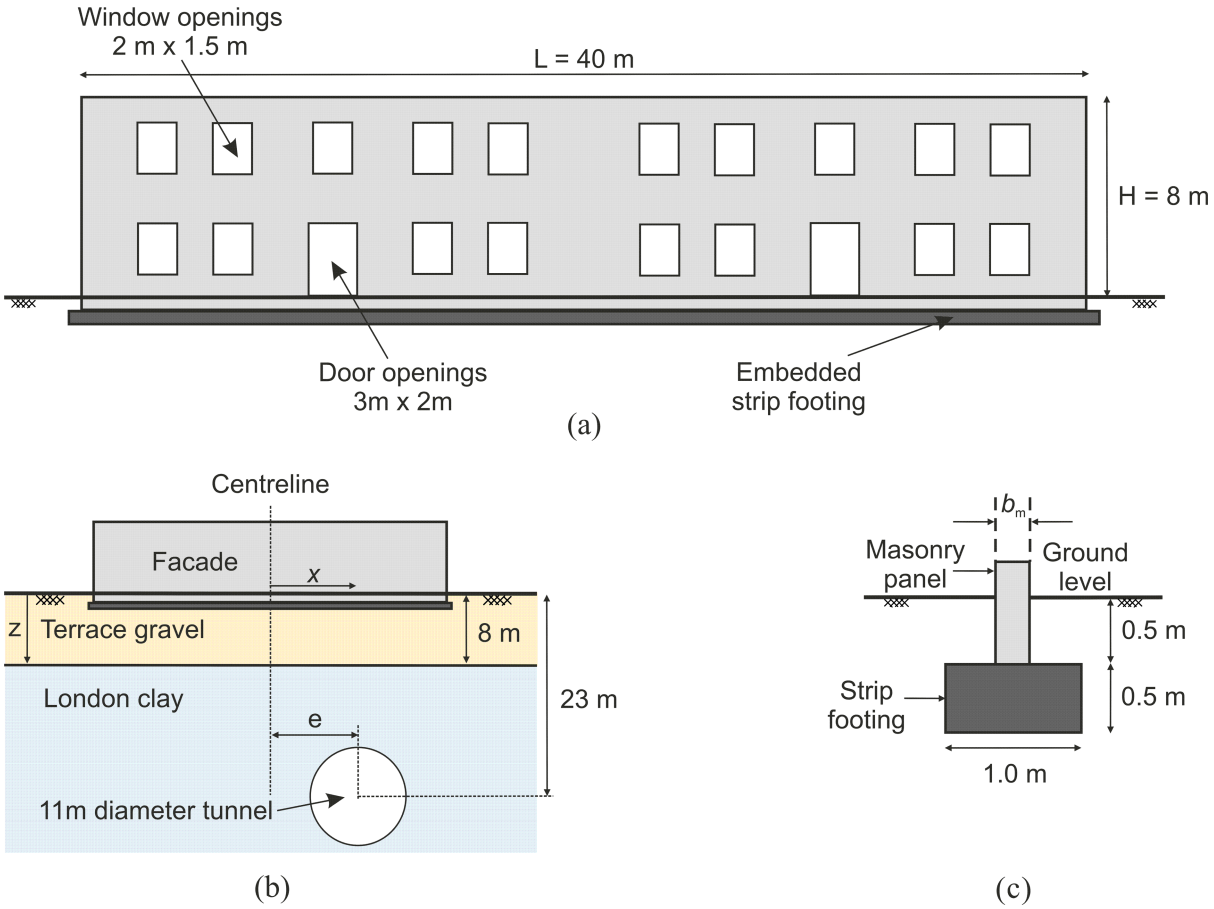


Figure 7.1: Façade, footing and tunnel configuration adopted for the case study: (a) façade geometry, (b) tunnel-façade configuration and (c) footing cross-section detail (modified from Yiu et al., 2017a).

Table 7.2: The parameters used for a single tunnel excavation scenario correspond to the greenfield displacements (Yiu et al., 2017a).

	Parameter	Value
Single tunnel	Tunnel diameter, D	11 m
	Tunnel depth, z_t	23 m
	Settlement volume loss, V_L	1.65 %
	Trough width parameter, K	0.57
	Tunnel eccentricity, e	$0 \leq e \leq 25$ m

The raw greenfield horizontal and vertical displacements data at the foundation base level ($z = -1.0$ m) provided by Yiu et al. (2017a) are implemented into the models as input prescribed deformations. The parameters defining the single tunnel excavation scenario determined from the 3D FE analyses performed by Yiu et al. (2017a) are given in Table 7.2.

7.2.3 Masonry material properties

The façade and the strip footing are modelled with linear elastic masonry material. Material and geometrical parameters used for the façade and the strip footing are given in Tables 7.3 and 7.4. The footing has the same linear elastic material properties as the masonry façade except for the unit weight which is defined as 19.50 kN/m^3 to make it identical with the unit weight of Terrace gravel for the convenience in the calculations (Yiu et al., 2017a; Burd et al. 2022).

Table 7.3: Masonry façade material and geometrical parameters (from Yiu et al., 2017a).

	Parameter	Value
Façade	Unit weight, γ_m	23.75 kN/m^3
	Young's modulus, E_m	3.0 GPa
	Poisson's ratio, ν_m	0.20
	Façade thickness, t_{facade}	0.215 m
	Façade height, h_{facade}	8.0 m
	Façade length, L_{facade}	40 m
	Façade surface area, A_{facade}	274 m^2

7.2.4 Soil and foundation properties

The soil interface stiffness parameters are chosen according to the linear elastic soil stiffness values presented in the S2M soil-foundation interaction model by Burd et al. (2022) for the same tunnel-soil-building interaction problem (Figure 7.1). Soil stiffness parameters are determined according to the calibration analysis conducted in a 3D FE model (Burd et al., 2022). To determine the vertical soil stiffness, k_v, gravity loads are applied to a plane façade

(which is supported on an embedded strip footing). Then the gravity loads applied to the footing are increased gradually and the corresponding vertical displacements at the footing base are calculated (Burd et al., 2022). The relationship between the applied gravity loads and the vertical displacements is used to determine k_v. For the determination of the horizontal soil stiffness, k_h, a strip footing is modelled in the 3D FE model (in which the self-weight of the footing is defined to be equal to the weight of the footing and panel combined). Then an external horizontal traction is applied to the one side of the strip footing in increasing order and the horizontal displacements at all footing nodes are calculated (Burd et al., 2022). Using the relationship between the applied horizontal tractions and the resultant horizontal displacements, k_h is determined. These data are provided in Table 7.4.

Table 7.4: Strip footing and soil-foundation interface parameters adopted from Yiu et al. (2017a) and Burd et al. (2022).

	Parameter	Value
Footing	Unit weight, γ_f	19.50 kN/m^3
	Young's modulus, E_f	3.0 GPa
	Poisson's ratio, ν_f	0.20
	Footing thickness, h_f	0.50 m
	Footing depth, d_f	1.0 m
	Footing width, b_f	1.0 m
Soil-foundation interface	Horizontal soil stiffness, k_h	14.6 MPa
	Vertical soil stiffness, k_v	28.7 MPa

7.3 DIANA Model Implementation

7.3.1 Building model

The built-in 6-node triangular plane stress elements called CT12M (based on quadratic interpolation with 3 integration points) available in the DIANA software are used to model the masonry façade and the strip footing (Figure 7.2). The strip footing is modelled separately from the façade with additional plane stress elements with a different thickness (footing width) than

the façade thickness. The mesh element size is chosen as 0.25 m for both façade and the strip footing. Elastic masonry properties are used for the façade and the strip footing (Tables 7.3 and 7.4).

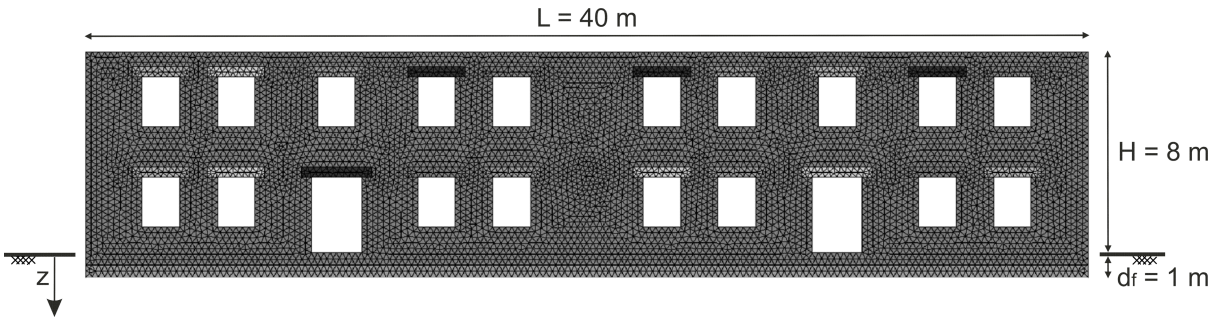


Figure 7.2: DIANA 2D FE continuum model demonsrating the mesh elements.

7.3.2 Soil-foundation interaction model

Soil-foundation interaction is represented with 2D structural line interface elements with zero-thickness, available as built-in CL12I quadratic displacement elements in DIANA FEA software. The CL12I line interface element comprises 6 nodes (3+3 on each line) and 3 integration points. The interface connection type is chosen as 'boundary interface' in which the horizontal and vertical displacements are prescribed with pinned supports beneath the strip footing. The interface elements are placed between the bottom edge of the footing and the pin-supported boundary conditions. This interface connection type enables the application of greenfield displacements as prescribed deformations to the bottom pin supports of the interface elements; the building displacements at the bottom edge of the footing are determined as a result of soil-structure interaction at the interface elements. The soil-foundation interaction is defined as linear elastic and the soil stiffness parameters are used as given Table 7.4.

7.3.3 Analysis procedure

Linear elastic analyses are started with the application of the self-weight loading and followed by the greenfield displacements loading; both loadings are applied in a single step.

7.4 EQFdc Model Implementation

7.4.1 Building model

Firstly, the geometrical model discretisation of the specified isolated façade example is generated in AutoCAD drawing software. The boundaries of the quad elements are determined according to the layout of the window and door openings. In this approach, the corners of adjacent openings are considered macro-element nodes. Sections between the macro-elements are defined as spandrel and pier elements according to the EQFdc model discretisation method described in Chapter 3. The EQFdc model representation is demonstrated in Figure 7.3. Material properties assigned to the elastic masonry façade is given in Table 7.3.

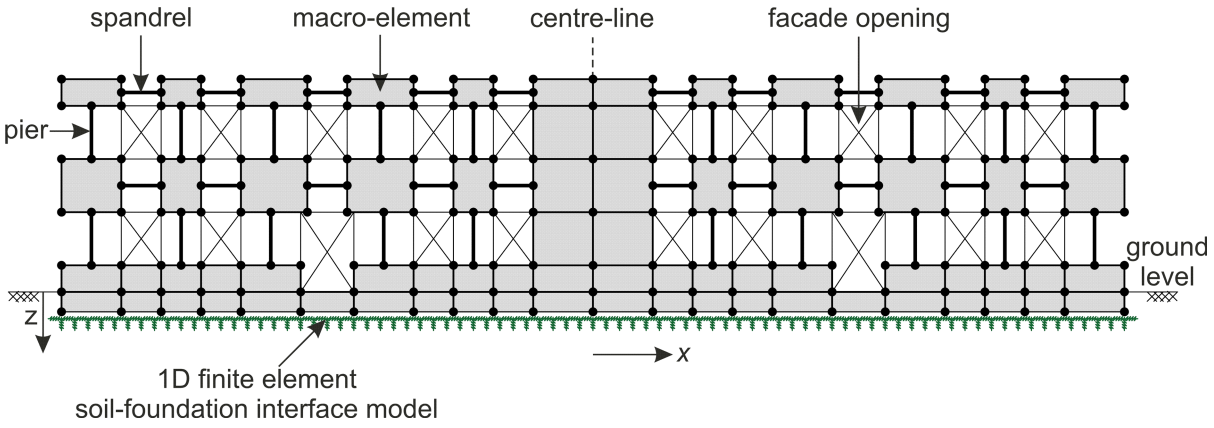


Figure 7.3: EQFdc model discretisation of the isolated façade.

7.4.2 Soil-foundation interaction model

Linear elastic material properties of the S2M soil-foundation interaction model (Table 7.4) are used in the EQFdc model to represent the soil-foundation interaction in the linear domain.

7.4.3 Analysis procedure

After the geometrical model generation (Figure 7.3) is completed, the following input data files are generated in Excel, including the information:

- nodes of each quad, beam and interface element,

- coordinates of the nodes,
- connections between the elements to define the corresponding interface type,
- material properties of all elements.

All the numerical models are coded (the code named as 'EQFdcsolver') as bespoke software in MATLAB R2021b. The datasets are organised for 'nodes', 'quads', 'beams', 'structural interfaces' and 'soil-foundation interface elements'. The EQFdc model is generated through the following routines written as MATLAB codes:

- Firstly, the element stiffness matrices of each quad, beam, structural and soil interface elements are computed and assembled into the global system stiffness matrix by mapping all the components accordingly.
- Secondly, the structural self-weight is applied to the system for the corresponding quad, beam and footing elements.
- The greenfield displacements at each integration point are imported into the model as prescribed deformations.

The Gaussian quadrature method is used to calculate the integrations in finite element formulations. The numbers of Gauss points used for the corresponding elements are chosen as 2 points per direction (along X and Y axis) for the quad, 11 for the beam and 5 for the interface elements.

7.5 Results Data Processing

The analysis results are processed as building displacements at the nodes of the footing elements, soil-foundation tractions at the Gauss points of the soil-foundation interface elements and the major principal tensile strains at the Gauss points of the façade elements for both the DIANA and the EQFdc models. However, the interpretation of the strain results requires an

additional procedure for the DIANA model as explained in the following section.

7.5.1 DIANA model

The magnitude of strains localised around the sharp corners is mesh-dependent; strains increase by reducing the mesh size in the DIANA model. This sharp corner effect (i.e. there are no sharp corners in reality) can be seen from the strain localisations around the opening corners in the major principal tensile strain contours for the DIANA model (Figure 7.4). Considering the first-storey façade portion from $x = 10$ m to $x = 15$ m, the strain distribution extends diagonally with a localised increase towards the corner of the openings (Figure 7.4). Without eliminating the mesh dependency of strains around the opening corners, the maximum strains determined from the finite element continuum models cannot be used to estimate the damage class of the building.

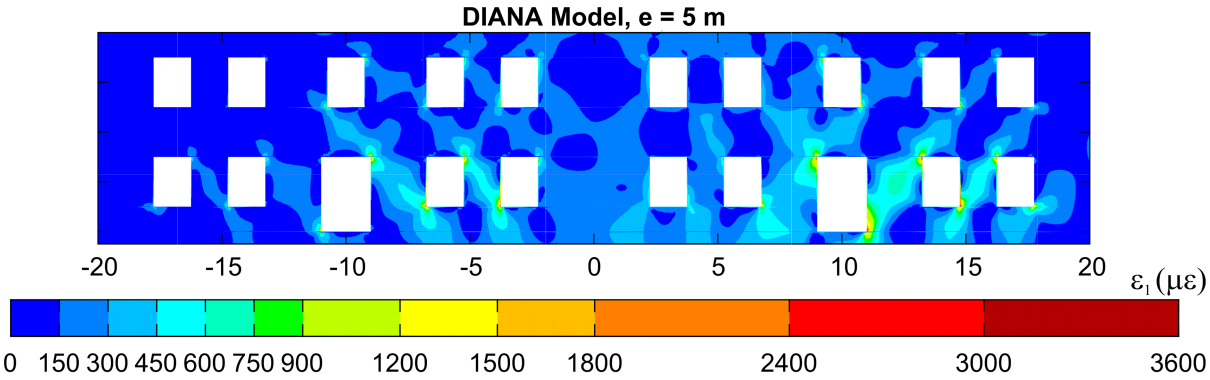


Figure 7.4: Major principal tensile strain contour plot for the DIANA model, e = 5 m.

To remove the mesh-size dependency, firstly, the ε_{99}^{t} method (i.e. sorting the strains at each Gauss point in decreasing order of magnitude and choosing the maximum strain as the one when the cumulative area of the Gauss points just exceeds 1.0% of the façade area) developed by Yiu et al. (2017a) is employed for the DIANA model. Figure 7.5(a) demonstrates the locations of the removed Gauss points by the ε_{99}^{t} method in the DIANA model (e = 5 m). It is seen that using ε_{99}^{t} method can also remove the Gauss points (which have high magnitude strains compared to the rest of the façade) even if they are far from the opening corners and

unaffected by mesh dependency. For example, the Gauss points located between $x = 10$ m and $x = 15$ m at the mid height of the door in Figure 7.5(a) are also removed by the ε_{99}^{t} method. This issue arises as the ε_{99}^{t} method indiscriminately removes high magnitude strains. As an alternative, a new method named 'radius search method' is developed in this research. The radius search method focuses on eliminating the mesh size effect by removing the high magnitude strains localised around the sharp corners of the model. The procedure developed for the radius search method for a FE continuum model is explained as follows:

- Store the major principal tensile strains, ε_1 at each integration (Gauss) point with their coordinates as 'strain database'.
- Specify the coordinates of the corners of openings.
- Define a radius upper limit and apply it in small steps up to the limit value (the radius search is conducted at each step).
- Start searching to find the neighbour integration points within the applied radius step around all the openings' corners.
- Find the maximum ε_1 strain outside the applied radius around all corners.
- Find the points within the neighbour integration points, which have higher strains than the maximum ε_1 strain determined in the previous step and exclude these (referred to as removed Gauss points) from the strain database.
- Set another area (for 2D FE models) or volume (for 3D FE models) limit depending on the continuum model type to prevent that the total area or the volume of the excluded points not to exceed this specified area or volume limit.

For the DIANA 2D FE continuum model, the radius upper limit is chosen as 0.4 m (considering approximately two standard UK bricks length) and the area limit is set as 1 m^2 (chosen as a unit dimension). The importance of specifying the coordinates of the openings can be clearly

seen from the difference in the locations of the removed Gauss points between the ε_{99}^{t} method (Figure 7.5a) and the radius search method (Figure 7.5b), which are applied to the same DIANA strain results.

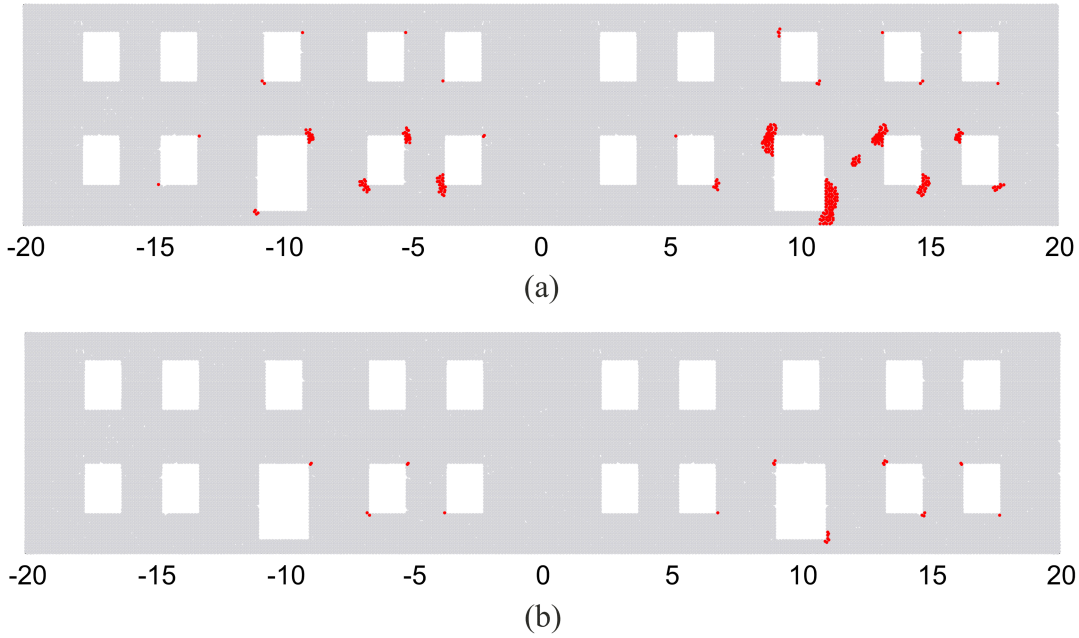


Figure 7.5: Locations of removed Gauss points (red color) in the DIANA model for the tunnel eccentricity with e = 5 m: (a) ε_{99}^{t} method, (b) radius search method.

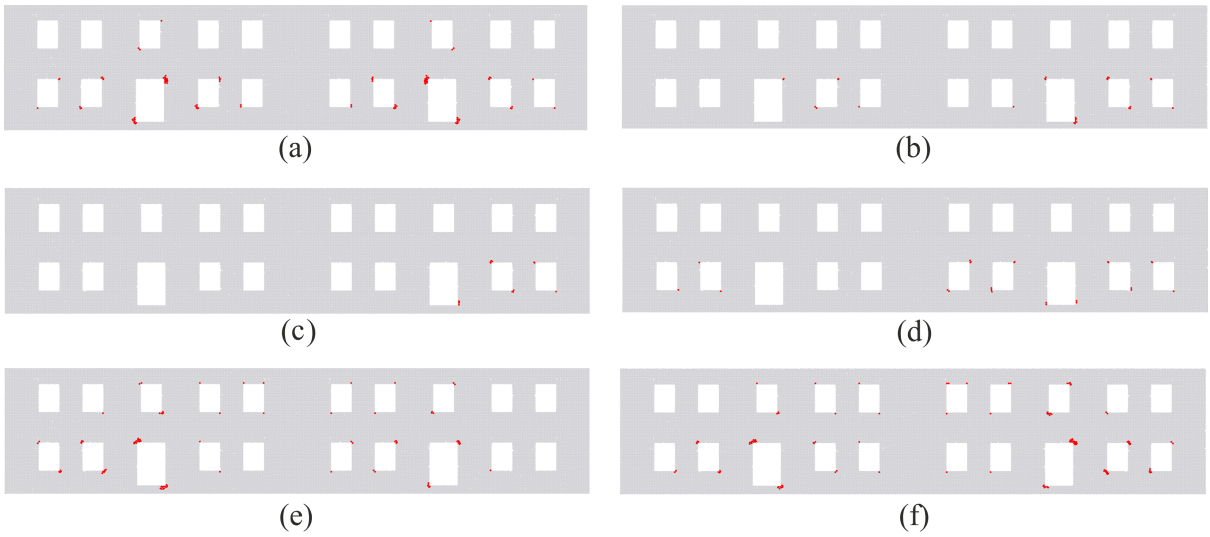


Figure 7.6: Locations of removed Gauss points (red color) at the sharp corners of the DIANA model for the tunnel eccentricity: (a) e = 0, (b) e = 5 m, (c) e = 10 m, (d) e = 15 m, (e) e = 20 m and (f) e = 25 m.

The locations of the removed Gauss points are shown in Figure 7.6. The total areas of the removed Gauss points correspond to 0.28%, 0.08%, 0.04%, 0.06%, 0.25% and 0.32% of the façade area for tunnel eccentricities from 0 to 25 m. The effect of sharp corners on the magnitude of the maximum ε_1 strains determined in the DIANA model can be seen from the difference in results with and without removing the strains in the opening corners (Figure 7.7).

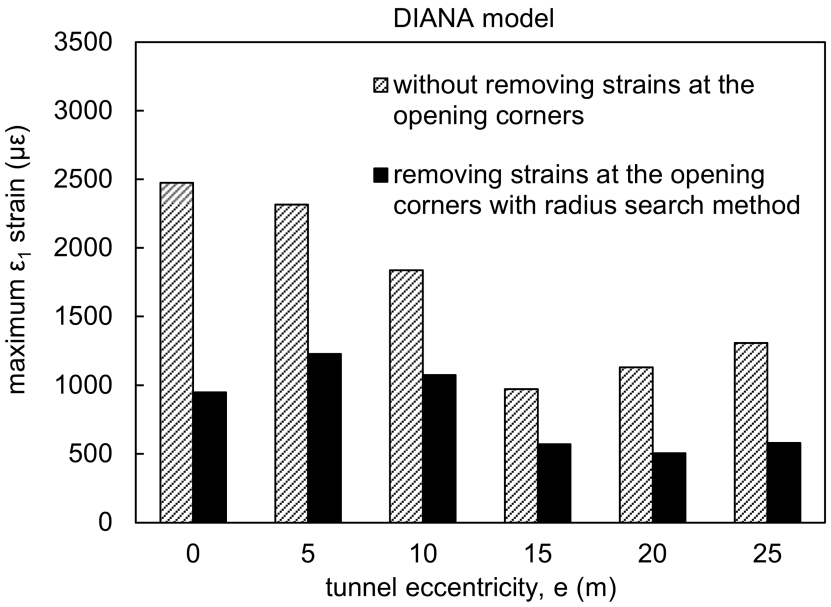


Figure 7.7: Maximum major principal tensile strains in the DIANA model with and without removing the strains at the opening corners.

7.5.2 EQFdc model

In contrast to the DIANA model, the radius search method is not used for the EQFdc model as beam elements do not exhibit mesh dependency. Maximum major principal tensile strains are presented without applying any strain removing to the results. However, for the calculation of the major principal tensile strains, parabolic shear strain distribution is employed for the elastic façade model. To achieve this, the section forces (N, V, M) determined at the end of the EQFdc model analysis for each beam element is processed to compute the parabolic shear strain distribution across the cross-sections instead of using the constant shear strain data determined as the analysis results.

The EQFdc model incorporates plotting features to present the critical output data (in terms of building displacement response, tractions in the soil-foundation interface and the major principal tensile strain distributions in the façade) achieved from the structural analysis.

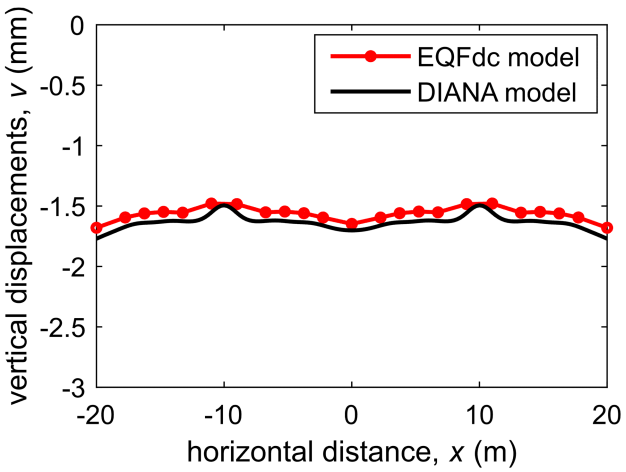


Figure 7.8: Self-weight-induced vertical displacements at the foundation level.

7.6 Results and Comparisons

In this section, the linear elastic analysis results determined from the EQFdc model are compared to the DIANA model findings. The façade displacements at the footing level and the tractions in the soil-foundation interface elements are presented separately for the self-weight and the greenfield loading applications. While the footing level refers to the depth of $z = -1.0$ m for the DIANA model, the centre of footing elements considered for the EQFdc model is at $z = -0.75$ m. The difference in elevation is due to the idealisation of footings as line elements in the EQFdc model. The major principal tensile strain distributions are also computed to estimate the tunnelling-induced damage class.

7.6.1 Displacement responses

7.6.1.1 Building response to self-weight loading

The vertical displacements results are presented in Figure 7.8. The EQFdc model is seen to agree well with the vertical displacements determined from the DIANA model. The average

vertical displacements under the self-weight loading are determined as −1.56 mm and −1.63 mm for the EQFdc and DIANA models. The self-weight of the structure, F_{weight}, is computed as −1789.1 kN in the EQFdc model. The average vertical displacement induced by the structural self-weight, v_{weight}, is also verified through numerical calculations as −1.56 mm.

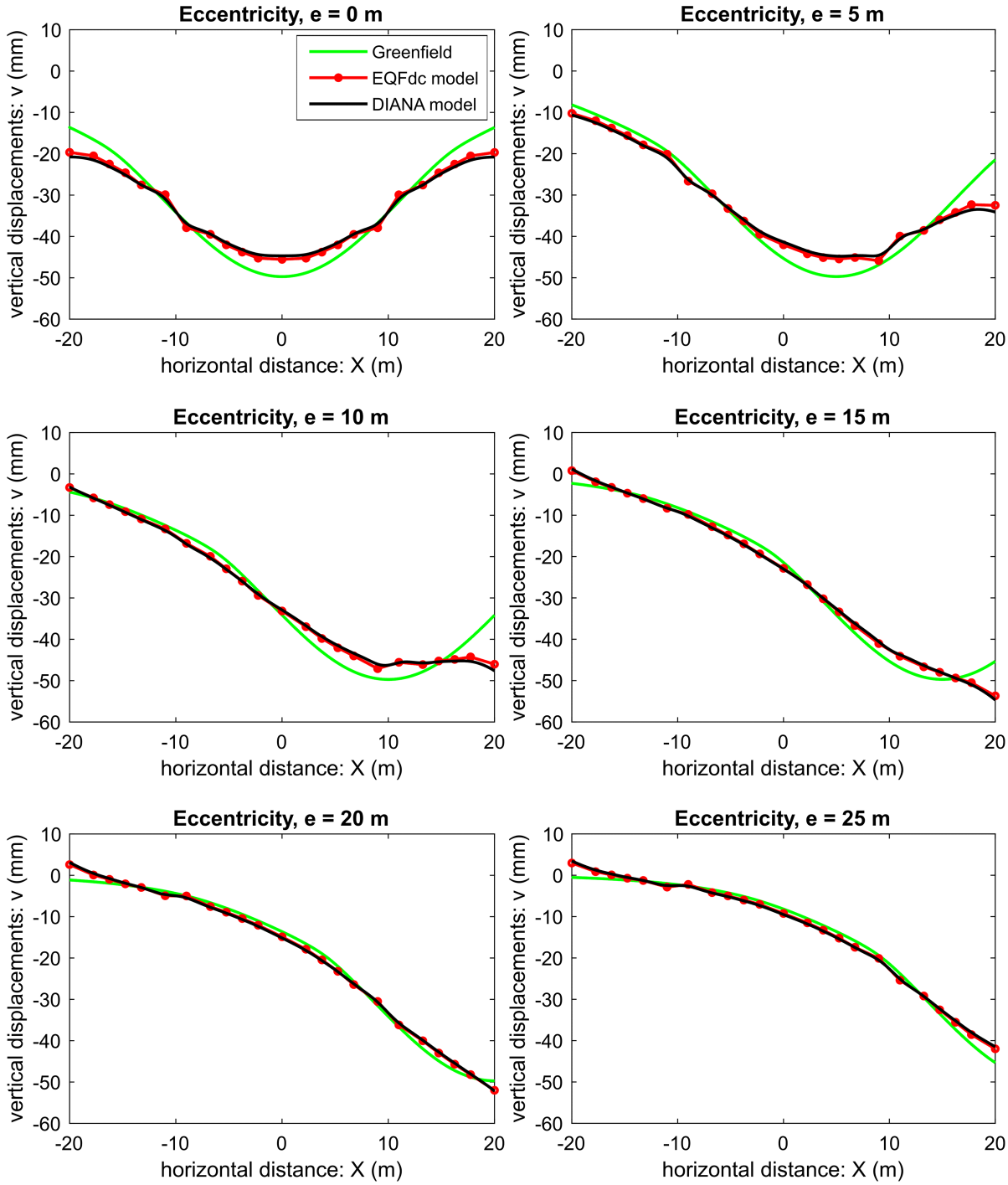


Figure 7.9: Façade vertical displacement responses at the foundation level induced by the greenfield displacements only.

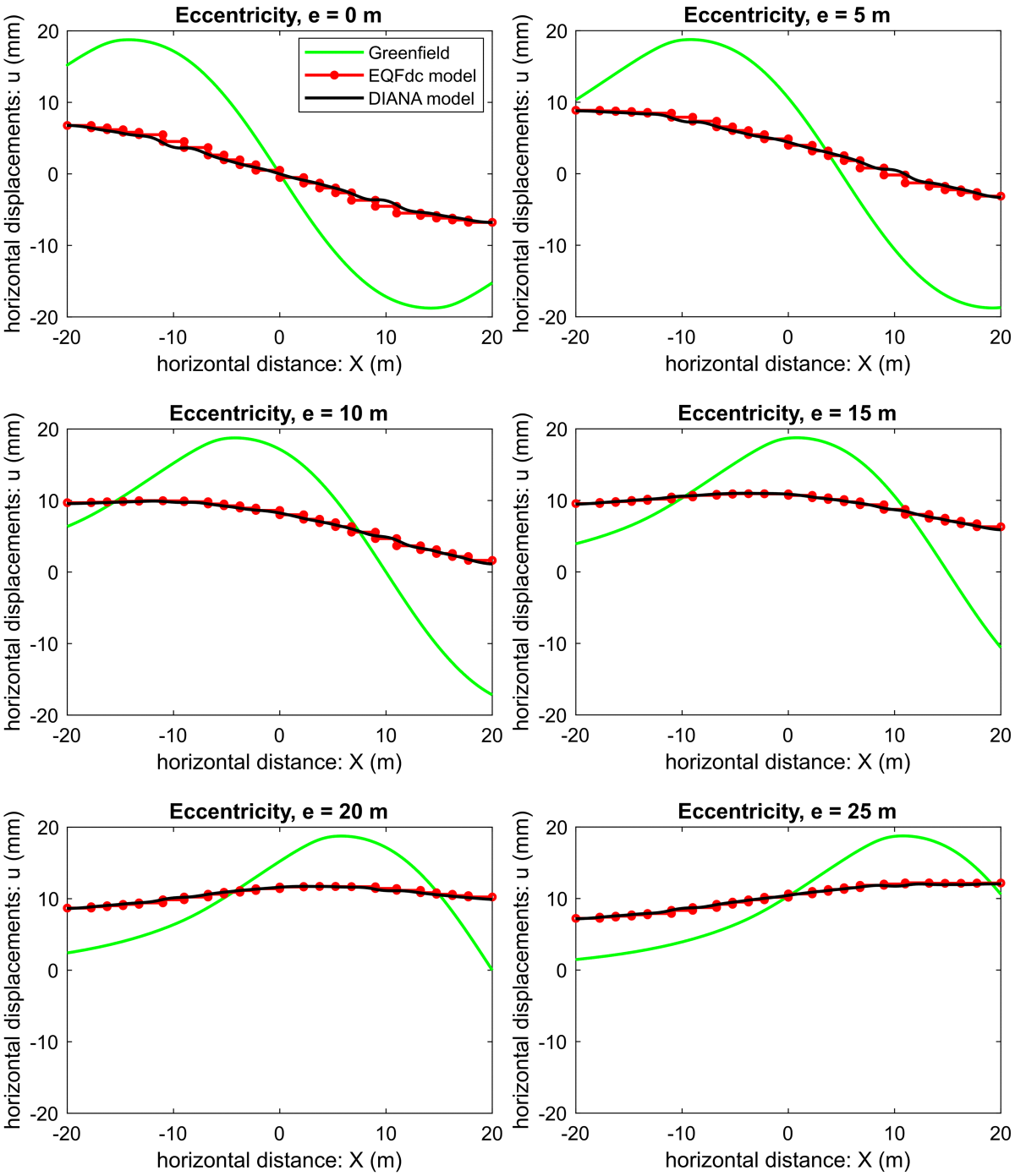


Figure 7.10: Façade horizontal displacement responses at the foundation level induced by the greenfield displacements only.

7.6.1.2 Building response to greenfield displacements

The central tunnel excavation and the tunnel eccentricity scenarios, *e* are considered in the greenfield displacement application. The building displacements presented in this section represent only the effect of greenfield displacements, in which they are determined by

subtracting the building displacements induced by the self-weight loading from the total displacements achieved at the end of the analysis.

The vertical and horizontal displacements computed at the footing elements of the EQFdc model are compared with the results determined from the DIANA model in Figures 7.9 and 7.10, respectively. The greenfield displacements are also shown together with the building displacement results. As a result of soil-structure interaction, the displacement patterns are modified and the façade experiences less differential displacement than indicated by greenfield displacements. The EQFdc model successfully simulates vertical and horizontal displacements determined from the DIANA model. This agreement emphasises the capability of the EQFdc model to reproduce almost the same results by using significantly fewer elements and degrees of freedom compared to the DIANA model.

7.6.2 Soil traction responses

7.6.2.1 Soil traction response to self-weight loading

Firstly, the normal tractions computed by the EQFdc model are compared with results determined from the DIANA model (Figure 7.11a). The average values of normal tractions are computed as -45 kN/m for the EQFdc model and as -47 kN/m for the DIANA model.

The accurate transfer of the self-weight loads to the soil-foundation interface elements in the EQFdc model is checked through the integration of normal tractions along the soil elements should be equal to the self-weight vector as:

$$F_{weight} = \int_0^{L_{facade}} p_{soil}\, dx = \sum F_v \tag{7.1}$$

As a result of the summation of integrated normal force vectors, $\sum F_v$ given in Figure 7.11(b), the total value is calculated as -1789.1 kN, which is same as the value determined from the exact solution mentioned in Section 7.6.1.1.

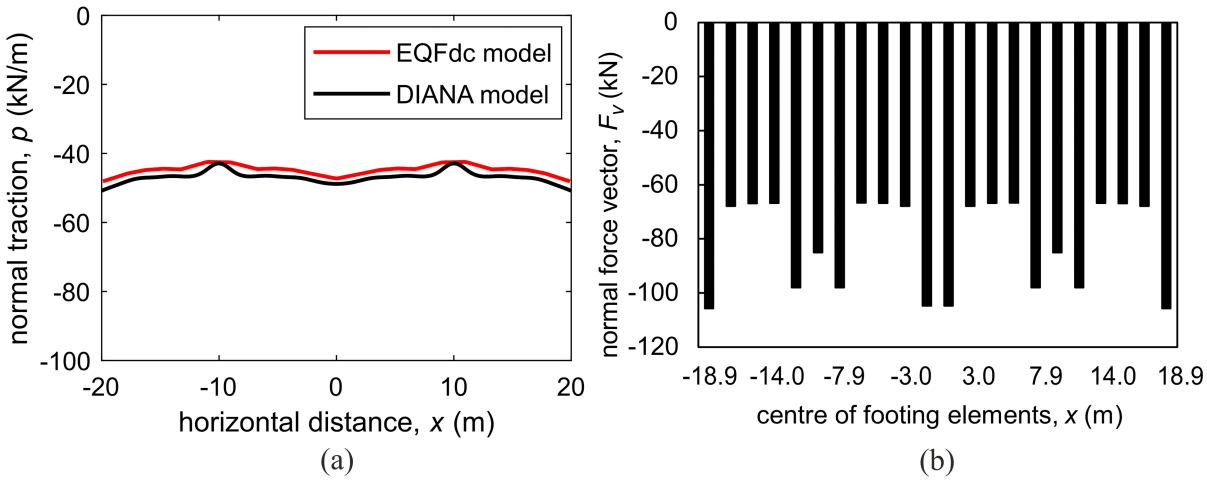


Figure 7.11: Effect of self-weight loading at the soil-foundation interface elements: (a) normal tractions and (b) integrated normal force vectors.

7.6.2.2 Soil traction response to total loading

The total loading refers to the combined effect of self-weight and greenfield displacement loadings computed at the end of the analysis. The normal and shear tractions determined at the soil-foundation interface elements under the total loading are shown in Figure 7.12. The EQFdc model is seen to produce results that are consistent with the DIANA model, especially for the shear traction (Figure 7.12b). However, slight differences are observed in the normal tractions at the edges of the footing elements (Figure 7.12a). However, the differences are minor.

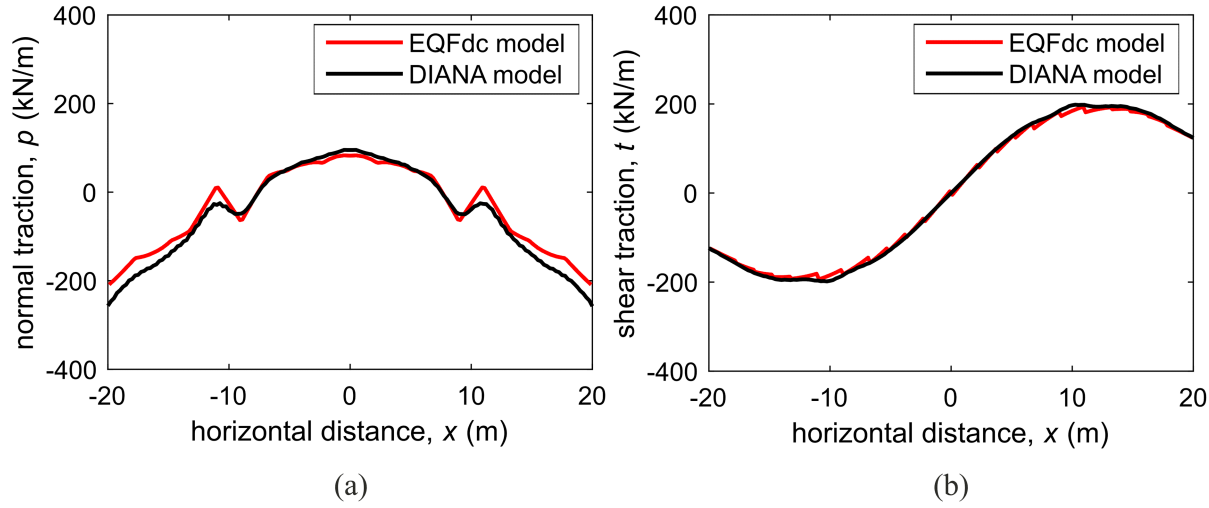


Figure 7.12: Total tractions including self-weight and greenfield displacement loadings at the soil-foundation interface elements: (a) normal tractions, (b) shear tractions.

7.6.3 Major principal tensile strain responses

Major principal tensile strain distributions are presented to emphasise only the effect of tunnelling-induced greenfield displacements. Strain contours are arranged in discrete levels, which provides detailed visualisation until 900 με then continue with 300 με and 600 με increments. The strains corresponding to the limiting tensile strain levels (750 με, 1500 με, 3000 με) from 'slight' to 'very severe' damage classes (Burland & Wroth, 1974; Boscardin & Cording, 1989) are also presented as the contour levels.

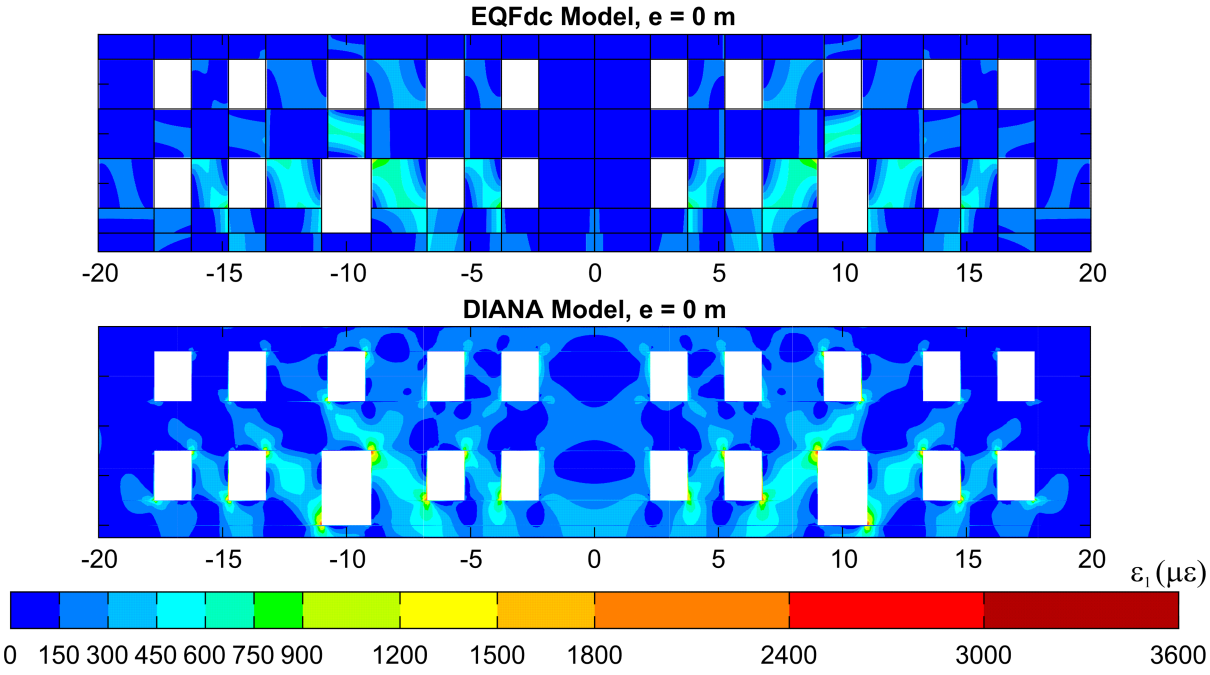


Figure 7.13: Major principal tensile strain contour plot comparisons between the EQFdc and DIANA models, e = 0 m.

Figure 7.13 shows the major principal tensile strain, ε_1 comparisons between the models for the central tunnel case (e = 0). Overall, the strain distributions are accumulated in the first and second storey elements as extending diagonally with increasing magnitude towards the corner of the openings in both models. Especially, the piers next to the doors are subjected to the higher strains, which extend diagonally and are localised at the corners of the openings. The EQFdc model provides a similar ε_1 distribution pattern overall with the DIANA model (Figure

7.13), successfully capturing the diagonal strain patterns in the first-storey piers and the spandrels over the door openings.

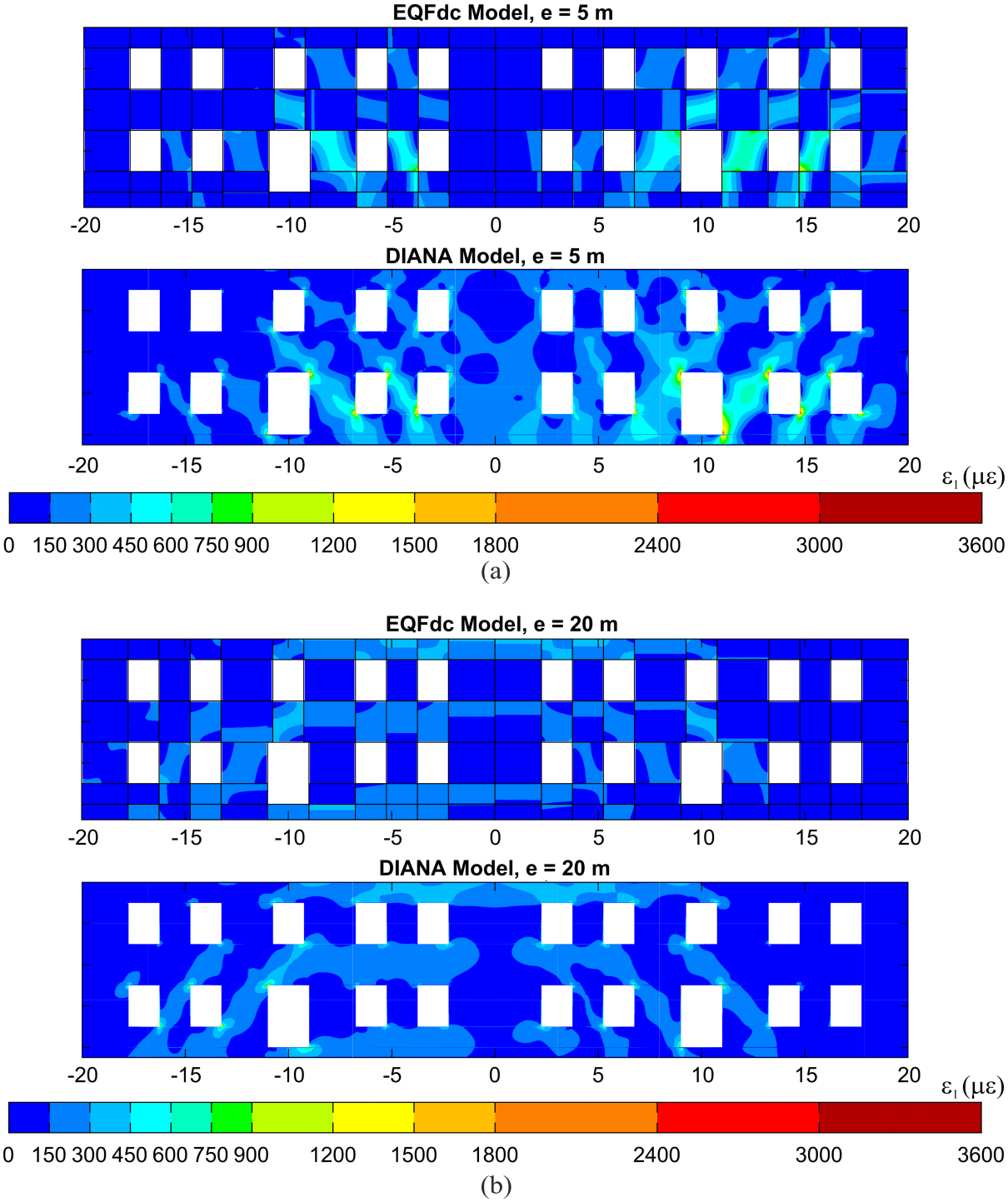


Figure 7.14: Major principal tensile strain contour plot comparisons between the EQFdc and DIANA models: (a) e = 5 m and (b) e = 20 m.

In the case of tunnel eccentricity with e = 5 m (Figure 7.14a), the DIANA model shows that

the piers in the first storey, especially the ones next to the door on the right side of the façade, are exposed to higher strains than other elements. This aspect is also represented by the EQFdc model. The diagonally extending and increasing strain pattern towards the corners of openings, especially in the first-storey piers between approximately 11 m $\leq x \leq$ 16 m are reasonably captured by the EQFdc model. Finally, the ε_1 distributions are compared under the tunnel eccentricity scenario of e = 20 m (Figure 7.14b). The DIANA model shows that the strains are spread towards the top storey spandrel elements, which is also reproduced by the EQFdc model. In this tunnelling scenario, the strain distributions at the top storey spandrels and the spandrel over the door and the quads below the door at $x = -10$ m are captured successfully by the EQFdc model. The results demonstrate that the EQFdc model agrees well with the DIANA model in terms of major principal tensile strain distributions.

7.6.4 Variation of maximum tensile strain with tunnel eccentricity

The variation of the maximum major principal tensile strain with tunnel eccentricity is presented in Figure 7.15. The maximum major principal tensile strains determined from the DIANA model (by removing the strains after the application of the radius search method) almost represent the same results with the EQFdc model. The standard building damage class limits of 500, 750, 1500 and 3000 με (Burland & Wroth, 1974; Boscardin & Cording, 1989) are also marked in Figure 7.15 to define the corresponding damage class of each tunnelling scenario easily. Accordingly, for the tunnel eccentricities at 0, 5 and 10 m, the masonry façade used is exposed to the 'slight' level of damage since the maximum major principal tensile strains occur in between damage class limits of [750, 1500] με. Meanwhile, the tunnel eccentricities of 15, 20 and 25 m correspond to the 'very slight' damage class having the maximum ε_1 strains in between limits of [500, 750] με.

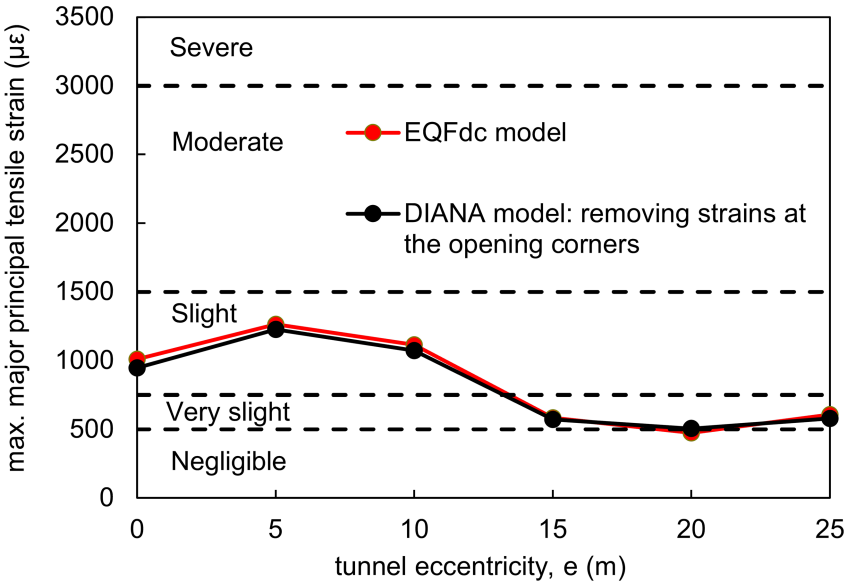


Figure 7.15: Comparison of the maximum major principal tensile strain variations with tunnel eccentricity for the EQFdc and DIANA models.

7.7 Conclusion

In conclusion, the EQFdc model can successfully simulate the linear elastic analysis results determined from the DIANA model for the specified case study by providing a computationally efficient approach (requiring significantly fewer elements and degrees of freedom) than the DIANA model. Interpreting the EQFdc model is straightforward whilst removing strains was necessary to eliminate the mesh dependency of the DIANA model. A new method called the radius search method is developed to eliminate the strain localisations around the corners of openings and enable comparisons between strain outputs and corresponding damage classes from the models. The comparisons between the model results encourage the use of the EQFdc model as an additional assessment model (Stage 2b) after conducting the simple elastic beam model in Stage 2 damage assessments. The EQFdc modelling approach is used to explore nonlinear aspects of the problem in the next chapter.

Chapter 8

Assessment of EQFdc Model: Nonlinear Analysis

8.1 Introduction

The EQFdc model is assessed with nonlinear analyses for a tunnel-soil-building interaction problem in this chapter. To assess the EQFdc results, an advanced 3D FE fully coupled model (referred to as 'PLAXIS model'), based on the model developed by Amorosi and Sangirardi (2021) in PLAXIS, is chosen as the reference model. A key advantage of using this PLAXIS model as a reference model for the nonlinear analysis comparisons is that the nonlinear masonry behaviour is represented by 1D stress-strain constitutive relationships, which can be easily implemented into the FE formulations developed for the EQFdc model in this thesis. Additionally, Amorosi and Sangirardi (2021) adopted the same tunnel-soil-building interaction problem used by Yiu et al. (2017a). Thus, the linear elastic behaviour of the case study presented in Chapter 7 is extended into the nonlinear domain in this chapter.

The analyses are conducted for two cases. Firstly, the masonry façade is modelled as linear elastic (EL façade). Secondly, a nonlinear constitutive model is used for the façade (NL façade). For both cases, a nonlinear constitutive model is defined for the soil.

The PLAXIS 3D FE analyses results used in this chapter are produced by Sangirardi (2023) for both EL façade and NL façade cases for all tunnelling scenarios. In addition to the PLAXIS model, the S2M model (i.e. combination of the 2D FE masonry façade and the S2M soil-foundation interaction model developed by Burd et al., 2022) is also used in the building displacement comparisons for specific tunnelling cases (e = 0 and e = 5 m) to validate the accuracy of the implementation of S2M soil-foundation interaction model into the EQFdc model. The EQFdc and S2M models use the same S2M soil-foundation interaction model (Burd et al., 2022) but the former utilises a macro-element and beam idealisation of the façade. The S2M model (i.e. linear elastic facade) analyses are conducted by Burd (2023).

The PLAXIS, the S2M and the EQFdc models are compared visually in Figure 8.1 in decreasing order of complexity. The PLAXIS model is the most complex model, featuring explicit modelling of soil and tunnel excavation in a 3D FE environment (Figure 8.1a). The S2M model (Burd et al., 2022) refers to an intermediate complexity, in which the tunnel-soil modelling complexity is reduced to the 1D interface element level and the structure is represented with a 2D plane stress model (Figure 8.1b). Finally, the EQFdc model incorporates the simplified modelling strategies, in which the isolated façade is modelled with beams (spandrels and piers) and macro-elements (Figure 8.1c) and the S2M soil-foundation interaction model (Burd et al., 2022) is adopted to represent the soil-structure interaction. The total number of elements and nodes used in each PLAXIS, S2M and EQFdc model are presented in Table 8.1 to emphasise the relative size of the models.

8.2 Problem Definition

The tunnel-soil-building interaction problem used in this chapter is identical to the one presented in Chapter 7. However, the material properties used for the masonry and the soil differ from those in the previous chapter.

Table 8.1: Comparisons between the PLAXIS, the S2M and the EQFdc models in terms of the number of elements and nodes.

	Description	Total number
PLAXIS model (Sangirardi, 2023)	Elements	66278
	Nodes	106399
S2M model (Burd et al., 2022)	Elements	2924
	Nodes	5997
EQFdc model	Elements	304
	Nodes	241

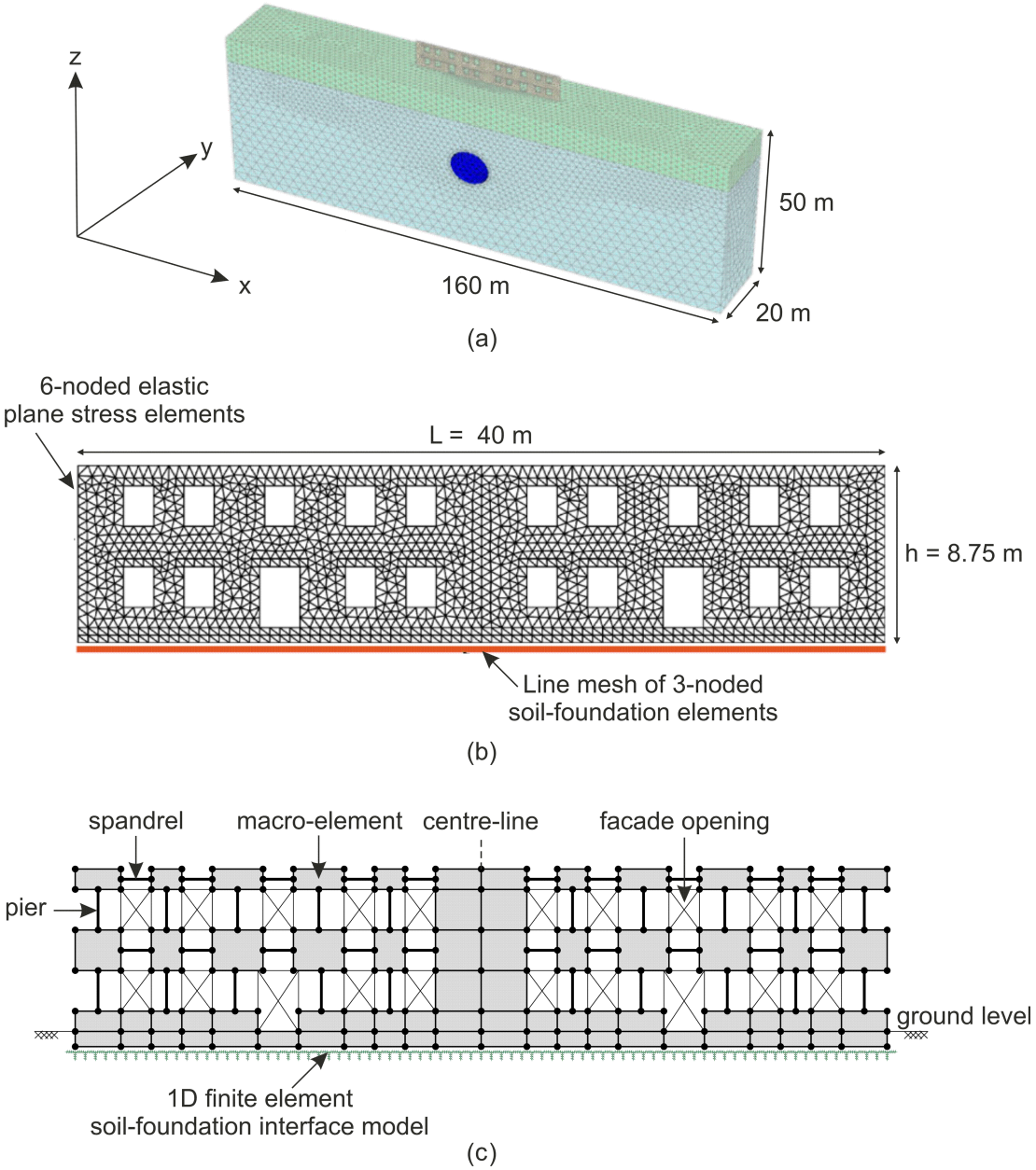


Figure 8.1: Comparison of modelling complexities: (a) PLAXIS model (Amorosi and Sangirardi, 2021; Sangirardi, 2023), (b) S2M model (Burd et al., 2022), (c) EQFdc model.

8.2.1 Building and tunnel configuration

The PLAXIS model generated by Amorosi and Sangirardi (2021) adopts the tunnel-soil-structure configuration in Figure 7.1. Only the isolated façade with single-step tunnel excavation (placed orthogonal to the façade) analyses with varying tunnel eccentricity scenarios, e where $0 \leq e \leq 25$ m, are used for the model comparisons in this chapter.

8.2.2 Loading scenario

The single tunnel excavation parameters are the same as given in Table 7.2. Similar to Yiu et al. (2017a), Amorosi and Sangirardi (2021) simulated the single-step tunnel excavation under undrained conditions, which only simulate short-term effects. The greenfield displacements determined from the PLAXIS analysis at the foundation base ($z = -1.0$ m) are provided by Sangirardi (2023) to be used to define the greenfield displacements in the soil-foundation interaction model.

8.2.3 Masonry material properties: EL façade

Masonry properties are separated into two cases. Firstly, the masonry façade is modelled as linear elastic (EL façade) in addition to the footing and lintel elements, which are defined with the elastic properties of the masonry for both cases. The material properties used for the façade and the footing are given in Tables 8.2 and 8.3, respectively. Amorosi and Sangirardi (2021) used the Young's modulus of the masonry as 0.8 GPa instead of 3.0 GPa (as employed by Yiu et al. (2017a), which was also adopted in the linear elastic analyses in Chapter 7) to match the vertical displacements computed from the PLAXIS model with the ones determined by Yiu et al. (2017a).

8.2.4 Masonry material properties: NL façade

Masonry material properties required for the nonlinear façade (NL façade) model is given in

Table 8.2 in addition to the elastic properties of the masonry. The NL façade properties required for the PLAXIS and the EQFdc models are presented separately in Table 8.2 since the PLAXIS model employs the JMM (i.e. jointed masonry model) directly (Section 2.4.3.2), whereas the EQFdc model incorporates separate nonlinear models (Chapter 6) to mimic the JMM.

Table 8.2: Masonry façade parameters for the JMM (adopted from the PLAXIS model by Amorosi & Sangirardi, 2021 and Sangirardi, 2023).

	Parameter	Value
EL façade	Unit weight, γ_m	23.75 kN/m^3
	Young's modulus, E_m	0.8 GPa
	Poisson's ratio, ν_m	0.20
NL façade: PLAXIS model (in addition to EL façade parameters)	Block aspect ratio, b/a	2
	Joints friction angle, φ_i'	30°
	Joints cohesion, $c_{0,i}$	0.14 MPa
	Contribution of tensile strength on head joints, $\sigma_{t0,1}$	0.10 MPa
NL façade: EQFdc model (in addition to EL façade parameters)	Block aspect ratio, b/a	2
	Friction angle for all elements, φ_i'	30°
	Cohesion for all elements, $c_{0,i}$	0.14 MPa
	Tensile strength of the spandrels, $\sigma_{T,s}$	0.24 MPa
	Tensile strength of the piers, $\sigma_{T,p}$	0.10 MPa
	Tensile strength of the vertical interfaces, $\sigma_{T,Vint}$	0.24 MPa
	Tensile strength of the horizontal interfaces, $\sigma_{T,Hint}$	0.10 MPa

8.2.5 Soil and foundation properties

The soil profile used in this case study is the same as indicated in Figure 7.1, where an 8 m Terrace gravel deposit (assumed to be dry) is placed over London clay soil (Yiu et al., 2017a). The parameters used for the strip footing and the Terrace gravel soil adopted are given in Table 8.3.

Amorosi and Sangirardi (2021) used the Hardening Soil model with small strain stiffness, HSsmall, (Schanz et al., 1999; Benz et al., 2009) as a nonlinear constitutive model for both soil layers in the PLAXIS model. The soil parameters (in addition to Table 8.3) required to describe the HSsmall soil behaviour can be found in the study of Amorosi and Sangirardi (2021). The

implementation of soil-foundation interaction models for the PLAXIS and the EQFdc models are described separately in the following sections.

Table 8.3: Strip footing and surrounding Terrace gravel soil parameters adopted from Amorosi and Sangirardi (2021).

	Parameter	Value
Footing	Unit weight, γ_f	19.50 kN/m^3
	Young's modulus, E_f	0.8 GPa
	Poisson's ratio, ν_f	0.20
	Footing thickness, h_f	0.50 m
	Footing depth, d_f	1.0 m
	Footing width, b_f	1.0 m
Terrace gravel	Unit weight, γ_s	19.50 kN/m^3
	Lateral earth pressure coefficient, K_0	0.425
	Effective friction angle, φ'	35°

8.3 PLAXIS Model Implementation

8.3.1 Building model

3D finite elements comprising 10-noded tetrahedral elements with 4-integration points (based on second-order interpolation of displacements) are used to model the façade in the PLAXIS model (Amorosi & Sangirardi, 2021).

8.3.1.1 Building model: EL façade

For the EL façade analyses, the façade is modelled using the elastic masonry properties given in Table 8.2.

8.3.1.2 Building model: NL façade

For the NL façade analyses, the façade is modelled with the JMM (Section 2.4.3.2). The parameters are given in Table 8.2.

8.3.2 Soil-foundation interface model

The soil-foundation interface model presented by Amorosi and Sangirardi (2021) is modified to be consistent with the S2M soil-foundation interaction modelling approach (Burd et al., 2022). For this purpose, the frictional interface elements are placed around the strip footing and the embedded portion of the façade under the ground level as shown in Figure 8.2(b) (Sangirardi et al., 2023). This represents a modification to the study of Amorosi and Sangirardi (2021), where the frictional interface was only placed between the footing base and the soil elements. The interface friction coefficient and the friction angle used at the embedded façade are given in Table 8.4.

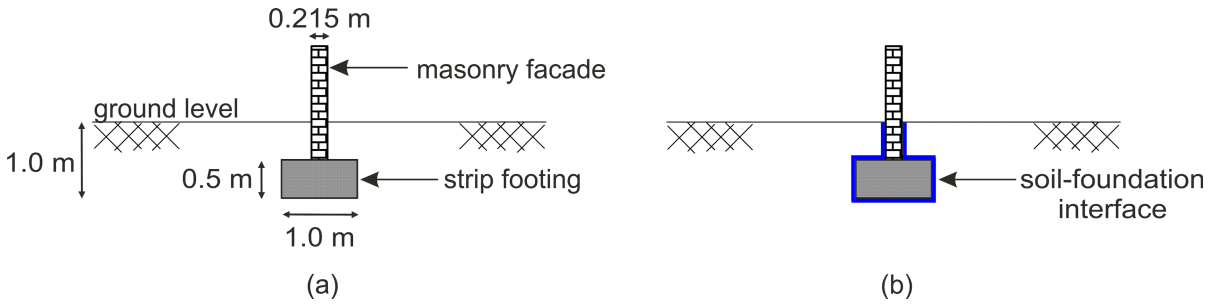


Figure 8.2: Schematic details of the soil-foundation interaction in the PLAXIS model: (a) strip footing, (b) soil-foundation interface elements (modified from Sangirardi et al., 2023).

8.3.3 Analysis procedure

A single-step tunnel excavation is conducted in the PLAXIS model (Amorosi & Sangirardi, 2021). First, the soil elements are activated to generate the geostatic stress conditions. The soil elements within the foundation volume are deactivated and followed by the activation of the strip footing and soil-foundation interface elements. In this case, since the unit weights of Terrace gravel and the foundation are the same (defined as identical in the case study for convenience), no additional external loads are imposed on the system due to the construction of the foundation. Later, the masonry façade is built, which corresponds to the self-weight loading in the analysis. The displacements and strains associated with the self-weight loading

are set to zero before simulating the tunnel excavation to consider only the effects of tunnel construction in the damage estimation process. Thus, all the building responses determined from the PLAXIS model only refer to the effect of tunnelling in this chapter (Sangirardi, 2023).

8.4 S2M Model Implementation

The S2M model (Burd, 2023) refers to the S2M soil-foundation interaction model employed for a 2D FE façade model as the modelling concept (Section 2.5.2.1) developed by Burd et al. (2022).

8.4.1 Building model

The S2M model analyses are only conducted for the EL façade cases, in this chapter. Thus, the elastic masonry properties given in Table 8.2 are used for the 2D FE façade in the S2M model (Burd, 2023).

8.4.2 S2M soil-foundation interaction model

The parameters used in the S2M soil-foundation interaction model to mimic the nonlinear soil behaviour defined in the PLAXIS model are presented in Table 8.4 in addition to the strip footing details given in Table 8.3.

8.4.3 Calibration analyses for the S2M soil-foundation interaction model

It is important to mimic the nonlinear soil behaviour used in the PLAXIS model by the S2M soil-foundation interaction model. To determine suitable parameters for the S2M soil-foundation interaction model, simple calibration analyses are conducted on the nonlinear soil used in the PLAXIS model by Sangirardi et al. (2023). Specifically, the calibration analyses are required to determine: i) vertical soil stiffness, k_v and softening parameter, a_v which

governs the nonlinear normal traction behaviour of the soil and ii) horizontal soil stiffness, k_h to define the shear behaviour of the soil in the S2M soil-foundation interaction model (Burd et al., 2022). The parameters determined from the calibration analyses performed in PLAXIS are given in Table 8.4 (Sangirardi et al., 2023). The limiting uplift resistance, p_t = 13.2 kN/m is adopted from Burd et al. (2022) (Table 8.4). Further details for the procedures employed in the calibration analyses can be found in Sangirardi et al. (2023).

Table 8.4: The parameters used in the S2M soil-foundation interaction model determined from the calibration analyses conducted in PLAXIS by Sangirardi et al. (2023).

	Parameter	Value
Soil-foundation interface	Horizontal soil stiffness, k_h	5 MPa
	Vertical soil stiffness, k_v	12 MPa
	Softening parameter, a_v	5 m^{-1}
	Limiting uplift resistance, p_t	13.2 kN/m
	Interface friction coefficient, μ_s	0.35
	Frictional interface angle at the embedded façade, φ	30°

8.4.4 Analysis procedure

The analysis procedure employed for the S2M modelling approach (Burd et al., 2022) is reviewed in Section 2.5.2.1. The analysis starts with the application of the self-weight of the façade and followed by the implementation of the prescribed greenfield displacements to the S2M soil-foundation interaction model (Burd et al., 2022). To conduct the S2M model analyses (Burd, 2023) presented in this chapter, the parameters given in Tables 8.2−8.4 are used and greenfield displacements determined at the foundation base of the PLAXIS model ($z = -1.0$ m) (Sangirardi, 2023) are imposed to the S2M soil-foundation interaction model as prescribed deformations (Burd, 2023).

8.5 EQFdc Model Implementation

8.5.1 Building model

The EQFdc model geometric idealisation of the specified problem is same as that presented in Figure 7.3. The procedures described in Section 7.4.1 for the geometrical representation of the EQFdc building model also applies for this chapter.

8.5.1.1 Building model: EL façade

For the EL façade analyses, the façade is modelled using the elastic properties of the masonry given in Table 8.2.

8.5.1.2 Building model: NL façade

The nonlinear constitutive models employed for the beams, quads and structural interface elements are described in Sections 6.2 and 6.3. Specifically, the parallel Iwan model is defined as elastic-perfectly plastic and the series Iwan model is formulated in elastoplastic behaviour with linear hardening by defining the plastic slope as 1% of the elastic slope. Since the shear force is the input and the shear strain is the output in the series Iwan model, to determine unique shear strain data, linear hardening behaviour is employed after reaching the shear plasticity limit. Otherwise, convergence problems are typically observed in the beam element level iterations (Section 4.3) for the elastic-perfectly plastic yielding condition due to increasing shear strain values during iterations.

The parameters required to calculate the tensile strengths of spandrels, $\sigma_{T,s}$ and piers, $\sigma_{T,p}$ (Section 6.2.1.2) are adopted from Amorosi and Sangirardi (2021), where the tensile strength of head and bed joints, $\sigma_{t0,1}$ and the cohesion, $c_{0,i}$ are given as 0.10 MPa and 0.14 MPa respectively together with a block aspect ratio, b/a of 2. The tensile strength of the spandrels and piers are determined as 0.24 MPa and 0.10 MPa according to Equation (6.1).

In the JMM, shear behaviour is modelled as coupled with the tensile strength of the masonry (Lasciarrea et al., 2019). Thus, the interlocking effect in the head joints also causes an artificial increase in the cohesion (Equation 2.11). However, in the EQFdc model, the shear behaviour of a beam element is decoupled from its fibre beam behaviour. Therefore, the interlocking effect for the cohesion of the head joints is eliminated in the EQFdc model, which results in assigning the same cohesion value to the spandrels and the piers (Section 6.2.2.2).

It is important to note that the lintels (corresponding to the particular fibre elements of the spandrels) in the EQFdc model are modelled as elastic in the NL façade case.

The determination of the tensile and shear strengths for the beam, quad and structural interface elements in the EQFdc model are described in Sections 6.2.1.2, 6.2.2.2, 6.3.1.2 and 6.3.2.2. The nonlinear masonry façade parameters required for the EQFdc model are given in Table 8.2. The nonlinear constitutive models used for the structural elements in the EQFdc model are summarised in Table 8.5.

Table 8.5: Nonlinear constitutive models used for the structural elements in the EQFdc model.

	Modelling method	Constitutive model
Fibre beam model	Parallel Iwan	Elastic – perfectly plastic yielding only in tension
Beam shear model	Series Iwan	Elastoplastic behaviour with linear hardening (1% plastic slope), yielding in both shear directions
Quad shear model	Parallel Iwan	Elastic – perfectly plastic yielding in both shear directions
Normal interface model	Parallel Iwan	Elastic – perfectly plastic yielding only in tension

8.5.2 S2M soil-foundation interaction model

The S2M modelling approach (Burd et al., 2022) is implemented into the EQFdc model to represent the soil-foundation behaviour. The parameters used for the soil-foundation interface

elements in the EQFdc model are presented in Table 8.4 and the strip footing is modelled as elastic with the parameters given in Table 8.3 for the specified geometry.

8.5.3 Analysis procedure

The loads are applied to the EQFdc model in two stages. Firstly, the self-weight of the façade is applied to the system for the quad and beam elements. Then, the greenfield displacements at the foundation base of the PLAXIS model ($z = -1.0$ m) (Sangirardi, 2023) are applied as prescribed deformations to the S2M soil-foundation interaction model implemented into the EQFdc model.

8.6 Results Data Processing

The results from the EL and NL façade analyses are processed in terms of building displacements at the nodes of the footing elements and the major principal tensile strains, ε_1, at the Gauss points of the façade elements for both the PLAXIS and the EQFdc models. The footing level refers to a depth of $z = -1.0$ m for the PLAXIS model and $z = -0.75$ m (corresponds to the centre of strip footing) for the S2M and the EQFdc models. Plastic points determined on the façade are also presented for the NL façade analyses. For both EL and NL façade cases, the self-weight loading-induced displacements and strains are subtracted from the total displacements and strains computed at the end of the analyses to emphasise the effect of only greenfield displacements on the structural response.

8.6.1 PLAXIS model

Similar to the discussion presented in Section 7.5.1, the PLAXIS model requires an additional procedure for the interpretation of the major principal tensile strain for elastic building analyses. Accordingly, the radius search method (Section 7.5.1) is employed for the PLAXIS model. The radius search is performed within a 0.4 m radius. However, in this case, a volume

limit criterion is employed for the PLAXIS model instead of defining an area limit in the radius search method since the 3D finite elements are used for the façade. Considering the façade thickness of 0.215 m, the volume limit is set as 0.215 m^3, which corresponds to the volumetric representation of a 1.0 m^2 area limit.

The maximum major principal tensile strains determined before and after applying the radius search method are presented in Figure 8.3. The radius search method significantly reduces the sharp corner effect in the continuum model and highlights the maximum strain that occurs in the rest of the façade. It is important to note that the volume of the removed Gauss points does not exceed 0.4% of the total façade volume in all analyses.

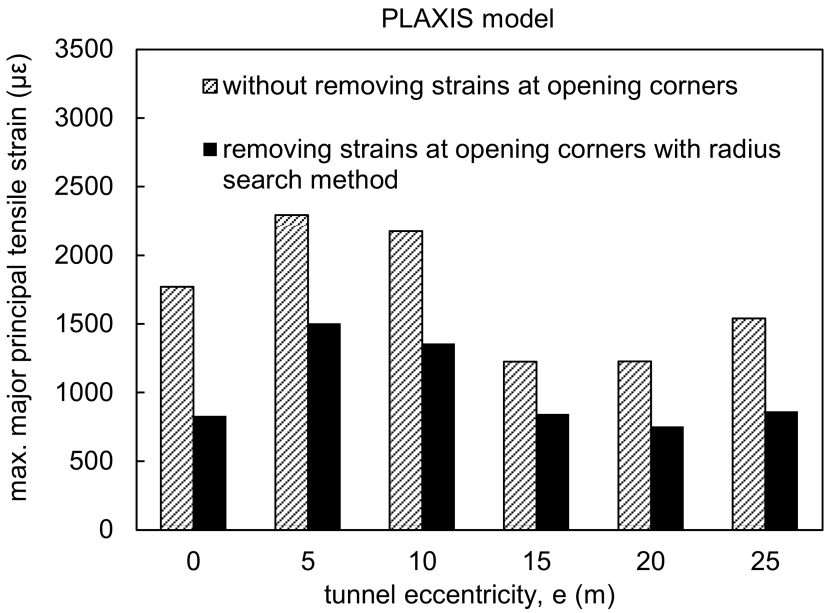


Figure 8.3: Maximum major principal tensile strains in the PLAXIS model with and without removing the strains at the opening corners.

8.6.2 S2M model

Only the building displacements (i.e. induced by the greenfield displacements) computed at the footing elements ($z = -0.75$ m) of the S2M model are presented as part of the EL façade analyses comparisons.

8.6.3 EQFdc model

The EQFdc model does not require a strain removing method as employed for the FE continuum models to determine the maximum major principal tensile strain. For the calculation of the major principal tensile strain distributions in the beam elements (Section 3.6.2), the shear strain results are processed according to the parabolic shear strain distribution principle for the elastic façade cases. However, parabolic shear strain calculations are not applicable for the nonlinear beam models. Thus, the constant shear strain results determined at the end of the EQFdc analysis are used directly in the major principal tensile strain distribution plots for the nonlinear façade cases.

8.7 Results and Comparisons: EL façade

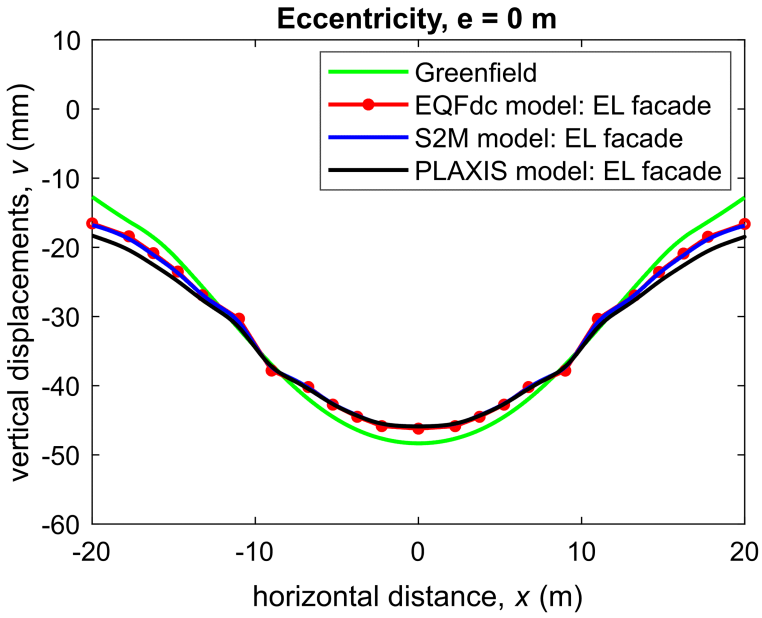
8.7.1 Displacement responses

The façade displacements at the footing level determined from the EQFdc model are compared to the results from the PLAXIS (Sangirardi, 2023) and the S2M models (Burd, 2023).

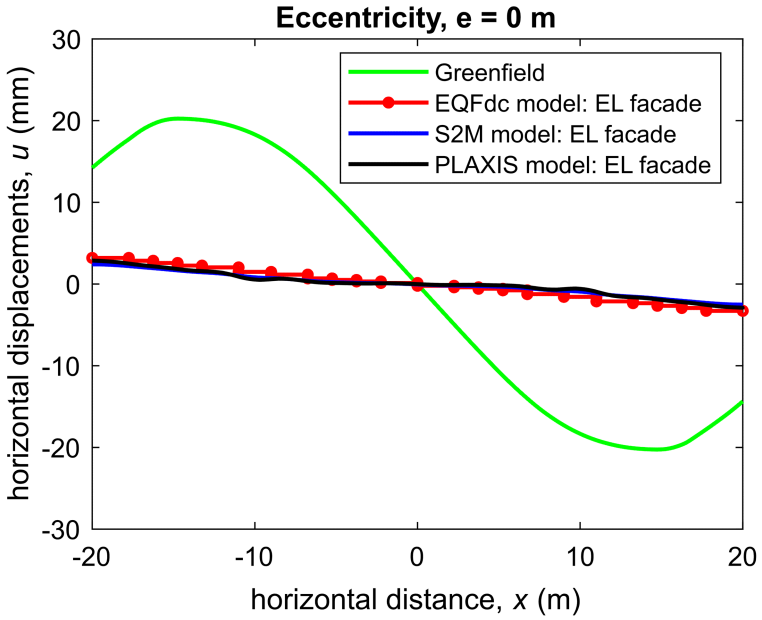
The vertical and horizontal displacements computed at the footing levels for the central tunnel case ($e = 0$) are plotted in Figure 8.4. The EQFdc and S2M model results match well in terms of vertical and horizontal displacement responses. This shows the success of the EQFdc model in simulating the 2D FE continuum façade behaviour by adopting the same soil-foundation modelling approach developed by Burd et al. (2022).

The S2M model demonstrates a good agreement with the PLAXIS displacement responses overall, for the central tunnel scenario (Figure 8.4). For the vertical displacements, the EQFdc model and the S2M model match closely at the façade centre with the PLAXIS results (Figure 8.4a). A slight difference is observed at the ends of the foundation (where $15\ \text{m} \leq x \leq 20\ \text{m}$ and $-20\ \text{m} \leq x \leq -15\ \text{m}$), in which both EQFdc and S2M models demonstrate smaller

displacements than the PLAXIS model. This is likely due to the stiffening effect of façade corners, which is not considered by S2M. For the horizontal displacements, all three models (PLAXIS, S2M and EQFdc) present almost the same results (Figure 8.4b).



(a)



(b)

Figure 8.4: Comparison of façade displacements at the foundation level ($z = -1.0$ m for the PLAXIS model and $z = -0.75$ m for the S2M and the EQFdc models) for the EL façade analysis (greenfield displacements determined at $z = -1.0$ m from the PLAXIS model are employed as inputs to the soil-foundation interaction models in the S2M and EQFdc analyses): (a) vertical displacements, (b) horizontal displacements.

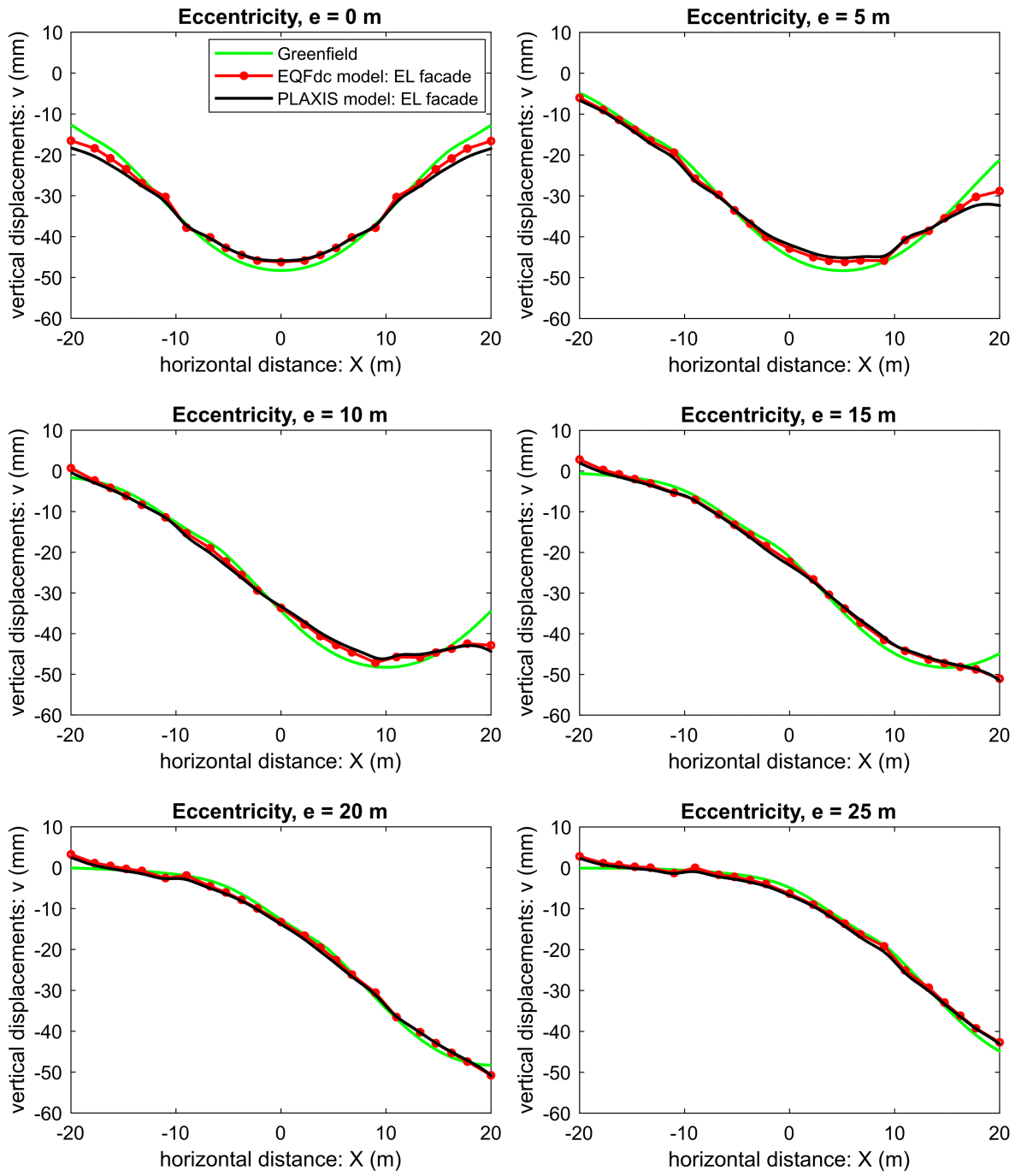


Figure 8.5: Façade vertical displacements at the foundation level induced by the greenfield displacements only for the EL façade analysis.

Comparisons for the vertical displacement responses of the façade is extended to tunnelling scenario with varying eccentricities, $e \in [0, 25]$ m. In this case, the vertical displacements in the EQFdc model are only compared with the PLAXIS model results, as shown in Figure 8.5. The EQFdc model successfully simulates the vertical displacement responses determined at the

foundation level of the PLAXIS model for all tunnel eccentricity conditions that have been considered.

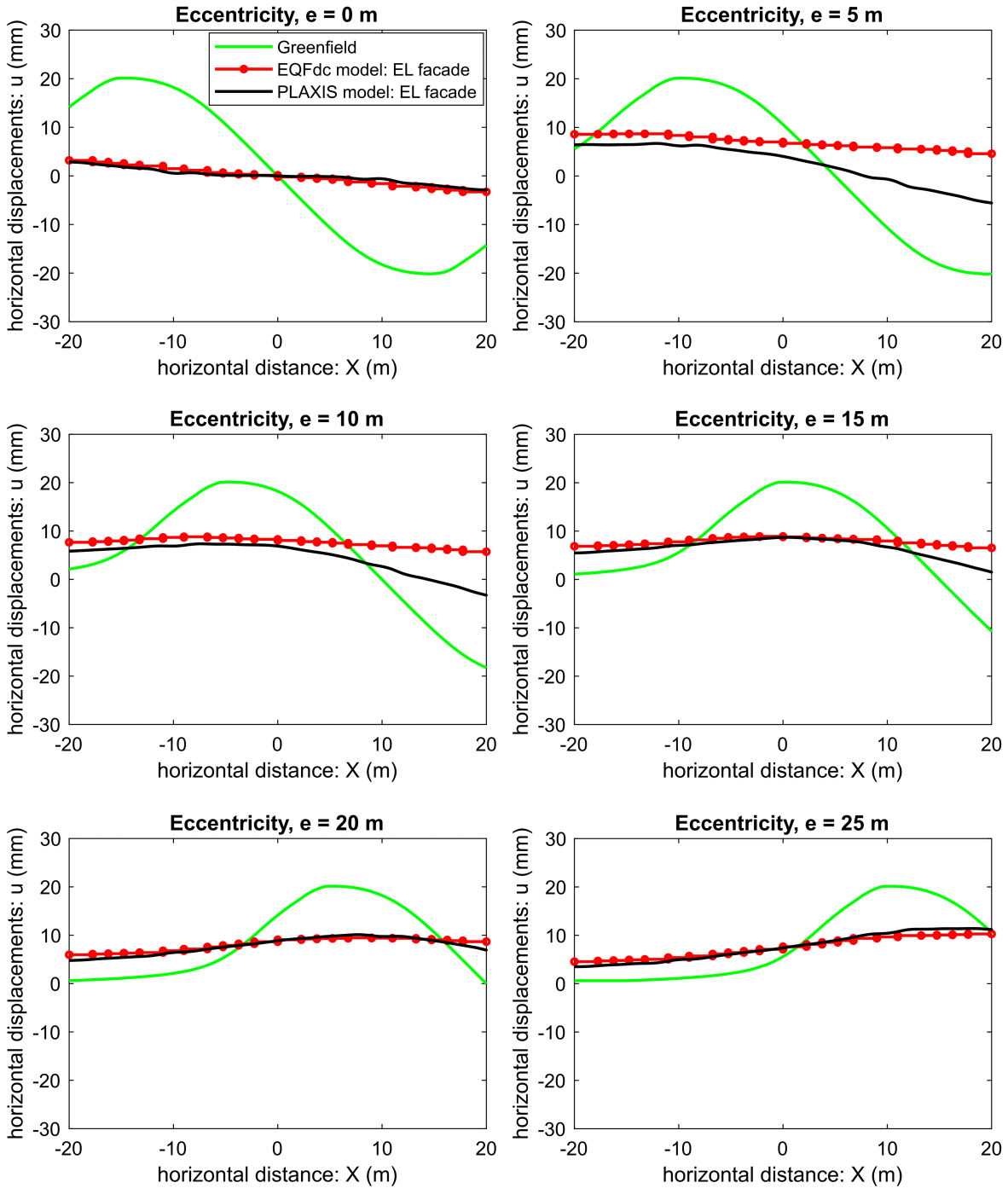


Figure 8.6: Façade horizontal displacements at the foundation level induced by the greenfield displacements only for EL façade analysis.

The horizontal displacements determined at the footing levels of the PLAXIS and EQFdc

models at each tunnel eccentricity are presented in Figure 8.6. While the horizontal displacements computed from the EQFdc model match well with the PLAXIS results for the eccentricities of $e = 0$, 20 m and 25 m, significant differences are observed between the model responses at the tunnel eccentricities between $e \in [5, 15]$ m, where the horizontal greenfield displacement is around -20 mm at the façade corner.

To understand whether this difference in the horizontal displacements is caused by the EQFdc model idealisation or the adopted soil-foundation interaction model, the footing displacement responses are additionally compared with the S2M model performed by Burd (2023) in Figure 8.7. The horizontal footing displacement comparison between the models for $e = 5$ m is shown in Figure 8.7. The difference between the EQFdc and PLAXIS horizontal displacements is significant. It is observed that the S2M model demonstrates almost the same horizontal displacements as the EQFdc model, which suggests that the difference with the PLAXIS model is caused by the implemented S2M soil-foundation interaction model used in the EQFdc model rather than the structural modelling approach.

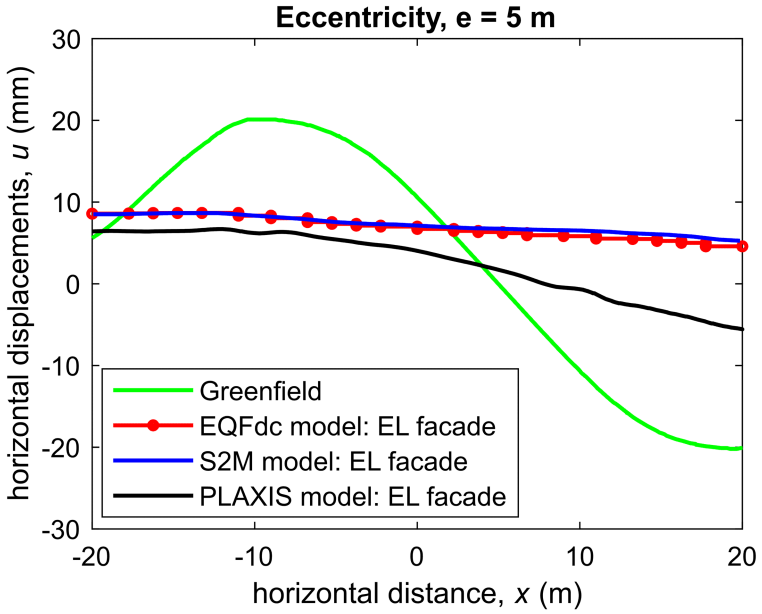


Figure 8.7: Façade horizontal displacements at the foundation level for the EL façade analysis.

This result highlights that the S2M soil-foundation interaction model needs further improvements to capture the horizontal displacements accurately (see Section 10.3.5). Currently, it underestimates the horizontal displacement response of the façade (Figure 8.6), specifically at the right corner of the façade ($X = 20$ m) for the tunnel eccentricities, $e = 5$ m and 10 m. This façade corner, where $X = 20$ m in Figures 8.6 and 8.7, experiences significant negative horizontal strain (the horizontal greenfield displacement is approximately -20 mm) for $e = 5$ m and 10 m. This can be explained by the stiffening effect of façade corners, which is not considered in the current S2M soil-foundation interaction model (Burd et al., 2022), which is shown to restrict the façade to demonstrate lower horizontal displacements than the PLAXIS model. Potential improvements for the S2M soil-foundation interaction model will be discussed briefly in the conclusion chapter. However, this is not within the main objectives of this thesis.

8.7.2 Major principal tensile strain responses

The major principal tensile strain, ε_1 contours for the EQFdc and PLAXIS models, are presented for the central tunnel scenario (Figure 8.8) and the eccentric cases at $e = 5$ m and $e = 20$ m (Figure 8.9). The strain contour levels are presented in discrete intervals. For the central tunnel case, the EQFdc model (Figure 8.8) captures the overall frame-like behaviour observed in the major principal tensile strain distributions of the PLAXIS model. In the EQFdc model (Figure 8.8), the major principal strains are mostly concentrated at the first-storey piers, especially at the elements next to the doors and at the spandrels over the door openings, where diagonal shear dominant behaviour is observed. According to the overall strain distributions, the highest strain falls into the contour boundaries of [750, 900] $\mu\varepsilon$ for the EQFdc model. However, strains in excess of 1500 $\mu\varepsilon$ can be observed around the corners of the openings at the first storey of the PLAXIS model due to the sharp corner effects.

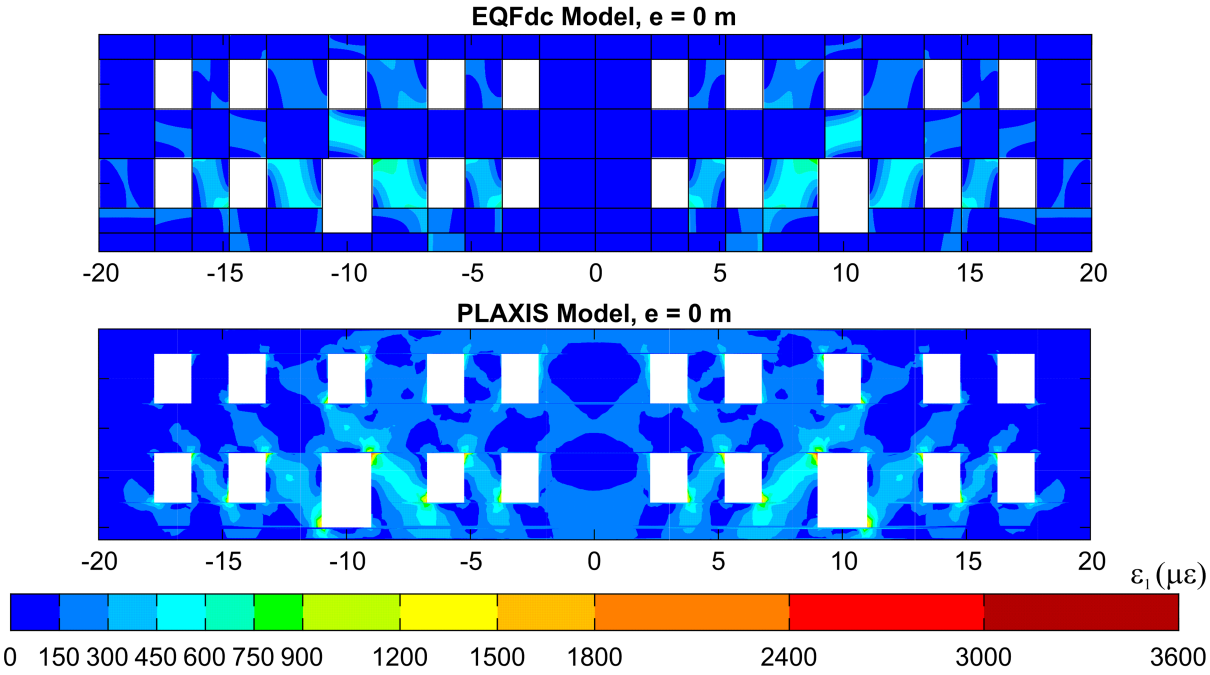


Figure 8.8: Major principal tensile strain contour plot comparisons between the EQFdc and PLAXIS models for the EL façade analysis, $e = 0$.

In Figure 8.9(a), the major principal tensile strain distributions are plotted for $e = 5$ m. According to the PLAXIS model results, the potential damage is concentrated, especially at the piers next to the doors at the first storey elements at the horizontal distances, where 7 m $\leq x \leq$ 16 m. For this tunnel eccentricity, the influence of the opening layout on the distribution of potential damage is evident. For the PLAXIS model for $e = 5$ m, the maximum tensile strain lies in the range [1800, 2400] $\mu\varepsilon$ before applying strain removing with the radius search method. In contrast, the EQFdc model indicates high strain concentrations in the range [1200, 1500] $\mu\varepsilon$ around the door openings for $e = 5$ m and it can still identify the pier and spandrel elements that experience high strains in the PLAXIS model (Figure 8.9a). However, the low-magnitude strains observed in particular structural components are expected since the soil-foundation interaction modelling approach used in the EQFdc model does not accurately capture the horizontal displacement behaviour of the façade for this eccentricity case, $e = 5$ m, as indicated in Figure 8.7.

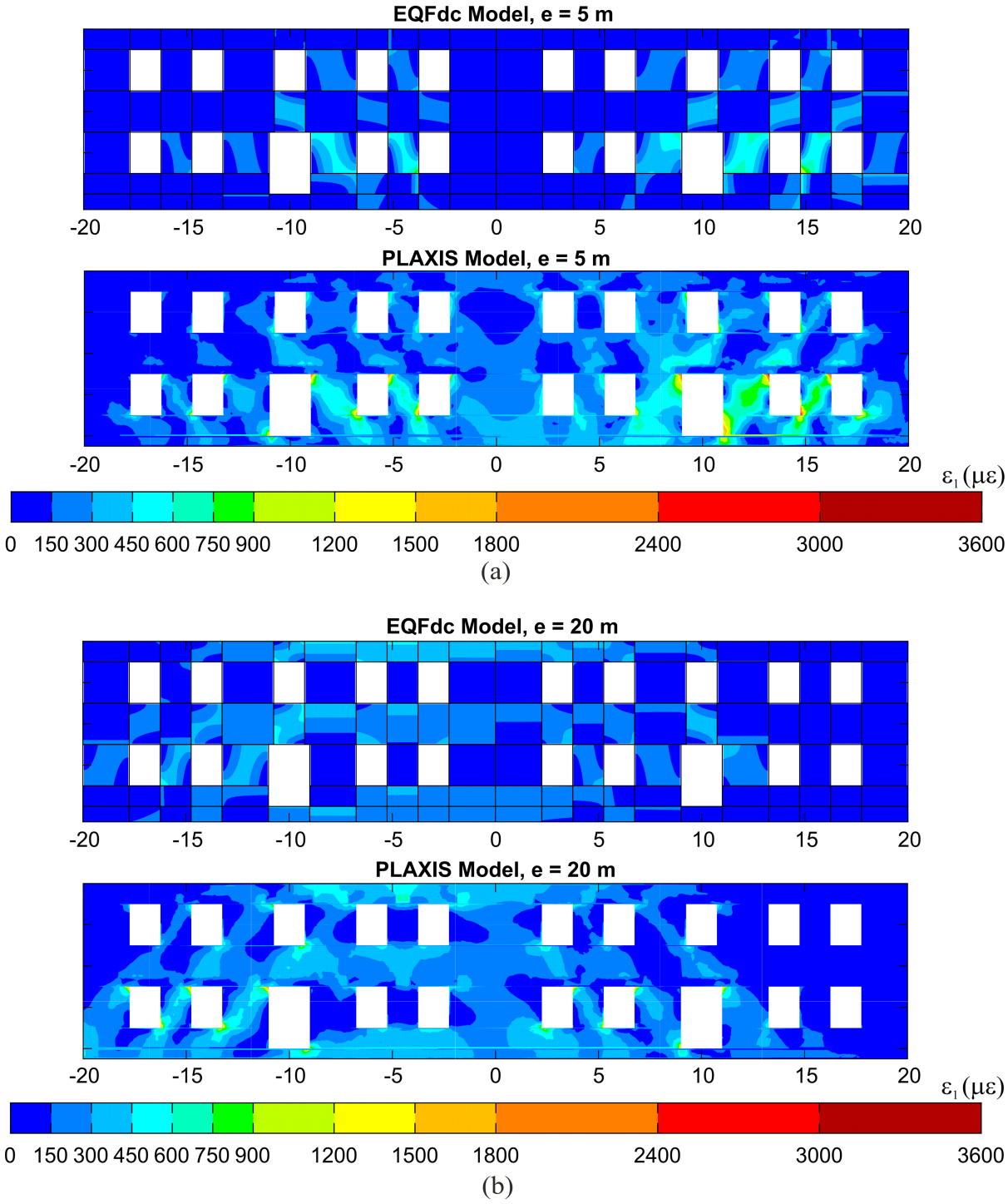


Figure 8.9: Major principal tensile strain contour plot comparisons between the EQFdc and PLAXIS models for the EL façade analysis: (a) $e = 5$ m, (b) $e = 20$ m.

The major principal tensile strain contours for $e = 20$ m are plotted in Figure 8.9(b). According to the PLAXIS model results, large strains are observed in the second storey spandrels and macro-elements over the openings and the piers at the first storey for $-16 \text{ m} \leq x \leq -11 \text{ m}$.

The EQFdc model also captures the strain distributions at the first and second storey spandrels and macro-elements.

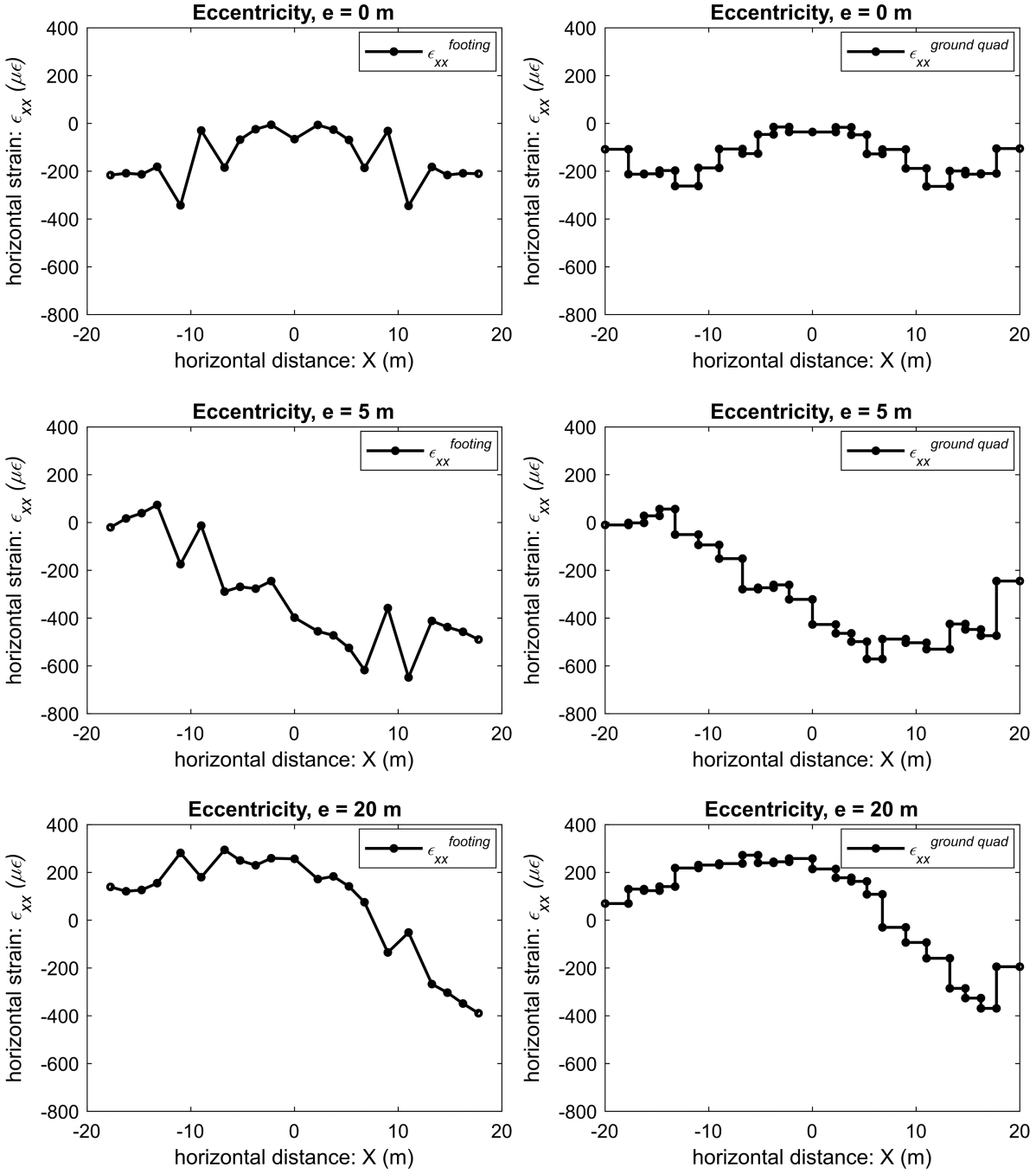


Figure 8.10: Horizontal strains computed at the nodes of footing and ground quad elements in the EQFdc model (with stiff soil and PLAXIS footing displacements) for the EL façade analysis for $e = 0$, $e = 5$ m and $e = 20$ m.

To investigate further the potential impact of the horizontal strain, ε_{xx}, transfer from the footing elements ($\varepsilon_{xx}^{footing}$) to the ground quad elements (ε_{xx}^{quad}), the PLAXIS footing

displacements are prescribed to the EQFdc model as an input deformation in place of the greenfield displacements. The soil-structure interaction is prevented by using stiff soil parameters in the soil-foundation interaction model. In this way, the EQFdc model reproduces the same footing displacement responses as the PLAXIS model. For this purpose, the horizontal footing displacements and the corresponding horizontal strains are computed at the nodes of footing and ground quad elements for $e = 0$, $e = 5$ m and $e = 20$ m (Figure 8.10).

Here, it is important to emphasise that while the horizontal strains at the footing nodes are calculated according to the relative displacements at the footing-footing interface elements (axial nodal springs) divided by the summation of half lengths of the adjacent footing elements, ε_{xx}^{quad} is computed by using the concept of partitioning the relative normal displacements at the vertical interfaces surrounding the ground quad elements as explained in Section 3.6.1. Additionally, since the horizontal and vertical strains within the macro-elements are generated only by the relative displacements at the surrounding interfaces, ε_{xx}^{quad} results show constant values along the x-axis of the quad element. Figure 8.10 demonstrates that the footing elements successfully transfer the horizontal strains to the ground quad elements since both $\varepsilon_{xx}^{footing}$ and ε_{xx}^{quad} plots represent similar trends for the ε_{xx} variations for the central and eccentric tunnel conditions.

The horizontal strain distributions are also evaluated by comparing the horizontal strain contours determined from the EQFdc (using stiff soil parameters and imposing PLAXIS footing displacements as input prescribed deformations) and PLAXIS models for the tunnel eccentricity for $e = 5$ m (Figure 8.11). Overall, horizontal strains, ε_{xx} computed from the EQFdc model compare well with the results from PLAXIS models. Note that the strain contour limits used in ε_{xx} contours differ from ε_1 contours presented earlier; compression strains are also plotted in Figure 8.11 to provide consistent comparisons with the values shown in Figure

8.10. The EQFdc model successfully reproduces the ε_{xx} distribution responses determined from the PLAXIS models (Figure 8.11). The compressive strain behaviour is shown to be dominant for $e = 5$ m, the compressive horizontal strains are concentrated at the first and second storey spandrel elements as well as the ground quad elements in the façade centre (Figure 8.11).

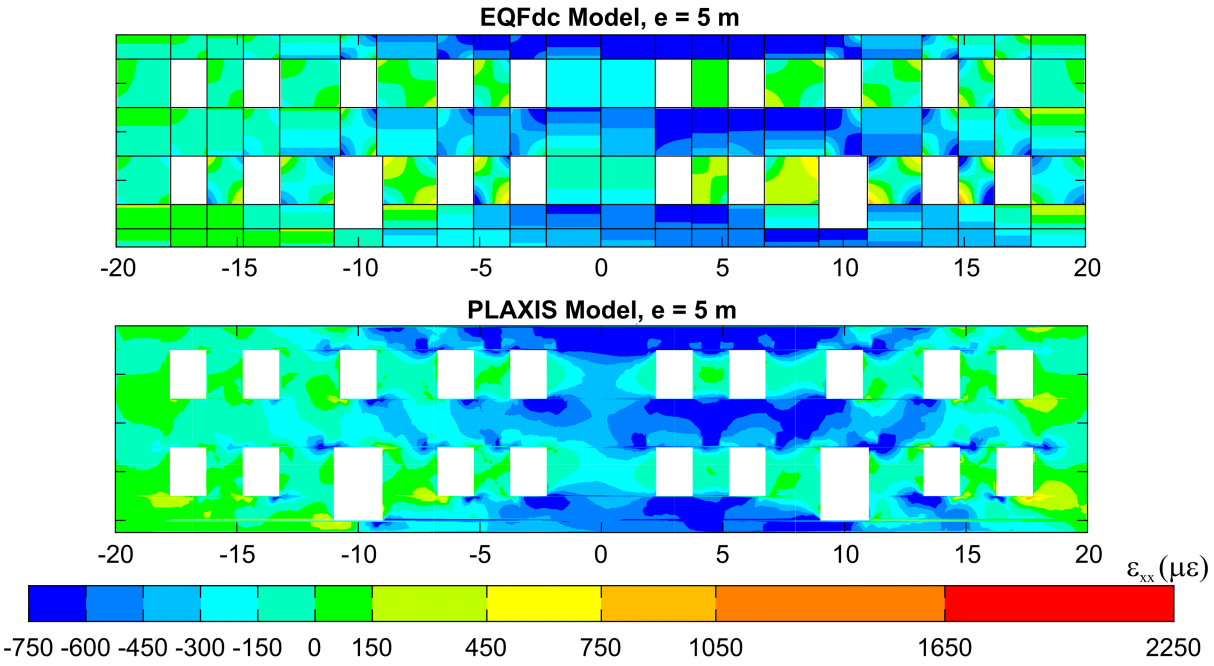


Figure 8.11: Horizontal strain contour plot comparisons between the EQFdc (with stiff soil and PLAXIS footing displacements) and PLAXIS models for EL façade analysis.

As a result of the horizontal strain comparisons, it can be concluded that the footing elements formulated in the EQFdc model can accurately transfer the horizontal strains to the ground quad elements. Also, the axial strain interpretations developed for the macro-elements can reproduce the horizontal strain distributions determined from the PLAXIS model.

The results determined from the EQFdc model are improved for the case of imposing the PLAXIS footing displacements. This is shown using the major principal tensile strain distributions obtained on the façade for $e = 5$ m (Figure 8.12). Overall, the major principal tensile strain response of the EQFdc model, which is determined by imposing the PLAXIS

footing displacements, presents better agreement with the PLAXIS results (Figures 8.12) compared to the EQFdc results determined when the greenfield displacements are imposed with the soil-structure interaction (Figure 8.9a).

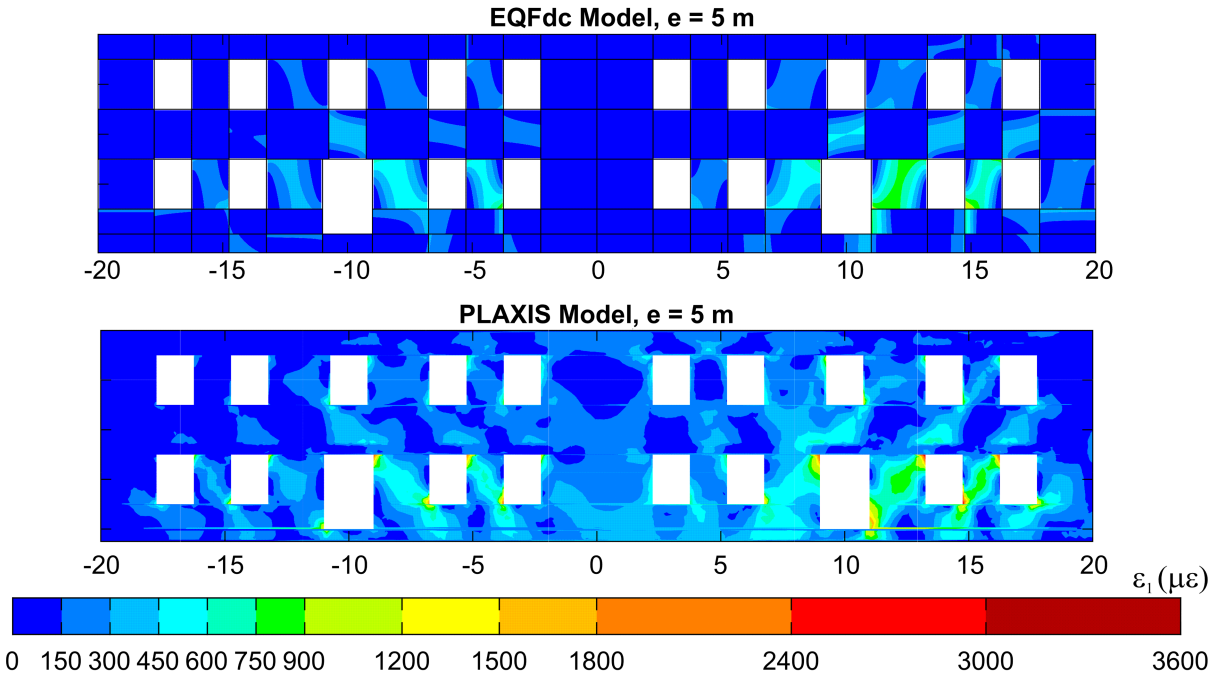


Figure 8.12: Major principal tensile strain contour plot comparisons between the EQFdc (with stiff soil and PLAXIS footing displacements) and PLAXIS models for the EL façade analysis.

8.7.3 Variation of maximum tensile strain with tunnel eccentricity

Figure 8.13 compares the maximum major principal tensile strains for the EQFdc and the PLAXIS models (after removing strains at opening corners with the radius search method). In addition to the original EQFdc model results (using greenfield displacements in the soil-structure interaction analysis), the results obtained by imposing the PLAXIS footing displacements into the EQFdc model with the stiff soil parameters are also presented in Figure 8.13 to show the changes obtained in the maximum major principal tensile strains. According to the standard building damage classifications (Burland & Wroth, 1974; Boscardin & Cording,

1989), the PLAXIS results mostly relate to the 'slight' damage class except for the case at $e =$ 5 m, in which the maximum strain is on the boundary of the 'moderate' damage class.

Overall, the original EQFdc model presents a similar strain variation trend to the PLAXIS model and although the magnitudes of the strains are slightly lower. The EQFdc model with the imposed PLAXIS footing displacements produced results that are closer to the PLAXIS model, especially for $e = 5$ m and $e = 10$ m, where the existing soil-foundation interaction model underestimates the horizontal displacements and leads to lower strains than the PLAXIS model. These findings suggest that with further improvements applied to the soil-foundation interaction model, the EQFdc model can successfully reproduce the PLAXIS model results.

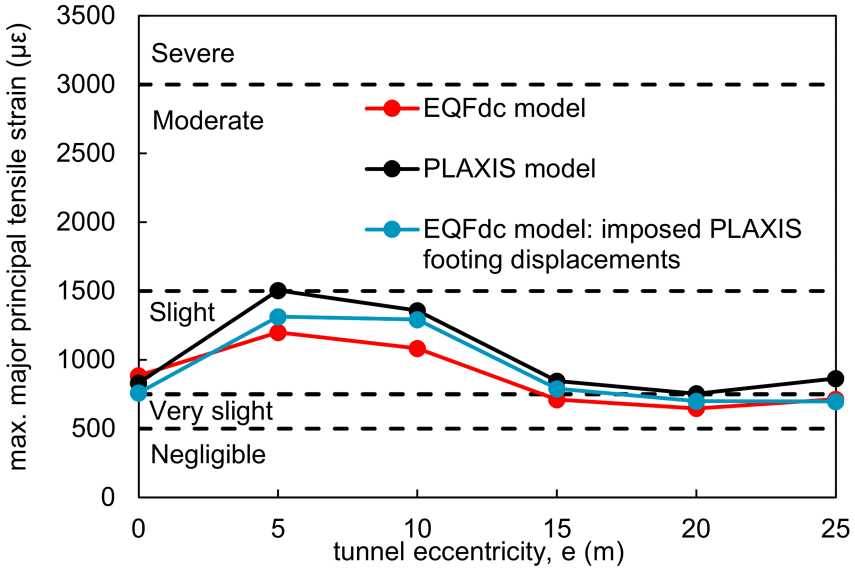


Figure 8.13: Comparison of the maximum major principal tensile strain variations with tunnel eccentricity for the EQFdc and PLAXIS models.

8.8 Results and Comparisons: NL façade

8.8.1 Displacement responses

Firstly, the vertical displacement responses of the façade at the footing level for the central and eccentric tunnel scenarios are presented in Figure 8.14. For the central tunnel case ($e = 0$), the EQFdc model successfully simulates the vertical displacement responses determined from the

PLAXIS model, especially at the façade centre, where the maximum displacement occurs. The difference in the vertical displacement responses becomes visible towards the ends of the façade, where 15 m $\leq x \leq$ 20 m and its symmetrical counterpart.

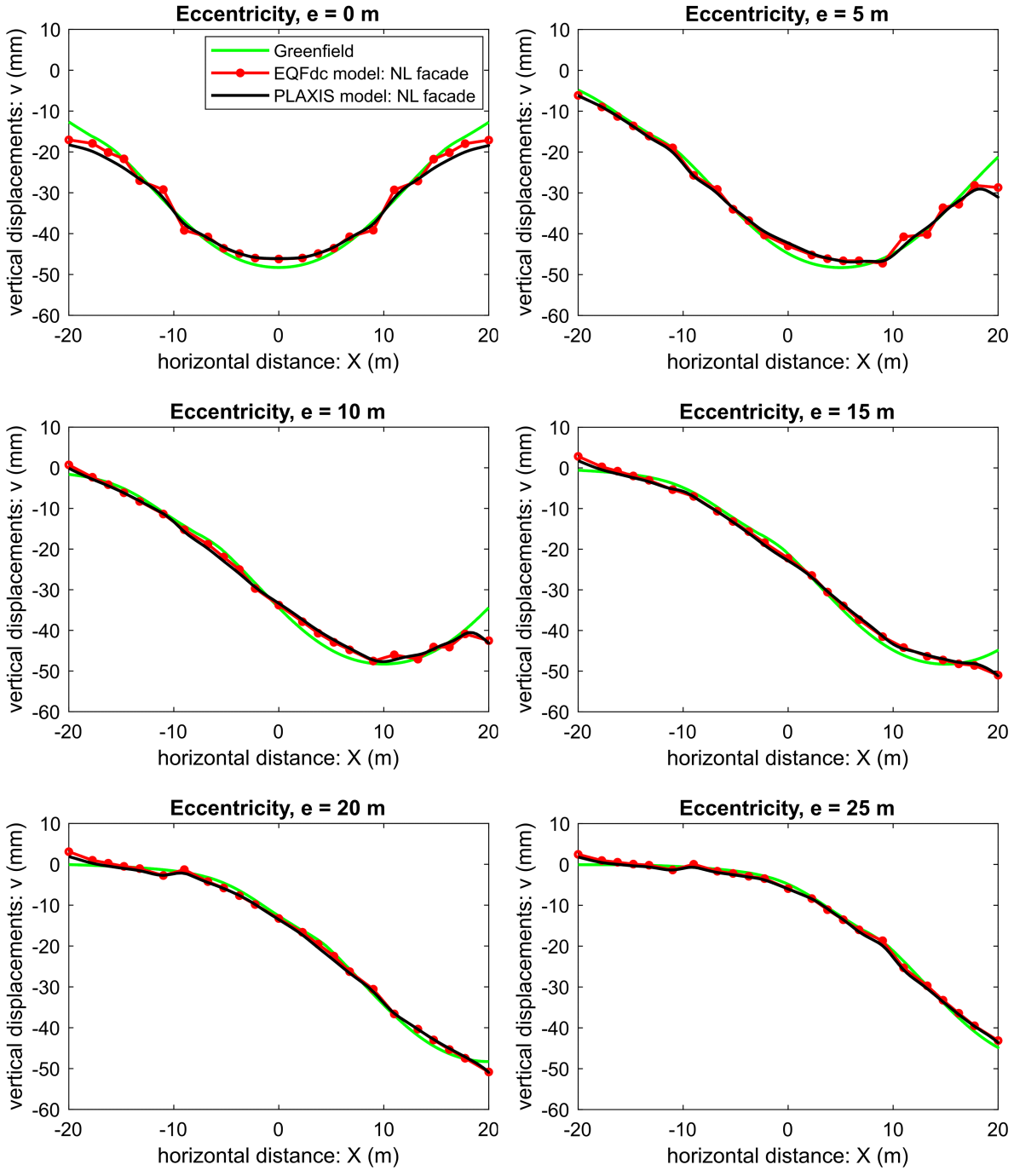


Figure 8.14: Façade vertical displacement responses at the foundation level induced by the greenfield displacements only for the NL façade analysis.

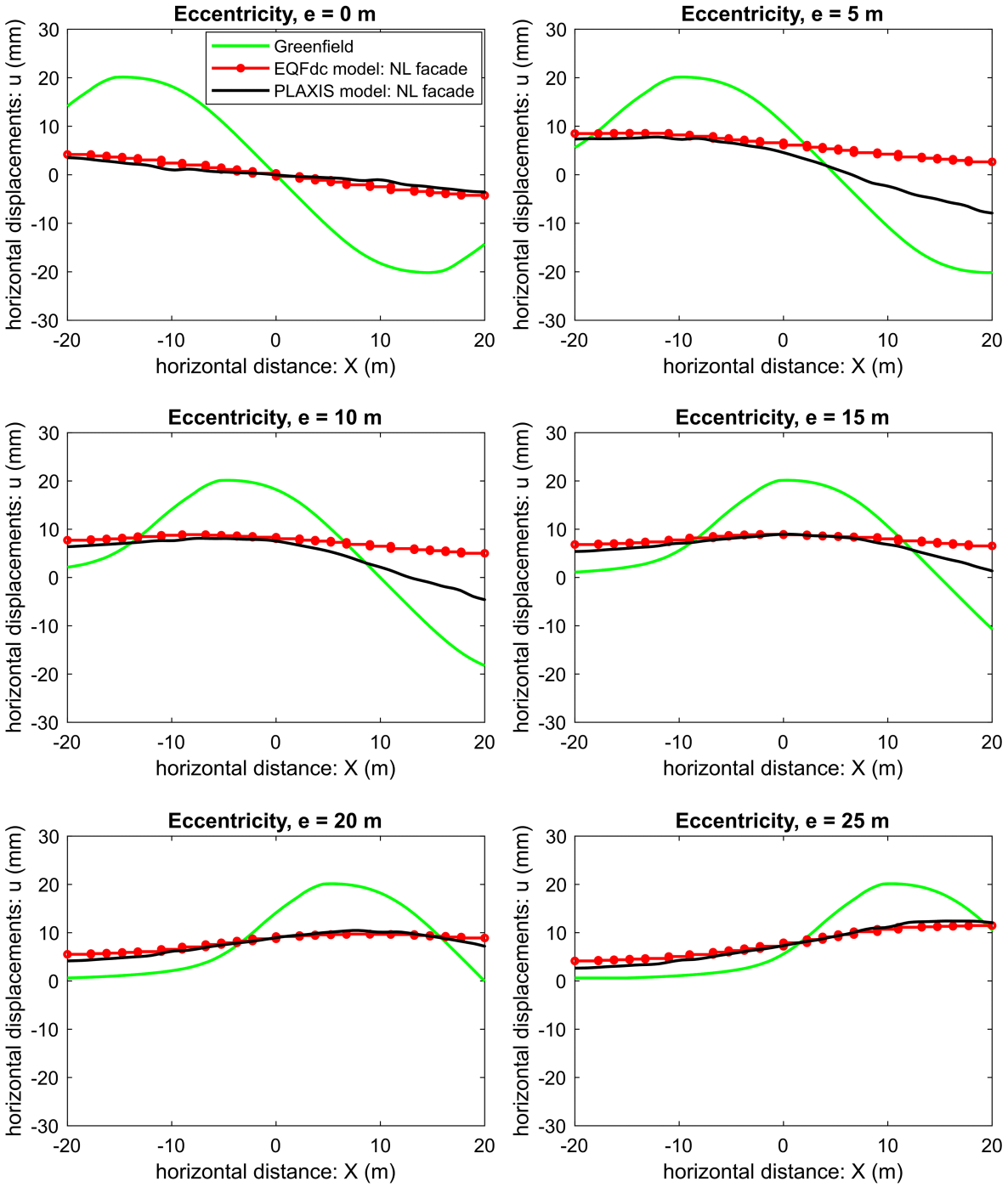


Figure 8.15: Façade horizontal displacement responses at the foundation level induced by the greenfield displacements only for the NL façade analysis.

The horizontal displacement responses of both EQFdc and PLAXIS models are presented in Figure 8.15 for the central and eccentric tunnel scenarios. The horizontal displacement responses present almost the same results for both models along the foundation for the central tunnel case ($e = 0$). Even the small jumps that occurred in the horizontal displacement profile

of the PLAXIS model, where they correspond to the elements under the door openings, are successfully captured by the nodal footing displacements of the EQFdc model for $e = 0$ (Figure 8.15).

Similar to the EL façade analyses results, the EQFdc model captures well the vertical footing displacements determined from the PLAXIS model (Figure 8.14). However, the horizontal displacement responses are underestimated by the existing soil-foundation interaction modelling approach used in the EQFdc model at the specified tunnel eccentricity cases, especially for $e = 5$ m and $e = 10$ m (Figure 8.15). For the vertical displacements, while the effect of soil-structure interaction is clear for the central tunnel scenario, the façade displacements almost follow the greenfield displacement curves in the eccentric tunnel cases. The frictional shear behaviour in the soil-structure interaction has nonnegligible effects on the horizontal displacement response of the façade.

8.8.2 Major principal tensile strain responses

Major principal tensile strain distributions of the nonlinear façade model for the central tunnel and the eccentric cases at $e = 5$ m and $e = 20$ m are presented in Figures 8.16 and 8.17 by comparing the EQFdc and the PLAXIS responses.

For the central tunnel case (Figure 8.16), the EQFdc model can identify the components more prone to high magnitude strains. For example, the spandrels at the first storey, especially the ones above the doors, where the shear failure has a dominant effect on the strain, are captured by the EQFdc model as consistent with the PLAXIS model response.

The shear strain is uniform across the beam section for the nonlinear façade model, the diagonal shear behaviour, which can be observed from the PLAXIS model, is not captured at the first storey pier elements of the EQFdc model (Figure 8.16). However, the EQFdc model is still able to represent the same damage class as the PLAXIS model, which is defined as ‘severe’

according to the standard building damage classifications (Burland & Wroth, 1974; Boscardin & Cording, 1989) corresponding to the major principal tensile strains exceeding 3000 με for the spandrels over the door openings.

For the tunnel eccentricity $e = 5$ m, the EQFdc model captures the shear failure dominant strain distributions at the first-storey spandrels, including the ones over the doors and windows for $x > 10$ m (Figure 8.17a). The pier elements near the doors, especially the ones $x > 10$ m, experience 'severe' damage induced by the shear failure behaviour, according to the PLAXIS model (Figure 8.17a).

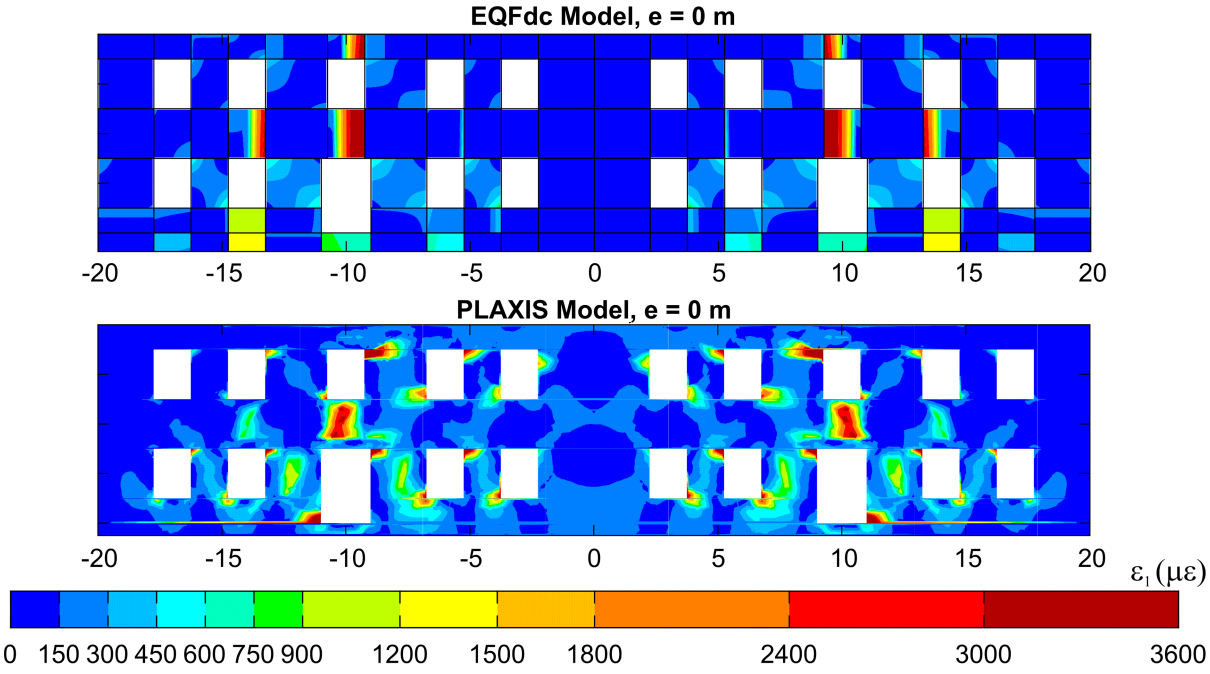


Figure 8.16: Major principal tensile strain contour plot comparisons between the EQFdc and PLAXIS models for the NL façade analysis, $e = 0$.

For $e = 20$ m, the PLAXIS model indicates the potential damage that is distributed towards the second-storey spandrels (Figure 8.17b), this is also captured by the EQFdc model. While the maximum tensile strain exceeds over 3000 με in the PLAXIS model, the highest strain indicated by the EQFdc model is around 1500 με.

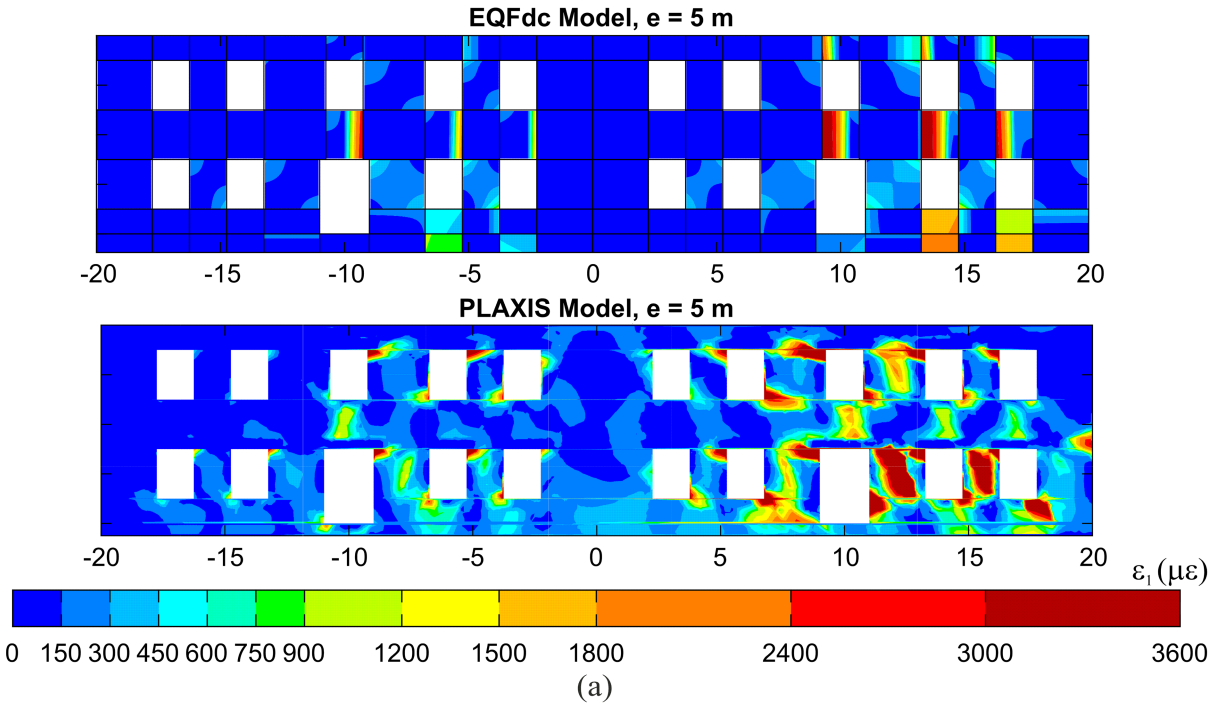


Figure 8.17: Major principal tensile strain contour plot comparisons between the EQFdc and PLAXIS models for the NL façade analysis: (a) $e = 5$ m and (b) $e = 20$ m.

The major principal tensile strain distributions in the nonlinear façade models show that the maximum values of ε_1 determined from the EQFdc and PLAXIS models reach large magnitudes once the plastic failure mechanism occurs at the particular Gauss points. This

prevents making a meaningful comparison regarding the variation of maximum major principal tensile strain with tunnel eccentricity as presented in Sections 7.6.4 and 8.7.3. Thus, another method that is directly related to the plastic failure behaviour observed in the Gauss points is adopted. This is explained in the next section. In addition to the major principal tensile strain and plastic point distributions, the relationship between the crack widths and the damage estimations will be explored in Chapter 9.

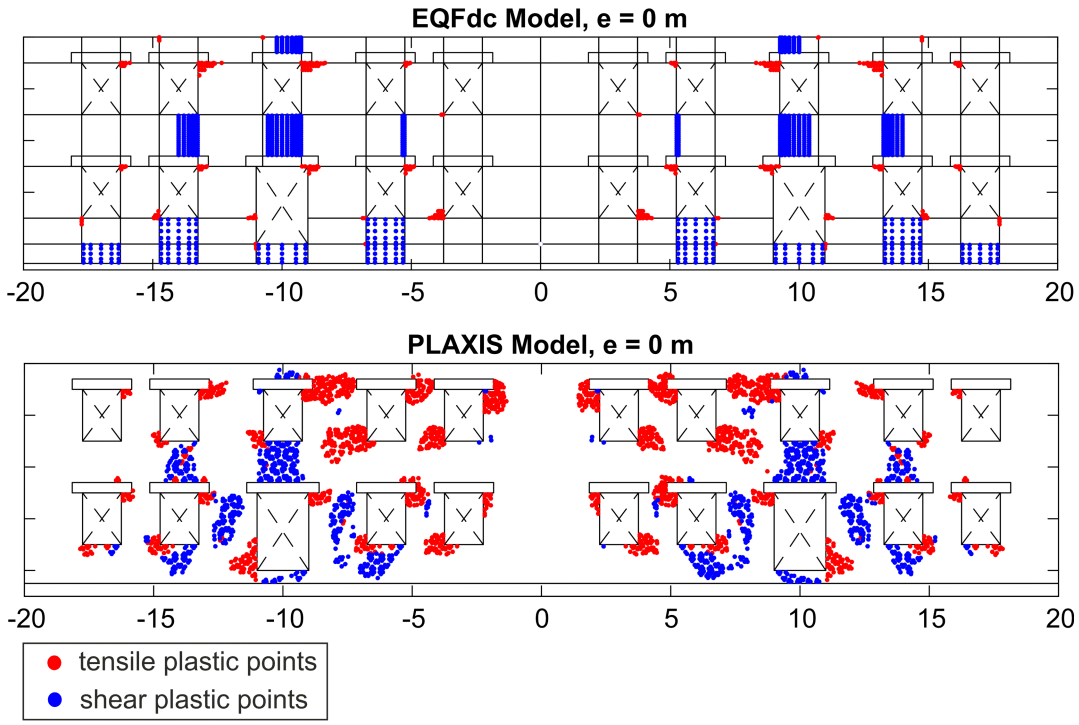


Figure 8.18: Locations of plastic failure points comparisons between the EQFdc and PLAXIS models for the NL façade analysis, $e = 0$.

8.8.3 Plastic failure responses

Figures 8.18 and 8.19 demonstrate the history (i.e. cumulative representation of the plastic points that occurred at each loading step) of plastic failure point locations when the Gauss point reached the tensile plastic (for beams and structural interfaces) and the shear plastic (for beams and quads) failure mechanisms for the central tunnel and eccentric scenarios at $e = 5$ m and $e = 20$ m. It should be noted that while tension plasticity is defined for the fibre beam and the structural interface elements in the normal direction, the shear plasticity is only considered for

the beam and quad elements. Additionally, it is important to note that all the points inside the quad elements experience constant shear strain. However, only the locations of the Gauss points are shown in the plots to indicate the shear plastic failure of the whole quad element.

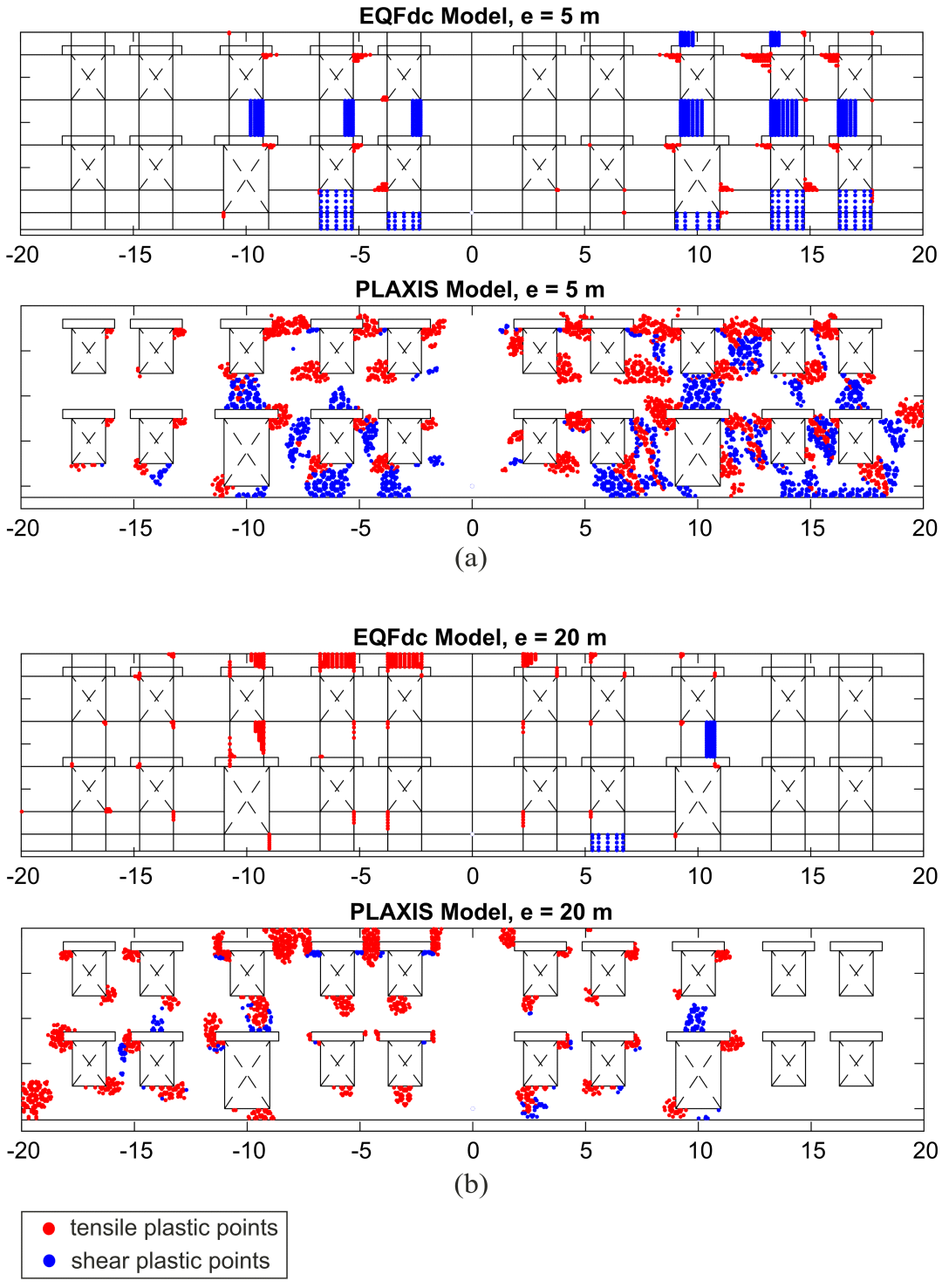


Figure 8.19: Locations of plastic failure points comparisons between the EQFdc and PLAXIS models for the NL façade analysis: (a) $e = 5$ m and (b) $e = 20$ m.

Consistent with the major principal tensile strain distributions for the central tunnel scenario, the spandrels at the first and second storeys demonstrate shear failure mechanisms in addition to the quad elements under the doors and the windows at the first storey (Figure 8.18).

Almost all piers at the first and second storeys experience tensile plastic failure at the corners of the elements. Although the intensity of damage is spread to larger portions of the façade in the PLAXIS model, the EQFdc model is able to define the particular structural components exposed to the potential damage.

For $e = 5$ m, the piers next to the doors and those on the right side of the façade at the second storey experience a combination of shear and tensile failure mechanisms in the PLAXIS model (Figure 8.19a). Tensile failures in these pier elements are also identified by the EQFdc model. Additionally, the shear plastic failure that occurs in the spandrels over the doors and in the quads under the first-storey windows is well captured by the EQFdc model. The EQFdc and PLAXIS models (Figure 8.19b) both show mainly tensile plastic behaviour for $e = 20$ m. Additionally, the tensile plastic failure at the corners of the openings is successfully captured by the corresponding corner of the beam elements or via interface elements in the EQFdc model. For $e = 20$ m, the shear plastic behaviour indicated by the PLAXIS model is also captured by the EQFdc model for the particular structural components such as for the spandrel element over the door, at $x = 10$ m and the ground quad element around $x = 5$ m (Figure 8.19b).

8.9 Conclusion

For both the EL and NL façade analyses, the footing vertical displacements computed by the EQFdc model agree well with the PLAXIS model. Regarding the horizontal displacement results, although the façade displacements are captured well for the central tunnel case, for the specific tunnel eccentricities, where the façade corner experiences significant horizontal

greenfield displacements (around −20 mm), the EQFdc model currently underestimates the horizontal displacement response of the façade compared to the PLAXIS results. The analysis comparisons between the S2M and the EQFdc models demonstrate that the difference in the horizontal displacement behaviour is caused by the S2M soil-foundation interaction model implemented into the EQFdc model, since the EQFdc model replicates the displacement results determined from the S2M model successfully. This result highlights that the S2M soil-foundation interaction model needs further improvements to capture the horizontal displacements accurately. In case of improving the existing S2M type soil-foundation interface model, the performance of the EQFdc model can be improved as demonstrated with the analysis comparisons produced by using the stiff soil parameters and employing the PLAXIS footing displacements directly to the soil-foundation interface elements in the EQFdc model.

The EQFdc model can reproduce the distributions of the major principal tensile strain and plastic failure locations that are obtained from the PLAXIS results. However, for the nonlinear façade analysis, since the shear strain is formulated in this case as constant across the element cross-sections, the diagonal distribution of shear strain determined in the PLAXIS models is not reproduced by the EQFdc model.

Overall, the EQFdc model is shown to be effective as reproducing the PLAXIS model responses in terms of façade displacements at the foundation level, major principal tensile strain and plastic failure distributions. Here, it is important to highlight that the EQFdc model presents a computationally efficient solutions. For the specified case studies, the EQFdc model comprises 304 elements and 241 nodes, while the PLAXIS model includes 66278 mesh elements and 106399 nodes. The EQFdc model completes a nonlinear tunnel-soil-structure interaction analysis for the elastic façade case in less than a minute and the nonlinear façade analysis takes 2 to 35 minutes, depending on the tunnel eccentricity case in a consumer-grade laptop (processor: Intel Core i7-1185G7 @ 3.00GHz 1.80 GHz, RAM: 16 GB). However, the

PLAXIS model requires approximately 1.30 hours to complete a nonlinear tunnel-soil-structure interaction analysis for the elastic facade with a central tunnel scenario and 2 hours for the nonlinear facade with an eccentric tunnel case (processor: Intel Core i7-10610U CPU @ 1.80 GHz 2.30 GHz, RAM: 32 GB). It should be noted that the EQFdc model can be optimised to run faster potentially. However, further improvements to reduce the analysis time for the EQFdc model have not been investigated in detail in this research. In conclusion, considering the ability of the EQFdc model to predict displacements and localise damage accurately with low computational requirements, this model can be potentially conducted as an additional tool before using 3D FE models in the existing tunnelling-induced damage assessment procedures.

Chapter 9

Comparison of EQFdc Model with Settlement Tests

9.1 Introduction

In addition to the numerical work presented in previous chapters, a collaborative field-testing project was conducted in Turkey ('the Turkey settlement tests project') during this DPhil research. In these field experiments, four half-scale masonry buildings were subjected to settlement profiles that simulate tunnelling-induced settlements. The design and construction details of the experimental setup are presented by Dalgic et al. (2021; 2023).

Innovative structural health monitoring systems comprising Fibre Bragg Grating (FBG) sensors and Imetrum Dynamic Monitoring Station (DMS) were used to investigate the structural response of the masonry buildings during the experiments. The strains in the buildings were measured by the FBG sensors; the building displacements were monitored by the DMS using the 2D Digital Image Correlation (DIC) technique.

The research presented in this thesis contributed to the Turkey settlement tests project in terms of providing the FBG and DIC instrumentation designs, performing the calibration tests before the field experiments, preparing the monitoring plans, installing the monitoring systems in the

field, conducting the experiments with other project partners, collecting the FBG and DIC monitoring data and performing the formal analyses for the initial step of data processing of the FBG and DIC measurements. Laser scan measurements were also conducted at the beginning, intermediate level loading and end of the experiments as additional measurement data. However, the details regarding the laser scanning method are out of the scope of this thesis. The data validation, formal analysis and data curation of the DIC and laser scan measurements are performed by Liu (2023). The laser scan data is only used to determine the coordinates of the DIC and FBG instrumentations in this chapter.

The main objective of this chapter is to conduct EQFdc model simulations to represent the experiments and present the comparisons between the analysis and experimental results. The analysis and experimental results are compared in terms of vertical building displacements, global damage patterns and the crack distributions at specific structural components.

9.2 Experimental Setup

The experimental setup was designed to investigate the influence of simulated tunnelling-induced settlements on half-scale masonry buildings (Figure 9.1). It explored buildings with different façade opening ratios, floor structures and weights. The buildings were designed to represent the Akaretler Row Houses, these are 19th century brick masonry buildings in Istanbul, Turkey.

9.2.1 Tunnelling scenario and settlement application

A single tunnel excavation orthogonal to the building was modelled in the experiments (Figure 9.2). The parameters describing the building geometries and the tunnelling scenario are given in Table 9.1 for the full-scale prototype and the half-scale model experimental setup. The greenfield settlement trough was computed according to the empirical Gaussian curve (O'Reilly & New, 1982) for sandy soil condition with the volume loss of 1.1% (Dalgic et al.,

2023). This causes a 50 mm tip settlement, v_s, at the east corner of the buildings (where the settlement is applied) at prototype scale. This corresponds to a 25 mm settlement at model experiments.

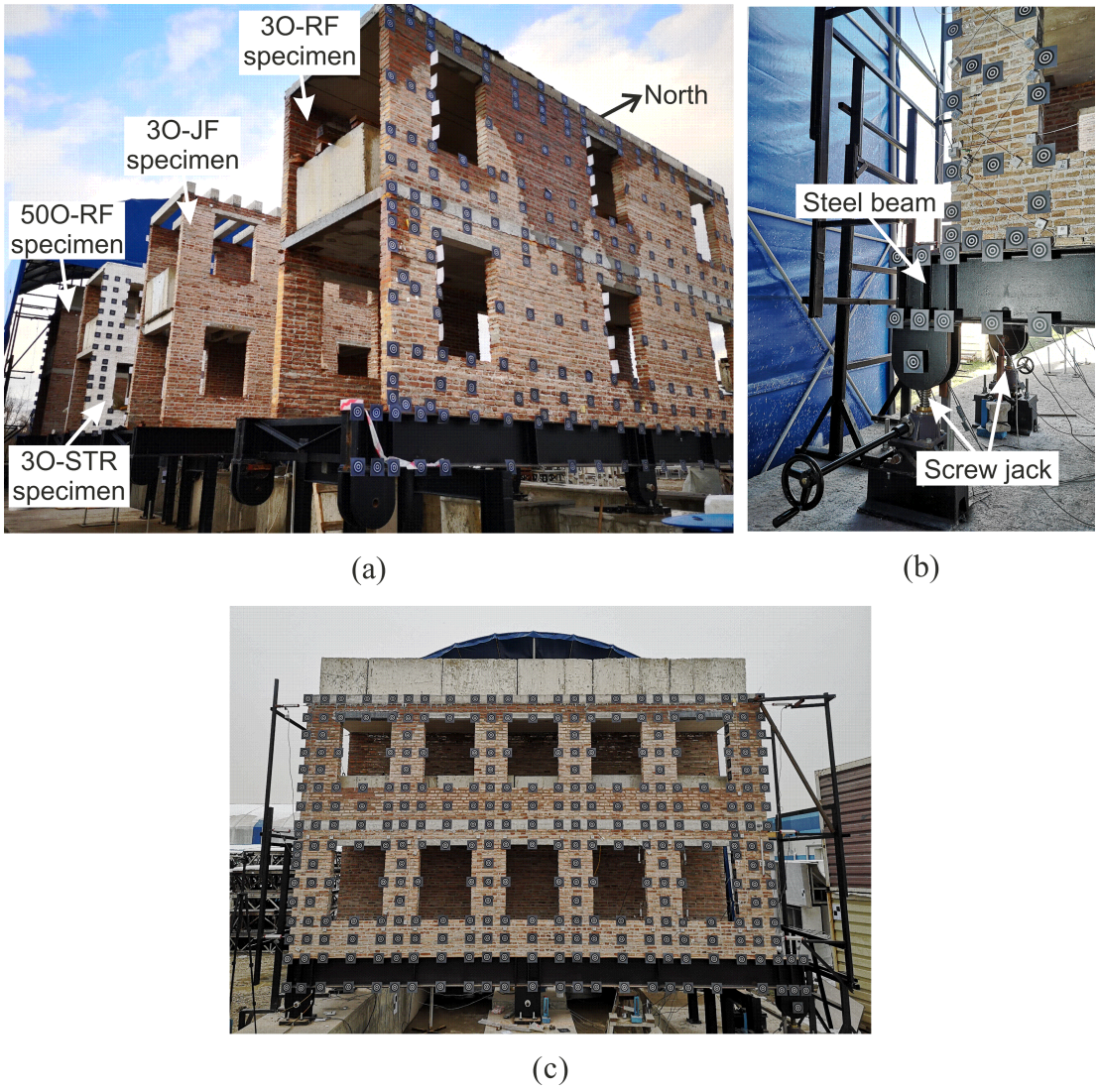


Figure 9.1: Experimental setup: (a) half-scale buildings, (b) screw jack detail, (c) 5O-RF building.

The buildings were constructed over two identical I-shape steel beams (IPE 330) with a mortar bedding joint between the steel beam and the base of the building. The steel beams were supported by machined steel hinge elements placed on reinforced concrete pedestals at the mid-spans and the west corners. The east corners of the steel beams were kept free (removable temporary supports were used before the experiments), where screw jacks were used to apply

vertical displacements (i.e. tip settlements) during the experiments (Figure 9.1b). Deformed shapes of the beams at the tip settlements represent tunnelling-induced settlement troughs, determined by the conventional Gaussian curve (O'Reilly & New, 1982) for the specified tunnel-building configuration scenario considered in the experiments (Figure 9.2). The same settlements were applied to both front and back façades of the buildings and this was ensured by monitoring the vertical displacements at each steel beam using the LVDTs (Linear Variable Differential Transformers) during the loading (Dalgic et al., 2023). The screw jacks can apply up to 100 mm of tip settlement, corresponding to about 4.5% volume loss (i.e. the volume loss is chosen as 1.1% for a 25 mm settlement in the model design but the capacity of screw jack is higher than this design value) in the tunnelling scenario. The cross-section of steel beams was chosen such that 100 mm tip settlement does not lead to plastic behaviour. Further details of the design and construction of the experimental setup are explained by Dalgic et al. (2023).

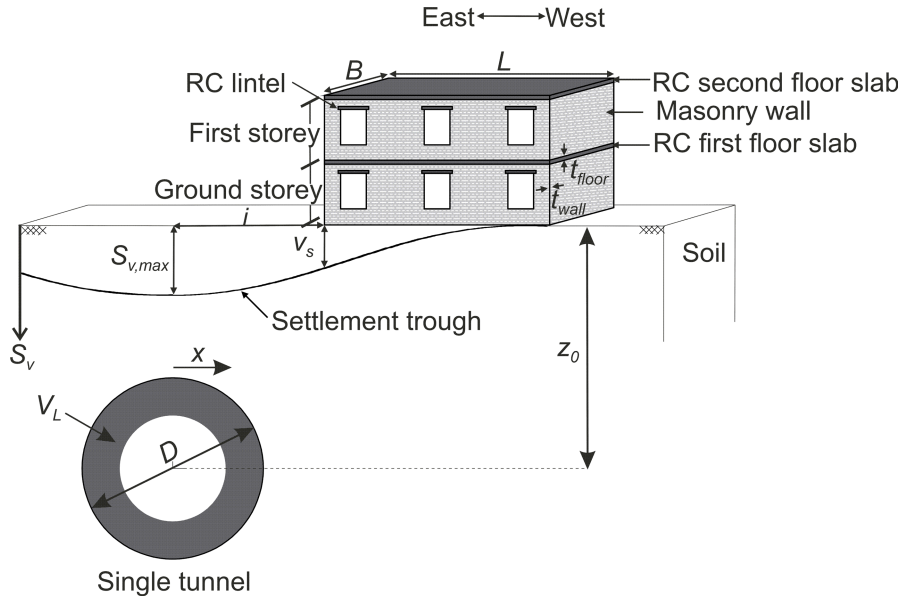


Figure 9.2: Tunnel-building configuration scenario considered in the experiments.

9.2.2 Building classifications

This chapter considers three buildings examined in the experiments, which are classified according to the building weights, the number of window openings per storey and the type of

floor structures.

In Figure 9.1, the 3O-RF building, has three window openings per floor at each wall (3O) and was constructed with a cast in-situ reinforced concrete (RC) slab (referred to as rigid floor, RF, in the following text) (Figure 9.3a). This building is treated as the reference building, 3O-RF. The 3O-JF building has the same window opening arrangements as the reference building but has flexible floors (Figure 9.3b) designed with joists (3O-JF) to investigate the effect of floor structures on the building response. The joist floors were built as RC beams (which means that they are flexible compared to cast in-situ RC slabs) and supported on metallic hangers aligned in the north-south direction between the masonry walls of the building. The final building (50O-RF) with the rigid floor is placed at the south end of the experimental setup is composed of two walls with different opening arrangements (Figure 9.1c). While the south wall has five window openings per floor (5O), the north wall is designed as a plain façade (0O) to observe the influence of façade openings on the building response.

Table 9.1: Prototype and model scale parameters used to represent the building geometry and the tunnel excavation scenario in the experimental setup (Dalgic et al., 2023).

	Parameters	Prototype	Model
Building	Length, L (m)	11.2	5.6
	Height, H (m)	6.4	3.2
	Width, B (m)	3.23	1.615
	Wall thickness, t_{wall} (m)	0.230	0.115
	Floor thickness, t_{floor} (m)	0.2	0.1
Tunnel	The maximum settlement, $S_{v,max}$ (m)	0.090	0.045
	Tip settlement, v_s (m)	0.050	0.025
	Volume loss, V_L (%)	1.1	1.1
	Tunnel diameter, D (m)	12.2	6.1
	Distance of inflection point, i (m)	5.50	2.75
	Trough width parameter, K (-)	0.25	0.25
	Tunnel axis depth, z_0 (m)	22	11

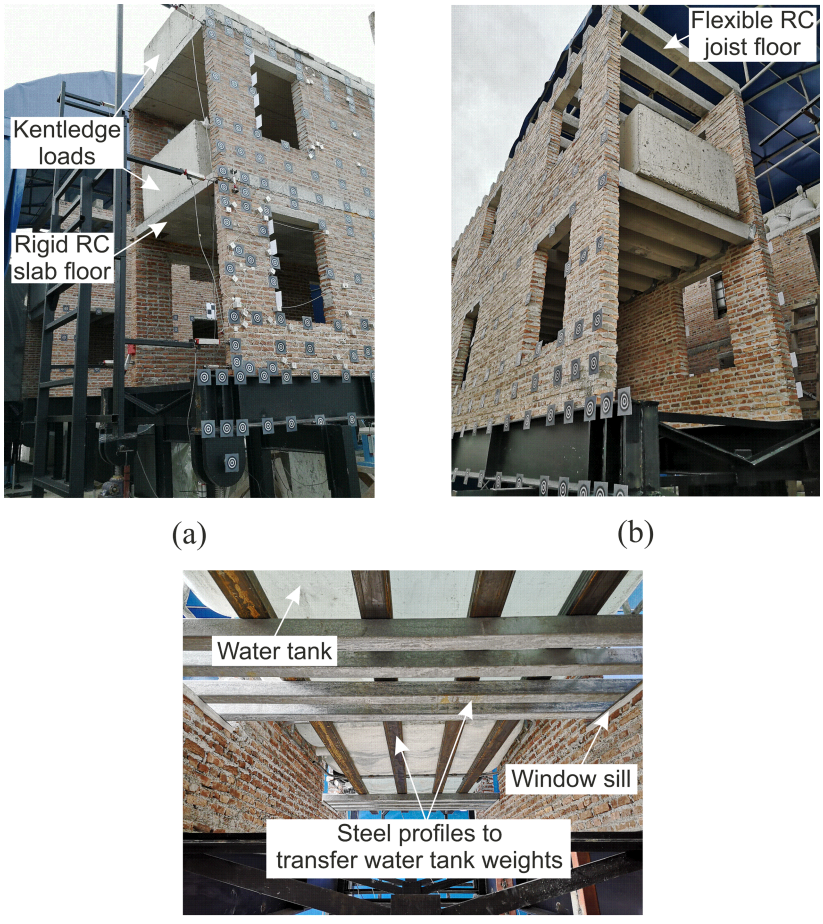


Figure 9.3: Floor construction types: (a) rigid RC slab floor, (b) flexible RC joist floor (before the placement of kentledge load to the top floor) and (c) suspended ground floor (used only for 3O-RF-W3 test).

For the realistic representation of vertical stresses induced by the structural self-weight at the base of the prototype buildings, extra weights must be added to the model scale buildings, which are exposed to 1g testing conditions (Giardina et al., 2012). Initially, the self-weight of all structural components is computed as 58 kN (without considering the window openings), corresponding to an approximate vertical stress of 0.09 MPa at the building base. However, to simulate the average vertical stress of 0.2 MPa at the base of prototype building walls (caused by the self-weights of two plain masonry walls and RC slabs in prototype scale), 78 kN of extra dead load was placed over both first and second-floor slabs of the buildings using concrete kentledge loads as shown in Figures 9.3(a) and 9.4(a) (Dalgic et al., 2023). This loading

arrangement is referred to as W1 weight scenario, which corresponds to the total building weight, including the self-weights of all structural components and the kentledge loads (i.e. precast concrete blocks shown in Figure 9.3a) in the ground and first storey floors (Figure 9.4a).

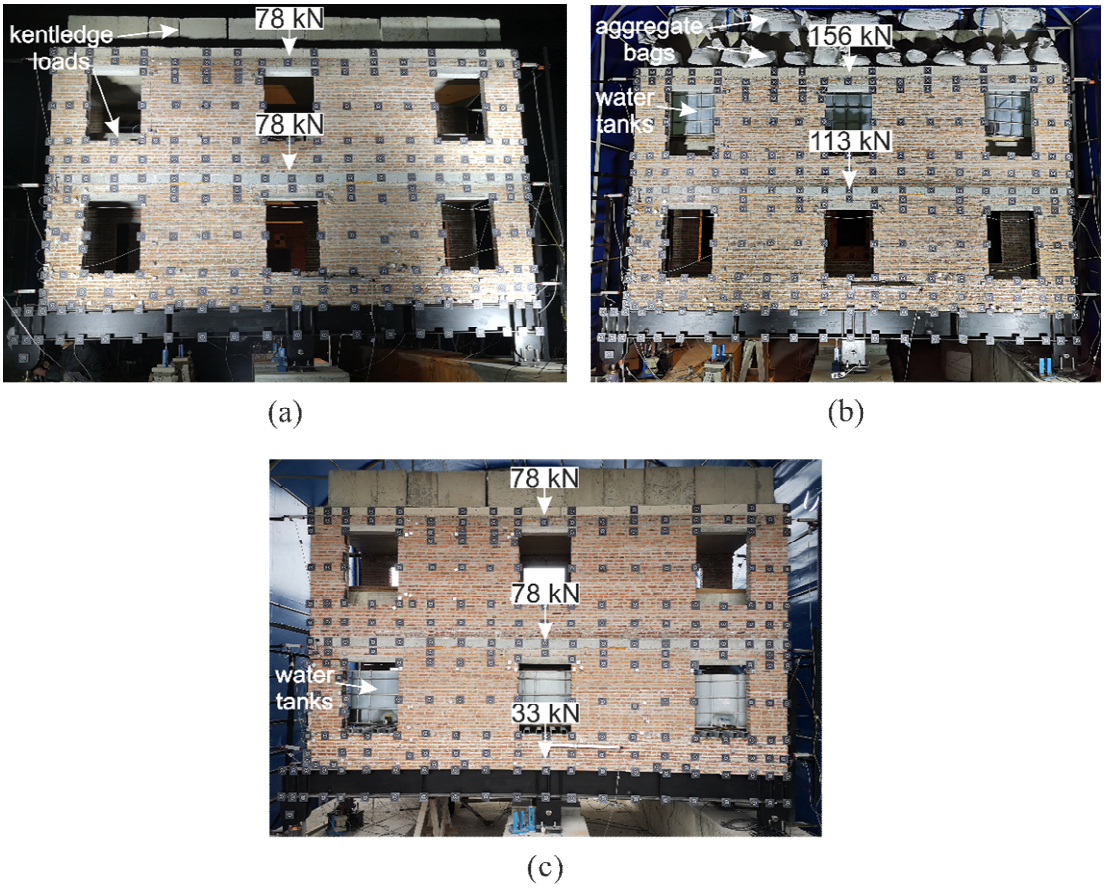


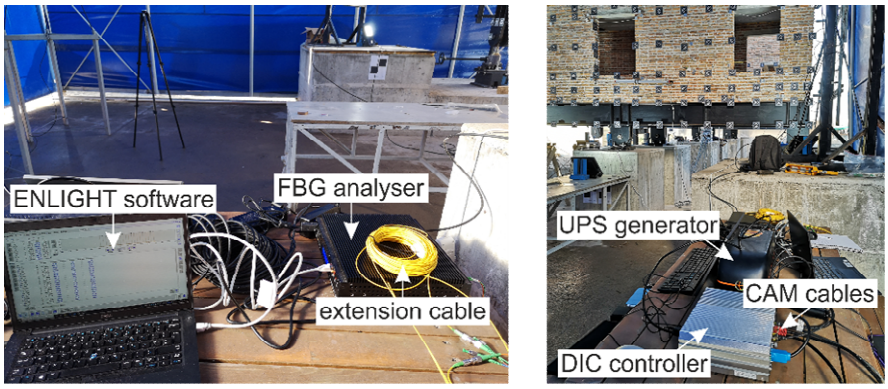
Figure 9.4: Building weight arrangements on the 3O-RF building: (a) W1, (b) W2, (c) W3.

To investigate the effect of structural weight on the building damage response under settlement applications, three weight arrangements were considered as W1, W2 and W3. The reference building (3O-RF) was tested under all three weight scenarios (Figure 9.4). Scenario W2 is associated with increasing the weights at each floor up to approximately 1.4 times W1 case (Figure 9.4b). For the W3 case (Figure 9.4c), additional loads provided by water tanks were applied from the ground-storey windowsills to represent suspended ground floor loading (Pickles, 2016). Due to the constructional work practicability, the water tanks are used on the

ground-storey instead of kentledge loads. The other buildings (3O-JF and 50O-RF) were tested under only W1 weight scenario.

9.2.3 Building material properties and scaling

The masonry material properties of the buildings (Dalgic et al., 2023) were chosen to represent Akaretler Row Houses, in which the prototype masonry is composed of English bond, incorporating regular-sized bricks with 10-30 mm thick mortar joints (Ispir, 2010; Ispir & Ilki, 2013). Half-sized solid clay bricks (with dimensions of 115×57.5×30 mm) and 10 mm thick mortar joints were used in the tests (Dalgic et al., 2023). To provide high stiffness and strength parameters compared to the masonry, the lintels (70 mm in thickness) and the rigid floors (100 mm in thickness) were constructed with C40 RC (Dalgic et al., 2023). The further construction details of the Akaretler buildings, which were mimicked in the experimental setup, are presented by Dalgic et al. (2023).



(a) (b)

Figure 9.5: Monitoring setup: (a) FBG analyser, (b) DIC controller.

9.3 Monitoring Measurement Techniques

9.3.1 FBG sensor strain measurements

The FBG sensor measurements were controlled using Micron Optics (Hyperion Platform) Sensing Instrument si255 FBG analyser, which serves as a light source and data logger (Figure

9.5a). The FBG analyser sends simultaneous light through two cables and the light is reflected by the sensor gratings in the fibre optic cables. Since each sensor grating has a different wavelength, the analyser can identify data corresponding to each sensor. Changes in wavelength is used to calculate temperature and/or strain at each sensor location. The FBG analyser is controlled by a laptop. The measurements were conducted using the Micron Optics ENLIGHT software.

Two fibre optic cables (coated with 1.0 mm Glass Fiber Reinforced Plastic and 0.5 mm High-Density Polyethylene) were used to measure strains in the masonry walls during each test. The regular FBG sensor spacing is 1.0 m, except that the first sensor is placed at 0.5 m from the start of the cable. Each cable incorporates 20 sensors, each with a strain resolution of 5 με. Fibre optic cables were fixed to the surface of the buildings with aluminium clamps; an FBG sensor was placed between the aluminium strain clamps (40×40 mm) to measure the average strains.

The wavelength of the FBG sensors is affected by mechanical and temperature-induced strain. Temperature changes also induce changes in the refractive index of the glass which also influenced the measurements. Therefore, temperature must be measured to identify strains accurately. At least one FBG sensor per cable was used as a temperature sensor placed inside an aluminium clamp (temperature clamp in the dimension of 40×60 mm) to determine the changes in temperature. These temperature sensors were configured in such a way that they are not subjected to any strains due to settlements.

The strain calculations based on the changes in the wavelength of an FBG sensor are briefly reviewed. The strain change is determined as follows using changes in FBG wavelength:

$$\frac{\Delta\lambda}{\lambda_0} = k\varepsilon + \alpha_\delta \Delta T = k(\varepsilon_m + \varepsilon_T) + \alpha_\delta \Delta T \tag{9.1}$$

where $\Delta\lambda$ is the wavelength shift, λ_0 is the initial wavelength at the start of the test, k is the gauge factor ($k = 1 - p$ and p is the photoelastic coefficient), ΔT is the temperature change in $°C$, α_δ is a constant that refers to the change of refraction index of glass with temperature, ε is the total strain change, composed of mechanical (ε_m) and temperature-induced (ε_T) strains, respectively. The temperature-induced strain can be expressed as follows:

$$\varepsilon_T = \alpha_{sp}\Delta T \tag{9.2}$$

where α_{sp} is the thermal expansion coefficient per $°C$ of the clamp if the sensor is placed inside a temperature clamp or it refers to the thermal expansion coefficient of the masonry, $\alpha_{masonry}$ for the strain measurements. In this case, the temperature clamp is made of aluminium material. Thus, α_{sp} is replaced with α_{alu} to represent the thermal expansion coefficient of aluminium temperature clamps. Equation (9.1) can be rearranged as followed:

$$\varepsilon = \varepsilon_m + \varepsilon_T = \left(\frac{\Delta\lambda}{\lambda_0} - \alpha_\delta \Delta T\right)\frac{1}{k} \tag{9.3}$$

$$\Delta T = \left(\frac{1}{k\alpha_{alu} + \alpha_\delta}\right)\frac{\Delta\lambda}{\lambda_0} \tag{9.4}$$

By using the temperature sensor, the change in aluminium clamp temperature is calculated. This provides a fair approximation in air temperature. When the fibre optic cable is fixed along a section on the building to measure strains, the FBG sensor signal changes due to both mechanical and thermal effects. In this case, the thermal expansion coefficient is associated with the masonry, $\alpha_{masonry}$ rather than the aluminium, α_{alu}. For a freely expanding body, mechanical strains due to temperature effects are negligible. However, since the measured masonry portions in the experiments were not always free to expand, mechanical strains may also be introduced due to temperature changes. Due to this reason, it is not always possible to differentiate mechanical strains due to settlement and temperature expansion. For this reason,

only total strains were measured (Equation 9.3) and the temperature changes were reasonably constant (less than −2ºC) during the experiments.

9.3.2 DIC displacement measurements

Imetrum's Dynamic Monitoring Station (DMS), comprising a DIC controller and digital cameras, was used to measure the displacements by tracking the movement of each target point on the building during the tests (Figure 9.5b). A 2D DIC monitoring technique was used instead of a 3D DIC method, which requires synchronizing cameras and overlapping the field of views of the cameras. While the 2D DIC method enables monitoring the in-plane displacements (in a 2D X, Y coordinate system), the 3D DIC method also provides measuring the out-of-plane movements (in Z direction, in a 3D X, Y, Z coordinate system) in addition to the in-plane displacements. However, monitoring the whole building by using a 3D DIC method would have been challenging due to its precise requirements during the equipment installation. Additionally, for the specified settlement application (Section 9.2.1), the buildings were expected to experience mainly in-plane displacements. The out-of-plane displacements were also monitored during the experiments and they were determined as negligible, which were measured less than 3 mm for all buildings at the target beam tip settlement of 25 mm at the location of the central window at the ground floor (Dalgic et al., 2023).

The DMS system provides both real-time and post-processing modes. In real-time processing, the DIC measurement data are generated using live images from the video cameras and the test archive can be saved as AVI files. New monitoring points can be added to the test archive or the existing measurements can be repeated in the post-processing mode. The Video Gauge software was used to collect the DIC monitoring data and to perform the initial data processing analyses of the displacement measurements.

The important steps before performing a live test on the building are choosing a suitable

location to set up the DMS system, calculating the required field of view, choosing a suitable camera and lens by considering the required number of cameras based on the field of view, selecting suitable target patterns for tracking and arranging lights to achieve a uniformly lit monitoring surface.

Selecting a suitable target pattern is an important aspect of the procedure to ensure precise measurements are obtained. The lighting and brightness of the targets affect the resolution and repeatability of the system. An axisymmetric bullseye shaped pattern with high greyscale contrast was used as DIC targets (printed on cards and glued to the wall surfaces). It could have been feasible to monitor the natural masonry patterns but DIC targets were preferred to reduce the errors caused by occlusions and shadows on rough masonry surfaces.

9.4 Instrumentation Designs

9.4.1 FBG sensor laboratory calibration tests

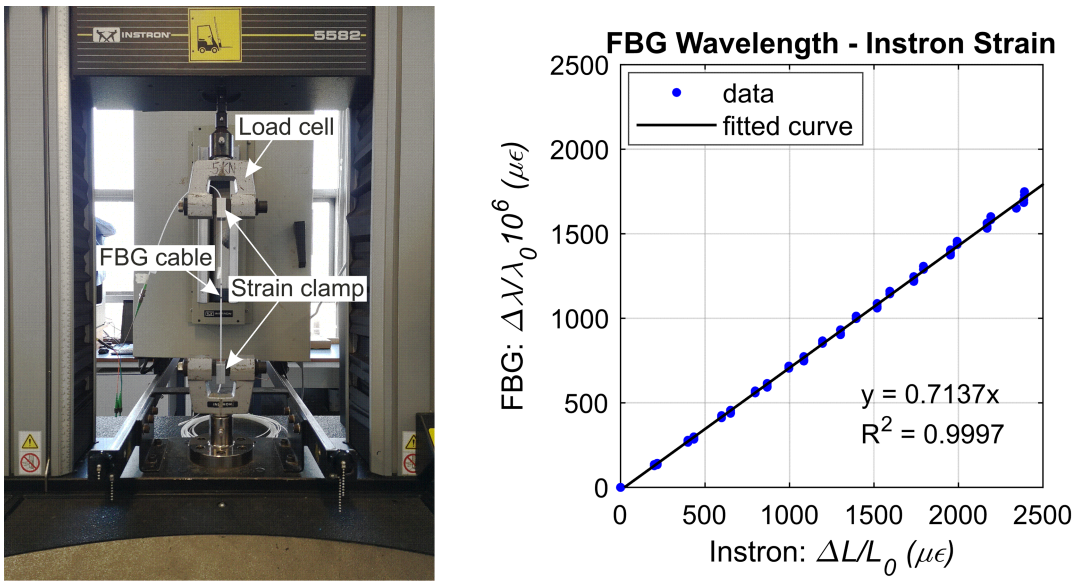
The wavelength of the FBG sensors is sensitive to strain and temperature changes. The parameters affecting the mechanical and temperature-induced strain calculations must be determined to capture the strains accurately. To achieve this, mechanical and temperature calibration tests were performed in the Department of Engineering Science, Oxford, before using the FBG sensors in the fieldwork. These procedures are described below.

9.4.1.1 FBG mechanical strain calibrations

The mechanical strain calibrations based on the tensile strain tests were conducted in an Instron 5582 vertical loading device with a load cell capacity of 5 kN (Figure 9.6a). An FBG sensor was placed between two aluminium strain clamps in a pre-tensioned state (to allow both compressive and tensile strains to be measured) and the initial length of the FBG cable fixed between the clamps was measured. Displacement-controlled tests were conducted to compare

the tensile strains measured from the FBG sensor with the variation of vertical displacements applied through the Instron device. These calibration tests aim to determine if any slip occurs between the clamps and the FBG cable and to calculate the correlation between the applied tensile strains and measured strains.

Before the tests, the initial wavelength of the FBG sensor was recorded and the strain reading from the specified sensor was set to zero. Then, the Instron device applied vertical displacements to the FBG cable with 0.1 mm increments. At the end of each displacement increment, sufficient time was given for the FBG sensor measurements to stabilise. The wavelength and the tensile strain were recorded at the end of each displacement increment. The tests were repeated six times by using different sensors and clamps, with the application of a maximum 1.3 mm displacement at the end of each test.



(a) (b)

Figure 9.6: Tensile strain calibration tests: (a) test setup, (b) test results showing the relationships between $\Delta\lambda/\lambda_0$ and $\Delta L/L_0$.

To determine the correlation between the tensile strains measured from the FBG sensor and the ones computed through the vertical displacement increments, ΔL, applied from the Instron device (where ΔL is divided into the initial length of the corresponding portion of the FBG

cable, L_0) the relationship between the variation of the wavelengths ($\Delta\lambda/\lambda_0$) and the strains ($\Delta L/L_0$) are demonstrated in Figure 9.6(b). The relationship between the changes in the FBG sensor wavelengths ($\Delta\lambda/\lambda_0 10^6$ in microstrain) and the $\Delta L/L_0$ values is linear as expected and the slope of the line is 0.714. This linear slope is associated with the gauge factor, k as a property of the FBG cable. This linear relationship suggests there was no observable slip between the FBG cable and the aluminium strain clamps.

9.4.1.2 Temperature compensation FBG sensors

Four aluminium clamps were used to measure the strains induced by the changes in temperature. FBG sensors were placed inside the aluminium temperature clamps following Acikgoz et al. (2022). This isolates the sensor from external mechanical strains; the sensor inside the temperature clamp is only affected by the thermal expansion of the aluminium clamp with the temperature changes.

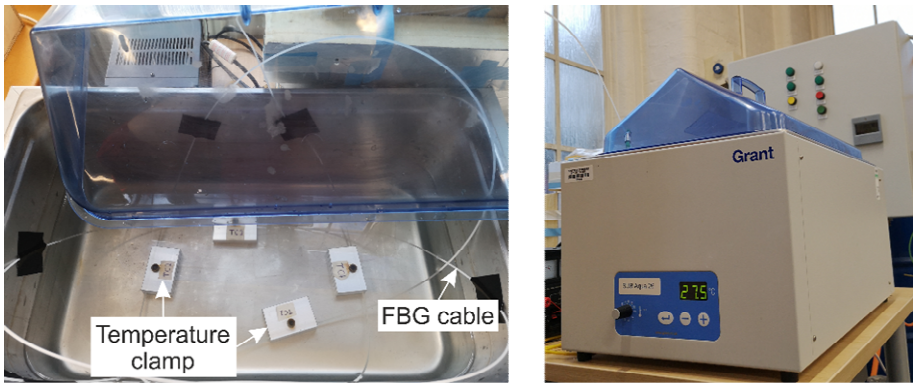


Figure 9.7: Temperature calibration test setup: (a) temperature clamps placed inside the water bath, (b) temperature of the water bath is gradually increased.

The temperature calibration tests were performed in a temperature-controlled water bath (Grant SUB Aqua 26) to determine the linear thermal expansion coefficient of the aluminium clamps (Figure 9.7). Accordingly, the four temperature clamps (with the FBG sensors inside) were placed inside the temperature-controlled water bath (Figure 9.7a). Two water bath tests were

performed, where the water bath temperature was increased from 18°C room temperature to the maximum of 38°C in 2°C increments (Figure 9.7b). After each increment, sufficient time was provided for the aluminium clamps to reach thermal equilibrium and the FGB sensor measurements to stabilise. However, due to their small thermal mass, aluminium clamps heat up quite quickly. The wavelengths on each temperature clamp were recorded at the end of each temperature increment. The relationship between the wavelength shifts measured by the FBG sensors and the temperature increments applied through the water bath is determined as linear as expected (Figure 9.8).

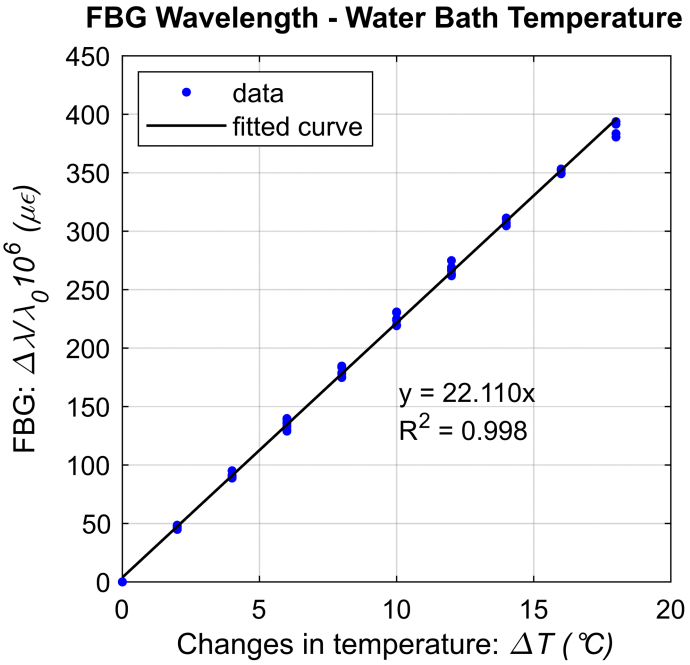


Figure 9.8: Correlation between the FBG sensor wavelength shifts and the temperature increments determined from the temperature calibration tests. As expected, the relationship is linear.

The thermal expansion coefficient of the aluminium clamps, α_{alu} is determined as $\alpha_{alu} = 22.1 \times 10^{-6}$(1/°C) using the linear relationship in Figure 9.8. This is consistent with the expected values for the aluminium alloy used to produce the clamps. For the calculations, the gauge factor, $k = 0.714$ (from the tensile strain calibration tests) and the change of refractive index of glass with temperature, $\alpha_\delta = 6.351 \times 10^{-6}$ (1/°C) (provided by the supplier) are used.

9.4.2 FBG sensor and DIC monitoring setup

The DIC was used as the main measurement technique since it allowed monitoring of the whole surface of the masonry façades. The displacement behaviour of the façade was tracked through the movements of the DIC targets (printed on cards with dimensions of 10×10 cm corresponding to 40×40 pixels in the image plane). The DIC targets were glued to the wall surfaces by considering the corners and mid-sections of the piers, spandrels and the connector elements in between (Figure 9.9). Accordingly, approximately three DIC targets were placed per length and width of each element. DIC targets were also placed onto the top flange of the steel beam to track the displacements on the steel beam.

The DIC and FBG monitoring setups designed for the 3O-RF reference building are illustrated in Figure 9.9. Regarding DIC monitoring, three GigE cameras, which are defined as in-plane cameras (CAM-1, CAM-2 and CAM-3) with 1/1.2″ sensors (used with 12 mm lenses) were placed 6.0 m away, with the camera sensors parallel to the façade. The cameras were fixed to the tripod head with an almost zero-pitch angle to monitor the in-plane movements of the façade.

In the instrumentation design with a 6.0 m camera-to-object distance, the field of view of each camera was 3.6×5.1 m^2 (H×V). The in-plane cameras were placed parallel to each other with a horizontal spacing of approximately 1.8 m and the heights of cameras from the ground level were 2.8 m (Figure 9.9). In this setup, the overlapping between the field of views of the cameras in the horizontal direction was around 1.2 m, this is sufficient to validate the displacements measured from adjacent cameras. Additionally, to monitor the out-of-plane movements of the façade, a fourth camera (CAM-4 in Figure 9.9) was placed with its sensors perpendicular to the façade surface (facing the inner surfaces of the windows' edges, where the out-of-plane DIC targets were glued onto). This camera was positioned approximately 6.0 m ($X \approx 6$ m, in

Figure 9.9) away from the furthest window opening.

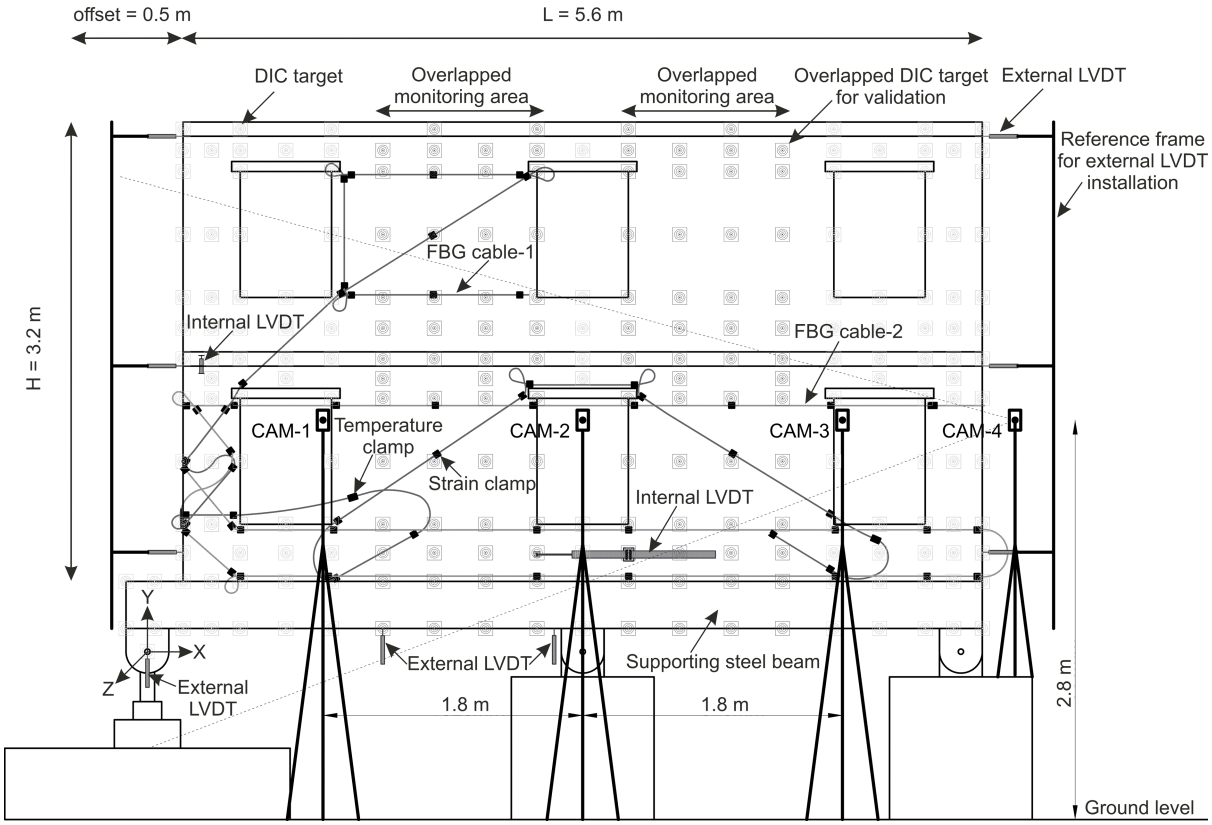


Figure 9.9: Monitoring setup designed for the reference 3O-RF building.

The DIC and FBG instrumentation details installed on the reference 3O-RF building are shown in Figure 9.10. The lighting also needs to be carefully considered during the DIC measurements. As shown in Figure 9.10(a), a movable tent was constructed to cover the buildings during the testing to prevent overexposure induced by the direct sunlight on the DIC targets. Uniform lighting inside the tent was provided by dimmable white LED lights. Regarding the camera positions demonstrated in Figure 9.10, the 6.0 m camera-to-object distance could only be maintained for the 3O-RF and 5O-RF buildings; due to the limited space between the buildings, the 3O-JF building was monitored from the inside of the strengthened building (3O-STR specimen in Figures 9.1a and 9.11a). Accordingly, three in-plane cameras were placed inside the 3O-STR building (Figur 9.11a), close to the windows, to monitor the 3O-JF building (Figure 9.11b).

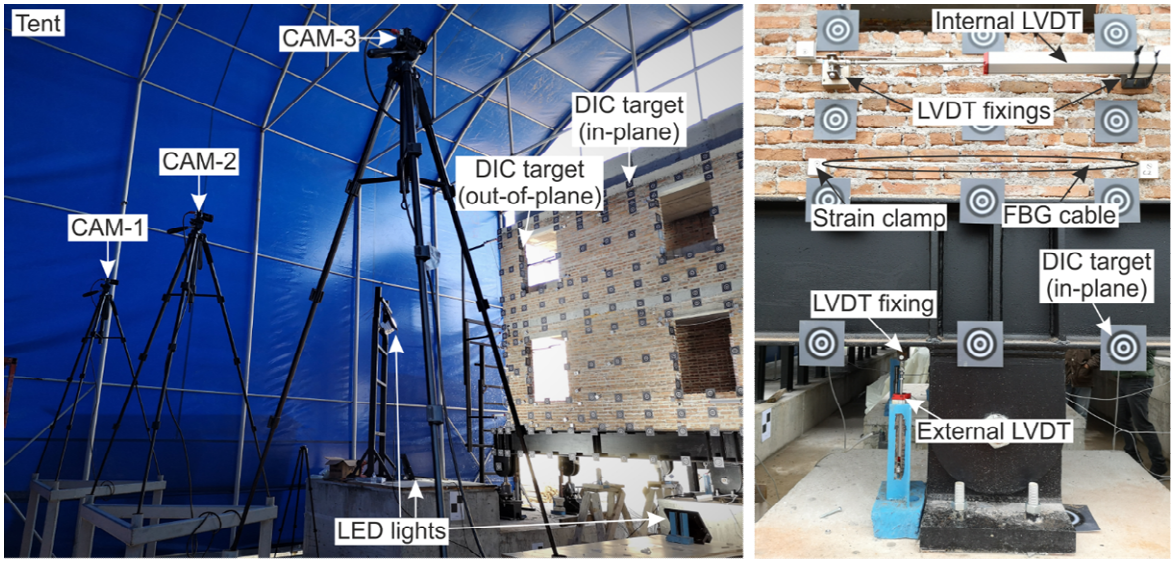


Figure 9.10: Photographs showing the instrumentation details for the reference 3O-RF building: (a) the primary DIC measurement system and (b) the secondary LVDT and FBG measurement systems.

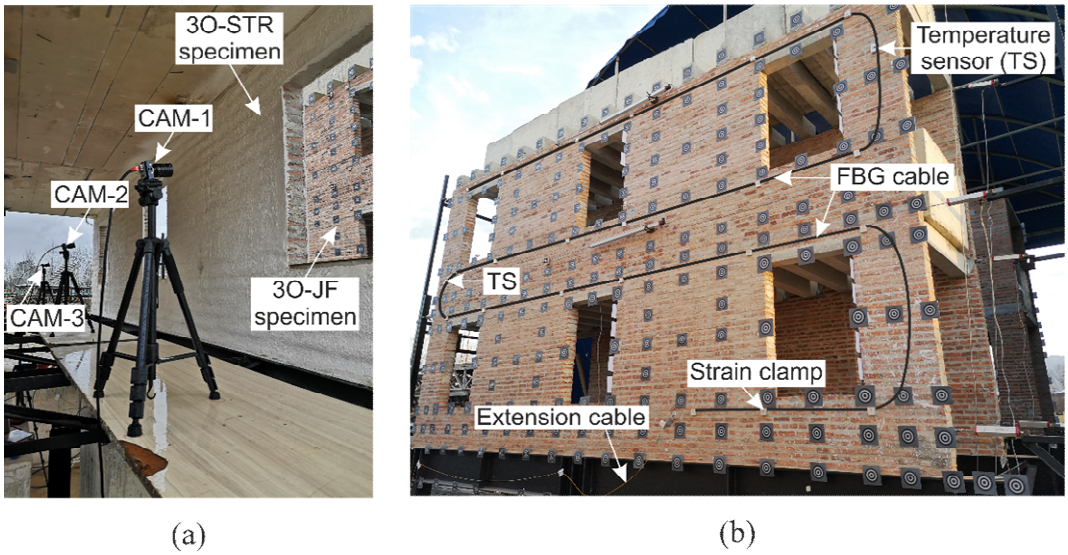


Figure 9.11: Instrumentation details for the 3O-JF building: (a) the DIC in-plane measurement setup and (b) the FBG cable installation (south façade).

The FBG sensor layout (Figure 9.11b) was designed mainly according to the layout of window openings and the damage behaviour of the buildings predicted by the 3D finite element analysis performed by Dalgic et al. (2021). According to the analyses, significant diagonal strains were expected to develop in piers while horizontal strain concentrations were expected in the

spandrels. To capture these aspects, FBGs were typically placed along the diagonals of critical pier elements and top and bottom fibres of spandrel elements (Figures 9.9 and 9.11b). After installing the strain clamps to the wall, pre-tension strains (approximately 500 – 1000 με) were applied to each sensor manually. The fixing quality was checked by gently tapping the strain clamps with a hammer. When the strain clamps were firmly fixed to the bricks, minimal strain fluctuations were observed. Prior to the experiments, the strain readings were set to zero.

The temperature (T) and temperature-compensated strain (S) sensors were defined in the ENLIGHT software prior to the experiments on each building. While the T sensor measures the changes in temperature (Equation 9.4), the S sensors compute the total strain values (Equation 9.3). The visualisation of the FBG sensors on the ENLIGHT software was set by using the specified building's photo taken after the instrumentation installations. The FBG sensor measurements were stored in raw wavelength data, total strain and changes in temperature for each test.

9.5 EQFdc Model Implementation

9.5.1 EQFdc model idealisations

The EQFdc model idealisations of the 3O-RF, 5O-RF and 3O-JF buildings are illustrated in Figure 9.12. To simplify the model generation, masonry portions above and below the rigid RC slabs (Figure 9.12b) are modelled as quad elements. The sections between the window openings along the horizontal axis are considered pier elements and formulated according to the flexibility formulations-based beams (Section 3.4). The masonry sections under the windows and above the steel beam are modelled as quad elements (Section 3.5.1).

In addition to the EQFdc modelling approaches described in Chapter 3, the modelling of slabs is also implemented into the code. The slabs are modelled using 'footing elements', based on rigid bar elements and lumped axial springs (Section 3.5.2). The experimental results (Dalgic

et al., 2023) demonstrated that the rigid RC slabs prevented the spreading of the damage to the upper storey (i.e. the masonry portions above the rigid RC slabs did not experience visible damage). To simulate this behaviour, restricting the deformation in the axial direction (i.e. using rigid bar elements) to model the rigid RC slabs is insufficient. To prevent the deformations for the masonry portions at the top and bottom of the rigid RC slabs, the interaction between the quads and the slabs is modelled by interface elements that are stiff compared to the normal stiffness of the other structural interface elements, K_n. In addition to the high stiffness of the quad-slab interface elements ($10^3 K_n$), their tensile strength ($10^3 \sigma_T$) is also defined much higher than the tensile strength of the other masonry sections, σ_T. The modelling details of the footing and the steel-building interface elements are explained in Section 9.5.3.

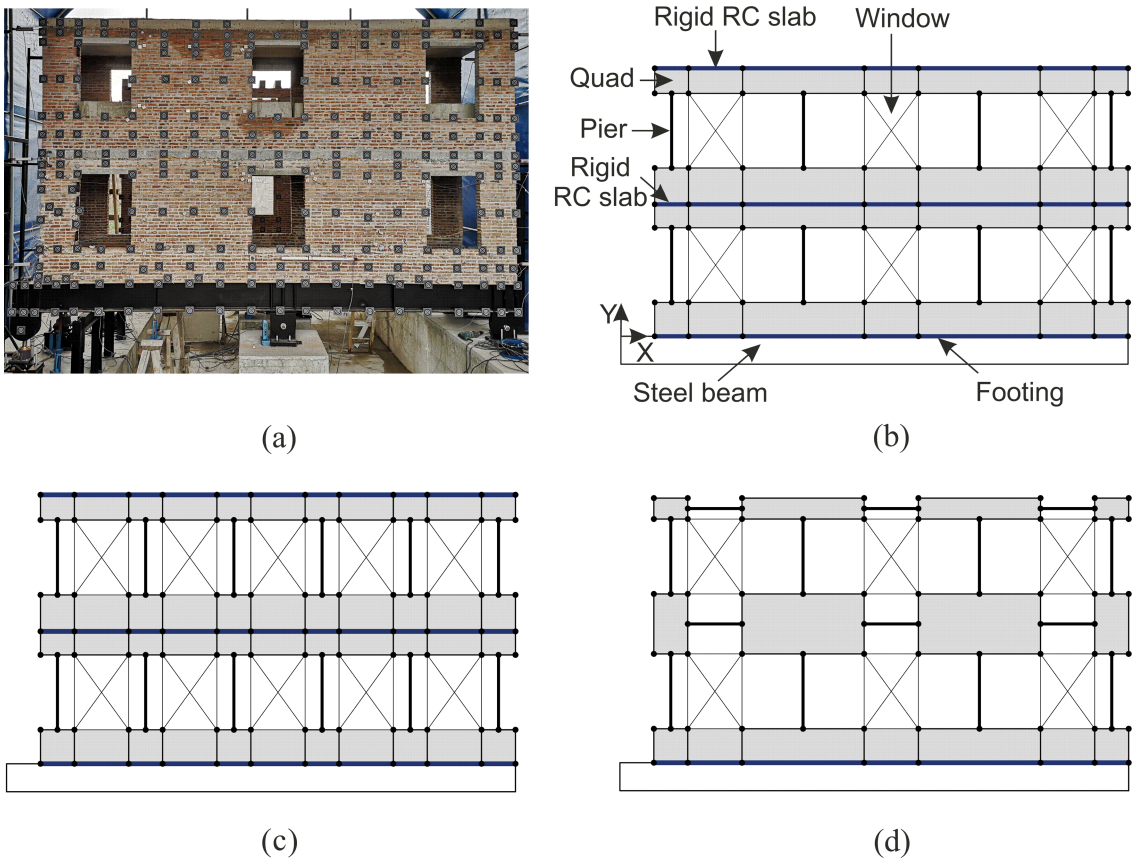


Figure 9.12: EQFdc model idealisations of the buildings: (a) 3O-RF building experimental setup, (b) 3O-RF model, (c) 5O-RF model, (d) 3O-JF model.

9.5.2 Loading scenario

The loading scenarios are examined in terms of structural weights and settlement applications. Accordingly, the 3O-RF-W1, 3O-RF-W3, 5O-RF-W1 and 3O-JF-W1 experiments are examined in this chapter. W1 and W3 weight arrangements are presented in Figures 9.4(a) and 9.4(c). For the 3O-RF-W2 experiment, since the W2 weight arrangement did not lead to notable difference in the building responses of the 3O-RF building compared to the W1 case (Dalgic et al., 2023), the W2 weight condition is not examined in this section. The unit weights of the masonry and RC materials used for the buildings are 18 kN/m^3 and 25 kN/m^3 (Dalgic et al., 2021). First, to simulate the loads applied in the W1 case in the EQFdc model, the self-weights of the pier and quad elements are determined. Then, the kentledge loads are applied to the model by increasing the unit weight of the slabs as $\gamma_{slab} = 111.25$ kN/m^3. To represent the W3 weight arrangement, the unit weight of all quad elements in contact with the steel beam, $\gamma_{ground\ quad}$ is defined by considering the weights of the water tanks placed inside the windowsills and the self-weight of the masonry section in that location, as $\gamma_{ground\ quad} = 82$ kN/m^3. The structural weights of each slab and quad element are represented in the model as external vertical forces. The self-weights of the pier and spandrel elements are implemented as the element loads into the model (Section 3.4.5).

For the definition of input greenfield vertical displacements in the model, the target Gaussian greenfield settlement profile is used, which indicates good agreement with the DIC-measured settlement profile at the top flange of the steel beam, as stated by Dalgic et al. (2023). The horizontal displacements measured by the DIC at the top flange of the steel beam are also implemented into the model as input prescribed deformations.In the experiments, the horizontal displacements determined at the steel beam were negligible compared to the vertical displacements, in which maximum horizontal displacement was measured as 5 mm at the tip settlement of 67 mm for the 3O-RF-W1 experiment.

9.5.3 Steel-building interface model

The soil-foundation interaction was not in the scope of the Turkey settlement tests project. The experimental buildings do not incorporate a foundation system and the steel beams only exist to transfer the vertical displacements applied through the screw jack (representing a tunnelling-induced settlement distribution curve along the steel beam) to the buildings. The determination of interface parameters used to simulate the experiments therefore differs from the soil-foundation interface calibration analyses described in the previous chapter.

The contact between the steel beam and the base of the masonry walls comprised mortar joints. Dalgic et al. (2021) defined the interface properties as frictional in shear and no-tension in the normal direction, allowing the gapping behaviour in the 3D FE predictions of the building tests. Since a S2M soil-foundation interaction model represents the frictional shear behaviour and the nonlinearity in the normal direction (Burd et al., 2022), it was used to model the steel-building interface. In this case, Young's modulus and the unit weight of the footing elements are defined as zero to remove the effect of footing elements in the steel-building interface model.

To directly transfer the input greenfield displacements to the footing elements, relatively stiff (compared to the footing stiffness) vertical and horizontal stiffness values are used in the steel-building interface model. To represent the frictional interface behaviour in shear, the interface friction coefficient is adopted as consistent with the material characteristics presented by Ispir (2010) and Dalgic et al. (2021). Additionally, the limiting uplift pressure is assigned as zero to simulate the no-tension behaviour in the normal direction while presenting a linear elastic relationship in compression. Thus, the steel-building interface model can be expressed as a frictional sliding (based on Equation 2.21) and no-tension model. The steel-building interface parameters used in the EQFdc model implementation of the buildings are given in Table 9.2.

Table 9.2: Steel-building interface parameters used in the EQFdc model implementation.

	Parameters	Value
Steel-building interface	Horizontal soil stiffness, K_h	0.1 GPa
	Vertical soil stiffness, K_v	0.1 GPa
	Interface friction coefficient, μ_s	0.61
	Softening parameter, a_v	0
	Limiting uplift resistance, p_t	0
	Lateral earth pressure coefficient, K_0	0

9.5.4 Masonry constitutive model

For the EQFdc model analysis, the plasticity based nonlinear models are used to model the masonry behaviour as described Chapter 6. The nonlinear constitutive models used for the beams, quads and the structural interface elements are identical to the ones given in Table 8.5.

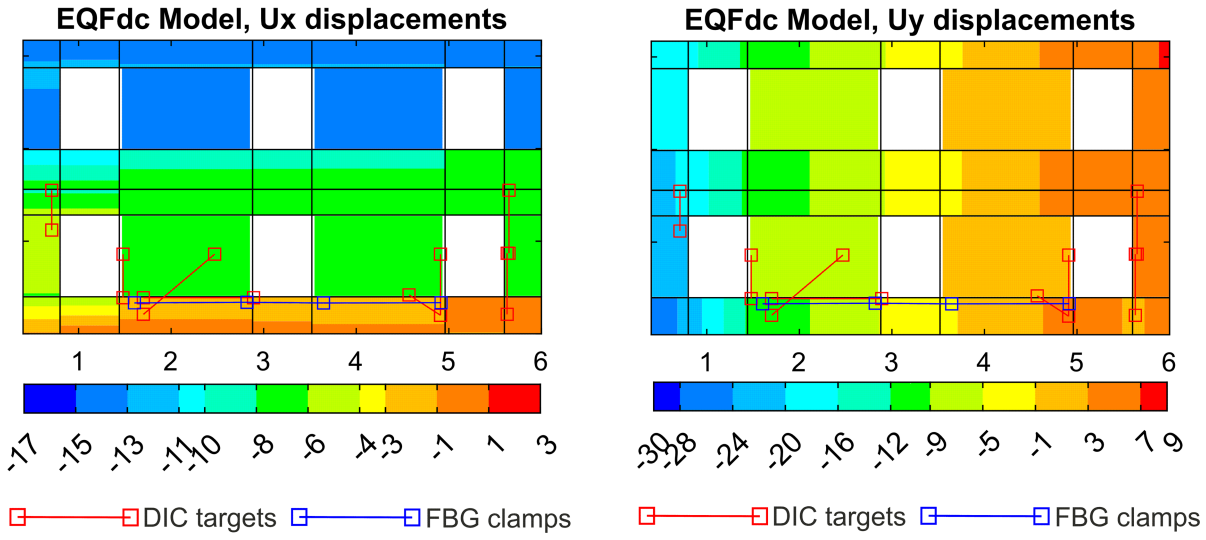
The material characteristics such as Young's modulus, Poisson's ratio, unit weight of the masonry and the RC slabs are adopted from the 3D FE predictions (Dalgic et al., 2021) (Table 9.3). The friction angle value suggested by Ispir (2010) and adopted in Dalgic et al. (2021), was used. For the EQFdc model analysis, the tensile strength of masonry, σ_T, is chosen as 0.1 MPa after conducting a parametric study to determine the value that captures the vertical displacement behaviour for all experiments.

Table 9.3: Parameters adopted from the 3D FE predictions for the masonry façade and the RC slab (modified after Dalgic et al., 2021).

	Parameters	Value
Masonry façade	Unit weight, γ_m	18.0 kN/m^3
	Young's modulus, E_m	3.0 GPa
	Tensile strength of masonry, σ_T	0.1 MPa
	Poisson's ratio, ν_m	0.15
	Friction angle, φ_i'	31°
RC slab	Unit weight, γ_{RC}	25.0 kN/m^3
	Young's modulus, E_m	34 GPa
	Poisson's ratio, ν_m	0.20

9.6 Interpretation of DIC and FBG Measurements

The DIC measurements were processed first to determine the vertical displacements at the top flange of the steel beam (i.e. the applied settlement profile) and at the wall base to represent the building response at the end of the loading tests. Secondly, the DIC measurements are used as crack gauges (defined as 'virtual LVDTs' in the Video Gauge software), in which the DIC targets orthogonal to the crack propagation are chosen as the end points of the virtual LVDTs and the relative axial displacement, Δu between these DIC targets are defined as the crack width. To compare the crack widths from the DIC measurements with the EQFdc model results, first, the global displacements are computed at the locations corresponding to the specified DIC target coordinates in the EQFdc model. Then Δu is calculated in the local coordinates of the virtual LVDTs.



(a) (b)

Figure 9.13: EQFdc model global displacement contours for the 3O-RF-W3 test (contour dimensions: mm): (a) horizontal displacements, (b) vertical displacements.

Similarly, the comparison between the FBG measurements and the EQFdc model results are presented in terms of relative axial displacements. To achieve this, Δu computed from the FBG total strain measurements at the end of the loading stage are compared with Δu determined

from the displacements computed at the corresponding locations of the FBG clamps in the EQFdc model. Figure 9.13 shows the global horizontal and vertical displacement contours computed from the EQFdc model for the 3O-RF-W3 test analysis, showing the placement of DIC target (the DIC targets are connected to represent working as the crack gauges) and FBG clamp locations in the model.

The relative axial displacements computed at the crack locations determined from the DIC and FBG measurements are compared with the EQFdc model results to estimate the damage class of the building according to the standard building damage classification system (Table 1.1) considered in half-scale (experimental model scale) (Burland & Wroth, 1974; Boscardin & Cording, 1989). To estimate the damage class of the model buildings, Dalgic et al. (2023) used the relationship between the damage class and the maximum crack widths determined at the end of the experiments, considering the half-scale of the standard building damage classification system. Thus, the limiting crack widths for the corresponding damage classes in half-scale are arranged as: < 0.05 mm (negligible), 0.05 – 0.5 mm (very slight), 0.5 – 2.5 mm (slight), 2.5 – 7.5 mm (moderate), 7.5 – 12.5 mm (severe) and > 12.5 mm (very severe).

9.7 Results and Comparisons

9.7.1 3O-RF-W1 test and analysis results

Firstly, the EQFdc analysis is performed for the 3O-RF-W1 experiment to provide a basis for the further comparisons to examine the effect of structural weight, façade openings and the floor structures. Figure 9.14 shows the comparison of the vertical displacement responses. The tip settlements applied to the 3O-RF-W1 building is 67 mm. According to the experimental results, the 3O-RF-W1 building behaved almost rigidly and rotated around the mid support resulting in a large gap between the wall base and the steel beam (Figure 9.14). The EQFdc model captures the DIC displacements well; a small discrepancy is observed between the

results towards the end of the wall.

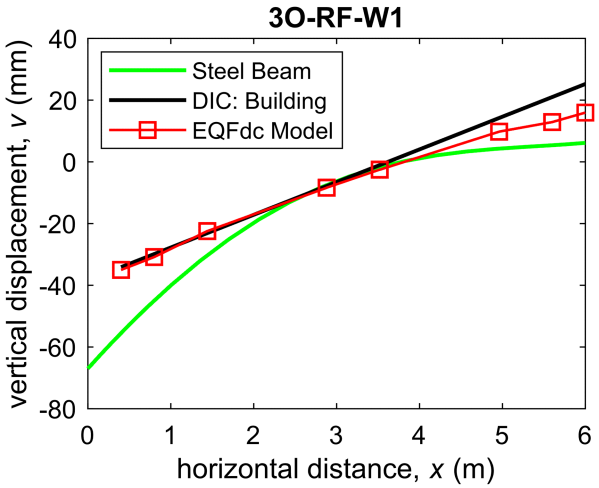


Figure 9.14: Vertical displacements at the wall base for 3O-RF-W1.

In the experiments, the 3O-RF-W1 building experienced almost no damage in the front wall other than a vertical crack that occurred under the central window at the ground storey (Figure 9.15b). To investigate the damage distributions on the wall, the major principal tensile strain, ε_1 distributions (Figure 9.16a) and the plastic failure point locations (Figure 9.16b) determined from the EQFdc model are plotted in Figure 9.16. High magnitude ε_1 strains are seen to occur at the top edges of the external ground storey piers, where the tensile plastic points are formed. However, during the experiment no damage was observed at those locations. This might be associated with very small cracks that might have occurred during the experiment but could not be captured by the monitoring methods. As demonstrated in Chapter 8, once the tensile strength is exceeded in the plasticity-based models, the strain increases in that location substantially. However, since the gap between the wall and the steel beam did not close at the end of the loading, this does not necessarily indicate large cracking. It is noteworthy that the limiting tensile strain criteria (Table 1.1) may not be indicative of cracking, therefore direct strain and virtual LVDT measurements will be used to evaluate the EQFdc results.

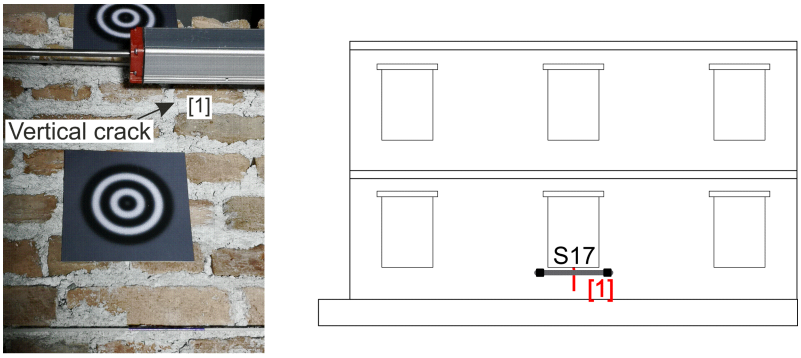


Figure 9.15: Crack distributions observed in 3O-RF-W1: (a) crack [1] on the front wall, (b) schematic demonstration of the crack [1] and sensor location.

The width of the central vertical crack in Figure 9.15 is measured as 1.0 mm by the DIC. However, the relative axial displacement, Δu in the location is computed as 0.1 mm from the EQFdc model (Table 9.4). While Δu measured by both the DIC (for crack no: [1]* in Table 9.4) and the FBG (for sensor no: S17* in Table 9.4) refer to 'slight' damage for the central vertical crack, Δu determine from the EQFdc model is associated with the 'very slight' damage.

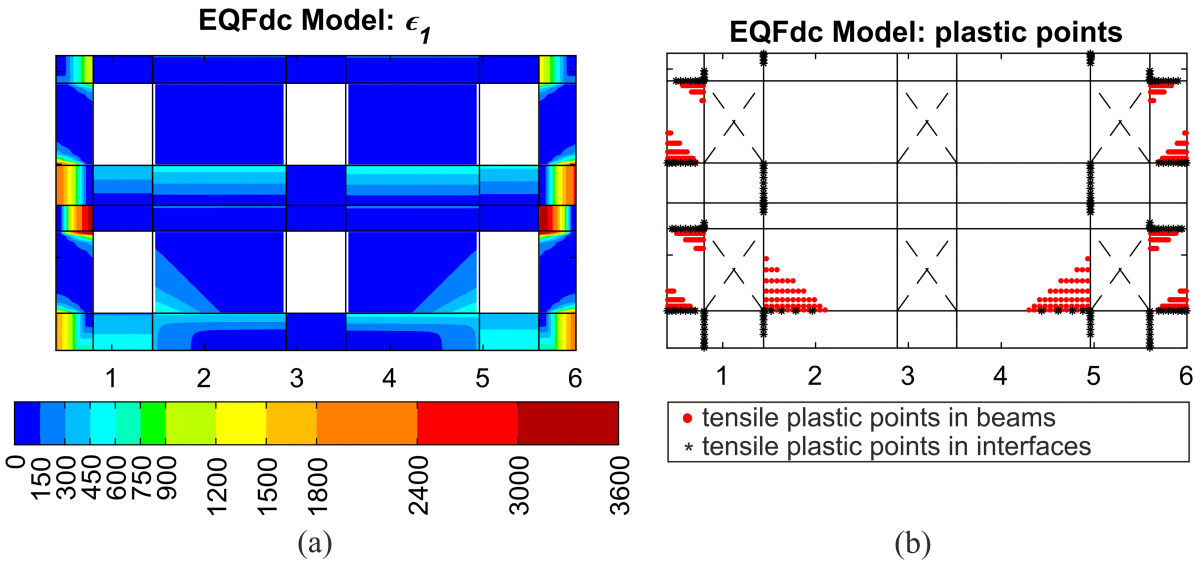


Figure 9.16: Comparison of the response of the 3O-RF-W1 test with the EQFdc analysis results: (a) major principal tensile strain distributions, (b) plastic point locations.

Alternatively, using a special beam element instead of the macro-element under the ground-storey window, which can interact with the steel beam (or footing elements in the EQFdc model formulations), might better capture this cracking behaviour. However, for the simplicity of the

model, macro-elements are used to represent the interaction between the steel beam and the building in a straightforward manner.

9.7.2 3O-RF-W3 test and analysis results

The effects of additional structural weight on the building responses are examined by the 3O-RF-W3 experiment. Considering the vertical displacements measured by the DIC, no gap opening was observed between the wall base and the steel beam for the 3O-RF-W3 building (Figure 9.17). The EQFdc model also captures this no gapping behaviour, consistent with the DIC building response.

Closure of the gap between the wall and the steel beam caused crack formations on both front and the back walls, symmetrically. Accordingly, the experimental results for the 3O-RF-W3 showed that the cracks were developed as: splits, which are labelled as [1], [7], and [8], at the top and bottom edges of the external ground-storey pier elements, the horizontal and diagonal cracks labelled as [2], [3], [4], [5] and [6] around the corners of the openings at the ground floor, which extend towards the centre of the façade (Figure 9.18a). The schematic distribution of cracks and the critical FBG sensor locations for the 3O-RF-W3 experiment are illustrated in Figure 9.18(b).

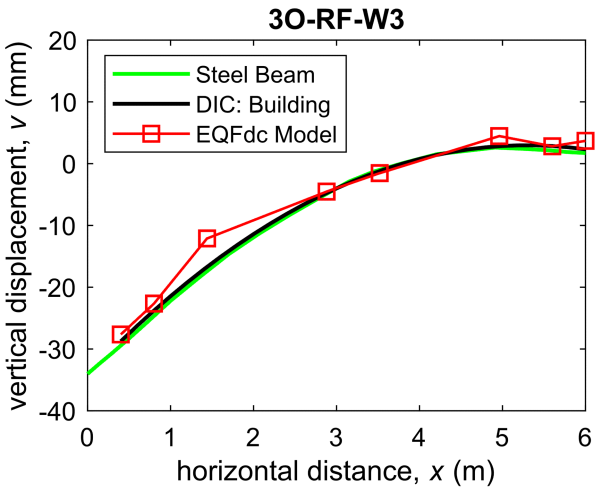
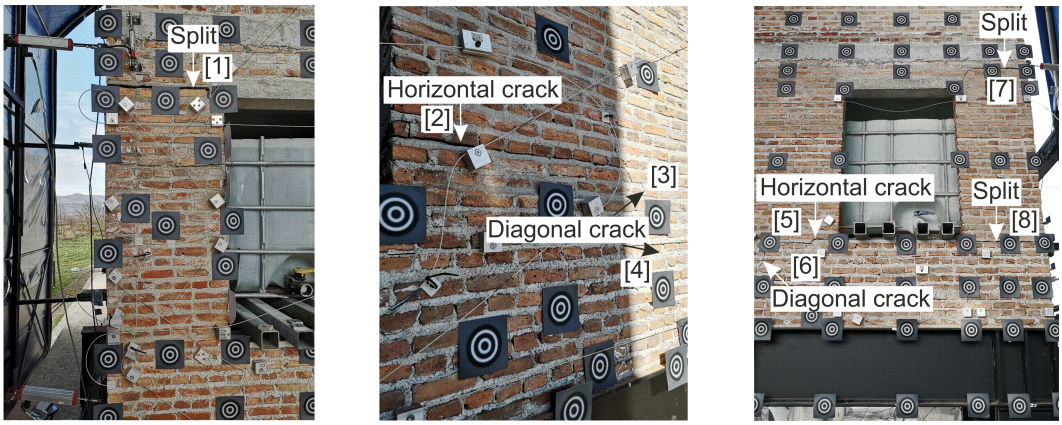
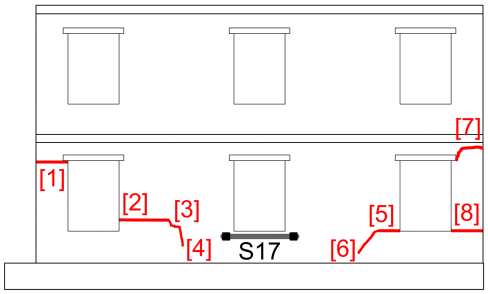


Figure 9.17: Vertical displacements at the wall base for 3O-RF-W3.

The analysis results from the EQFdc model represents the high magnitude tensile strains accumulated at the top and bottom edges of the external piers and at the top edges of the ground storey macro-elements (Figure 9.19a), where tensile plastic failures are observed at those locations (Figure 9.19b). The EQFdc model analysis results show that the failure mechanisms are mainly caused by tensile plastic failure in the piers and structural interface elements (Figure 9.19b). Although all the structural elements are modelled with the nonlinear constitutive relationships in these analyses, the quad and beam elements behaved as linear elastic in shear behaviour; in contrast, some fibre beams and interface elements sections reached tension plasticity (Figure 9.19b). Both the locations of the high magnitude ε_1 strains and the plastic points match with the locations of the cracks (Figure 9.18).



(a)



(b)

Figure 9.18: Crack distributions observed in 3O-RF-W3: (a) cracks on the front wall, (b) schematic demonstration of the crack and sensor locations.

Comparison of Δu determined from the DIC, FBG measurements and the EQFdc model for the

3O-RF-W1 and 3O-RF-W3 experiments at the corresponding crack and FBG sensor locations are presented in Table 9.4. For each Δu comparison, the associated damage classes based on the half-scale of the standard building damage classification system (Burland & Wroth, 1974; Boscardin & Cording, 1989) are also presented in Table 9.4. For the cracks [2], [5], [6] and [7], the EQFdc model presents close results to the DIC measurements and refers to the same damage classes. Regarding crack [1], although there is a significant difference in Δu results from the DIC and the EQFdc, both results indicate the same damage class. Similarly, the width of crack [8] is also underestimated; in this case, the difference in Δu results also change the damage classes that the DIC and the EQFdc predict. The damage on the top and bottom edges of the piers seem to spread around a larger area (Figure 9.19b) compared to the split cracking observed in the experiment (Figure 9.18). It appears that the use of plastic constitutive laws without softening smears the crack over a wider region and underestimates crack width.

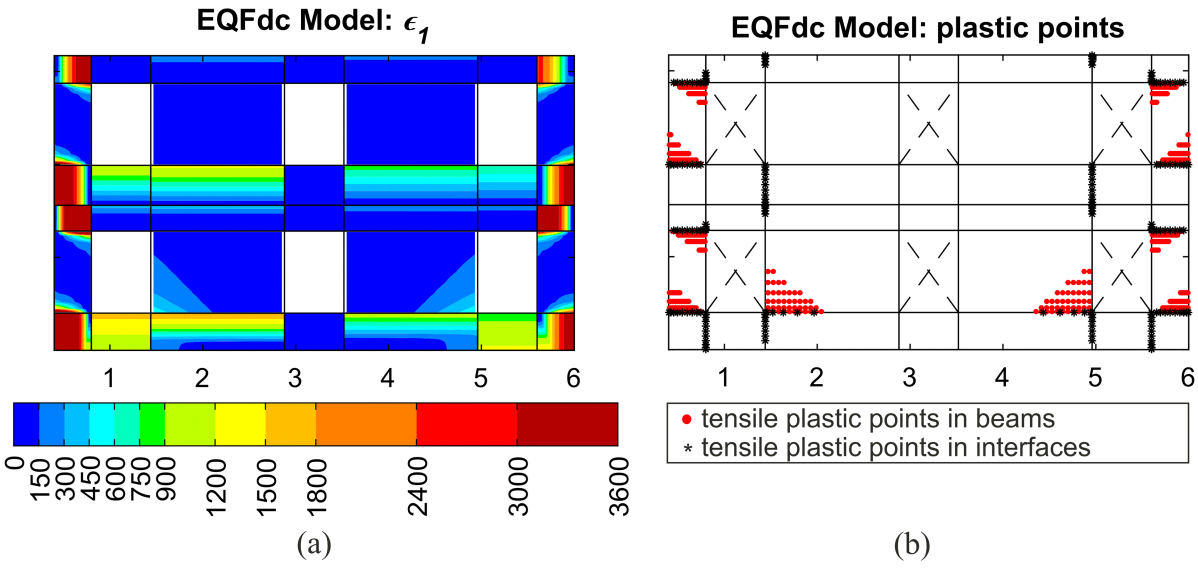


Figure 9.19: Comparison of the response of the 3O-RF-W3 test with the EQFdc analysis results: (a) major principal tensile strain distributions, (b) plastic point locations.

Potentially, using an advanced level constitutive model can capture the split cracking behaviour better than the implemented plasticity models. In this regard, a plasticity model with softening behaviour has been investigated for the beam elements. However, due to the high

computational time (from a few hours to days) required to complete the analysis with the softening behaviour, the current plasticity models (i.e. without softening) are used for the rest of the analysis.

Table 9.4: Comparisons between Δu results determined from the DIC and FBG measurements and the ones computed from the EQFdc model for the 3O-RF-W3 experiment.

	Crack no	DIC, Δu (mm)	EQFdc model, Δu (mm)	DIC: damage class (based on ½ experiment scale)	EQFdc model: damage class (based on ½ experiment scale)
DIC measurements vs. EQFdc model comparisons	[1]	7.4	3.1	moderate	moderate
	[2]	4.2	3.7	moderate	moderate
	[3]	2.0	3.0	slight	moderate
	[4]	1.0	0.0	slight	negligible
	[5]	3.8	2.6	moderate	moderate
	[6]	2.6	2.8	moderate	moderate
	[7]**	1.2	1.1	slight	slight
	[8]	6.0	1.2	moderate	slight
	[1]*	1.0	0.1	slight	very slight
FBG measurements vs. EQFdc model comparisons	FBG sensor	FBG, Δu (mm)	EQFdc model, Δu (mm)	FBG: damage class (based on ½ experiment scale)	EQFdc model: damage class (based on ½ experiment scale)
	S17	0.6	0.1	slight	very slight
	S17*	0.8	0.1	slight	very slight

* Refers to only the 3O-RF-W1 test and analysis results.

** The maximum crack width for the crack [7] is measured as 1.2 mm by the DIC at the end of the final loading stage. However, the split [7] in Figure 9.18 corresponds to approximately 6.5 mm crack width measured by a manual crack ruler after a long waiting period before the unloading stage, which demonstrates that this crack width increased after the maximum tip settlement was reached.

Another inconsistency in the Δu results are also observed for the crack [4] between the DIC measurements and the EQFdc model results. Since the axial and transverse displacements are constant within the quads, the relative axial displacement at the specified element height is zero. Considering the FBG and the EQFdc comparisons (Table 9.4), the EQFdc model presents

smaller values than the Δu results measured by the FBG sensors. This again can be explained due to using macro-elements at the ground storey in place of the beam elements. Alternatively, using the beam elements might lead to better agreement for Δu comparisons at these FBG sensor locations. As a result, although the building responses are compared under the different settlement applications, the effect of an increase in the structural weight can be easily observed from the change in damage distributions between the 3O-RF-W1 (Figure 9.15a) and 3O-RF-W3 (Figure 9.18a) experiments. Considering the maximum crack width obtained from the DIC measurements at the external pier, the damage class for the 3O-RF-W3 experiment is determined as 'moderate', which is consistent with the EQFdc model (Table 9.4).

9.7.3 5O-RF-W1 test and analysis results

For 5O-RF-W1, the EQFdc model successfully reproduces the vertical displacements measured by the DIC at the wall base, which follows the steel beam displacements without any base gaps (Figure 9.20).

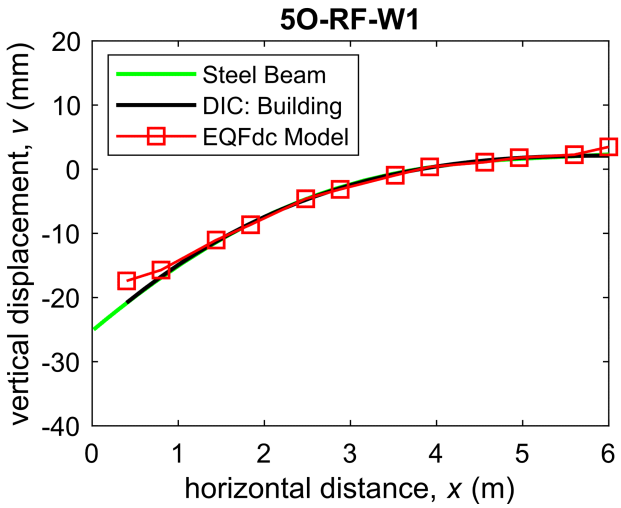
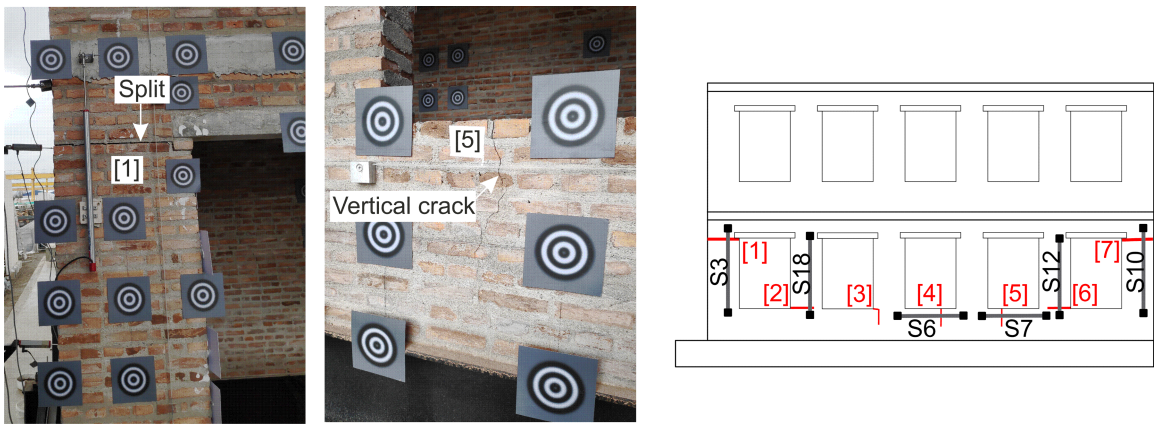


Figure 9.20: Vertical displacements at the wall base for 5O-RF-W1.

The increase in the façade openings caused the building to become more prone to damage. This can be clearly distinguished from the crack distributions observed at the maximum tip settlement of 25 mm applied for the 5O-RF-W1 experiment (Figure 9.21) compared to the 3O-

RF-W1 experiment with the maximum tip settlement of 67 mm, which the building experienced only 'slight' damage (Figure 9.15). The crack distributions measured from the 5O-RF-W1 experiment at the ground storey comprise the splits ([1], [7]), developed at the top edges of the external pier elements, the horizontal cracks ([2], [6]) near the bottom corners of windows and the vertical cracks ([3], [4], [5]) under the windows (Figure 9.21).

The major principal tensile strain distributions highlights the increasing magnitude of strains at the top and bottom edges of the external piers; this can be related to the split cracks observed in these piers (Figure 9.22a). The plastic points (Figure 9.22b) accumulate at these locations. Additionally, the high strain localisations at the ground macro-elements (Figure 9.22a) can be associated with the vertical and horizontal cracking behaviour observed around the bottom edges of windows at the ground storey (Figure 9.21b).



(a) (b)

Figure 9.21: Crack distributions observed in 5O-RF-W1: (a) cracks on the front wall, (b) schematic demonstration of the crack and sensor locations.

In terms of comparing the relative axial displacements, overall, the EQFdc results compare well with the DIC measurements except for the cracks [1], [6] and [7], which consist of splits and horizontal cracks at the top and bottom edges of the pier elements. Δu results measured by the FBG sensors (S3, S12 and S10), which are placed orthogonal to these crack locations ([1], [6] and [7]) indicated larger cracks than the EQFdc model. Similar to the argument mentioned

for the split cracks earlier, the damage seems to smear over a larger area in the simulations rather than affecting only the top and bottom edges of the piers (Figure 9.22b). Potentially, using advanced level nonlinear constitutive models for the structural elements could capture Δu results better. For the rest of the DIC, FBG and the EQFdc comparisons, all the Δu results imply the same damage classes (Table 9.5).

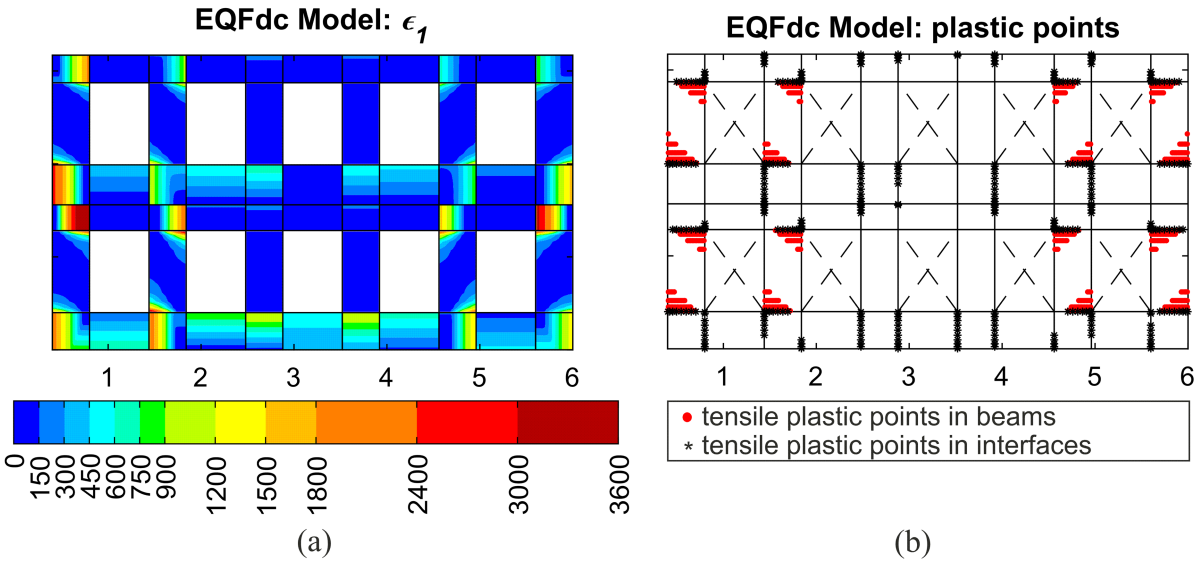


Figure 9.22: Comparison of the response of the 5O-RF-W1 test with the EQFdc analysis results: (a) major principal tensile strain distributions, (b) plastic point locations.

Overall, considering the maximum crack width determined for the split crack [7], the damage class of the 5O-RF-W1 building is determined as 'moderate' according to the DIC and the FBG (sensor no: S10) measurements. However, the EQFdc model defines the standard building damage class as 'slight' damage considering the maximum Δu determined as less than 2.5 mm by the EQFdc model.

9.7.4 3O-JF-W1 test and analysis results

For 3O-JF-W1, the EQFdc model demonstrates consistent vertical displacement results with the DIC measurements without creating any gap openings between the wall base and the steel beam (Figure 9.23). The maximum tip settlement applied in 3O-JF-W1 was 32 mm; at this settlement the building suddenly experienced 'very severe' brittle damage. Figure 9.24(a)

shows the vertical crack along the façade height and the unseated lintel. The schematic representation of the crack distributions with the FBG sensors nearby is presented in Figure 9.24(b).

Table 9.5: Comparisons between Δu results determined from the DIC and FBG measurements and the ones computed from the EQFdc model for the 5O-RF-W1 experiment.

	Crack no	DIC, Δu (mm)	EQFdc model, Δu (mm)	DIC: damage class (based on ½ experiment scale)	EQFdc model: damage class (based on ½ experiment scale)
DIC measurements vs. EQFdc model comparisons	[1]	3.7	1.8	moderate	slight
	[2]	1.9	1.8	slight	slight
	[3]	1.3	1.0	slight	slight
	[4]	0.8	0.5	slight	slight
	[5]	1.9	0.7	slight	slight
	[6]	3.0	0.1	moderate	very slight
	[7]	4.9	0.2	moderate	very slight
FBG measurements vs. EQFdc model comparisons	FBG sensor	FBG, Δu (mm)	EQFdc model, Δu (mm)	FBG: damage class (based on ½ experiment scale)	EQFdc model: damage class (based on ½ experiment scale)
	S3	3.5	1.4	moderate	slight
	S6	0.9	0.5	slight	slight
	S7	1.2	0.6	slight	slight
	S10	3.7	0.7	moderate	slight
	S12	2.0	0.5	slight	slight
	S18	2.0	0.8	slight	slight

* The strain measurements for the FBG S10 sensor were stopped and strain clamps were released after the specified strain value in this experiment.

The damage behaviour of the building observed in the experiment is compared with the analysis results determined from the EQFdc model by examining the major principal tensile strain (Figure 9.25a) and the plastic failure point distributions (Figure 9.25b). Accordingly, the vertical cracks along the façade height shown as [1], [2] and [3] in Figure 9.24(a) are consistent with the high strain magnitudes at the spandrel and the macro-elements around the central windows observed in the analysis (Figure 9.25a). A similar damage pattern is also captured

through the tensile plastic points developed especially at the central spandrel elements and the surrounding vertical interfaces (Figure 9.25b).

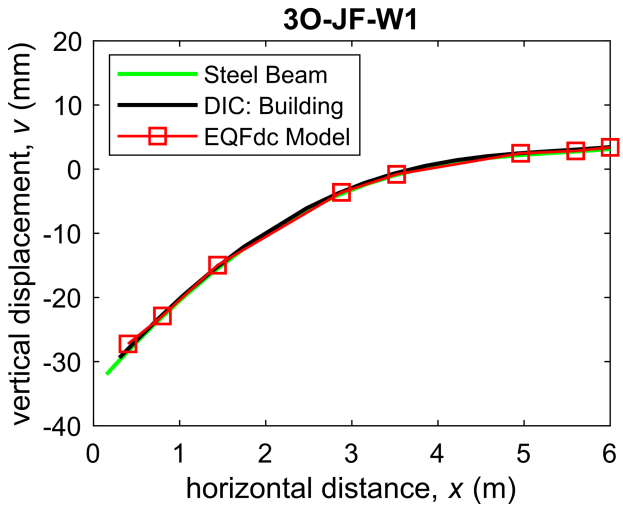
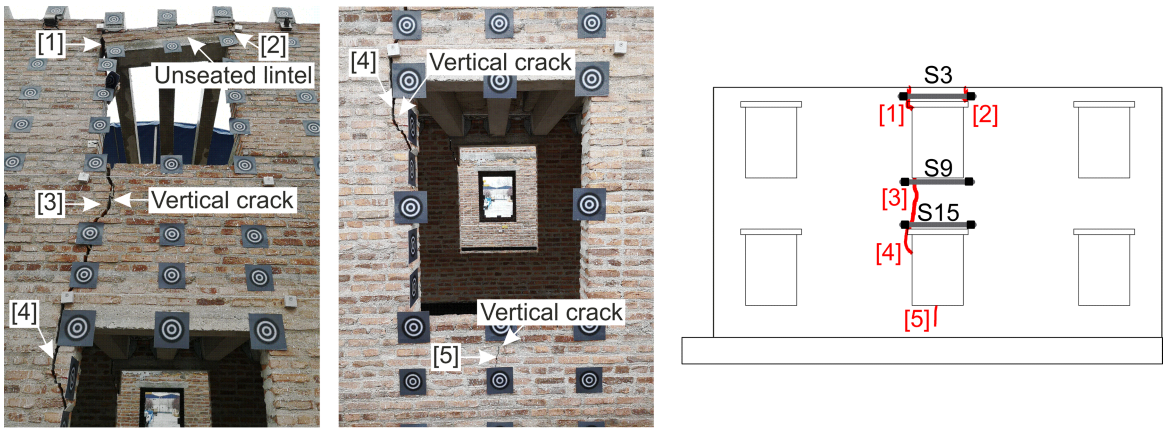


Figure 9.23: Vertical displacements at the wall base for 3O-JF-W1.



(a) (b)

Figure 9.24: Crack distributions observed in 3O-JF-W1: (a) cracks on the front wall, (b) schematic demonstration of the crack and sensor locations.

The comparison between the relative axial displacements determined from the DIC and FBG measurements and the EQFdc model are presented in Table 9.6. Considering the crack widths determined from the DIC measurements over 12.5 mm (cracks [1], [2], [3] and [4] in Figure 9.24), the façade experienced 'very severe' damage according to standard building damage classifications (Burland & Wroth, 1974; Boscardin & Cording, 1989). However, the EQFdc model predicts the damage class as 'severe' for these cracks (in which Δu is less than 12.5

mm). On the other hand, the crack [5] is associated with the 'moderate' damage class considering both the DIC and the EQFdc Δu results.

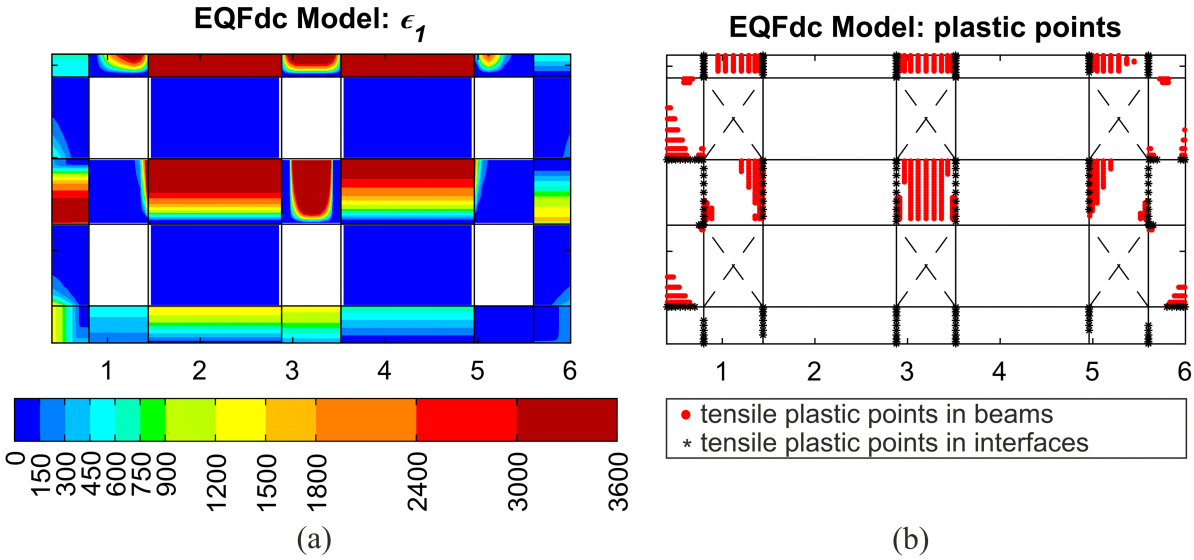


Figure 9.25: Comparison of the response of the 3O-JF-W1 test with the EQFdc analysis results: (a) major principal tensile strain distributions, (b) plastic point locations.

Table 9.6: Comparisons between Δu results determined from the DIC and FBG measurements and the ones computed from the EQFdc model for the 3O-JF-W1 experiment.

	Crack no	DIC, Δu (mm)	EQFdc model, Δu (mm)	DIC: damage class (based on ½ experiment scale)	EQFdc model: damage class (based on ½ experiment scale)
DIC measurements vs. EQFdc model comparisons	[1]	33.1	8.6	very severe	severe
	[2]	18.8	8.6	very severe	severe
	[3]	19.1	11.5	very severe	severe
	[4]	12.7	5.3	very severe	moderate
	[5]	4.2	2.8	moderate	moderate
FBG measurements vs. EQFdc model comparisons	FBG sensor	FBG, Δu (mm)	EQFdc model, Δu (mm)	FBG: damage class (based on ½ experiment scale)	EQFdc model: damage class (based on ½ experiment scale)
	S3	6.1	16.7	moderate	very severe
	S9	8.0	11.2	severe	severe
	S15	11.2	8.2	severe	severe

The FBG sensors measured high magnitude strains for the cracks classified as 'severe'. While comparing the FBG measurements from sensors of S3, S9 and S15 with the EQFdc analysis

results, Δu is determined from the nearby quad elements since the FBG clamps are located outside of the spandrel elements in these sections (Figure 9.24b). For Δu results corresponding to S9 and S15 sensor locations, both the FBG measurements and the EQFdc model indicate 'severe' damage class considering Δu over 7.5 mm. For the S3 sensor location, the EQFdc model computes Δu = 16.7 mm, which is almost the total of the crack widths of [1] and [2] in Table 9.6. This numerical result is expected considering the S3 sensor is placed longer than the length of the spandrel over the window (Figure 9.24b). However, S3 sensor gives smaller Δu value for this spandrel. This is mainly caused by the fact that the cracking occurred just next to both FBG clamps for the S3 sensor (Figure 9.24a) in the experiment and the stability of the clamps; the strain measurements are therefore affected by this 'very severe' collapse (labelled as 'unseated lintel' in Figure 9.24a). Thus, a meaningful comparison between the FBG measurements and the EQFdc model for the S3 sensor is not possible.

Overall, the EQFdc model captures the masonry portions that experienced brittle damage in the experiment even though the damage class is identified as 'severe' by the EQFdc model compared to the 'very severe' damage determined by the DIC measurements.

9.8 Conclusion

In this chapter, the EQFdc model analyses are conducted to simulate the 3O-RF-W1, 3O-RF-W3, 5O-RF-W1 and 3O-JF-W1 experiments. The analysis results determined from the EQFdc model are compared with the DIC and FBG monitoring measurements. The analyses results show that the EQFdc model can reproduce the vertical displacement behaviour and can capture the overall damage distributions of the buildings. However, in its current form, EQFdc model features some limitations. While computing the relative axial displacements at the split crack locations (which correspond to the piers' top or bottom edges) and at the vertical cracks, which occurred inside the macro-elements, the EQFdc model presents smaller values than the DIC

and the FBG results. For the split cracking behaviour, considering plastic points locations in the EQFdc model results, the damage implied by the model seems to spread to a larger area instead of localising at the element edges as in the experiments. This smearing may explain why the models predicted smaller relative axial displacements than the DIC results. This discrepancy can be resolved by using softening nonlinear constitutive models and accounting for shear-tensile failure interactions for the beam elements. To capture the vertical cracks inside the macro-elements, using a finer mesh or using higher order beam elements may be explored. However, specifically capturing these cracks may not be necessary since the EQFdc model is intended to broadly capture damage mechanisms rather than simulating specific cracks. In conclusion, the EQFdc model can capture the overall effects of structural weight, façade openings and floor structures on the building damage responses. This highlights the clear advantage of the EQFdc model, which can be an additional tool (for example as Stage 2b) to the simple beam model used in Stage 2 analysis.

Chapter 10

Conclusion

10.1 Research Contributions

10.1.1 Development of EQFdc modelling approach

To represent the detailed 3D masonry building geometry with an intermediate complexity model as a combination of beam and 2D macro-elements by considering the layout of façade openings (research objective 1 in Section 1.2), a novel approach is developed in this thesis by idealising the masonry building as 'equivalent frame model with deformable connectors' (EQFdc model).

- **EQFdc idealisation of the masonry building**

Existing methods available in the literature to idealise the masonry buildings' geometry vary from elastic simple beam models to 3D FE continuum models. Although the equivalent frame models with rigid connectors and the macro-element models are widely used in the earthquake engineering field, this research presents the first application of these modelling techniques for the tunnel-soil-building interaction problem. Preliminary work on adopting equivalent frame models resulted in an overestimation of building stiffness and a consequent underestimation of building displacements due to the use of rigid connectors (Gulen et al., 2021). Other investigations demonstrated that modelling the masonry building with only macro-elements

required using a fine mesh of macro-element discretisation to capture the strain distributions (similar to the beam elements) on the façade (Gulen et al., 2022). Thus, the EQFdc modelling approach was developed to combine the advantages of equivalent frame and macro-element modelling. This approach enables effective representation of the beam-like behaviour of piers and spandrels and replaces the rigid connectors between spandrel and pier elements with deformable connections.

- **Implementation of flexibility-based beam formulations and fibre beam model**

To model the beam elements in the EQFdc model, the flexibility-based formulations of fibre beam models are developed. These formulations ensure modelling accuracy since they satisfy force equilibrium. They also facilitate the practical implementation of nonlinear material models as they require 1D constitutive models. The modelling work under this heading also contributes to the research objective about developing practical models to represent the nonlinear behaviour of the masonry.

- **Formulation of macro-elements as deformable connectors**

Rigid connectors are widely used in existing equivalent frame models (e.g. Lagomarsino et al., 2013; Bracchi et al., 2015). However, in the current research the rigid connectors are replaced by the deformable connectors, which are modelled with the macro-elements. This eliminates the overestimation of building stiffness caused by the rigid connectors and removes ambiguities associated to discretisation of pier and spandrel elements in equivalent frame models. Although the EQFdc model is developed within the context of the tunnelling problem in this thesis, the EQFdc modelling approach represents a significant modelling contribution and may be employed for the earthquake engineering field for the idealisation of masonry buildings.

More specifically, the finite element-based formulations developed for the macro-elements in this research differ from the existing formulations in the literature, which are based on discrete

element (Caliò et al., 2012) and finite element formulations (Minga, 2017). The new formulations feature four degrees of freedom (DOF) defined at the centre of the quad as presented in Section 3.5.1. Additionally, the shear behaviour is formulated with constant shear strain DOF in this research, which is different from using two diagonal internal springs inside the macro-element as presented by Caliò et al. (2012) and Minga (2017).

- **Major principal tensile strain calculations for the macro-elements**

Determination of major principal tensile strain distributions is required to estimate the damage class that the masonry building experiences due to tunnelling (Burland & Wroth, 1974; Boscardin & Cording, 1989). However, the existing macro-element models (Caliò et al., 2012; Minga, 2017) do not provide an interpretation of strain distributions inside the quad element. The formulation presented in Section 3.6.1 is a unique contribution of this research to the existing macro-element modelling methods. Overall, this contribution aligns well with the research objective of developing a practical numerical model for the assessment of the tunnelling-induced damage in the masonry buildings.

10.1.2 Development of soil-structure interaction modelling approach

- **Modelling of ground quad elements**

In existing macro-element modelling approaches (Caliò et al., 2012; Minga, 2017), the interaction of the masonry façade with the foundation system is not considered. Due to the importance of soil-structure interaction in the tunnelling problem, a practical method is presented in this research to represent the interaction of the embedded façade portion with the foundation system. Accordingly, the embedded portion of the façade is modelled as ground quad elements (in which the bottom edge of the quad is extended up to the centre of the strip

footing) and the connection between the quad element and the strip footing is represented by quad-footing interface elements.

- **Footing elements and axial springs**

As part of the soil-structure interaction modelling approach, rigid footing elements are modelled to connect the ground quads and the soil-foundation interface elements. The deformations between the adjacent rigid footing elements are represented by axial springs.

- **Implementation of 1D soil-foundation interaction model**

To investigate soil-structure interaction by using a 1D FE nonlinear Winkler soil-foundation interaction model (research objective 2 in Section 1.2). The S2M soil-foundation interaction model (Burd et al., 2022) is implemented into the EQFdc model. This model simply requires the input data of greenfield displacements and the parameters for the footing and soil-foundation interface. As a result, the model delivers the output data of soil tractions and allows the implementation of any soil-foundation interaction model into the code, which is formulated in a similar way.

- **Integration of greenfield displacements into the assessments**

To incorporate the tunnelling-induced ground displacements into the soil-foundation interaction model (research objective 3 in Section 1.2), greenfield displacements determined from the 3D FE models (Chapters 7 and 8) or the experimental monitoring results (Chapter 9) are implemented into the model as prescribed input deformations. The developed code also enables to compute greenfield displacements using Gaussian profiles (Section 2.3.1). This feature can significantly reduce the time and cost spent for the computational analysis in the industrial projects.

10.1.3 Practical representation of nonlinear masonry behaviour

To implement practical constitutive models to capture the nonlinear masonry behaviour (research objective 4 in Section 1.2), 1D Iwan models are used in parallel and series forms. The choice of the nonlinear constitutive model is an important aspect of efficiently representing the nonlinear masonry behaviour by reducing the complexities in the model formulations. Thus, this research presents the implementation of practical parallel and series Iwan models, which can mimic the nonlinear masonry behaviour of the jointed masonry model (Lasciarrea et al., 2019; Amorosi & Sangirardi, 2021). In summary, the elastic-perfectly plastic constitutive law is formulated by the parallel Iwan model for the following relationships:

i) axial stress-strain in fibre beam elements (plasticity is defined only in tension),
ii) internal shear strain behaviour in quad elements (plasticity is defined in both shear directions),
iii) normal traction and relative vertical displacements in normal tractions of structural interface elements (plasticity is defined only in tension).

The series Iwan model represents the shear force-strain relationship in beam elements, where the plasticity is defined in both shear directions. To overcome the convergence problem in the beam element level iterations, elastoplastic behaviour with linear hardening (plastic slope is as 1% of the elastic slope) is defined for shear force-strain relationship.

10.1.4 Settlement tests on half-scale buildings

As part of the Turkey settlement tests project (Dalgic et al., 2023), the settlement tests on half-scale buildings are conducted also during this DPhil study. The experiments aimed to investigate the damage responses of the buildings exposed to settlements (that mimic

tunnelling-induced settlement profiles) by considering the effect of structural weight, facade openings and the floor structures. The building responses are monitored by the DIC (displacement and crack width measurements) and FBG (average axial strain measurements) structural health monitoring methods.

In conclusion, this testing project provides valuable experimental data for the tunnelling problems, considering that there was no experiment in this scale before and the existing ones also ignored the effects of the floor structures. The experimental results demonstrated that masonry buildings become more prone to damage with increasing structural weight and façade openings and decreasing floor stiffness.

10.2 Validation of Numerical Model and Key Results

To validate the EQFdc model (research objective 5 in Section 1.2), the analyses results are compared with the results determined from: i) the DIANA 2D FE model elastic analysis (Chapter 7), ii) the PLAXIS 3D FE model (Amorosi & Sangirardi, 2021; Sangirardi, 2023 presented in Chapter 8) nonlinear analysis and iii) the half-scale settlement experiments (Chapter 9). The analysis results are evaluated in terms of building displacements, soil-foundation tractions, major principal tensile strain distributions and plastic failure point locations (research objective 6 in Section 1.2).

To compare strain results obtained from elastic FE continuum models, a radius search method is developed in this research. This method removes the mesh size dependency in the FE continuum models influenced by strain singularities at sharp corners and it enables comparisons between the newly developed EQFdc and reference FE continuum models.

Key results determined from the case studies and simulation of the experimental buildings are summarised in the following sections.

10.2.1 Linear elastic analysis comparisons

The linear elastic analysis results achieved from the EQFdc model are compared with the 2D FE continuum model generated in DIANA FEA software. The vertical and horizontal displacements computed at the footing elements of the EQFdc model are shown to match successfully with the DIANA model results at both central and eccentric tunnel conditions. A similar agreement is noted in the major principal tensile strain distributions, where the EQFdc model captures the DIANA model strain patterns and magnitudes. The resulting EQFdc model predicts the same damage classes as the DIANA model (after the application of the radius search method and corresponding strain removing around the corners of openings) when the maximum principal tensile strains are compared at each tunnel eccentricity. The linear elastic analysis comparisons demonstrate the success of the EQFdc model, which can be considered as an additional method (such as Stage 2b) to the simple elastic beam model (Burland & Wroth, 1974; Mair et al., 1996) used in Stage 2 of the tunnelling-induced damage assessment procedures.

10.2.2 Nonlinear analysis comparisons: elastic façade

The PLAXIS 3D FE continuum model (Amorosi & Sangirardi, 2021; Sangirardi, 2023) is used as a reference model for the numerical validations of the EQFdc model with the nonlinear analysis. Firstly, the façade is considered as linear elastic and the soil is modelled as nonlinear with the S2M soil-foundation interaction model (Burd et al., 2022), which is calibrated (Sangirardi et al., 2023) according to the soil model adopted for the Terrace gravel in the PLAXIS model.

As a result of the analysis comparisons, the EQFdc model successfully reproduces the vertical footing displacement responses determined from the PLAXIS model. However, some discrepancies are observed in the horizontal footing displacement responses between the

EQFdc and PLAXIS models, especially at the tunnel eccentricities of 5, 10 and 15 m, where the façade corner experiences significant horizontal compression (such as the horizontal greenfield displacement is around -20 mm at the specified façade corner). Further investigations show that the implemented S2M soil-foundation interaction model is the source of this discrepancy in horizontal footing displacements. However, the discrepancy induced by the S2M soil-foundation interaction model can still be considered as acceptable, since it is a simplified model and incorporates with the EQFdc model effectively to provide a preliminary damage assessment procedure. Subjecting the PLAXIS base displacements to the EQFdc model demonstrated that EQFdc models can accurately idealise structural response by localising strain concentrations and accurately predicting strain magnitudes.

10.2.3 Nonlinear analysis comparisons: nonlinear façade

For the further numerical validations of the EQFdc model with the PLAXIS model, the masonry façade is modelled using a nonlinear (elastoplastic) constitutive model. Consistent with the analysis with an elastic façade, the EQFdc model captures the overall building displacements computed by the PLAXIS model for the nonlinear façade case. Regarding the major principal tensile strain distributions and the plastic point comparisons, the EQFdc model can capture the general response of the PLAXIS model by identifying the elements that experience the most damage. However, due to the constant shear strain formulations adopted in the beam elements of the EQFdc model, the diagonal shear responses observed in the PLAXIS model could not be captured accurately.

In case of reducing the computational time required to complete a nonlinear tunnel-soil-structure interaction analysis (research objective 7 in Section 1.2), the EQFdc model requires less than a minute for the elastic façade case and the EQFdc model analysis takes from 2 to 35 minutes for the nonlinear façade case depending on the tunnel eccentricity in a consumer-grade

laptop (processor: Intel Core i7-1185G7 @ 3.00GHz 1.80 GHz, RAM: 16 GB). Although no special effort had been made to optimise the current EQFdc model for speed, it is considered likely that significant speed improvements could be achieved by optimising the code.

10.2.4 Nonlinear analysis comparisons: experimental results

In Chapter 9, the EQFdc model is employed for the simulation of the settlement tests on half-scale buildings. The EQFdc model analyses results are compared with the experimental results obtained from the DIC and FBG measurements based on the relative axial displacements. The EQFdc models successfully reproduce the vertical displacement response of the buildings compared with the DIC displacement measurements for each experiment (3O-RF-W1, 3O-RF-W3, 5O-RF-W1 and 3O-JF-W1). In terms of comparing the damage distributions measured by the DIC with the major principal tensile strain distributions and the plastic point locations, the EQFdc model is shown to capture the overall response of the damage distributions observed in the experiments. More specifically, considering the relative axial displacement comparisons, although there are limitations to capture the experimental results accurately (especially at the split crack locations and the cracks within the macro-elements), the EQFdc model can often predict the identical damage classes determined by the DIC and the FBG measurements.

10.3 Recommendations for Future Work

10.3.1 Improvements in nonlinear masonry models

An improvement can be considered for the nonlinear shear model used for the beam elements. Although the global failure modes in shear are captured well by the EQFdc model, the shear strain variations cannot be represented by the existing formulation where the shear strain is formulated as constant across the beam cross-section. This modification in the shear strain variations might capture the diagonal shear failures observed in the pier elements of the PLAXIS nonlinear façade model. As observed from the nonlinear analysis comparisons, once

the damage initiated in the model then the strains increase rapidly. This prevents making a meaningful comparison when determining the damage class based on strains.

10.3.2 Exploring building geometries with irregular openings

The existing equivalent frame models with rigid connectors in the literature (e.g. Lagomarsino et al., 2013; Bracchi et al., 2015; Quagliarini et al., 2017) includes uncertainties (Figure 2.10) for the determination of the pier element geometry as discussed in Section 2.4.1.3. This problem is solved by the developed EQFdc modelling approach by introducing the macro-elements as deformable connectors in the model idealisations. Building geometries with irregular façade openings are not examined in this thesis. However, the EQFdc modelling approach can also be applied to the buildings with irregular façade openings. Using macro-elements (i.e. deformable connectors) in the sections, where implementing beam elements is challenging is an advantage of the EQFdc model idealisation. Thus, the buildings with irregular façade openings can be practically represented by the EQFdc model.

10.3.3 Modelling complete building with the EQFdc model

The isolated façade modelling approach (Yiu et al., 2017a) can simulate the effects of ground displacements induced by the orthogonal tunnel with central and eccentric examples. However, in case of a non-negligible skew angle (e.g. 45 and 60 degrees of skew angle as examined by Amorosi & Sangirardi, 2021) between the building layout and tunnel central axis, modelling the complete building with step-by-step tunnel excavation analysis might be required to investigate the damage induced by the skew tunnel case. To model the complete building, there are alternative approaches that can be considered such as: i) connecting the front, rear and transverse façades modelled by the 2D EQFdc model together with tie elements as presented by Burd et al. (2000), ii) considering the effect of transverse walls by using beam elements attached to a 2D façade model as proposed by Prosperi et al. (2024) or iii) extending the current

EQFdc model formulations into 3D.

10.3.4 Investigating the effects of skew tunnelling and tunnel progression

Only the effects of the orthogonal tunnel (including eccentricities) with the single-step tunnel excavations are investigated in this research. For the skew angles over 45º, Amorosi and Sangirardi (2021) noted that the progress of the tunnel excavations needs to be considered to determine the transient effects on the building damage responses. To achieve this, further developments might be required for the S2M soil-foundation interaction model (Burd et al., 2022), which is currently formulated for monotonic loads. Then, the skew tunnel analysis can be conducted and the results can be compared with the ones determined from an advanced 3D FE model for further investigation.

10.3.5 Potential improvements to S2M soil-foundation interaction model

Modifying the S2M soil-foundation interaction model was not within the main research objectives of this thesis. However, some aspects of the S2M soil-foundation interaction model that are open to potential improvements are identified during the analysis comparisons. Accordingly, at specific tunnel eccentricities (Chapter 8), some discrepancies in the horizontal building responses are observed at the façade corner, which is exposed to significant horizontal greenfield displacements in compression. The S2M soil-foundation interaction model causes these discrepancies due to deficiencies in estimating the stiffening effect of building corners, which is neglected in the current model for simplicity. Potential improvements to consider the corner effects can improve the horizontal building response of the EQFdc model in comparison with advanced 3D FE models. Additionally, the constitutive models representing the loading

and unloading states in the S2M soil-foundation interaction model are needed to simulate tunnel excavation progress.

10.4 Final Research Outcomes

The research objectives defined in Section 1.2 mostly are achieved in the study. Considering the gap between the simple beam models and the advanced 3D FE models in the exiting tunnelling-induced damage assessment procedures, the developed EQFdc model provides alternative solutions to the current engineering practices. More specifically, the linear elastic EQFdc model can be an alternative to the simple elastic beam model used in Stage 2 damage assessments. Additionally, the nonlinear EQFdc model can be considered as a computationally efficient, intermediate complexity level damage assessment procedure that can be used as an additional step before adopting advanced 3D FE models.

References

Acikgoz, S., Fidler, P.R.A., Pascariello, M. N., Kechavarzi, C., Bilotta, E., DeJong, M. J. & Mair, R.J. (2022). A Fibre-optic Strain Measurement System to Monitor the Impact of Tunnelling on Nearby Heritage Masonry Buildings. *International Journal of Architectural Heritage*, 16:9, 1347-1365.

Addenbrooke, T. I., Potts, D. M. & Puzrin, A. M. (1997). The influence of pre-failure soil stiffness on the numerical analysis of tunnel construction. *Géotechnique* 47, No. 3, 693–712.

Amorosi, A. & Sangirardi, M. (2021). Coupled three-dimensional analysis of the progressive tunnelling-induced damage to masonry buildings: is it always worth it? *Tunnelling and Underground Space Technology*, *118*, 104173.

Amorosi, A., Boldini, D., de Felice, G., Malena, M. & Sebastianelli, M. (2014). Tunnelling-induced deformation and damage on historical masonry structures. *Géotechnique*, 64(2), 118–130.

Attewell, P. B., Yeates, J. & Selby, A. R. (1986). Soil movements induced by tunnelling and their effects on pipelines and structures. Blackie, Glasgow.

Augarde, C. E. & Burd, H. J. (2001). Three-dimensional finite element analysis of lined tunnels. *International Journal for Numerical and Analytical Methods in Geomechanics*, 25(3), 243–262.

Augenti, N. (2006). Seismic behaviour of irregular masonry walls. In *Proceedings of the 1st European Conference on Earthquake Engineering and Seismology*, Geneva.

Bakerloo line extension. (2019). Background to Consultation Summary Report October 2019. https://consultations.tfl.gov.uk/tube/bakerloo-extension/user_uploads/background-summary-report.pdf, Accessed: March 2020.

Belmouden, Y., & Lestuzzi, P. (2009). An equivalent frame model for seismic analysis of masonry and reinforced concrete buildings. *Construction and Building Materials*, *23*(1), 40–53.

Benz, T., Vermeer, P.A., Schwab, R., (2009). A small-strain overlay model. *Int. J. Numer. Anal. Meth. Geomech.*, 33 (1), 25–44.

Bilotta, E., Paolillo, A., Russo, G., & Aversa, S. (2017). Displacements induced by tunnelling under a historical building. *Tunnelling and Underground Space Technology*, *61*, 221–232.

Boscardin, M. D. & Cording, E. J. (1989). Building response to the excavation-induced

settlement. *Journal of Geotechnical Engineering*, 115(1): 1–21.

Bracchi, S., Rota, M., Penna, A., & Magenes, G. (2015). Consideration of modelling uncertainties in the seismic assessment of masonry buildings by equivalent-frame approach. *Bulletin of Earthquake Engineering*, *13*(11), 3423–3448.

Brinkgreve, R.B.J., Kumarswamy, S., Swolfs, W.M., Waterman, D., Chersaru, A. & Bonnier, P.G. (2022). Plaxis 3D User Manual.

Brown, P. T., & Booker, J. R. (1985). Finite element analysis of excavation. *Computers and Geotechnics*, *1*(3), 207–220.

Burd (2023). S2M model analyses and results. (personal communication).

Burd, H. J., Houlsby, G. T., Augarde, C. E. & Liu, G. (2000). Modelling tunnelling-induced settlement of masonry buildings. *Proceedings of the Institution of Civil Engineers-Geotechnical Engineering*, 143(1), 17–29.

Burd, H. J., Yiu, W. N., Acikgoz, S. & Martin, C. M. (2022). Soil-foundation interaction model for the assessment of tunnelling-induced damage to masonry buildings. *Tunnelling and Underground Space Technology*, *119*.

Burland, J. B. & Wroth, C. P. (1974). Settlement of buildings and associated damage: Session V review paper. *Conference on Settlement of Structures*, 611–654.

Burland, J. B. (2001). Assessment methods used in design, In *Building Response to Tunnelling: Case Studies from Construction of the Jubilee Line Extension, London*, Vol. 1, Thomas Telford, pp. 23–43.

Burland, J. B., Broms, B. B. & De Mello, V. F. B. (1977). Behaviour of Foundations and Structures. In *9th International Conference on Soil Mechanics and Foundation Engineering*, (pp. 495–546).

Caliò, I., Marletta, M. & Pantò, B. (2012). A new discrete element model for the evaluation of the seismic behaviour of unreinforced masonry buildings. *Engineering Structures*, *40*, 327–338.

D'Asdia, P. & Viskovic A. (1995). Analyses of a masonry wall subjected to horizontal actions on its plane, employing a non-linear procedure using changing shape finite elements. *Trans Modell Simul*, 10:519–26 [WIT Press].

Dalgic, K. D., Gulen, B., Liu, Y., Acikgoz, S., Burd, H., Marasli, M. & Ilki, A. (2023). Masonry buildings subjected to settlements: Half-scale testing, detailed measurements, and insights into behaviour. *Engineering Structures*, *278*.

Dalgic, K. D., Gulen, D. B., Acikgoz, S., Burd, H., Hendriks, M. A. N., Giardina, G. & Ilki, A. (2021). Large Scale Experimental Settlement Tests to Evaluate Structural Models for Tunnelling-Induced Damage Analysis. In: Barla, M., Di Donna, A., Sterpi, D. (eds). *Challenges and Innovations in Geomechanics. IACMAG 2021. Lecture Notes in Civil*

Engineering, vol 126. Springer, Cham.

Dalgic, K. D., Hendriks, M. A. N., Ilki, A. & Broere, W. (2018). A two-stage numerical analysis approach for the assessment of the settlement response of the pre-damaged historic Hoca Pasha Mosque. *International Journal of Architectural Heritage*, *00*(00), 1–21.

Dalgic, K. D., Yesilyurt, C., Gulen, B., Liu, Y., Acikgoz, S., Marasli, M. & Ilki, A. (2023). Design and Construction of a Test Setup to Investigate Ground Settlement Response of Large-Scale Masonry Building Models. In: Chastre, C., et al. *Testing and Experimentation in Civil Engineering*. TEST&E 2022. RILEM Bookseries, vol 41. Springer, Cham.

Deck, O. & Singh, A. (2012). Analytical model for the prediction of building deflections induced by ground movements. *International Journal for Numerical and Analytical Methods in Geomechanics*, *36*(1), 62–84.

Department for Communities and Local Government. (2008). English Housing Survey: Housing stock report.

Department for Transport. (2023). Department for Transport Annual Report and Accounts 2022-23 https://assets.publishing.service.gov.uk/government/uploads/system/uploads/attachment_data/file/1172898/dft-annual-report-and-accounts-2022-23.pdf Accessed: August 2023.

DIANA Finite Element Analysis User's Manual Element Library. Release 10.2 September (2017). DIANA FEA BV Delft, The Netherlands.

Doherty, J. P. & Muir Wood, D. (2013). An extended Mohr–Coulomb (EMC) model for predicting the settlement of shallow foundations on sand. *Géotechnique*, 63, No. 8, 661–673.

Dolce, M. (1991). Schematizzazione e modellazione degli edifici in muratura soggetti ad azioni sismiche. *L'industria delle Costruzioni*, 25:44–57. [in Italian].

Farrell, R., Mair, R., Sciotti, A. & Pigorini, A. (2014). Building response to tunnelling. *Soils and Foundations*, *54*(3), 269–279.

Fogang, V. (2021). Timoshenko Beam Theory: First-Order Analysis, Second-Order Analysis, Stability, and Vibration Analysis Using the Finite Difference Method. Preprints, 2021050252.

Giardina, G., Marini, A., Hendriks, M.A.N., Rots, J.G., Rizzardini, F. & Giuriani, E. (2012). Experimental analysis of a masonry facade subject to tunnelling-induced settlement. *Eng Struct*, 45:421–34.

Giardina, G., van de Graaf, A. V., Hendriks, M. A. N., Rots, J. G. & Marini, A. (2013). Numerical analysis of a masonry façade subject to tunnelling-induced settlements. *Engineering Structures*, *54*, 234–247.

Giordano, A., Mele, E. & De Luca, A. (2002). Modelling of historical masonry structures: Comparison of different approaches through a case study. *Engineering Structures*, *24*(8),

1057–1069.

Gulen, D. B., Acikgoz, S. & Burd, H. J. (2021). Equivalent frame model for the assessment of tunnel-induced damage to masonry buildings. In *Proceedings of the Tenth International Symposium on Geotechnical Aspects of Underground Construction in Soft Ground*, (eds Elshafie, M., Viggiani, G. & Mair, R.). IS-Cambridge 2022, Cambridge, United Kingdom, 27-29 June 2022.

Gulen, D. B., Acikgoz, S. & Burd, H. J. (2022). A macro-element model for the assessment of tunnelling-induced damage to masonry buildings. *Geotechnical Engineering for the Preservation of Monuments and Historic Sites III - Proceedings of the 3rd International Issmge TC301 Symposium, 2022*, 1026–1038.

Harris, D. I. & Franzius, J. N. (2006). Settlement assessment of running tunnels–a generic approach. *Geotechnical Aspects of Underground Construction in Soft Ground: Proceedings of the 5th International Symposium TC28*, Amsterdam, the Netherlands, 15-17 June 2005, 225.

Hills, D. A. & Dini, D. (2011). Characteristics of the process zone at sharp notch roots. *International Journal of Solids and Structures*, *48*(14–15), 2177–2183.

Houlsby, G. T. (1999). A model for the variable stiffness of undrained clay, In *Proc. 2nd International Symposium on Pre-Failure Deformation Characteristics of Geomaterials*, Vol. 1, Turin, Italy, pp. 443–450.

Houlsby, G. T., Liu, G. & Augarde, C. E. (2000). A tying scheme for imposing displacement constraints in finite element analysis. *Communications in Numerical Methods in Engineering*, 16(10), 721–732.

Infrastructure and Projects Authority.(2017). Analysis of the National Infrastructure and Construction Pipeline.https://assets.publishing.service.gov.uk/media/5a82a589ed915d74e3402d92/Analysis_of_National_Infrastructure_and_Construction_Pipeline_2017.pdf

International Tunnelling and Underground Space Association. (2019). Tunnel Market Survey.

Ispir, M. & Ilki A. (2013). Behavior of Historical Unreinforced Brick Masonry Walls under Monotonic and Cyclic Compression. *Arab J Sci Eng*, 38:1993–2007.

Ispir, M. (2010). A comprehensive experimental research on the behaviour of historical brick masonry walls of 19th-century masonry buildings. PhD Thesis, Istanbul Technical University.

Iwan, W. D. (1967). On a Class of Models for the Yielding Behavior of Continuous and Composite Systems. ASME. *J. Appl. Mech*., 34(3): 612–617.

Lagomarsino, S., Penna, A., Galasco, A. & Cattari, S. (2013). TREMURI program: An equivalent frame model for the nonlinear seismic analysis of masonry buildings.

Engineering Structures, *56*, 1787–1799.

Lasciarrea, W. G., Amorosi, A., Boldini, D., de Felice, G. & Malena, M. (2019). Jointed Masonry Model: A constitutive law for 3D soil-structure interaction analysis. *Engineering Structures*, *201*.

Liu, Y. (2023). Displacement and Damage Monitoring for Masonry Buildings Subjected to Ground Movements Induced by Underground Construction. DPhil Thesis, University of Oxford.

Losacco, N., Burghignoli, A. & Callisto, L. (2014). Uncoupled evaluation of the structural damage induced by tunnelling. *Géotechnique*, *64*(8), 646–656.

Lourenço, P. B. (1996). Computational strategies for masonry structures. PhD Thesis (Vol. 70(08).

Macchiarulo, V., Giardina, G., Milillo, P., González Martí, J., Sánchez, J. & Dejong, M. J. (2019). Settlement-induced building damage assessment using MT-INSAR data for the crossrail case study in London. *International Conference on Smart Infrastructure and Construction 2019, ICSIC 2019: Driving Data-Informed Decision-Making*, 721–727.

Macorini, L. & Izzuddin, B. A. (2011). A non-linear interface element for 3D mesoscale analysis of brick-masonry structures. *International Journal for Numerical Methods in Engineering*, *85*(12), 1584–1608.

Magenes, G. & Della Fontana, A. (1998). Simplified non-linear seismic analysis of masonry buildings. *Proc. of the British Masonry Society*, Vol. 8, pp. 190-195.

Mair, R. J. & Taylor, R. N. (1997). Theme lecture: bored tunneling in the urban environment. In *Proceedings of the 14th international conference on soil mechanics and foundation engineering*, Hamburg, 6–12 September 1997, pp. 2353–2385. Rotterdam, the Netherlands: Balkema.

Mair, R. J. (2013). Tunnelling and deep excavations: ground movements and their effects. In *Proceedings of the 15th European Conference on Soil Mechanics and Geotechnical Engineering - Geotechnics of Hard Soils - Weak Rocks (Part 4):* Vol. l (Issue Part 4).

Mair, R. J., Taylor, R. N. & Burland, J. B. (1996). Prediction of ground movements and assessment of risk of building damage due to bored tunnelling. In *Proc. 4th International Symposium on Geotechnical Aspects of Underground Construction in Soft Ground*, AA Balkema, pp. 713–718.

Maleki, M., Sereshteh, M., Mousivand, M. & Bayat, M. (2011). An equivalent beam model for the analysis of tunnel-building interaction. *Tunnelling and Underground Space Technology*. 26, 524–533.

Marini, A. & Spacone, E. (2006). Analysis of reinforced concrete elements including shear effects. *ACI Structural Journal*, *103*(5), 645–655.

Martino, R., Spacone, E. & Kingsley, G. (2000). Nonlinear Pushover Analysis of R/C

Structures. *Structures Congress, Advanced Technology in Structural Engineering*, M. Elgaaly, ed., ASCE, 8.

Minga, E. (2017). 3D Meso- and Macro-Scale Models for Nonlinear Analysis of Masonry Systems. PhD thesis, Imperial College London.

Neuenhofer, A. & Filippou, F. C. (1997). Evaluation of Nonlinear Frame Finite-Element Models. *Journal of Structural Engineering*, *123*(7), 958–966.

O'Reilly, M. P. & New, B. M. (1982). Settlements above tunnels in the United Kingdom- their magnitude and prediction. In M. J. Jones (ed.). *Proceedings of Tunnelling*, 82: 173–181. London, UK: Institute of Mining and Metallurgy.

Pascariello, M. N., Luciano, A., Bilotta, E., Acikgoz, S. & Mair, R. (2023). Numerical modelling of the response of two heritage masonry buildings to nearby tunnelling. *Tunnelling and Underground Space Technology*, *131*, 104845.

Peck, R. B. (1969). Deep excavations and tunnelling in soft ground. *Proc. 7th Int. Conf. Soil Mech. Found. Engng*, 225–290.

Pickhaver, J. A., Burd, H. J. & Houlsby, G. T. (2010). An equivalent beam method to model masonry buildings in 3D finite element analysis. *Computers and Structures*, *88*(19–20), 1049–1063.

Pickles D. (2016). Energy Efficiency and Historic Buildings: Insulating Suspended Timber Floors.

Potts, D. M. & Zdravković, L. (2001). Finite element analysis in geotechnical engineering application. Thomas Telford, London.

Prosperi, A., Longo, M., Korswagen, P.A., Korff, M. & Rots, J.G. (2024). Accurate and Efficient 2D Modelling of Historical Masonry Buildings Subjected to Settlements in Comparison to 3D Approaches. In: Endo, Y., Hanazato, T. (eds) *Structural Analysis of Historical Constructions*. SAHC 2023. RILEM Bookseries, vol 46. Springer, Cham.

Quagliarini, E., Maracchini, G. & Clementi, F. (2017). Uses and limits of the Equivalent Frame Model on existing unreinforced masonry buildings for assessing their seismic risk: A review. *Journal of Building Engineering*, *10*, 166–182.

Rampello, S., Callisto, L., Viggiani, G.M.B. & Soccodato, F. (2012). Evaluating the effects of tunnelling on historical buildings: the example of a new subway in Rome. Geomech. Tunnelling, 5 (3) (2012), pp. 275-299.

Rankin, W. J. (1988). Ground movements resulting from urban tunnelling: predictions and effects. In *Engineering Geology of Underground Movements. Proc. of the 23rd Annual Conference of the Engineering Group of the Geological Society*, Vol. 5, pp. 79–92.

Ritter, S. (2018). Experiments in tunnel-soil-structure interaction. PhD thesis, University of

Cambridge.

Roca, P., Molins, C. & Marí, A. R. (2005). Strength Capacity of Masonry Wall Structures by the Equivalent Frame Method. *Journal of Structural Engineering*, *131*(10), 1601–1610.

Rowe, R. K., Lo, K. Y. & Kack, G. J. (1983). A method of estimating surface settlement above tunnels constructed in soft ground. *Canadian Geotechnical Journal*, 20(1), 11–22.

Sangirardi, M. (2023). 3D FE PLAXIS model analyses and results (personal communication).

Sangirardi, M., Gulen, D. B., Acikgoz, S. & Burd, H. J. (2023). Calibration of a simplified soil-structure interaction model for rapid assessment of tunnelling-induced damage in masonry buildings founded on shallow footings. Proceedings 10th NUMGE 2023. In *10th European Conference on Numerical Methods in Geotechnical Engineering*, Zdravkovic L, Kontoe S, Taborda DMG, Tsiampousi A (eds).

Schanz, T., Vermeer, P. & Bonnier, P. (1999). The hardening soil model: formulation and verification. In: *Proceedings of 1st international PLAXIS symposium on beyond 2000 in Computational Geotechnics*. Balkema. p. 281–96.

Siano, R., Roca, P., Camata, G., Pelà, L., Sepe, V., Spacone, E. & Petracca, M. (2018). Numerical investigation of non-linear equivalent-frame models for regular masonry walls. *Engineering Structures*, *173*, 512–529.

Spacone, E., Filippou, F. C. & Taucer, F. F. (1996). Fiber Beam-Column Model for Nonlinear Analysis of R/C Frames, Part I: Formulation. *Earthquake Engineering and Structural Dynamics*, V. 25, pp. 711-725.

Taucer, F. F., Spacone, E. & Filippou, F. C. (1991). A Fiber Beam-Column Element for Seismic Response Analysis of Reinforced Concrete Structures.

Timoshenko, S. (1957). Strength of materials - Part I, D van Nostrand, London.

Torp-Petersen, G. E. & Black, M. G. (2001). Geotechnical investigation and assessment of potential building damage arising from ground movements: CrossRail. *Proceedings of the Institution of Civil Engineers: Transport*, *147*(2), 107–119.

Viggiani, G. & Soccodato, F. M. (2004). Predicting tunnelling-induced displacements and associated damage to structures. *Rivista Italiana di Geotechnical*, 4, 11-25.

Wan, M. S., Standing, J. R., Potts, D. & Burland, J. B. (2017). Measured short-term ground surface response to EPBM tunnelling in London Clay. *Géotechnique*. 67(5), 420–445.

Withers, A. D. (2001), Keetons Estate, Bermondsey, In *Building Response to Tunnelling: Case Studies from Construction of the Jubilee Line Extension*, London. Vol. 2, Thomas Telford, pp. 755–774.

Yiu, W. N., Burd, H. J. & Martin, C. M. (2017a). Finite-element modelling for the assessment

of tunnel-induced damage to a masonry building. *Géotechnique*, *67*(9), 780–794.

Yiu, W. N., Burd, H. J. & Martin, C. M. (2017b). Soil–building interaction in finite element analysis of tunnelling-induced building damage. In *Proceedings of the IV international conference on computational methods in tunneling and subsurface engineering*, (eds G. Hofstetter, K. Bergmeister, J. Eberhardsteiner, G. Meschke and H. F. Schweiger), Innsbruck, Austria: University of Innsbruck. 381–388.